Studies of Biomolecular Self-organization through Time-Resolved Fluorescence Microscopy

Jan-Hagen Krohn

München 2025

Studies of Biomolecular Self-organization through Time-Resolved Fluorescence Microscopy

Jan-Hagen Krohn

Dissertation
an der Fakultät für Physik
der Ludwig–Maximilians–Universität
München

vorgelegt von
Jan-Hagen Krohn
aus Brunsbüttel, Deutschland

München, den 29.April 2025

Erstgutachter: Prof. Dr. Petra Schwille
Zweitgutachter: Prof. Dr. Don C. Lamb
Tag der mündlichen Prüfung: 21. Juli 2025

Zusammenfassung

Technologischer Fortschritt war und ist Treiber wissenschaftlichen Fortschritts. Zur Beantwortung schwieriger Fragen ist oft spezialisierte Technologie nötig, sowie angepasste Strategien in der Anwendung dieser Technologie. Der *bottom-up*-Ansatz der synthetischen Biologie stellt uns viele Werkzeuge bereit zur Untersuchung der Prinzipien, welche der Organisation des Lebens zugrunde liegen. Dazu gehören künstliche Membransysteme, Tröpfchen aus phasentrennenden Proteinen, auf Speicherung und Nutzung von Information programmierte Nukleinsäuren und viele andere. Um die Details der zugrunde liegenden physikalischen Chemie zu erforschen, sind oft neuartige biophysikalische Techniken nötig. Fluoreszenztechniken zeichnen sich durch hohe Sensitivität sowie räumliche und zeitliche Auflösung aus, und sind somit gut geeignet fur Untersuchungen der Dynamiken von Biomolekülen.

Die Anforderungen an Methoden steigt dabei stetig mit zunehmender Komplexität der biomimetischen Systeme und zunehmender Bedeutung quantitativer Fragestellungen. Wir verbessern zeitaufgelöste Fluoreszenztechniken für die Anwendung an diversen biomolekularen Systemen welche derzeit für *bottom-up* synthetische Biologie von Interesse sind. Wir entwickeln verbesserte Messvorschriften und damit assoziierte Software inbesondere für Fluoreszenz-Korrelationsspektroskopie.

Wir untersuchen die Selbsassemblierung von DNA-Origami-Nanopartikeln im Kontext biologischer Membranen mit Einzelmolekülmikroskopie. Wir verbinden dabei *DNA-PAINT*-Mikroskopie-basierte Charakterisierung von Morphologie mit Mobilitätsanalyse mittels Einzelmolekülverfolgung und Untersuchung des zeitlichen Verlaufs der Selfsassemblierung durch Bildkorrelationsspektroskopie. In Studien zur Entmischung von Proteinen befassen wir uns mit experimentellen Herausforderungen in konfokaler Fluoreszenz-Korrelationsspektroskopie an biomolekularen Kondensaten. Wir etablieren experimentelle Standards und stellen Software für automatisierte Korrektur häufiger Artefakte in den Daten bereit. Als nächstes widmen wir uns filamentbildenden Proteinen und allgemeiner polydispersen Teilchenmischungen. Hier stellen wir uns die Frage, wodurch Bestimmung von Partikelgrößen-Verteilungen mittels Fluoreszenz-Korrelationsspektroskopie limitiert ist. Wir diskutieren die experimentellen Herausforderungen und stellen einen allgemeinen Rahmen für die Datenanalyse vor. Zuletzt stellen wir ein weiteres Software-Tool vor für teilautomatisierte Aufnahme und Analyse für Fluoreszenz-Korrelationsspektroskopie-Daten mit hoher Qualität an biologischen Membranen. Dabei tragen wir publizierte Ideen zusammen, welche sich für diese Art von Probe typischen Herausforderungen widmen.

Die entwickelten Messvorschriften und Hilfmittel werden der Forschung in der synthetischen Biologie helfen, mit verschiedene erwartbaren Schwierigkeiten in zukünftigen quantitativen Experimenten umzugehen. Damit eröffnen sich nun eine große Zahl wissenschaftlicher Fragestellungen zu Selbsassemblierung und Selbstorganisation auch ausserhalb des Gleichgewichts, welche in der Folge angegangen werden können. Während die Methoden an und für biomimetische Systeme entwickelt wurden, sollten die hier erzielten Erkenntnisse auch für Lebendzellstudien von interesse sein. In diesen besteht ebenfalls ein großer Bedarf an verbesserten experimentellen Methoden zur Bewältigung im Wesentlichen der gleichen Herausforderungen.

Abstract

Progress in technology has always been a driver of progress in science. Answering challenging questions requires bespoke technology and strategies in its use. The expanding toolbox of bottom-up synthetic biology allows us to study the organization principles underlying life. This include artificial membrane systems, phase-separating protein droplets, nucleic acids programmed to encode and use information, and many others. To study the details of the underlying physical chemistry, novel biophysical techniques are often needed. Fluorescence techniques allow studying the dynamics of biomolecules with high sensitivity and at high spatial and temporal resolution.

With increasing complexity of biomimetic systems and scientific questions moving towards more detailled quantitative characterization, the challenges encountered by the methods employed also become greater. We adapt and improve time-resolved fluorescence techniques for application to various biomolecular systems currently of interest to bottom-up synthetic biology. We improve experimental protocols and develop associated software tools especially for fluorescence correlation spectroscopy.

We investigate self-assembly of DNA origami nanoparticles in the context of biological membranes using single molecule imaging. DNA-PAINT microscopy-based morphology characterization is complemented by single particle tracking and image correlation spectroscopy to characterize particle mobility and the time-course of assembly. Turning to liquid-liquid phase separation, we investigate the experimental challenges that arise in confocal fluorescence correlation spectroscopy in protein condensates. We propose best practices in experiment design, and distribute software for data processing that automates compensation of various frequent artifacts. We then turn to filament-forming proteins, and polydisperse particle mixtures in general. Here, we ask what limits the performance of fluorescence correlation spectroscopy in characterizing particle size distributions. We discuss experimental challenges, and propose a general framework for data analysis. Finally, another software tool is developed for partial automation of high-quality acquisition and analysis of fluorescence correlation spectroscopy on membranes, based on published ideas for dealing with challenges characteristic for this setting.

The developed protocols and tools will be of use for the synthetic biology community to avoid pitfalls in quantitative measurements. Thus, many questions relating to self-assembly and non-equilibrium self-organization may be addressed in the future. Of note, while the protocols and tools have been developed on and for synthetic biomimetic samples, the insights gained should be just as valuable for live-cell studies. There, experimenters face the urgent need for improved methods to tackle essentially the same challenges.

Publications and Manuscripts

Publications Included in this Thesis in Full

Qutbuddin Y[†], **Krohn JH** [†], Brüggenthies GA, Stein J, Gavrilović S,Stehr F, Schwille P: Design Features to Accelerate the Higher-Order Assembly of DNA Origami on Membranes. *J. Phys. Chem. B. 2021* (see Chapter 4) [1]

Krohn JH, Babl L, Isnel L, Qutbuddin Y, Schwille P: Measuring Partition Coefficients of In Vitro Biomolecular Condensates Using Fluorescence Correlation Spectroscopy, in Dame RT: Bacterial Chromatin: Methods and Protocols. *Methods in Molecular Biology 2024* (see Chapter 5) [2]

Krohn JH, Mamot A, Kaletta N, Qutbuddin Y, Schwille P: Fluorescence correlation spectroscopy for particle sizing: A notorious challenge. *Biophysical Journal 2025* (see Chapter 6) [3]

Publication Partially Described in this Thesis

Merino-Salomón A, Scheider J, Babl L **Krohn JH**, Sobrinos-Sanguino M, Schäfer T, Luque-Ortega JR, Alfonso C, Jiménez M, Jasnin M, Schwille P, Rivas G: Crosslinking by ZapD drives the assembly of short FtsZ filaments into toroidal structures in solution. *eLife 2025* (see Chapter 7) [4]

Additional Publications not Included

Balakrishnan A, Hemmen K, Choudhury S, **Krohn JH**, Jansen K, Friedrich M, Beliu G, Sauer M, Lohse M, Heinze KG: Unraveling the hidden temporal range of fast β2-adrenergic receptor mobility by time-resolved fluorescence. *Communications Biology 2022* [5]

Kanaparthi D, Lampe M, **Krohn JH**, Zhu B, Klingl A, Lueders T: The reproduction of gram-negative protoplasts and the influence of environmental conditions on this process. *iScience 2023* [6]

Kanaparthi D, Lampe M, **Krohn JH**, Zhu B, Hildebrand F, Broesen T, Klingl A, Phapale P, Lueders T: The reproduction process of Gram-positive protocells. *Sci Rep 2024* [7]

Guinart A[†], Qutbuddin Y[†], Ryabchun A, **Krohn JH**, Schwille P, Feringa BL: Elucidating the physicochemical processes of light activated rotary motors embedded in lipid membranes. *accepted manuscript, Chem 2025*

Betaneli V, **Krohn JH**, Mücksch J, Schwille P: Fluorescence Correlation Spectroscopy to Examine Protein–Lipid Interactions in Membranes, in Kleinschmidt JH: Lipid-Protein Interactions: Methods and Protocols *accepted manuscript, Methods in Molecular Biology 2025* (third, revised edition of [8])

[†] These authors contributed equally to this work

Contents

Part I

Scientific Context

1 Introduction

1.1 Origin of life and synthetic biology

Many big questions that have puzzled humanity since the early days of known history could be answered once the right technology was within reach. Telescopes revealed critical details about the motion of planets that led to an understanding of the organization of the solar system, and keep revealing more and more information about the nature of astronomical objects [9]. Microscopes allowed us understand structure and function of organisms as emerging from the organization of individual cells [10, 11]. X-ray diffraction and particle accelerators allow studying the structure of matter at (sub-)atomic level [12, 13].

The question of what is the origin of life encounters a special challenge: What we would like to study simply does not exist any more, and will not re-appear. No geological record of the origin of life is preserved. Life cannot realistically emerge again on Earth a second time either, as existing life occupies practically every habitable niche of the planet and would consume the prebiotic molecules as nutrients. Therefore, the traditional empirical approach in science fails to deliver definite answers of how and where life emerged. What is possible is to empirically study extant life on its most fundamental level, recreate its building blocks, and understand how biological function emerges from their interplay. That way, hypotheses about the origin of life can be generated, whose plausibility can then be judged given reconstructions of early Earth environments. Albert Eschenmoser rationalized this approach by stating that "[t]he origin of life cannot be 'discovered', it has to be 're-invented'" [14].

This reconstruction of fundamental biological functions is the topic of bottom-up synthetic biology [15]. A typical approach in bottom-up synthetic biology is to mix in a test tube a known set of compounds, which can be naturally derived or fully synthetic, and find conditions in which they replicate, or modify, a known function in biology, such as sorting of molecules into distinct positions, or replication of genetic information. That way, minimal combinations of modules needed for a given function of interest can be identified. In the following, hypotheses can be found about which molecules and environmental cues on early Earth could have played the roles of these modules.

Bottom-up synthetic biology is closely connected to biophysics. The bottom-up approach yields systems of limited complexity and noise. Therefore, they are more accessible to detailled physical characterization and modelling than intact living systems. Biophysical characterization helps in understanding exactly how the interac-

tion of biological or biomimetic modules leads to life-like functionality. This bring us back to the topic of technological progress, as a driver of scientific progress: Even though we cannot expect a definite answer about the origin of life no matter what technologies become available, the ability to perform more and more detailled biophysical measurements is crucial to make progress towards developing and testing viable hypotheses.

1.2 Self-organization in biology

A recurring theme in biophysics, especially in the context of bottom-up synthetic biology, is self-organization. Organisms with anatomy as complex as vertebrates emerge from a single zygote with little external instructions. Thus, life is capable of highly complex intrinsic organizing principles [16,17]. However, as life is constrained by the laws of chemistry and physics, it must be possible to explain these self-organization principles physically. Self-organization occurs on many scales, from molecules working together to perform a complex function, to the dynamics of swarms of fish or birds. Bottom-up synthetic biology and the study of the origin of life are mostly concerned with molecular self-organization, though, as it forms the basis which then allows self-organization to occur at larger scales as well.

The key principle of biological self-organization is to exploit energy taken up from the environment to create internal order [16, 18]. Obvious examples where one can understand easily how life uses energy to achieve organized processes on a (sub)-cellular level are active processes involving the cytoskeleton like the contraction of muscle fibers, cargo transport along axons, or segregation of cell content during cell division [16, 19] These examples are only obvious realizations of the general concept that living systems operate far from thermodynamic equilibrium. Symmetry of chemical reactions is broken, with reactions preferentially proceeding in one direction and producing specific stereoisomers of the products [20]. Molecules are kept in distinct compartments, rather than mixing homogeneously [21,22]. Processes are held in locked states until a suitable trigger allows them to proceed [23]. All this is achieved by directly or indirectly coupling the processes of life on a molecular level to the degradation of high-energy molecules, typically adenosine triphosphate (ATP). Various proteins are optimized in evolution to perform a specific function while degrading ATP, thereby biasing that function to proceed in an ordered, unidirectional manner. Regeneration of ATP in turn is couled to the degradation of nutrients.

Distinct from self-organization in the strict sense, but closely connected, is the topic of self-assembly (Section 2.5). Many biomolecules can assemble from solution into mesoscopic complexes which possess properties that the individual macromolecule cannot provide. A paradigmatic example of self-assembly of proteins is the cytoskeleton, where individually globular proteins self-assemble into long filaments that serve as scaffold along which other processes are organized. Self-assembly is thus often at the heart of non-equilibrium self-organization. Another related process of interest is phase separation, *i.e.*, the macroscopic segregation of molecules into distinct subvolumes (Section 2.4). Both self-assembly and phase separation are key tools for synthetic biology to build complex structures from simple building blocks, and both likely played important roles for the origin of life.

Self-organization is characterized by the emergence of system properties that are

not obvious from the properties of system constituents alone. Therefore, their study often requires investigation at the boundary between the dynamics of individual particles and macroscopic material properties. High-end microscopy is therefore a crucial technology for the study of molecular self-organization processes.

1.3 From "pictures" to quantitative biophysics

Some of the earliest scientific instruments in human history were tools to aid visual observation of nature. During ancient and medieval times, astronomical observation was a driver of developments in technology and mathematics. While relying on the resolution and sensitivity of the naked eye, these studies already used instruments to assist determination of positions or time [9]. Many authors argue that the scientific revolution of the 17th and 18th century was enabled by a small number of key inventions, of which two are instruments of visual observation: the telescope and the microscope, complemented depending on the author by *e.g.*, the vacuum pump and the pendulum clock [24, 25].

In more modern times, Nobel prizes are often cited as proof of the significance of a topic for science and technology. The very first physics Nobel prize was awarded to Wilhelm C. Röntgen in 1901 for the discovery of X-rays, which had been immediately recognized as a means of observing structures that were previously invisible. Recent awards went to Eric Betzig, Stefan W. Hell, and William E. Moerner in 2014 for the development of super-resolution light microscopy, and to Jacques Dubochet, Joachim Frank and Richard Henderson in 2017 for the development of cryo-electron microscopy. These and other Nobel prizes for development of imaging technology, and many more awards with strong but more implicit links to scientific imaging, make clear that progress of imaging technology continues to drive progress in science.

Two related but distinct terms appeared in the previous two paragraphs: The "visual observation" was used when referring to science in the 17th and 18th centuries, and "scientific imaging" for more contemporary approaches. What changed? The introduction of photographic plates/film, eventually succeeded digital cameras and computers, drastically changed the meaning of images in science. The first implication the use of detectors other than the human eye in scientific imaging is the possibility to acquire observe outside the capabilities of human perception (sSection 2.6). Structures can be seen using types of radiation invisible to the human eye, and equally importantly, images can be generated at speed and/or sensitivity impossible for the human eye and brain. Further, these innovations opened opened the path for calibration, standardization, and automation of image acquisition and analysis. Images then are no longer simply "pictures" displaying structures of interest, but can be described in terms of quantitative brightness information. Such quantitative image data can then be interpreted based on physical models and/or statistical tools (Section 2.7).

This revolution of using images (acquired in optical microscopes) as quantitative scientific data is the background of the work described in this thesis. Modern microscopy techniques push the resolution and sensitivity of measurements to the single-molecule regime, allowing to observe the physical chemistry through which molecules undergo their respective functions in real time (Section 2.6). Fluorescence

techniques with their superior signal to background ratio are especially useful for measurements in the single-molecule regime (Section 2.1). Fluorescence techniques combined with modern high-sensitivity detection also a perfect match to time-resolved microscopy and spectroscopy down to the nanosecond time scale (and in some cases even faster), which is particularly valuable for obtaining information about physical mechanisms underlying dynamic processes like self-organization (Section 2.7).

Thus, extremely detailled quantitative data can be generated to study the mechanisms underlying self-organization. However, such studies remain technically challenging in for all but the simplest systems. Measurement protocols and data treatment need to be optimized to the specific challenges of the sample of interest. In this thesis, I describe the results of my work exploring and adapting time-resolved (near) single-molecule fluorscence microscopy techniques for the study of multiple self-organizing systems of interest to the bottom-up synthetic biology community.

2
Theoretical Background

2.1 Fluorescence and Photophysics

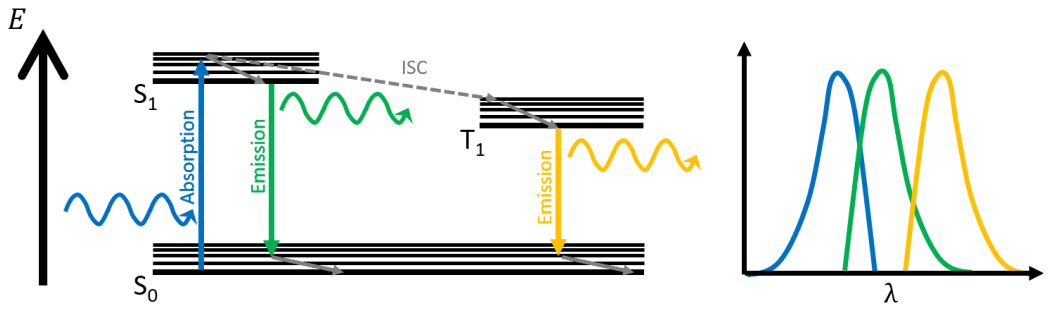

Figure 2.1. Jabłoński diagram of important photophysical transitions. The Jabłoński diagram illustrates the different major energy levels S_0, S_1, and T_1 and some of the transitions between them. Some transitions that are relevant in practical fluorescence microscopy or spectroscopy are omitted for clarity. The right panels schematically shows spectra for excitation (blue), fluorescence emission (green), and phosphorescence emission (yellow). ISC: Inter-System Crossing. See main text for details.

All studies described in this thesis use fluorescence techniques. The basis of fluorescence is a sequence of transitions between different energy levels, illustrated in the Jabłoński diagram Figure 2.1. The molecules in general reside at the electronic ground state called S_0, with higher electronic states S_N unoccupied. The S_N states are separated from the S_0 state by discrete energy gaps. To transition into the S_1 state, the molecule must absorb energy ΔE to match the energy gap (blue arrows). This can correspond for example to absorption of a photon of matching wavelength λ, where $\Delta E = hc\lambda^{-1}$ (ingoring the impact of refractive index). The S_1 state is instable, that

therefore will decay back to S_0 within a short time, releasing the excess energy. This energy release can again happen as emission of a photon, besides other pathways of which a few will be mentioned below (green arrows). This excitation upon photon absorption followed by emission of another photon is fluorescence. The S_0 and S_1 levels are split into further energy levels defined by rotational and vibrational degrees of freedom (back lines). Between excitation and emission, the molecule will rapidly relax into a low vibrational energy level within the S_1 electronic level (solid grey arrows), meaning that ΔE for emission is typically smaller than for excitation. Therefore, fluorescence emission is generally red-shifted compared to the excitation (spectra in the right of Figure 2.1). This is known as Stokes shift, after George Gabriel Stokes who first recognized this frequency shift [26].

The Stokes shift makes fluorescence a valuable tool for microscopy and spectroscopy: Excitation light (illumination) and emission (sample response) can be spectrally separated. A single modern spectral filter can suppress backscattered excitation light by more than 10^6-fold with only few-% loss in the detected fluorescent emission. Thus, fluorescence detection can be performed with very high signal to background ratio (Figure 2.2). In addition, the fact that the energy gaps, and thus wavelengths, of the fluorescence photocycle are specific to the fluorescent molecule means that multiple dyes can be observed in parallel, separating their signals by wavelengths (*via* sequential excitation, split detection, or both). Combination of fluorescence with chemical or biotechnological strategies for specific linkage of fluorescent dyes to target particles can therefore be used to characterize spatial and/or temporal relations between multiple structures of interest, with excellent sensitivity and specificity [27–29].

Besides the photocycle mentioned above, other transitions can occur upon excitation of fluorophores. For example, instead of decaying back into the S_0 level, a molecule can undergo intersystem crossing into the T_1 triplet state (ISC, dashed grey arrow in Figure 2.1). ISC is a "forbidden", rare transition. However, if ISC does occur, the T_1 state is typically relatively long-lived for the same reason. Transition from the T_1 state back to S_0 with photon emission is known as phosphorescence (yellow arrows). The T_1 state can also be quenched in triplet-triplet annihilation processes with oxygen, which under aerobic conditions is often the dominant pathway (not shown in Figure 2.1). A concern here is that this triplet quenching by oxygen leaves the oxygen molecule in a chemically highly reactive excited state, which can subsequently chemically react with the fluorophore (or another molecule in the vicinity). Such reactions mean degradation of the fluorophore, which is often irreversible. This degradation of fluorophores is referred to as photobleaching, as it is a photoinduced loss of fluorophore molecules. Note that photobleaching can also occur *via* other pathways that do not involve oxygen. Besides photobleaching, photodamage can also be relevant as damage to the sample itself, for example toxic effects on observed cells or photo-crosslinking of observed molecules [30].

The described fluorescence photocycle is a sequence of dicrete events. The time delays follow characteristic rates, which for a simple fluorophore under low-intensity conditions, where most particles reside in the ground state at any given time, can be summarized as:

$$\frac{\partial N_0}{dt} = -\frac{\partial N_1}{dt} \approx -\phi_{h\nu}\alpha N_0 + (k_r + k_{nr})\, N_1 \tag{2.1}$$

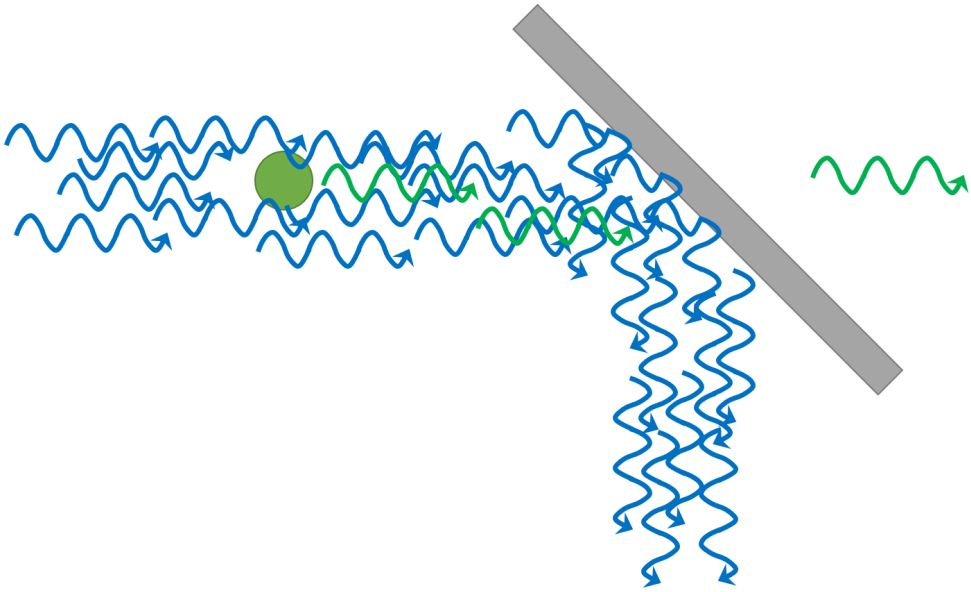

Figure 2.2. Specificity of fluorescence detection. Schematic illustration of how fluorescence allows extreme specificity of detection. An excess of excitation light (blue wavy arrows) excites fluorescence from a particle to be detected (green dot). While the intensity of emitted fluorescence is relatively low (green wavy arrows), insertion of a spectral cutoff filter (grey bar) that rejects light at the excitation wavelength but not at the detection wavelength allows to detect the available fluorescence signal with extremely low background.

where $N_{0/1}$ are the numbers of molecules in the $S_{0/1}$ states. ϕ_{hv} is the photon flux (photons per area and time), which is proportional to local illumination intensity. α is the interaction cross section for absorption/excitation. It is essentially a single-particle level description of the extinction coefficient accessible in standard absorption spectrometers. α is a wavelength-dependent parameter whose spectral profile corresponds to the blue line in Figure 2.1. $k_{r/nr}$ are the rate constants characterizing the radiative and nonradiative decays. Radiative and nonradiative decays are $S_1 \rightarrow S_0$ decay pathways with photon emission, or with the energy being lost nonradiatively into other channels, respectively. These rates also determine the fluorescence quantum yield η as overall probability for photon emission after excitation:

$$\eta = \frac{k_r}{k_r + k_{nr}} = k_r \tau_{fl} \tag{2.2}$$

The product $\alpha\eta$ thus determines the intrinsic brightness of the fluorophore, at least under non-saturating conditions. This intrinsic brightness, together with the excitation intensity and instrumental sensitivity of the microscope or spectrometer, yield the effective molecular brightness that we will encounter again in section 2.7. In Eq. 2.2, we introduce the excited-state lifetime $\tau_{fl} = [k_r + k_{nr}]^{-1}$ as the average time delay between excitation and excited state decay, commonly also called fluorescence lifetime. For many commonly-used dyes emitting at visible wavelengths, τ_{fl} is in the range of one or a few nanoseconds. k_r, and thus τ_{fl}, is physically linked to other parameters characterizing the fluorophore and its immediate environment [31]:

$$k_r = 2.880 \cdot 10^{-1} n^2 \frac{\int I(\tilde{\nu})\, d\tilde{\nu}}{\int I(\tilde{\nu})\, \tilde{\nu}^{-3} d\tilde{\nu}} \int \frac{\varepsilon(\tilde{\nu})}{\tilde{\nu}} d\tilde{\nu} \tag{2.3}$$

with wavenumber $\tilde{\nu}$ and refractive index n. In words, the radiative decay rate depends on the absorption and emission spectra in position and shape, on the magnitude of the absorption spectrum, and, importantly, on the surrounding refractive index. The latter in turn depends on the chemical composition of the environment. k_{nr} characterizes for example energy transfer processes quenching the excited state, which also depend on the chemical environment of the particle. Direct and distinct measurement of k_r and k_{nr} is difficult and requires specialized approaches (*e.g.*, [32,33]), but τ_{fl} is relatively easily accessible with contemporary time-correlated single photon counting (TCSPC) hardware (Figure 2.4 [34]).

In TCSPC, over an acquisition time of typically seconds to hours, the sample is repeatedly excited with short laser pulses (blue in Figure 2.4). The pulsed laser is synchronized with single-photon detection electronics for precise time tagging of fluorescence photons (green). Laser power is kept low to detect at most one photon per cycle (usually even less due to electronic dead time exceeding cycle duration). This way, histograms of excitation-emission delays representing the average profile of the excited state population decay are directly accumulated. τ_{fl} is then extracted by fitting to exponential decay models. Combining TCSPC or other lifetime measurement methods with microscopy is called fluorescence lifetime imaging microsocpy (FLIM, [34,35]), a robust method for characterizing heterogeneities of chemical environment within samples.

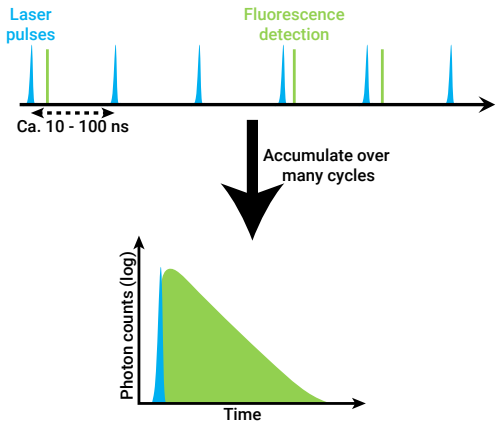

Figure 2.3. Time-correlated single photon counting (TCSPC). Following repeated excitation pulses, single photons are detected and a histogram accumulated of their excitation-emission delay. For details, see text.

Returning to Eqs. 2.1 and 2.2, among the processes neglected so far are ISC and other rare transitions, as well as vibrational relaxations, and stimulated emis-

sion. Stimulated emission is the inversion of absorption (*i.e.*, photoinduced emission), which becomes relevant under high-intensity conditions. Vibrational relaxations within the $S_{0/1}$ are much faster (typically picoseconds scale) than fluorescence emission and therefore have a negligible impact on the overall kinetics of the photocycle. Transitions into the triplet state and photoinduced isomerizations typically occur on much longer time scales. As a consequence, they occur rarely: Compare Eq. 2.2 to consider the quantum yield for a very slow transision. Therefore, they too have negligible impact on the photocycle under low excitation power conditions. As triplet or isomerization transitions lead to intermittency of fluorescence signal at longer time scales, these transitions are often also summarized as "blinking", which will be mentioned again later. As indicated above in the explanation of the role of oxygen in triplet state quenching, the rates of blinking processes can often be tuned over lange ranges, which does make them usable for many different purposes if they are controlled [36,37].

2.2 Light Microscopy

As mentioned in the previous section, fluorescence is a powerful tool for use in light microscopy. While light microscopes are diverse in construction and operating principles, they have in common that they are built to visualize, and in modern times quantitatively measure, structures that are too small to be visible to the naked eye. A unifying construction principle is the use of an objective lens with short focal length, which translates to high magnifying capabilities. Further lenses in the microscope's optical system may then further increase magnification, for example to help the human eye make full use of the available information. However, these additional lenses do not add further information to the image that is not captured by the objective. Therefore, the theoretical resolution limit of a microscope is determined by the objective lens as recongized by Ernst Abbe [38], often referred to as the Abbe limit or diffraction limit:

$$d_{min} = \frac{\lambda}{2NA} = \frac{\lambda}{2n \sin \alpha} \tag{2.4}$$

where d_{min} is the smallest distance at which two points are still distinguishable. NA is the numerical aperture of the objective, a measure of its light collection capabilities given by the opening half-angle α and the immersion medium refractive index n between objective and sample. λ is the wavelength used in observation. Wavelengths visible to the human eye, as well as the spectra of most commonly-used fluorophores, are restricted to $\lambda \gtrsim 400\,nm$ (shorter-wavelength fluorophores often having relatively poor photophysical properties). Obviously, $\sin \alpha \leq 1$, and practically useful refractive indices do not far exceed that of water ($n \approx 1.34$). $n \gtrsim 1.45$ is typically restricted to imaging of immobilized and polymer-embedded samples, or specialized applications. Therefore, in practice, features at scales much smaller than $d_{min} \approx 200\,nm$ usually remain unresolved.

In more detail, the resolution of a microscope is described by its point spread function (PSF). The PSF describes the blurred image that the microscope produces of an infinitesmally small point (individual emitter/scatterer particle) in the sample. An entire image then is a convolution of the spatial emitter distribution with the PSF.

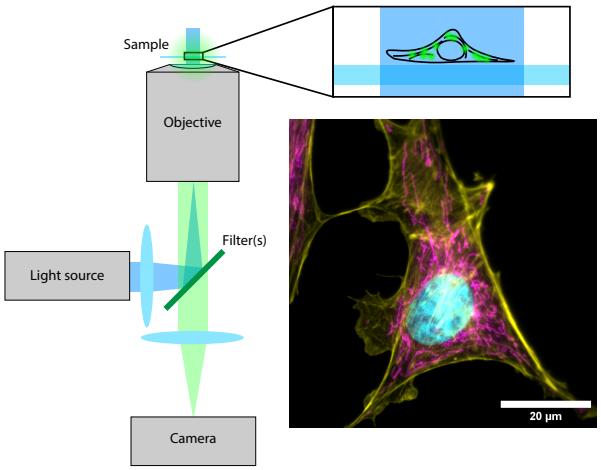

Figure 2.4. Simple fluorescence microscope. The schematic shows a simple fluorescence microscope setup. Light from the excitation light source is focused into the back focal plane of the objective to obtain even illumination within the sample. Fluorescence light is collected through the same objective, separated from back-scattered excitation light using spectral filters, and imaged onto a camera. The example image shows 3-color image acquired at a Zeiss Elyra7 microscope equipped with an 63x NA 1.46 oil immersion objective. Sample: Fixed adherent cells(FluoCells, Invitrogen) with fluorescently stained nuclei (cyan), actin (yellow), and mitochondria (magenta).

For a diffraction-limited microscope, the two-dimensional section through the point spread function in the focal plane is given by:

$$I(r) = I(0)\left[\frac{2J_1\left(\frac{2\pi rNA}{\lambda}\right)}{\frac{2\pi rNA}{\lambda}}\right]^2 \tag{2.5}$$

where r is the distance from the actual emitter position and $J_1(x)$ is a zero-order Bessel function of the first kind. This profile, known as an Airy pattern, consists of a pronounced central maximum, and a series of surrounding concentric rings (solid lines in Figure 2.5). For practical purposes, the Airy pattern is often approximated by a Gaussian profile, which is sufficiently accurate for many applications (red dashed lines in Figure 2.5). The Abbe resolution limit (Eq. 2.4) then approximately equals the full width at half maximum of the central maximum of the PSF.

The three-dimensional profile of the PSF is more complex, and different descriptions are used depending on the application. An approximation that will be used in later chapters is a simple three-dimensional Gaussian ellipsoid (see Section 2.7, Eq. 2.23). The 3D-Gaussian model is a rather crude approximation, but convenient and sufficient for many purposes like those described in Section 2.7. An alternative, slightly more accurate, model is the Gaussian beam propagation model, also sometimes called Gauss-Lorentzian model. In this model, the intensity distribution in the plane perpendicular to the optical axis is described by a Gaussian profile, while the

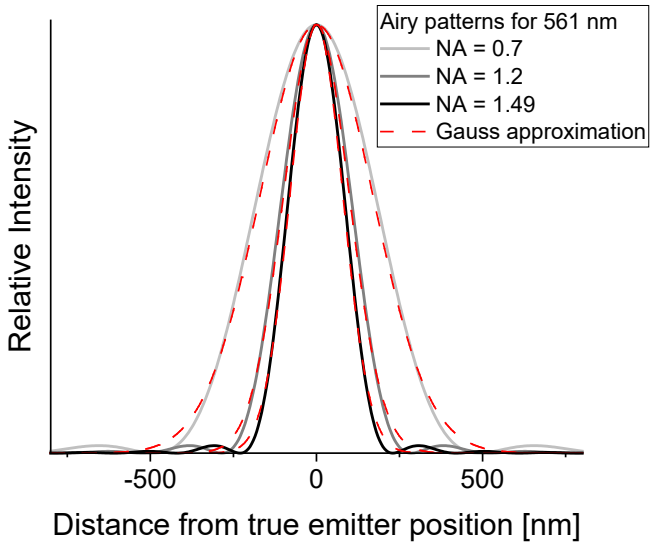

Figure 2.5. Airy pattern. Shown are Airy patterns calculated according to Eq. 2.5 for different numerical apertures: A typical dry objective with $NA = 0.7$, a typical water immersion objective with $NA = 1.2$ used frequently in Fluorescence Correlation Spectroscopy (Section 2.7), and an oil immersion objective as used in TIRFM with $NA = 1.49$. Overlayed are fits with Gaussian profiles to highlight the accurary with which the central maximum is described by this approximation.

width and amplitude of the Gaussian profile change along the optical axis to yield an hourglass shape [39]. This model will be discussed in more detail in Section 8.2, where it becomes relevant. More accurate models tend to involve numeric integration schemes [40, 41].

In practice, the resolution is often even lower than predicted by Eq. 2.4 if the microscope suffers from aberrations. A frequent concern in the techniques used in this work is spherical abberation. Spherical aberration occurs if not the entire wavefront is focused into the same plane. For spherical lenses, the periphery of a typical lens focuses the beam more strongly than central parts of the lens. Spherical aberration always increases the overall size of the PSF, and distorts its shape. Modern objectives are lens combinations compensating this effect. However, the correction only works for a specific beam path between objective and sample, for example only water and a standard thickness glass coverslip. Deviations from this configuration will induce spherical aberration even with an otherwise aberration-corrected objective. Various other aberrations exist, and will not be discussed here in detail [42].

Two specialized designs of microscopes that will be of particular interest to this work are the total internal reflection fluorescence (TIRF) microscope, and the confocal laser scanning microscope (CLSM, often simply called confocal microscope). Both often use fluorescence. First, the confocal microscope will be discussed.

In a confocal microscope, the field of view is not illuminated in its entirety at once. Rather, the illumination is focused into an hourglass shape, yielding a single diffraction-limited spot in the focal plane within the sample (Figure 2.6). The size of that spot is given approximately by Eq. 2.4. Laser illumination is the most con-

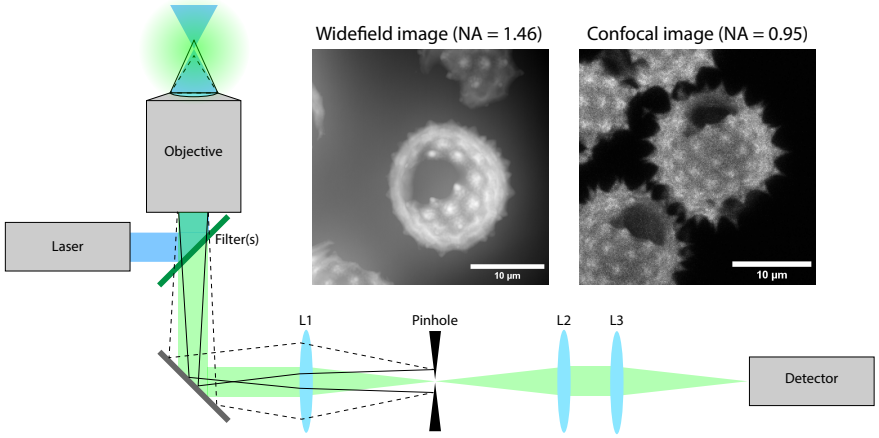

Figure 2.6. Confocal microscope. The schematic drawing shows the key components of a confocal microscope: The objective focuses the excitation laser (blue) into an hourglass shape, with ideally diffraction-limited beam waist diameter. Filters separate backscattered excitation light from the fluorescence emission (green). Lenses L1 and L2 then focus the light through the confocal pinhole to eliminate out-of-focus light (illustrated by solid and dashed black lines representing marginal rays for emitters above and below the focal plane, respectively) and permit only emitted light from a small three-dimensionally confined region on the detector. Scan mirrors are omitted from schematic. The two images were acquired on the same sample, but on different microscopes and with different objectives. Note how the confocal image includes more details in spike structures and lower background, at the cost of lower signal to noise ratio, despite being acquired with an objective of much smaller NA. The widefield image was acquired at a Zeiss Elyra7 microscope equipped with an 63x NA 1.46 oil immersion objective. The confocal image was obtained on an Evident FluoView4000 confocal microscope equipped with 40x NA 0.95 dry objective. In both cases the image shown is a maximum intensity projection (MIP) of a stack of images through the sample. Sample: Section through *Bellis* flower (As651d, JOHANNES LIEDER GmbH & Co. KG).

venient option to achieve the coherence required for such a diffraction-limited spot. This spot is optically conjugated with a single-point detector, typically a photomultiplier tube, an avalanche photodiode, or similar. Thus, fluorescence is excited in a diffraction-limited spot, and fluorescence emission (as well as backscattered excitation light) is collected by the same objective. Excitation and emission are spectrally separated, and the detector measures the signal that is proportional to the local fluorophore concentration within the observation volume. Image formation is achieved by scanning either the sample through the beam [43], or, nowadays more frequently, scanning the beam through the sample [44]. The former is achieved with the help of a motorized stage, the latter using fast-tilting scan mirrors.

The defining feature that turns the laser scanning microscope described so far into a confocal microscope is a small aperture, called pinhole, that is optically conjugated to observation spot and detector in an intermediate image plane (therefore "confocal") [43, 45]. The confocal pinhole discards light that stems from planes within that

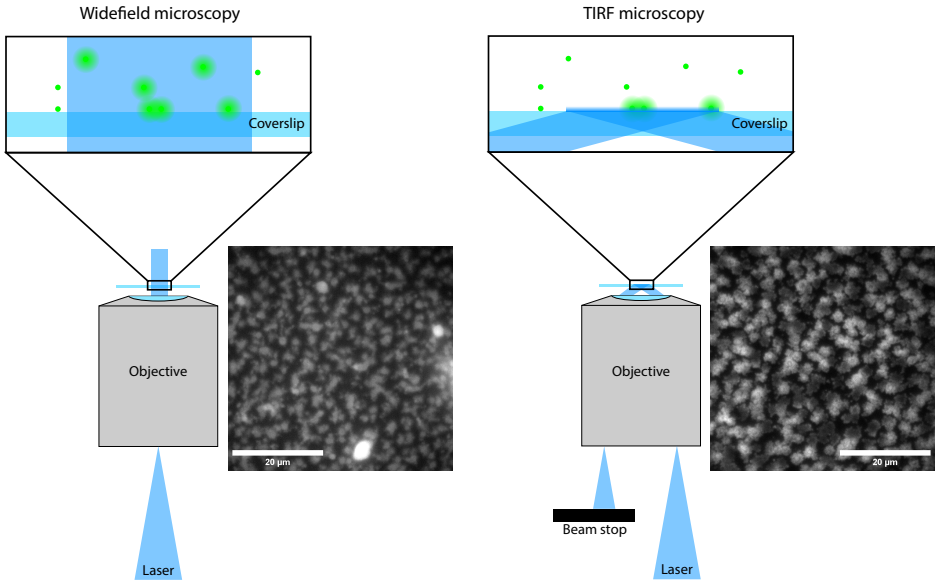

Figure 2.7. TIRF microscopy. Compared to widefield microscopy, in TIRF microscopy, only fluorophores immediately adjacent to the coverslip surface are excited by the evanescent field at the glass-water interface. Total internal reflection illumination is achieved by coupling in the light off-center, so that the objective illuminates the sample at a shallow angle. The immersion oil is omitted from the figure for simplicity. This leads to extreme reduction in background. Note the improved contrast in the TIRF image in the right. Sample: Cy3B-labelled RNA produced *in situ* by RNA polymerase tethered to a supported lipid bilayer membrane (sample by Adam Mamot, MPI for Biochemistry, Martinsried), imaged on a Zeiss Elyra7 microscope using a 63x NA 1.46 oil immersion objective.

sample that are above or below the focal plane of interest, as such light is out-of-focus in the pinhole plane and hits the aperture. That way, a confocal microscope creates a three-dimensionally confined observation volume. The suppression of out-of-focus signal during imaging allows for sharp images even in thick samples.

Besides the option to image in thick samples, the small observation volume is of particular interest to single molecule detection, as signal within the region of interest can be detected with high signal to noise ratio while out-of-focus background is efficiently suppressed. In addition, in modern confocal microscopes, the detector can usually be read out at with repetition rates in the microsecond or even sub-microsecond time range. This makes the confocal microscope attractive for observing sub-millisecond dynamics at small scales. Acquiring images of larger fields of view is relatively slow though, often requiring seconds or even minutes.

In constrast, the TIRF microscope is a design in which the full field of view is illuminated at once. The coverslip-sample interface is illuminated with the excitation laser at a shallow angle. Total internal reflection occurs at the interface between glass and (typically aqueous) sample. Upon total internal reflection, the illuminating light is reflected back into the objective and discarded, but an evanescent field allows fluorophores just beyond the interface to be excited. The excitation probability decreases exponentially with distance from the surface. That way, excitation is restricted to a layer of thickness in the order of 100 nanometers [46,47]. Note that this is only possi-

ble with oil immersion objectives, or illumination schemes that use other components than the objective for illumination such as prisms [46] or waveguides [48].

Detection of fluorescence emission in a TIRF microscope can be performed with a conventional beam path creating the image on a camera chip, without a pinhole discarding a fraction of the light. Together with the high numerical aperture, this means that a TIRF microscope usually has a higher light collection efficiency than a confocal microscope. Therefore, TIRF microscopy is the method of choice for sensitive observation of processes confined to a thin layer that can be positioned adjacent to the coverslip surface - conveniently matching the requirements for imaging cell membranes of adherent cells [46]. Of note, the fact that in TIRF microscopy the optical sectioning is achieved in excitation, rather than in detection as in the confocal microscope, means that photodamage is also confined to a smaller volume. Among systems widespread in synthetic biology, TIRF microscopy is an especially good match for,*e.g.*, supported lipid bilayers or surface-immobilized nanoparticles. TIRF microscopy is also used frequently for single-molecule imaging approaches due to its extreme suppression of out-of-focus background that surpasses even the confocal microscope. However, in observations of very small fields of view, TIRF microscopy is typically restricted to observation at time scales slower than those accessible in confocal microscopy, typically not faster than the millisecond or upper microsecond regime. The acquisition speed in TIRF microscopy scales favorably for larger fields of view compared to the confocal microscope, though.

With typical biological cells being a few (often tens of) micrometers large, it is generally not difficult to achieve resolution with light microscopy that is sufficient to resolve and, *e.g.*, localize and count individual cells. However, cells possess substructures down to scales of tens of nanometers (for example, small vesicles). Individual macromolecules like proteins are as small as a few nanometers. Therefore, while conventional light microscopy can reveal a lot about the structure and dynamics of life, there are plenty of features that require resolution beyond the diffraction limit. Super-resolution microscopy [49] makes such structures accessible, with some super-resolution microscopy approaches achieving resolution down to the size of an individual macromolecule, or even its substructure [50, 51]. However, much can be learned by combining diffraction-limited microscopy with information that goes beyond spatial distributions, such as evolution of the signal in time or spectral information. The evolution of the signal with time can for example reveal information about diffusion or binding processes. Such time-resolved microscopy techniques, in particular fluorescence correlation spectroscopy which will be explained in Section 2.7, are the topic of this work.

2.3 Diffusion and Binding

Living systems are never static. Particles move sometimes randomly, and sometimes directed. Both directed and random motion can be the source of self-organization phenomena. To understand how mobility is linked to self-orgaization in biology, we will first introduce the concept of molecular self-diffusion. Reports by Robert Brown about spontaneous motion of pollen grains in unperturbed solution [52] eventually led to an understanding of this thermal motion based on an understanding that all matter consists of finite-sized particles. Smoluchoswki summarizes the following

observations by Brown and other experimenters who studied "Brownian motion" [53]:

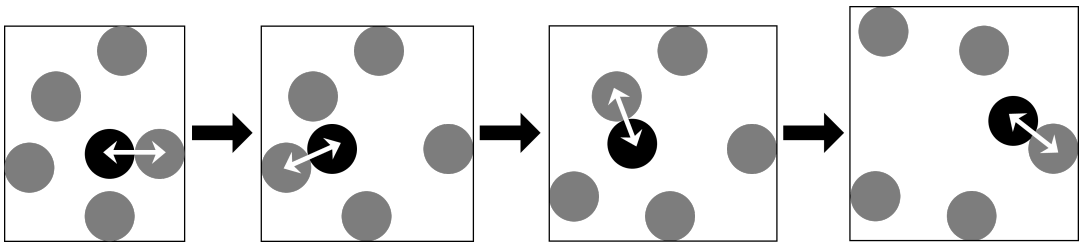

Figure 2.8. Illustration of random walk. Shown is a small ensemble of particles at subsequent time steps. In each time step, the black particle and only one of the grey particles are moved, with each time point showing the black particle just before the next collision. Note how the box is expanding, illustrating how a series of collisions causes the ensemble to drift apart.

- Brownian motion is an undirected dithering motion that occurs ubiquitously, not restricted to specific kinds of particles.
- Brownian motion is faster with smaller particle size, lower solvent viscosity, and higher temperature.
- Mobility does not cease unless particles sediment or get stuck at obstacles, even over months. It is extremely robust against external perturbations, unless these cause a change in the above-mentioned variables.
- Brownian motion does not cease under conditions that prohibit significant thermal convection.
- Reports on whether or not the chemical nature of the particle matters were contradictory: In some reports for example, colloidal silver particles were reported to be more mobile than colloidal iron particles; other reports find no systematic dependence.

If particles of finite size are mobile, *i.e.*, in solution or gas phase, they will necessarily undergo collisions. Einstein [54] and Smoluchowski [53] independently realized that a large number of such collisions from random directions will not cancel out to zero net displacement. Instead, even if the center of mass of an ensemble of unconstrained particles remains the same, each individual particle will tend to drift away from its initial position in what is now called a random walk. This is illustrated in Figure 2.8. In a random walk, a particle performs a large number of short, independent, ballistic movements within a short time. Therefore, a Gaussian distribution describes the probability distribution of the net displacements well:

$$P(x) = \frac{1}{\sqrt{4\pi D\tau}} \exp\left(-\frac{x^2}{4D\tau}\right) \tag{2.6}$$

The net mobility in Brownian motion, or self-diffusion, is characterized by a diffusion coefficient D in units of m^2/s, which can be understood as a scaling factor

of position variance over time. This scaling is concisely described by the Einstein-Smoluchowski relation:

$$\langle \Delta \vec{r}^2(\tau) \rangle = 2MD\tau \tag{2.7}$$

where $\langle \Delta \vec{r}^2(\tau) \rangle$ is the mean squared displacement (MSD) from the position at time point $\tau = 0$ expected for a particle of diffusion coefficient D moving in M dimensions over lag time τ.

On a macroscopic (ensemble) level, the Einstein-Smoluchoski relation is of limited direct use. Here, one rather refers to Fick's laws (Figure 2.9). Consider particles moving accordidng to Eq.2.7 through a layer of area A and thickness Δx with a concentration gradient $\Delta c(t)$. Inspecting the mass balance of this motion yields Fick's first law, describing the diffusion-mediated net flux of particles J_x at a concentration gradient $\partial c(x,t)/\partial x \approx \Delta c(t)/\Delta x$:

$$J_x = -DA\frac{\partial c(x,t)}{\partial x} \tag{2.8}$$

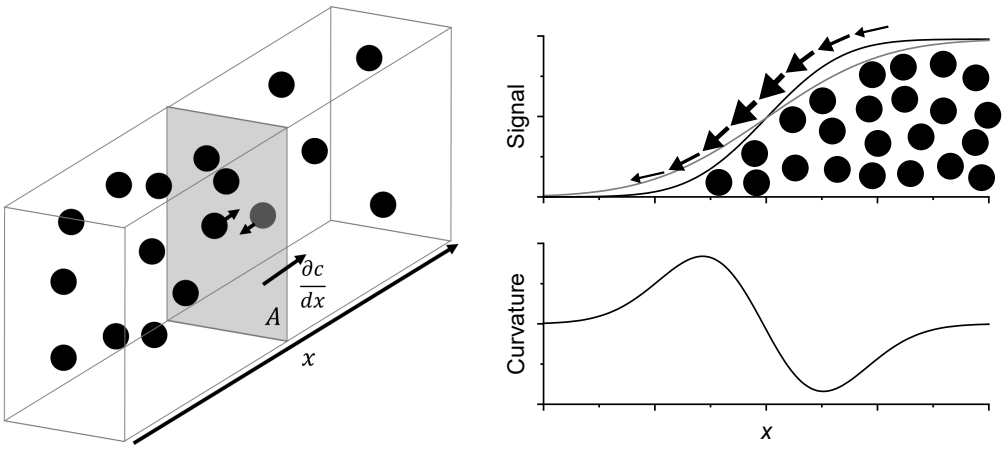

Figure 2.9. Fick's laws of diffusion. Left: Area A separates two volumes with differnt particle concentrations. Fick's first law describes the net particle flux through A. Right: A continuous concentration gradient over x is shown in this case. Fick's second law describes the diffusion-mediated change in local concentration over time (change from black to grey profile), which is proportional to the local inbalance between influx and outflux, *i.e.*, the local curvature.

Fick's second law, also known as the diffusion equation, deals with the time-dependence of concentration profiles. The fastest decrease in concentration will be observed at a sharp egde of concentration between two plateaus of different concentrations. On the other hand, if the gradient is smooth over long disntances, even a steep concentration gradient will not yield significant changes in local concentration over time. Thus, Fick's second law relates the rate of change of local concentration

to the local curvature of the concentration profile in space. The one-dimensional expression reads:

$$\frac{\partial c\,(x,t)}{\partial t} = D\frac{\partial^2 c\,(x,t)}{\partial^2 x} \tag{2.9}$$

The quantitative scaling of D with the above-mentioned variables for a spherical particles in solution is known as the Stokes-Einstein equation:

$$D = \frac{k_B T}{f} = \frac{k_B T}{6\pi\eta r_H} \tag{2.10}$$

with Boltzmann constant $k_B \approx 1.38 \cdot 10^{-23} JK^{-1}$, absolute temperature T, friction f, solvent viscosity η and particle hydrodynamic radius r_H. The hydrodynamic radius characterizes the effective particle radius including not only the particle itself, but also its bound hydration shell which diffuses with the particle. Of note, the mass of the particle does not directly affect the diffusion coefficient.

The friction term f takes different forms for other particle shapes. For example, for stiff rods, the following term has been proposed [55–57]:

$$f = \frac{6\pi\eta L}{2ln\left(\rho\right) + 0.632 + 1.165\rho^{-1} + 0.1\rho^{-2}} \tag{2.11}$$

where L is the length of the filament, and ρ is the "axial ratio", the ratio of length and thickness of the rod. As another example, for 2-dimensional mobility in membranes, an entirely different scaling is observed, described by the theory of Saffman and Delbrück that explicitly considers both the viscosity within the membrane η_{2D} and of the surrounding medium η_{3D} [58–60]:

$$f = 4\pi\eta_{2D} h \left[ln\left(\frac{\eta_{2D} h}{\eta_{3D} a}\right) - \gamma \right]^{-1} \tag{2.12}$$

with membrane thickness h, in-plane particle radius a, and Euler's constant $\gamma \approx 0.5772$.

Of course, particles do not always move randomly (Figure 2.10). Convection or active transport mechanisms can yield a linear mobility characterized by a velocity u, in which case $\langle \Delta\vec{r}^2\,(\tau)\rangle = u^2\tau^2$. Alternatively, hindered mobility of particles can lead to sub-linear scaling of the MSD with time, so-called sub-diffusion. Such hindered motion can be due to confinement to finite-sized domains, or transient trapping at immobile or low-mobile sites. Detailled theoretical models exist, although it remains challenging to match them to experimental data. A challenge is that in real systems, such anomalous sub-diffusion usually occurs only transiently over limited time and length scales, before transitioning into seemingly free diffusion [61]. In constrast, idealized physical models of anomalous diffusion show anomalous behavior at all time scales [62]. Experimentally, anomalous diffusion is often characterized by a generalized Einstein-Smoluchoski equation:

$$\langle \Delta\vec{r}^2\,(\tau)\rangle = 2M\Gamma\tau^{\alpha} \tag{2.13}$$

where the transport coefficient Γ replaces the diffusion coefficient, and the coefficient α quantifies the deviation from normal Brownian motion. The factors $2M$ have

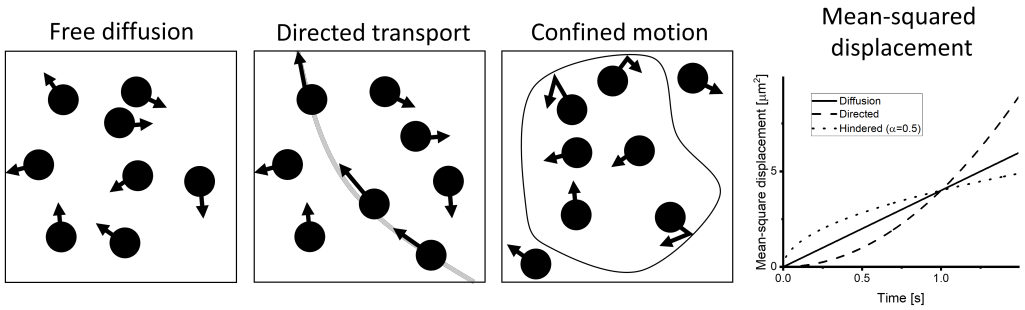

Figure 2.10. Different types of molecular mobility. Freely diffusing particles move independently, unconstrained, and in an undirected manner. Directed transport leads to mobility with greater presistence in direction, for example due to transport along a cytoskeleton filament. Depending on the mechanism of the directed motion, mobility can be correlated between particles (convection) or independent (cytoskeletal transport). Confined motion can for example occur if particles are confined in a boundary that they cannot easily cross. In the right, idealized mean-square displacements are shown for the different modes of motion, varying α with fixed numeric value of $\Gamma = 1\mu m^2 s^{-\alpha}$.

been included for consistency with Eq. 2.7, such that for $\alpha = 1$ (*i.e.*, normal diffusion), $\Gamma = D$, although sometimes these are omitted in the literature. For linear transport, $\alpha = 2$, for anomalous subdiffusion, $\alpha < 1$.

Diffusing particles do not always elastically repel each other upon collision. As indicated by the above-mentioned discrepancies in early observations regarding the significance of the chemical nature of particles for Brownian motion, chemical interactions can accelerate or inhibit mobility. Acceleration for example of metal nanoparticles can stem from catalytic activity [63], although for individual enzymes the plausibility of such effects is debatable [64]. A simple example of non-Brownian-motion dynamics slowing down overall mobility is binding of particles, in the simplest case due to electrostatic attraction of opposite charges. If two particles form a complex, the resulting particle will normally be larger, and thus, as mentioned above, slower. Therefore, analysis of particle mobility is a frequently used method for characterization of particle size, and indirectly binding of particles. Chapter 6 discusses such approaches.

Binding kinetics are in the simplest case characterized by two rate constants (Figure 2.11): Association is goverened by the on-rate k_{on} for the transition from monomers L and R to complex RL, which depends on the mobility of particles, and on the probability that a collision will be "productive" in the sense of leading to a longer-lived bound state. This probability is for example lower if the encounter has to occur from a narrowly defined angle. The observable "effective" on-rate depends on the concentrations of both A and B, as both species need to encounter each other in the first place for association to happen. In contrast, the off-rate k_{off} characterizing the decay of RL into L and R is typically unrelated to molecular mobility, and instead reflects the forces holding the complex together. The balance of particle flux between these species can be described as:

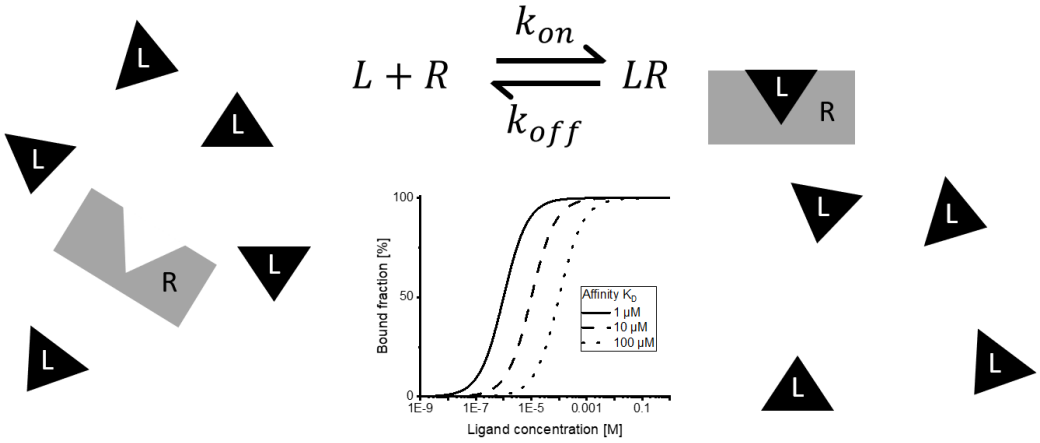

Figure 2.11. Receptor-ligand binding kinetics. The receptor R is surrounded by an excess of ligand L, meaning that the binding reaction introduces relatively small changes to the ligand concentration. Under these conditions, 2.15 describes the fraction of occupied R as function of ligand concentration. The resulting profile is shown for a few K_D values as example.

$$\begin{aligned} \frac{\partial[L]}{\partial t} &= -k_{on}[L][R] + k_{off}[RL] \\ \frac{\partial[L]}{\partial t} &= \frac{\partial[R]}{\partial t} = -\frac{\partial[RL]}{\partial t} \end{aligned} \tag{2.14}$$

where square brackets denote concentration of the respective species. Often in biology, an interesting scenario is to consider a ligand L associating with a target site ("receptor") R, where L is present in excess over R (Figure 2.11). In this case, $[L]$ does not significantly change during equilibration of the binding process, and we can describe the concentrations in steady-state ($\partial[L]/\partial t \approx 0$) as:

$$\frac{[RL]}{[R]} = \frac{[L]}{\frac{k_{off}}{k_{on}} + [L]} = \frac{[L]}{K_D + [L]} \tag{2.15}$$

Here, the dissociation constant K_D was introduced as measure for the affinity of binding. K_D is related to the free energy of binding as $\Delta G = Rln(K_D)$. K_D can also be interpreted as the ligand concentration that yields half-saturated binding.

In biology, especially in self-organizing systems, the picture is often more complex. Multivalent binding is common, for example as a linear, in principle arbitrarily long chain in cytoskeleton filaments, or as short-lived network-like interactions in biological condensates (details in the following sections). Very often, multivalent interactions are cooperative. A well-characterized and relatively simple example is hemoglobin, a tetrameric protein that has four binding pockets for one oxygen molecule each [65]. In hemoglobin, the oxygen affinity of all binding pockets increases with oxygen loading of the tetramer, and decreases with unloading. This

mechanism ensures that hemoglobin is fully loaded with oxygen in the lung, and fully releases its oxygen cargo in oxygen-consuming tissue. Cooperativity is often described by the Hill equation, an extension of Eq. 2.15 with an exponent n that changes the steepness of the $[RL]$ ($[L]$) curve (Figure 2.12):

$$\Phi = \frac{[L]^n}{K_D^n + [L]^n} \tag{2.16}$$

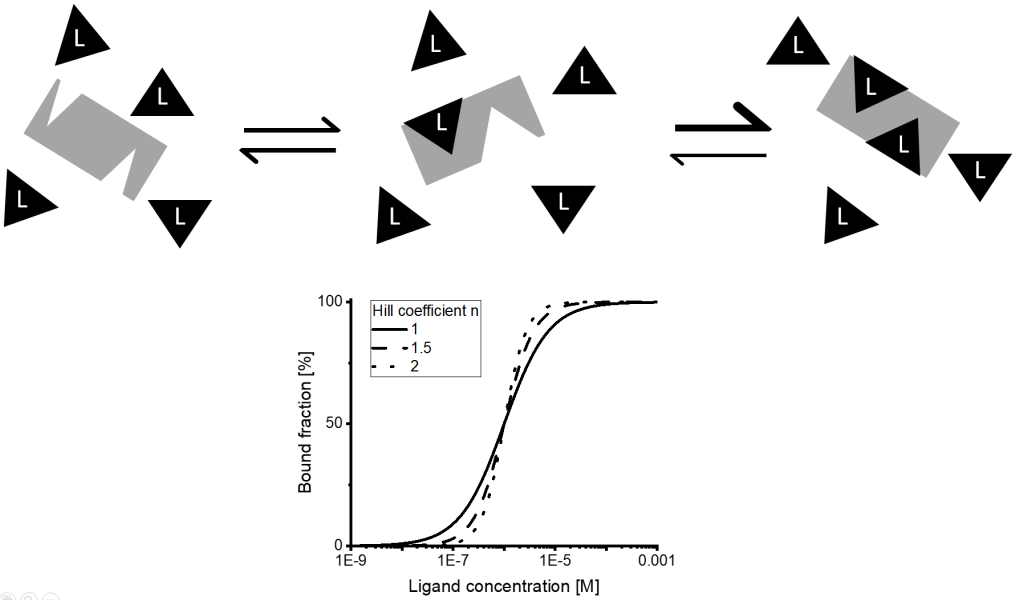

Figure 2.12. Cooperative binding. Compare Figure 2.11. The receptor R now has two distinct binding sites for ligand L. The binding sites are initially in a relatively low-affinity state, but upon binding a first ligand, the second binding site also transitions to a higher affinity open state, allowing loading with a second ligand to happen faster. This is reflected by a Hill coefficient $n > 1$, which is shown in the plot of receptor occupancy: The effective K_D is kept constant at $1\mu M$, but n is varied as indicated.

where Φ is the fraction of occupied binding sites. Here, K_D has to be considered an apparent dissociation constant that is only equivalent to the above defintion of K_D for $n = 1$. For $n > 1$, binding is positively cooperative as in the case of hemoglobin. Negatively cooperative binding with $n < 1$ means that binding sites inhibit each other. Life uses negative cooperativity to tune the activity of proteins to the ligand concentration present, for example in enzymes inhibited by their own product molecules. In practice, expressions analogous to Eqs. 2.15 and 2.16 are often used to describe binding, but replacing K_D or Φ with and "apparent K_D" or a "50%-effective concentration" EC_{50}. This is a more appropriate description if the experimental observable is suspected to scale nonlinearly with binding.

Cooperative binding is frequently the basis for molecular self-organization in the sense of pattern formation, *i.e.* partinioning of particles into high-concentration and low-concentration regions. An example for this are pattern-forming proteins such as the bacterial MinDE proteins [21]. These proteins cycle between a slow moving membrane-bound state and a fast-moving state in solution. The key to achieving pattern formation, rather than spatially homogeneous binding/unbinding dynamics, in

this system is that both membrane recruitment and membrane detachment of the MinD protein proceed in a cooperative manner: Membrane-bound MinD stabilizes membrane binding of additional MinD by forming higher-order complexes. MinE, which induces detachment of MinD from the membrane, acts in a "persisting" manner, detaching multiple MinD proteins within a short time once it gets recruited to the membrane [17,21].

Other examples of more complex physics govered by relatively simple underlying binding kinetics are mesoscopic self-assembling systems like cytoskeletal filaments, and the formation of phase-separated condensates. The Liquid-liquid phase separation will be addressed in the next section (Section 2.4). Self-assembling systems including cytoskeletal filaments and synthetic DNA nanotechnology systems will be covered in Section 2.5.

2.4 Liquid-liquid phase separation

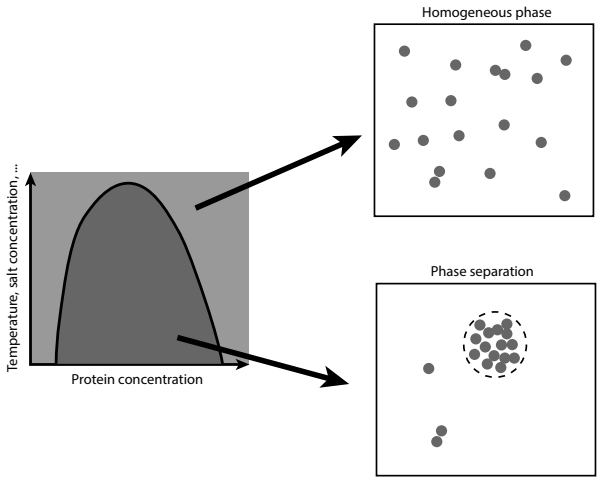

Figure 2.13. Illustration of liquid-liqud phase separation. Shown in the left is the illustration of a binodal, the result of Eq. 2.17 which describes at which combinations of external variables and concentrations a protein remains homogeneously soluble (top right), or condenses into droplets (bottom right).

Alexander Oparin speculated about the Origin of Life, the very first cell, in the form of a "coacervate" of molecules that phase-separate from their surroundings [66]. This showcases the general opinion on the physical nature of the cell at the time, inspired by physics of colloids [67,68]. Displaced by the concepts of molecular biology and largely ignored by the cell and molecular biology communities for a long time, interest in Oparin's and similar ideas resurged after it was discovered that, while the cell in its entirely is not organized as a coacervate, it does contain coacervate droplets which act as distinct functional units [69].

These coacervates are now often called condensates or membrane-less organelles, and quickly attracted tremendous attention. Condensates in the broader sense can be

formed by a variety of processes that are not always easy to distinguish [70]. Of particular interest to this work however are condensates formed through liquid-liquid phase separation (LLPS, Figure 2.13). LLPS occurs when a solution of two or more components enters a regime of concentrations (and external variables like temperature) in which the free energy associated with homogeneous mixing of the components is unfavorable compared to the demixing into two separate liquid phases, where the mixing energy cost competes with the surface energy of the interface between the demixed phases [71]. While a familiar example is the inmiscibility of oil and water, in the case of biomolecules, phase separation more commonly is driven by associative interactions [72]. In this case of associative phase separation, one speaks of coacervation.

Soon, a plethora of different membrane-less organelles were discovered, with researchers reconsidering the organizing principles of many previously known organelles like the nucleolus, the nuclear pore complex, and stress granules [22]. The biological functions that are proposed for condensates are extremely broad, and a variety of such functions has already been demonstrated [22] (Figure 2.14). These include sorting of molecules [69,74], physical adapter function [75], and buffering of intracellular protein concentrations [76]. However, condensates are also suspected to be involved in pathological processes like virus assembly [77] or formation of disease-associated amyloid deposits [78]. Prokaryote cells, previously often thought to be largely homogeneous in content given their lack of internal membranes (ignoring special cases like cyanobacterical thylakoids), also contain condensates which are thought to contribute to, *e.g.*, chromosome organization and segregation [79–81].

Returning to the topic of the Origin of Life, the question of the physical compartmentalization mechanism of the first cell(s) is still unanswered. Many ideas are being discussed with their respective strengths and weaknesses, including the seemingly obvious assumption of a primitive membrane envelope, microscopic cracks within rocks, or more unusual ideas like local up-concentration within eutectic ice phases [82] (Figure 2.15). Another popular idea returns to Oparin's ideas by proposing condensate protocells. This idea is attractive as it allows micrometer-scale protocells without depending on external geometric cues, and permits selective accumulation of nutrients from the environment [83–85]. It should be noted though that coacervate formation tends to require rather high concentration of the phase-separating molecules, raising doubts about prebiotic plausibility [82]. While a condensate protocell is no easy way out of the difficulties encountered by other Origin of Life scenarios, there is tremendous interest in the phenomenon of biomolecular condensation motivated both by interest in understanding extent life and by trying to reconstruct the early history of life.

Importantly, while LLPS is reminiscent of precipitation beyond a solublity limit, in LLPS both demixed phases remain liquid. A successful model to conceptualize the interactions involved in LLPS of many proteins, at least intrinsically disordered ones, is the "stickers-and-spacers" model that represents the protein sequence as association-driving "sticker" motifs, and inert "spacer" sequences [86]. Multivalent binding interactions are the key to for condensate growth to be favorable (free energy gain with volume increase), while the spacers ensure that interactions remain short-lived to allow the coacervate to remain fluid. Nonetheless, biological condensates often are not ideal liquid-phase coacervates. Rather, the droplets tend to ex-

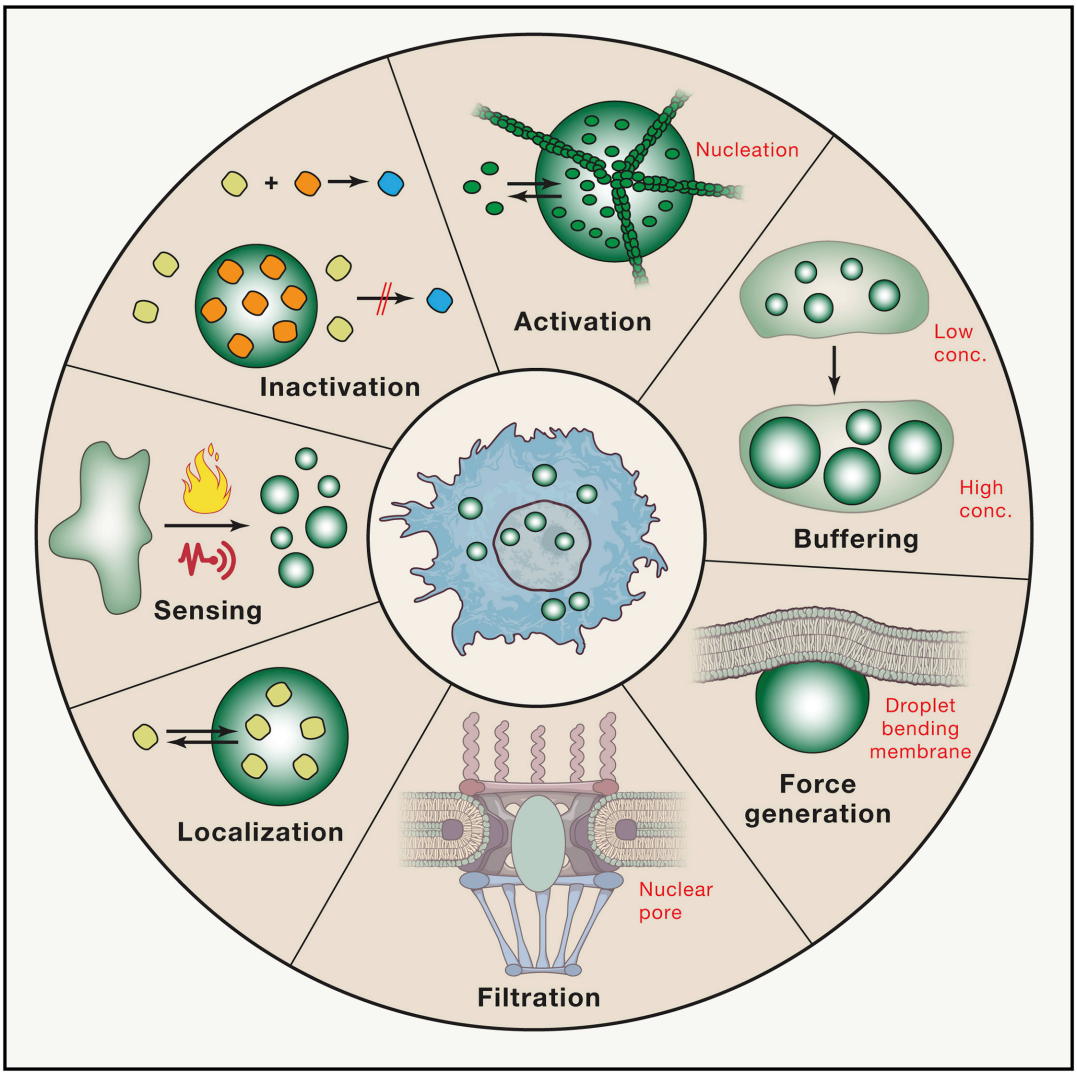

Figure 2.14. Functions of biological condensates. The illustration shows a range of functions that condensates have been shown, or are suspected, to play within biological cells. Some function relate to the increased local concentration of particles within droplets (activation/nucleation, inactivation, and localization), others to the dynamic exchange of droplet material with the surroundings (concentration buffering and sensing) or to the physical properties of the condensates themselves (force generation, filtration). Reprinted from Alberti, Gladfelter, and Mittag 2019 [73] with permission from Elsevier.

hibit viscoelastic properties, and their properties can change with age of the droplet, which has been associated with formation of the above-mentioned amyloids [77, 87]. In addition, biomolecular or biomimetic condensates have been artificially created with highly interesting properties for use as building blocks in synthetic biology efforts. Some examples are active phase-separated matter with extreme dynamics at the phase boundary [88], multiple phases that remain associated but demixed [89], subtructure formation within still-fluid droplets [90], or seeding of filament growth [91].

The most widespread theory for describing phase separation quantitatively is that

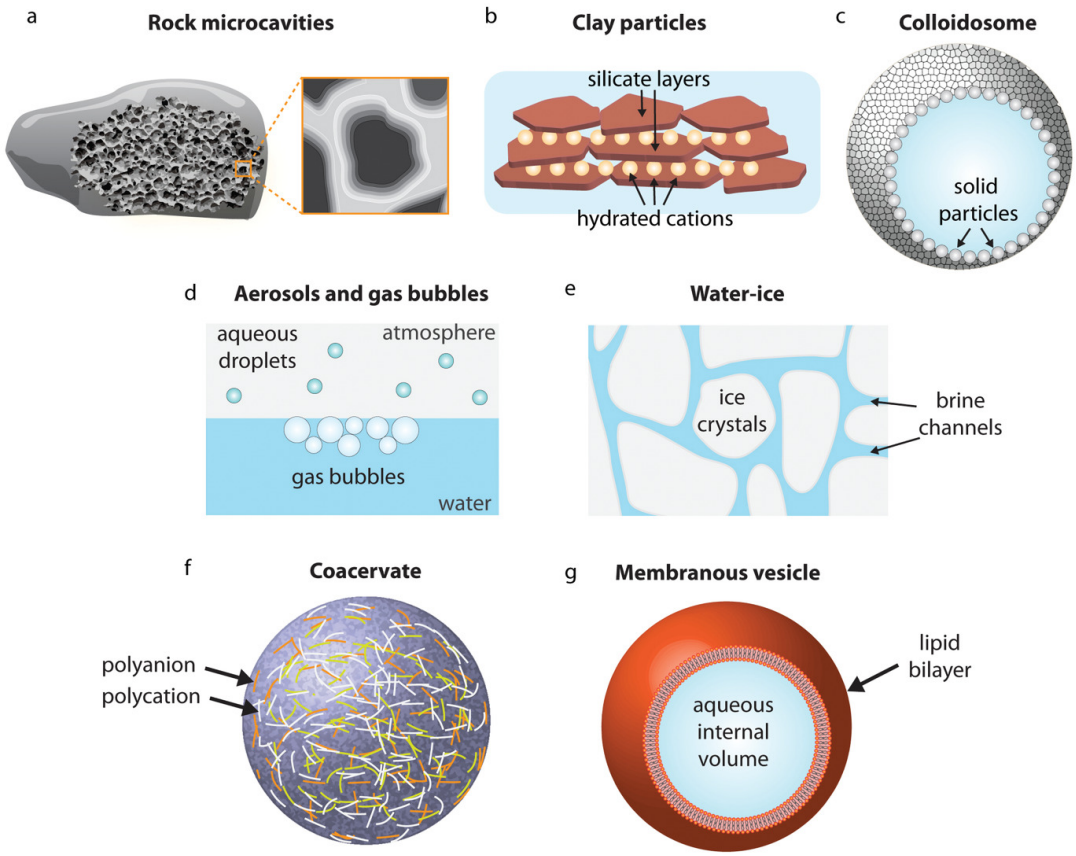

Figure 2.15. Prebiotic compartmentalization. Various models are schematically displayed that are being discussed as candidates for compartmentalization of prebiotic molecules. Membranous vesicles (g) are the closest to extant life, and certainly must have taken over the role of the primary mechanism of compartmentalization in living systems at some point. However, a number of other mechanisms are of interest for hypotheses about earlier stages of the emergence of life as they do not require biomolecules as building blocks (a-e). Finally, coacervates, *i.e.*, liquid-liquid phase separation, is of interest as in this case, the biomolecules to compartmentalize and the compartment-forming particles can be one and the same (f). Reprinted from Gözen et al. 2022 [82] with permission from John Wiley and Sons.

by Huggins and Flory [92–94], which describes the mixing free energy $f\left(\phi\right)$of a dispersed solution of a polymer in a bath of smaller solvent molecules as a function of the polymer volume fraction ϕ:

$$\frac{f\left(\phi\right)}{k_B T} = \frac{\phi}{N} ln\phi + \left(1-\phi\right) ln\left(1-\phi\right) + \chi\phi\left(1-\phi\right) \tag{2.17}$$

where N describes chain length of the polymer under study, and χ describes the interaction energy of the mixing. Thus, while the first two terms on the righthand side of Eq. 2.17 describe mixing entropy, the last term is the enthalpic term that describes if interaction favors phase separation. The model can be generalized to mixing/unmixing of more than two components [94]. Depending on the value of χ, different ϕ (*i.e.*, concentration) regimes favor phase separation over mixing. This is described in the phase diagrams by so-called binodals, which describe the threshold

concentrations for onset of phase separation, typically as function of some parameter that influences χ (Figure 2.13). Inside the binodals, the disperse solution is supersaturated and phase-separation is favored. Once LLPS occurs, the concentrations in dense and dilute phases will usually be the concentrations on the right and left arms of the binodal lines, respectively. Only the volume fractions of the phases will change with overall concetration. This means that studying concentations inside and outside condensates is of key interest for understanding they physical chemistry, as these concentrations allow to directly measure the binodal and thus characterize the thermodynamics of the underlying interactions.

2.5 Molecular self-assembly

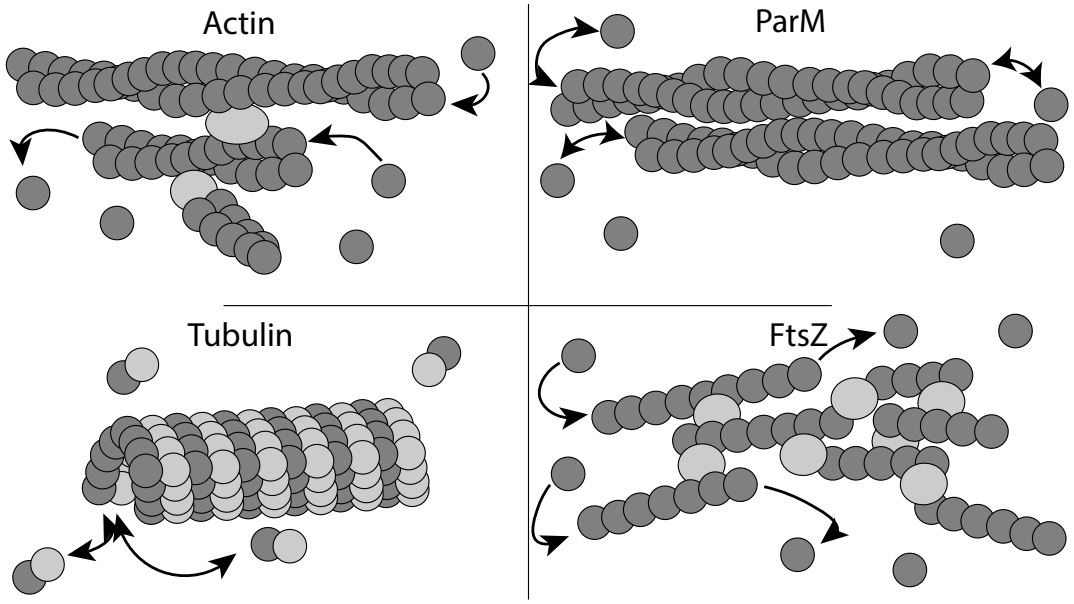

Figure 2.16. Filament-forming proteins. Schematic illustrating structure and growth/decay of the eukaryote cytoskeleton proteins actin and tubulin in comparison to their prokaryote homologs ParM and FtsZ. Actin often undergoes treadmilling dynamics, recruiting monomers at one end while decaying at the other. It is also often cross-linked into thicker bundles, and/or branched into complex networks. ParM forms double-helical filaments that are thought to form antiparallel bundles. ParM is thought to grow and decay symmetrically, unless an end is capped. Tubulin forms heterodimers (alpha- and beta-tubulin), which assemble further into hollow tubes called microtubules. Microtubule ends tend to switch between a growing and a decaying state. FtsZ is a tubulin homolog whose protofilaments are presumably crosslinked into a meshwork that forms the basis of the Z-ring in dividing bacteria.

Many molecular self-organization processes in living systems have some form of molecular self-assembly at their core. An instructive example are filament-forming proteins: While cytoskeleton filaments in live cells are an active material with complex out-of-equilibrium dynamics, the key principle underlying all of those is assembly and disassembly of protein monomers into long oligomers, often followed by mutual binding of these oligomers into higher-order structures (Figure 2.16). The active dynamics then emerge from an abundance of mechanisms to locally (in space

and time) modulate the rate constants of the underlying binding processes.

As an example, actin filaments in eukaryote cells are double-helical thin protein filaments [19,95]. The structure of an actin filament can in essence be though of as two parallel strings of beads, the beads being globular actin proteins. Like many other cytoskeleton filaments, filamentous actin (F-actin) exhibits "treadmilling" dynamics: At typical concentrations of monomeric actin (G-actin) in live cells, one end of the filament tends to elongate by incorporating new G-actin while the other end retracts by dissociation of monomers, thereby facilitating directed net movement of the filament. This non-equilibrium aspect of actin filament dynamics is due to a switching mechanism that allows G-actin to change the affinity with which it binds to the filament: ATP-bound (high-energy) actin monomers bind each other with high affinity, tending to form and elongate filaments. After some time, the catalytic activity of actin cleaves the ATP molecule, creating ADP-bound actin which binds the filament with reduced affinity and therefore tends to dissociate. Details of the difference (asymmetric) binding interfaces involved in the binding process and their response to the ATP cleavage ensure that the treadmilling occurs in a predictable direction. Thus, actin treadmilling shows how binding and unbinding with an (energy-dissipating) mechanism to modulate binding rates is sufficient to create directional collective dynamics, in this case active motion of a micrometer-sized filament [96].

The average filament length $\langle j \rangle$ (in monomers) in an ensemble of protein filaments in steady state is determined by the ratio of growth and decay rates:

$$\langle j \rangle = \frac{k_{growth}}{k_{decay}} \tag{2.18}$$

As both growth and decay can happen at both ends, to model the growth and decay of actin, k_{growth} and k_{decay} each are the result of multiple reaction rate constants: Distinct growth rates and decay rates characterize the barbed and pointed ends. Thus, there are various options to regulate actin dynamics by differentially tuning these rates of end growth and decay. The picture becomes even more complex when considering the effect of branching and cross-linking factors.

Closely related to actin is the bacterial protein ParM. ParM is part of the bacterial chromosome segregation machinery. While ParM monomers are structurally very similar to G-actin and self-assembly is ATP-driven, the filaments behave different from actin: Instead of unidirectional treadmilling, ParM filaments are thought to grow and decay symmetrically at both ends, unless capped by other factors [97]. The kinetics of ParM assembly and disassembly therefore remain rather ill-understood and a topic of ongoing research.

A distinct family of filament-forming proteins are tubulin and its homologs. Tubulin in mammalian cells assembles into microtubules, protein tubes that consist of thirteen linear protofilaments held together tightly by lateral interaction. Characteristic for microtubule dynamics is a behavior called "dynamic instability", which refers to a switching of microtubule ends from a state of growth to a state of decay, although the details of the underlying mechanism remain somewhat unclear [98]. Tubulin has bacterial homologs such as FtsZ. FtsZ does not intrinsically form tubes like tubulin does. However, FtsZ does assemble into a dynamic ring-like structure in living cells that plays a key role in bacterial cell division. For this, FtsZ cooperates with a large number of interaction that presumably cross-link FtsZ protofilaments [99].

Besides natural systems, biomimetic molecules can also be designed to undergo self-assembly in order to create easier-tunable self-assembling systems. These can then serve as a platform for further bottom-up synthetic biology experiments. An example of a chemically very different technology that also builds mesoscopic assemblies from few-nanometers building blocks is DNA nanotechnology. DNA nanotechnology is a versatile toolbox for synthetic biology [100, 101]. The geometry of DNA nanostructures is determined largely by Watson-Crick-Franklin base pairs: adenosine bases form base pairs with thymidine, and guanidine with cytidine. Other interactions such as i-motif or G-quadruplex can also play a role, but are generally of lower importance unless enforced by design [102, 103]. Thus, the interactions governing the structure are easy to predict, making sequence-structure - and therefore sequence-function - relations much easier to understand and design in DNA than in, *e.g.*, proteins [104]. Thus, DNA nanotechnology offers convenient access to designed structure and function in synthetic biology.

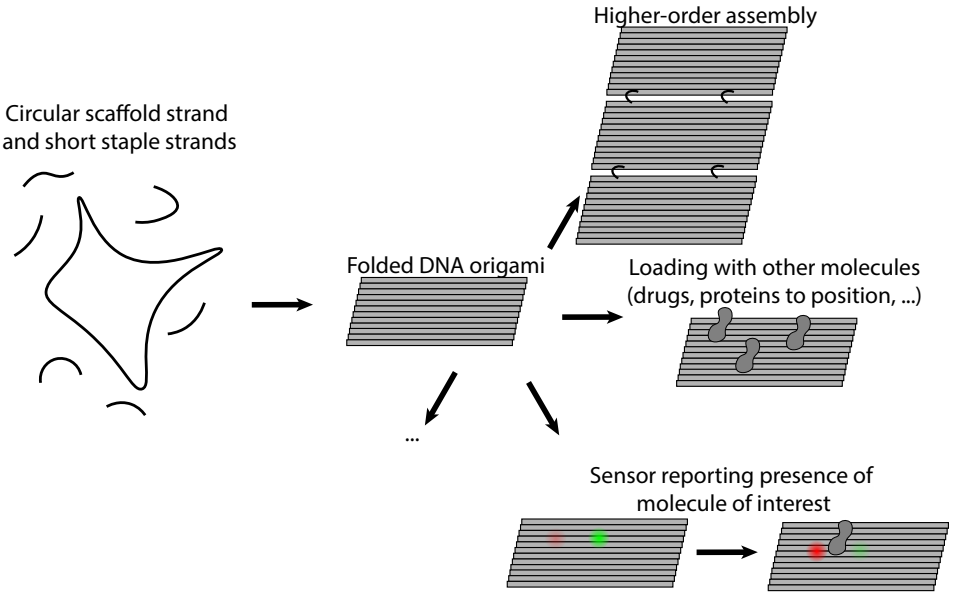

Figure 2.17. Schemtic of DNA origami nanotechnology DNA origami is assembled from a single long scaffold strand and a large number of short staple strands. A temperature ramp is typically used to guide the kinetics of the assembly ("folding") into the designed target structure, here a simple rectangle. Such origami particles can then be further functionalized for various downstream applications, of which only a few are indicated here. Of particular interest to synthetic biology are the possibility to use DNA origami as a platform for positioning of other molecules, and the higher-order assembly of DNA origami as basis for large-scale structure.

DNA nanotechnology nowadays find applications as drug carrier [105], as rationally designed binder for detection or for sequestration of target particles (usually by functionalizing the DNA nanostructure with other molecules [106, 107]), as template structure for the self-assembly of other molecules [108, 109], as a calibration standard with well-understood binding and conformational dynamics [110], or as a carrier on which to position other particles in defined geometry [111–114].

A particularly versatile branch of DNA nanotechnology is DNA origami (Figure

2.17). DNA origami was proposed in 2006 as a concept to design DNA nanostructures on the scale of tens to hundreds of nanometers, with few nanometer resolution in defining the shape [115]. DNA origami consists of two key components: The "scaffold" is a single-stranded DNA plasmid, typically the circular M13mp18 bacteriophage genome (7249 base pairs long) or a derivative of that plasmid. The scaffold is folded into a desired two- or three-dimensional shape by complementary binding of hundreds of "staple strands", ssDNA oligonucleotides that are a few ten base pairs long each [116]. The highly modular design and easy production make DNA origami extremely popular for design of mesoscopic particles for various applications.

Self-assembly of macromolecules into higher-order structures is a phenomenon frequently underlying biological self-organization, and a valuable tool for bottom-up synthetic biology in building up structures of increasing complexity. Thus, characterizing the physical chemistry underlying self-assembly of a macromolecule of interesting is frequently of interest in order to understand poaaibilities to fine-tune and better exploit the formed structures. For this, single-molecule methods are often of value to resolve details that would remain obscured in ensemble-level studies.

2.6 Single-Molecule Microscopy

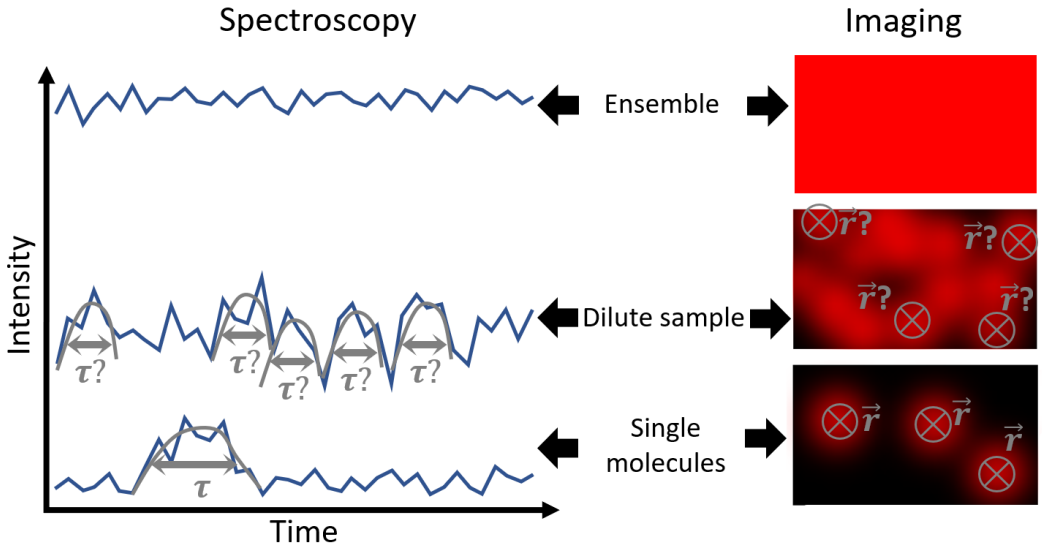

Figure 2.18. Concept of single-molecule microscopy. Shown are schematic illutrations of the transition from ensemble-level observation to single-molecule observation both in time-resolved spectroscopy and in imaging. At high concentrations of observed particles, a relatively homogeneous average brightness is observed. Dilution of particles yields a regime where local fluctations become visible that stem from single molecules, but assignment of signal to individual molecules remains ambiguous. Statistical techniques can be used in this regime to extract characteristics invisible in the ensemble, though. Further dilution combined with highly sensitive detection finally leads to true single-molecule detection, where signal can be unambiguously assigned to individual particles, indicated by the assignment of dicrete duration to a signal burst in the left, and discrete positions to particles in the right.

With improvements in laser and detector technology, in the late 1980s, direct optical detection of single molecules in dense phase became feasible under favorable conditions. While the first demonstration was based on absorption of illuminating light [117], soon fluorescence detection was used and became the method of choice due to its superior signal to background ratio [118], which also allowed room temperature single molecule detection (SMD) experiments, first to detect molecule transits in solution [119, 120], and later also in direct imaging of molecules [121]. SMD opened up various new opportunities for physical chemistry and related fields. The key breakthrough is that SMD allows to see not only ensemble averages of parameters of interest, but also distiributions broadened by particle heterogeneity. For example, when measuring absorption of an ensemble, the observed line shape often does not agree with theory, due to inhomogeneous broadening, *i.e.*, the molecules in the ensemble experiencing many different local environments. SMD allows resolving the broadening and assigning a distinct absorption peak to each molecule [117].

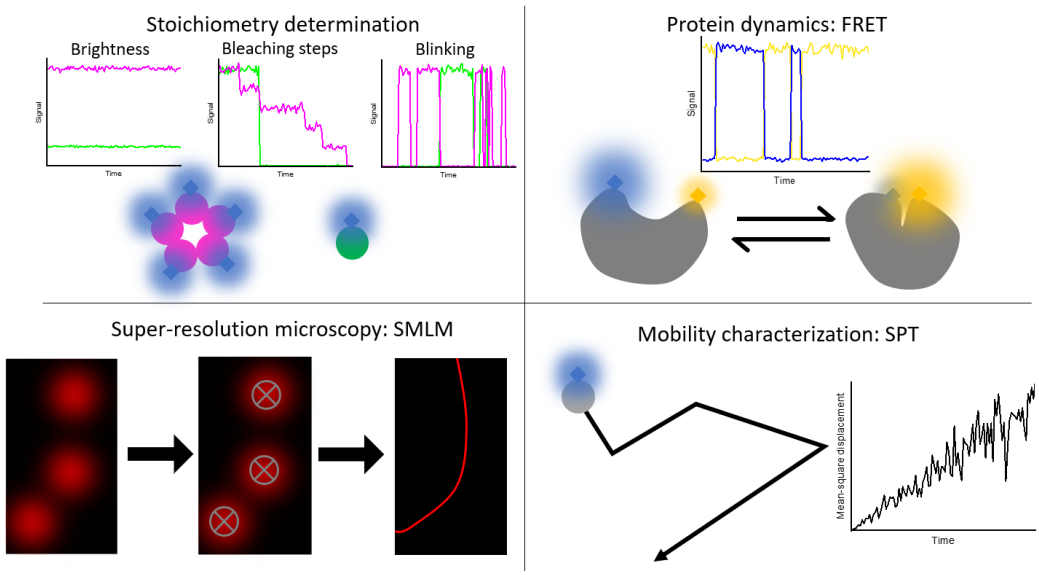

Figure 2.19. Applications of single-molecule microscopy in biophysics. Stoichiometry determination: Different readouts of single-particle parameters can be used to estimate the number of subunits within a complex. For example, in simple systems, the j-mer is j times brighter than the monomer. One can count the steps in sequential photobleaching of fluorophores. Alternatively, one can exploit the blinking of the particle in comparison to the blinking of the monomer to infer the number of fluorophores. Protein dynamics: FRET and similar approaches allow to determine time scales on which conformational changes occur within a protein of interest. Super-resolution microscopy: By detecting only a small subset of well-separated particles at a given time, one can precisely determine their position and accumulate a super-resolved image. Mobility characterization: By tracking a mobile particle over a number of image frames, one can reconstruct a trajectory of motion and infer statistics of mobility.

More typical applications in biophysics are (Figure 2.19):

- Observing binding kinetics and determining stoichiometries of supramolecular complexes, typically through analysis of brightness differences within a single-

particle spot [122, 123], or through alternative methods such as the statistics of blinking events [124, 125].

- Observing single macromolecules execute a specific function that would be invisible in an ensemble, such as conformational changes by combination with Förster Resonance Energy Transfer [126–128].
- Obtaining super-resolution spatial information through single molecule localization microscopy (SMLM) [36, 129–132].
- Observing mobility of molecules by tracking their position over time (single particle tracking SPT) [133, 134].

Of course, combinations of these exist, as do other applications that do not fit in any of these categories. More detail will be given in the following about SMLM and SPT.

In SMLM, a family of super-resolution microscopy techniques, sub-diffraction scale information is obtained based on SMD. While two emitters separated by a distance below the diffraction limit cannot be conventionally resolved, it is relatively easy to localize the position of a single isolated fluorophore with sub-diffraction scale precision *via* the centroid of the emitter image, fitting a Gaussian peak, or similar approaches. The super-resolved image is then reconstructed as a map of individual emitter localizations. The challenge in SMLM is essentially threefold [135]: Firstly, one has to maximize the signal to noise ratio of the emitter images to maximize resolution. Quantitatively, the uncertainty with which an emitter can be localized scales with the invserse square root of the number of photons that contribute to the emitter image. Secondly, minimization of aberrations, linkage error (distance between fluorophor and actual particle of interest due to linkage chemistry), and similar factors is crucial to ensure that determined emitter image centroids are representative of the actual positions of molecules of interest. Finally, and concentually most critically, one must create conditions where the emitters in the sample can be imaged sequentially as single particles. This is achieved by causing particles to stochastically "blink", *i.e.*, switch between an "on" state in which they can be imaged, and an invisible "off" state. At every time point throughout the acquisition, the vast majority of particles is kept in the off-state, and only a small subset, in extreme cases only a single particle [136, 137], is imaged and localized. Typically, thousands or even tens of thousands of frames are acquired in that manner to accumulate a single super-resolved reconstruction.

Different concepts for blinking have been proposed, essentially falling into the categories of photochemical blinking where fluorophore molecules themselves are switched between "bright" and "dark" states ("Photoactivated Localization Microscopy" PALM [130] and "(direct) Stochastic Optical Reconstruction Microscopy" (d)STORM [36, 131]), and binding-based blinking where the "on" state is bright because a fluorophor becomes immobilized at a target position rather than diffusing rapidly in diffuse background ("Points Accumulation for Imaging of Nanoscale Topography" PAINT [129]). PAINT microscopy is often implemented exploiting the hybridization of DNA [138], making the combination DNA-PAINT especially attractive for studies involving DNA nanotechnology. In Chapter 4, DNA-PAINT will play a prominent role.

Single particle tracking (SPT) is based on the same single emitter localization concept as SMLM. Different from SMLM however, SPT is not primarily a technique for image formation, but rather for continuously observing a particle over time to characterize their mobility. Therefore, experiments are performed with slower blinking than in SMLM, if any. Emitter localizations are linked between subsequent frames into a track representing the movement of the particle. The localizations within a track can then be analyzed further to extract information on the mobility. SPT was first implemented in the 1980s based on the scattered light from colloidal gold nanoparticles [139, 140], and later was transferred to the use of fluorescence-based SMD [141]. A straightforward method to analyze particle mobility so is the direct calculation of the mean-squared displacement (MSD) over time $\langle \Delta\vec{r}^2(\tau) \rangle$ which can be directly related to physical models of particle mobility (compare Section 2.3):

$$\langle \Delta\vec{r}^2(\tau) \rangle = \langle \left(\vec{r}(t+\tau) - \vec{r}(t)\right)^2 \rangle \tag{2.19}$$

where $\langle \ldots \rangle$ denotes averaging. The averaging can be over particles and/or over time, depending on the application and the expected underlying physics [133]. SPT has found widespread application in the characterization of mobility in relatively slow-moving systems such as molecules embedded in biological membranes [122, 141]. However, it often struggles with fast-moving particles due to the unavoidable trade-off between signal to noise ratio (which must be high for the SMD required for SPT, see above) and acquisition speed: Shorter signal integration time would allow to follow faster movement, but means that less signal is available per data point, prohibiting reliable localization.

Besides the direct observation of single molecules, there are other approaches to capture molecular mobility *in situ*, of course. For example, a relatively straightforward ensemble method to measurement of diffusion coefficients is Fluorescence Recovery After Photobleaching (FRAP [142, 143]), in which fluorescent particles within a region of interest are bleached, and the recovery of fluorescence signal is observed over time. Depending on the system under study, FRAP can also be used to measure binding kinetics [143]. FRAP comes with various downsides in practice though, in particular artifacts that may result from the use of high laser power. In addition, depending on the available prior knowledge of the sample, modelling of the recovery data can be ambiguous [144]. At its conceptual basis, FRAP is a perturbation technique that pushes the sample out of equilibrium in a defined manner, and then observes the kinetics of system relaxation back into equilibrium. A third approach that does not perturb the sampleand can often be performed with similar hardware as FRAP is Fluorescence Correlation Spectroscopy (FCS) [145–147].

FCS operates at a boundary between ensemble-level observation and SMD. The key conceptual difference between FCS and FRAP is that FCS does not actively perturb the sample, but rather observes spontaneous fluctuations in a steady-state signal. Different from SPT however, FCS characterizes recurring patterns caused by underlying single-molecule dynamics without assigning the signal fluctuations to individual molecules. FCS plays a key role in all following chapters, and will therfore be dicussed in more detail in the next section.

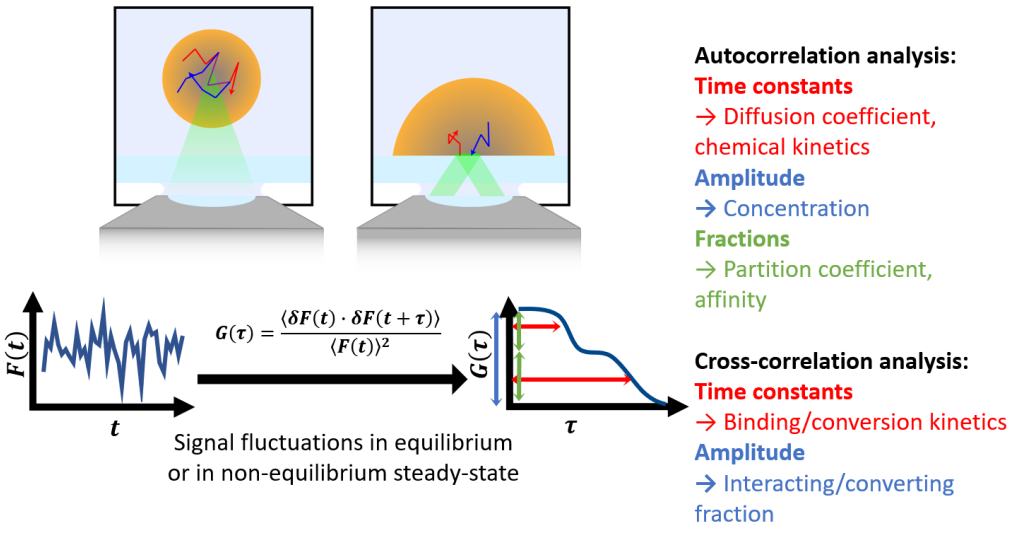

Figure 2.20. Fluorescence correlation spectroscopy. Signal fluctuations that originate from random single molecule dynamics observed in a dilute sample are measured typically in confocal microscopy (upper left), but other microscope types such as a TIRF microscope (upper right) are viable as well. Observed fluctuating time traces are correlated in time (lower schematic) to yield a correlation function that represents recurring patterns of signal fluctuations. Amplitudes and time constants can be extracted to determine different parameters of interest, listed in the right. In dual-color setups, dual-color cross-correlation gives access to additional parameters.

2.7 Fluorescence Correlation Spectroscopy

In FCS, one typically acquires a high time resolution fluorescence time trace $F(t)$ in a diffraction limited confocal observation volume $V_{eff} < 1\ fl$ (Figure 2.20) [145, 148, 149]. Fluctations in $F(t)$ are then statistically analyzed to distinguish photon shot noise from signatures of single-molecule dynamics. Photon shot noise arises from the discrete excitation-emission events in fluorescence, but for that reason, it is for most widely used fluorescent labels uncorrelated beyond time scales of a new nanoseconds. Processes typically investigated through FCS occur mostly on the time scales of microseconds or milliseconds, so nanosecond-scale signatures of the fluorescence photocycle are negligible and can be treated as random noise.

At sufficiently low particle concentrations, the fluctuations arising from stochastic fluctuations in the numbers and states of individual particles within the observation volume become significant. By analyzing amplitudes (*i.e.*, essentially the variance) and time-correlations of fluctuations in $F(t)$, one can therefore extract information about concentration of particles with spatial resolution limited by the microsocope resultion, and about the kinetics of any process that leads to changes in fluorescence intensity. If the observed fluorescence fluctuations are due to diffusion, the data can be used to estimate the average residence time of the molecules in the observation volume, and therefore the diffusion coefficient.

FCS is a versatile technique that, depending on the experiment design, can be

used to answer a variety of different questions. Firstly, the autocorrelation function of a diffusing particle will report on the average time that a particle spends in the observation volume. Such diffusion time measurements can be used to probe the microenvironment within living cells *via* the diffusion of particles of known size. For example, Wachsmuth and co-workers show that diffusion of a fluorescent protein is far slower in the cytoplasm and nucleus of cells than in solution, and that diffusion in the nucleus shows greater deviations from Brownian motion [150]. In other words, both cytosol and nucleus appear quite viscous, and the nucleus also contains barriers (or binding sites) interrupting mobility. Diffusion coefficient measurements can also be exploited to observe changes in particle size, and therefore oligomerization. Sarkar and co-workers demonstrated the possibility to resolve Å-scale changes in particle size with an optimized experimental setup [151]. Closer to typical applications is the FCS-based measurement of binding/unbinding of small particles to/from larger less mobile ones *in situ* [152]. FCS approaches can also be used to measure concentrations *in situ*. For example, it has been used to estimate the concentration of RNA copies within cells [153]. Particle brightness is valuable to characterize oligomerization states and has for example been applied to receptor oligomerization studies [154]. The combination of concentration and brightness information can be exploited to calibrate a confocal microscope such that a fluorescence image can be recalculated to an absolute concentration map [155]. Beyond diffusion characterization, FCS can also characterize various other dynamics of interest such as the photophysics of dyes [156, 157], or rotational dynamics [5, 158].

Data analysis most frequently is based on the fluorescence fluctuation autocorrelation function (ACF) $G(\tau)$ [147, 159, 160]:

$$G(\tau) = \frac{\langle \delta F(t)\, \delta F(t+\tau) \rangle}{\langle F(t) \rangle^2} = \frac{\langle F(t)\, F(t+\tau) \rangle}{\langle F(t) \rangle^2} - 1 \tag{2.20}$$

with lag time or correlation time τ and fluorescence fluctuation $\delta F(t) = F(t) - \langle F(t) \rangle$. $\langle \ldots \rangle$ denotes time averaging. Both of the expressions given for $G(\tau)$ are in use, and they are equivalent, differing only by the offset. Consider detection within an observation volume described by a point spread function profile described by a dimensionless parameter $\hat{W}(\vec{r})$ normalized such that $Max\left[\hat{W}(\vec{r})\right] = 1$. If one assumes a population of similar particles of concentration/density (in three or two dimensions, respectively, depending on the system) $c(\vec{r}, t)$ and brightness ε, the fluorescence signal at a given time can be described as:

$$F(t) = \varepsilon \int \hat{W}(\vec{r})\, c(\vec{r}, t)\, d\vec{r} \tag{2.21}$$

where $\int \ldots d\vec{r}$ denotes integration over the entire sample volume. ε cancels out after insertion into $G(\tau)$, and the latter becomes:

$$G(\tau) = \frac{\langle \int \hat{W}(\vec{r})\, \delta c(\vec{r}, t)\, d\vec{r} \int \hat{W}(\vec{r})\, \delta c(\vec{r}, t+\tau)\, d\vec{r} \rangle}{\langle \int \hat{W}(\vec{r})\, c(\vec{r}, t)\, d\vec{r} \rangle^2} \tag{2.22}$$

To solve this expression, one usually assumes ergodicity, *i.e.*, equivalence of averaging in space and averaging in time, such that $\langle c(\vec{r}, t) \rangle_t = \langle c(\vec{r}, t) \rangle_r = \langle c \rangle$. Time-dependent and time-independent terms are separated such that the time-dependence

in $G(\tau)$ is expressed through the particle concentration correlation function. For the detection volume profile $\hat{W}(\vec{r})$, the most typical model is a 3-dimensional Gaussian with e^{-2} width w_0 perpendicular to the optical axis (xy plane) and with $z_0 = Sw_0$ along the optical axis (z):

$$\hat{W}(\vec{r}) = \exp\left[-2\left(\frac{x^2+y^2}{w_0^2} + \frac{z^2}{S^2 w_0^2}\right)\right] \tag{2.23}$$

The concentration correlation function $\langle \delta c(\vec{r},t)\, \delta c(\vec{r}+\vec{\rho}, t+\tau)\rangle$ (with spatial shift variable $\vec{\rho}$) can be evaluated through a Gaussian solution of the diffusion equation to obtain an expected distribution of displacements for many particles, each starting at position $\vec{r}$:

$$\delta c(\vec{r}+\vec{\rho},\tau) = \frac{\delta c(\vec{r},0)}{(2\pi D\tau)^{3/2}} \exp\left(-\frac{|\vec{\rho}|^2}{4D\tau}\right) \tag{2.24}$$

with diffusion coefficient D. Lastly, the initial condition for interpretation of $\delta c(\vec{r},0)$ in Eq. 2.24 comes from the assumption that the obeserved molecules are dilute and non-interacting. In that case, (spatial) cross-correlations between distinct molecules vanish, and Poisson statistics govern the amplitude of observed fluctuations:

$$\langle \delta c(\vec{r},0)\, \delta c(\vec{r}+\vec{\rho},0)\rangle = \begin{cases} \langle c\rangle, & |\vec{\rho}| = 0 \\ 0, & |\vec{\rho}| > 0 \end{cases} \tag{2.25}$$

With these assumptions in place, and the additional definition for the average particle number in the observation volume $\langle N\rangle = \langle C\rangle \int \hat{W}(\vec{r})\, d\vec{r}$, Eq. 2.22 can be solved to obtain:

$$\begin{aligned} G(\tau) &= \frac{\gamma}{\langle N\rangle} \frac{1}{1+\frac{4D\tau}{w_0^2}} \sqrt{\frac{1}{1+\frac{4D\tau}{S^2 w_0^2}}} \\ &= G_0 \frac{1}{1+\frac{\tau}{\tau_{diff}}} \sqrt{\frac{1}{1+\frac{\tau}{S^2\tau_{diff}}}} \end{aligned} \tag{2.26}$$

with the diffusion time $\tau_{diff} = w_0^2/4D$, based on the Einstein-Smoluchowski equation (Eq. 2.7) for diffusion over the squared distance w_0^2. In other words, the diffusion time can be interpreted as an average residence time of a single molecule within the observation volume. γ is a shape factor that depends on the definition of the observation volume. Many authors define the observation volume such that $\gamma = 1$, but throughout this thesis γ will be defined as:

$$\gamma = \frac{\int \hat{W}^2(\vec{r})\, d\vec{r}}{\left(\int \hat{W}(\vec{r})\, d\vec{r}\right)^2} \tag{2.27}$$

for the three-dimensional Gaussian model of $\hat{W}(\vec{r})$, $\gamma = 2^{-3/2} \approx 0.35$. In practice, one usually determines τ_{diff} and G_0 *via* nonlinear least-squares fitting of this model or analogous expressions to experimental ACFs. Determination of these time scale

and amplitude parameters requires little *a priori* knowledge about the experimental system: S is the only other parameter, and has a relatively small impact on the former two (Figure 2.21). G_0 and τ_{diff} can then be interpreted in terms of concentrations and diffusion coefficients with knowledge about the shape and size of $\hat{W}(\vec{r})$, expressed through w_0 and S. Thus, an experimental workflow for FCS usually begins with calibration measurements of dyes with known diffusion coefficient to characterize w_0 and S.

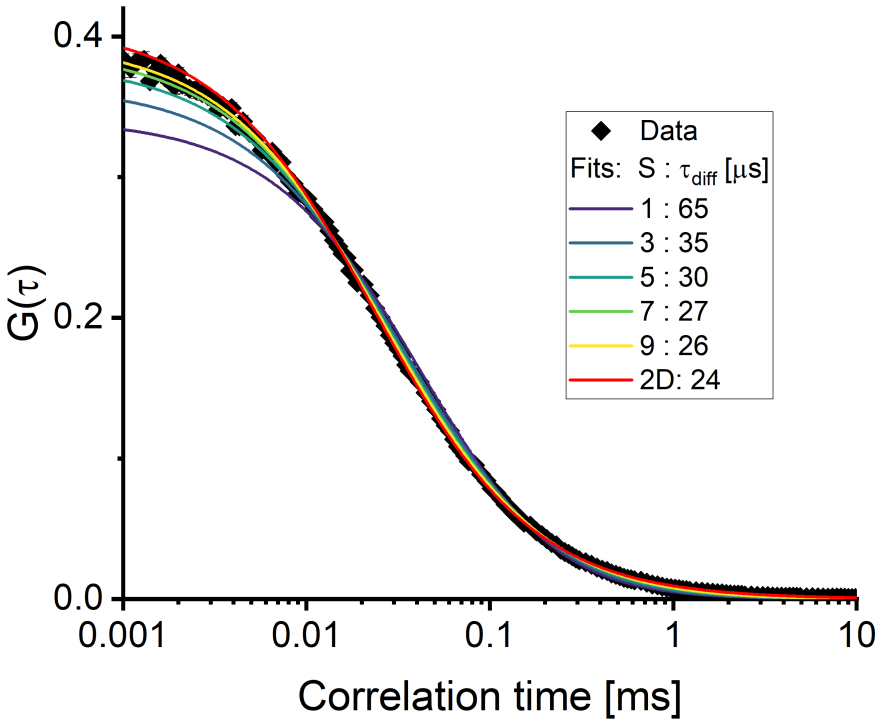

Figure 2.21. Effect of S on ACF Fitting. Shown is an experimental ACF measured from Alexa Fluor 488 carboxylate (Thermo Fisher) in aqueous buffer at 23°C with a series of fits in which S was fixed at different values. Based on other calibration data, $S \approx 5$ is found to be the correct value, a typical value for the microscope used (Picoquant MicroTime 200 with Olympus 60x NA1.2 UPlanApo water immersion objective and $30\mu m$ pinhole diameter). The slight deviation at short lag times is likely due to blinking dynamics (the detector afterpulse pattern has been removed using Fluorescence Lifetime Correlation Spectroscopy FLCS, see section 8.1.3).

Besides the described model for three-dimensional diffusion, many other models have been derived for frequently observed dynamics in FCS. Here, we enumerate some of the most important ones. Application-specific adaptations of these models are presented in later sections where needed.

- Two-dimensional diffusion (in the xy plane). This is effectively the limit case of Eq. 2.26 for $S \to \infty$.

$$G(\tau) = \frac{\gamma}{\langle N \rangle} \frac{1}{1 + \frac{\tau}{\tau_{diff}}} \tag{2.28}$$

with τ_{diff} as above. Here, $\gamma = 0.5$.

- Blinking of fluorescent dye molecules. Blinking typically follows exponential kinetics, and is thus described by an off-state fraction F_{blink} and a relaxation time τ_{blink}.

$$G(\tau) = G_0 g_{diff} \left[1 + \frac{F_{blink}}{1 - F_{blink}} \exp\left(-\frac{\tau}{\tau_{blink}} \right) \right] \tag{2.29}$$

where $G_0 g_{diff}$ corresponds to the righthand sides of Eqs. 2.27 or 2.28, depending on whether motion is in two or three dimensions.

- Multi-species mixtures. In the simple case of multiple noninteracting species, the measured ACF is a sum of the ACFs of the different species. However, the molecular brightness ε does not cancel out from the expression as before, and instead must be considered as a weighting factor for the summation of species ACFs. In this case, every species i is characterized by its own diffusion time $\tau_{diff,i}$, brightness ε_i, and particle number $\langle N_i \rangle$. In the case of 2D/3D mixtures, different species-wise γ_i also have to be considered:

$$G(\tau) = \frac{\sum_i \gamma_i \langle N_i \rangle \varepsilon_i^2 g_{diff,i}(\tau)}{\left[\sum_i \langle N_i \rangle \varepsilon_i \right]^2} \tag{2.30}$$

Note that the molecular brightness ε and particle number $\langle N \rangle$ appear only as products and therefore cannot be distinguished in multi-species mixtures based on the ACF alone.

Besides the single-spot confocal FCS based on autocorrelation analysis, many related techniques have been developed in acquisition and data analysis.

An important extension of the FCS concept is cross-correlation analysis. Dual-color fluorescence cross-correlation spectroscopy (FCCS [161, 162]) exploits the spectral specificity of fluorescence to distinguish signal from multiple fluorophores acquired in parallel. Cross-correlation of the signals from the distinct species then yields information about their interaction: Particles from non-interacting molecule species will show independent fluorescent fluctuations, with negligible cross-correlation function. If the particles interact, the cross-correlation function will show a significant amplitude as fluctuations in the two signal traces will occur simultaneously. The FCCS concept can also be generalized to other signatures that allow to distinguish labelled particle species, such as fluorescence lifetime and anisotropy decay characteristics [163, 164].

Optically, FCS has been extended to the use of observation volumes other than the conventional confocal observation volume [165]. The use of total internal reflection excitation [166–171], or its inverse, supercritical angle fluorescence emission [172], allows extreme background suppression when observing processes adjacent to a glass

surface, for example diffusion on a supported lipid bilayer or in the membrane of adherent cells, or binding to surface-confined particles. Stimulated emission depletion (STED)-FCS [173,174] exploits the super-resolution information revealed by STED microscopy [175,176] to reveal diffusion information on length scales below the diffraction limit, for example to probe lengthscale-dependent mobility, *i.e.*, anomalous diffusion. Different kinds of nanophotonic devices have been used for purposes similar to STED-FCS, as well as for enhancement of signal to background ratio and/or signal to noise ratio, at the cost of more complex sample preparation [177–179].

FCS acquisition strategies have also been has been extended to observation of multiple positions in parallel. This can be achieved through different means. Firstly, dual-focus techniques based on parallel data acquisition in two distinct diffraction-limited observation volumes allow acquiring data that is similar to single-spot FCS, but including auto- and cross-correlation functions of two distinct positions [151,180,181]. The cross-correlation functions reveal diffusion coefficients *via* the timescale of displacement over the distance between observation spots, which is more robust against optical aberrations than the diffusion time of the single-spot ACF. The concept has been generalized to more than two positions, with particular emphasis on detecting unidirectional motion or obstacles [182,183]. Modern scientific camera chips can be exploited for massive parallelization [170,184,185]. Scanning FCS techniques acquire data with non-stationary observation volume. This can be exploited to parallelize data acquisition in many positions, or to introduce a defined pattern in space and time into the data which again can robustify diffusion coefficient quantification [186–189].

Alternative statistical frameworks have been developed to use the same fluorescence fluctuation data in a different, complementary analyses. This can be useful to avoid some of the ambiguities of the ACF, in particular that of $\langle N \rangle$ and ε in multi-species mixtures. Among the earliest ideas to achieve this was the use of higher-order correlation functions using two-point correlations with individual data points raised to higher powers, which responds differently to differences in ε compared to differences in $\langle N \rangle$ [190,191]. This noise-prone approach never became very widely adopted, and the same is true for the analysis of higher moments, which is equivalent to the analysis of the amplitudes of higher-order correlation functions. A more popular framework that emerged from these ideas is the Photon Counting Histogram (PCH [192,193]), which essentially predicts the probability mass distribution for observing n_{nv} photons within a given time given $\langle N \rangle$ particles with brightness ε. As many dim particles will yield a different PCH than few bright particles, PCH analysis allows simultaneous estimation of $\langle N \rangle$ and ε, even in multi-species mixtures in which these parameters remain ambiguous in FCS. PCH has been extended to analysis with variable bin time, explicitly considering the effect that diffusion and blinking have [194]. This in turn allowed this so-called Photon Counting Multiple Histograms (PCMH) approach to be combined with ACF analysis in a single global analysis framework [195].

FCS is a family of techniques suitable for the study of many parameters of interest for studying self-organization, self-assembly, phase-separation, and other related phenomena. In the work described in this thesis, FCS was used and developed further in various contexts.

3
Contents of this thesis

Progress in bottom-up synthetic biology creates more and more sophisticated model systems that allow us to study the physical principles underlying the organisation of living system in increasing detail. Time-resolved (near-)single-molecule techniques like fluorescence correlation spectroscopy and single-molecule imaging allow detailled study of the dynamics of the involved biomacromolecules. However, these synthetic systems exhibit intermediate complexity between the frequently studied extremes of intact living organisms on the one hand, and purified molecules in homogeneous solution on the other. Thus, to make the full use of the information content offered by single-molecule studies in biomimetic systems, bespoke measurement protocols often need to be developed, as non-trivial experimental challenges arise when using these complex methods methods. I collaborated with colleagues developing and studying different protein- and/or DNA nanotechnology-based biomimetic systems to develop experimental workflows to address their questions:

- Jointly with Yusuf Qutbuddin, Gereon Brüggenthies, and others, I studied the higher-order self-assembly of DNA origami nanoparticles (Chapter 4). Here, the focus was on the one hand on the use of SMLM to characterize assembly morphologies, and on the other hand to characterize assembly kinetics using techniques based on time-resolved image analysis.

- With Leon Babl and Lise Isnel I studied liquid-liquid phase separation (LLPS) (Chapter 5). Fluorescence correlation spectroscopy (FCS) is an attractive technique for studying the physical chemistry of LLPS that gives access to many relevant parameters. However, there are specific technical difficulties in FCS in condensates that are often overlooked or ignored. We explored these challenges and propose best practices to circumvent them.

- With Adrián Merino-Salomón, Nastasja Kaletta, Adam Mamot, and others, I studied the self-assembly of bacterial cytoskeleton filaments. First, we performed FCS studies on the self-assembly of the *E. coli* FtsZ protein, in particular to study its interaction with the cross-linking protein ZapD (Chapter 7). This was followed by studies of other filament-forming proteins, and led to the more general question of how to optimally deal with polydisperse systems in FCS (Chapter 6).

- All the aforementioned projects, and other side projects not included in this dissertation, required custom software solutions for data analysis, simulation, and/or acquisition. I newly developed or adapted a number of software tools for fluorescence correlation spectroscopy and single-molecule imaging, with contributions from Yusuf Qutbuddin and others. Some of these tools are widely applicable and are expected to continue to be useful beyond the projects that motivated their development. The theoretical basis and technical implementation of these tools are described in Chapter 8.

The investigations described here mostly deal with the question of *how* measurements could be done, and less *what* those measurements taught about biochemistry and physics of life. The work described in this thesis forms a basis for performing robust measurements to answer various questions of current interest within the research program of the Department of Cellular and Molecular Biophysics of the Max Planck Institute of Biochemistry, and in the synthetic biology community in general.

Part II

Results and Discussion

4

Design Features to Accelerate the Higher-Order Assembly of DNA Origami on Membranes

DNA origami is a versatile platform for construction of synthetic biomimetic molecular structures (see Section 2.5). Frequently, DNA origami particles are assembled further into higher-order structures to reach even higher structural and functional complexity [196], or to achieve larger structures with repeating units, *e.g.*, to cover a certain area [197–200]. This process tends to be slow though, with incubation times for structure assembly often reported in the range of hours, or overnight.

Built from DNA, DNA origami are a natural match for analysis via DNA-PAINT microscopy [138,201]. In DNA-PAINT microscopy, reversible binding of dye-conjugated "imager strands" to complementary "docking strands" conjugated to the structure of interest creates a blinking effect. At suitable imager strand concentrations, only a sparse subset of docking sites is labelled at a given time, allowing for super-resolution image build-up following the principle of single-molecule localization microscopy [36, 130, 131].

In early implementations, DNA-PAINT originally was very time-comsuming in acquisition [138]. More recent advances systematically accelerated the acquisition through optimization of buffer conditions and optimized DNA sequence design [202, 203]. In particular, a tremendous speed gain could be achieved by combining the use of short imager strand sequences with high off-rates of binding with repetitive, low-complexity, sequences. The use of repetitive sequences has the effect of creating effectively multiple binding sites within a single docking site DNA overhang, thus increasing the on-rate strongly. That way, both on-rate and off-rate, and thus the overall binding turnover and acquisition speed, were increased [203].

The research project described in the following section was motivated by the success in accelerating DNA-PAINT microscopy in two ways: Firstly, the acceleration of DNA-PAINT microscopy should make feasible the imaging of structures that under more traditional protocols would have been too dynamic for high-quality image acquisition. Secondly, we reasoned that the same concepts used to accelerate DNA-PAINT microscopy could be used to accelerate the higher-order self-assembly of DNA origami nanoparticles diffusing on lipid membranes.

We designed DNA origami structures capable of diffusing on supported lipid bilayer membranes, and suitable for imaging using DNA-PAINT microscopy for struc-

tural characterization, or for bright continuous labelling for mobility characterization. We confirmed that when the DNA origami particles diffuse, DNA-PAINT is incapable of acquiring distinctive images of DNA origami particles. After addition of cross-linking DNA strands, DNA origami "monomers" assembled into higher-order structures, which were greatly reduced in mobility and could be resolved by accelerated DNA-PAINT with acquisition times of ca. 5-8 min. We compared structures formed by different cross-linkers and found small but reproducible differences, with too-short linkers insufficient for formation of stable higher-order structures, and too-long linkers increasing propensity for cross-linking in unintended geometries. Finally, and importantly, we find that using low sequence-complexity cross-linking oligonucleotides accelerate the cross-linking process dramatically. In fact, DNA-PAINT no longer offered sufficient time resolution to observe the kinetics of the process under our conditions. Thus, we opted for a faster temporal image correlation spectroscopy approach which could observe self-assembly kinetics with an effective time resolution in the order of 10 s, as verified by simulations. Using these analysis tools, we confirmed an order of magnitude acceleration of DNA origami self-assembly through low sequence complexity cross-linkers, as compared to conventional cross-linking strategies via binding to specific positions on the scaffold strand.

The insights we gained in this study using single-molecule imaging approaches help in further studies of self-assembly phenomena on membranes. Further studies in the same lab continued to successfully use the same strategies [198, 204].

Design Features to Accelerate the Higher-Order Assembly of DNA Origami on Membranes

Yusuf Qutbuddin†, Jan-Hagen Krohn†, Gereon A. Brüggenthies, Johannes Stein, Svetozar Gavrilović, Florian Stehr, Petra Schwille*

Author contributions:

PS, JS, and YQ conceived the project. YQ and **JHK** performed all experiments. JS, and FS contributed to the DNA PAINT and SPT methodology. YQ, **JHK**, and GB designed the DNA origami. **JHK** performed SPT and image correlation analysis, and simulations. SG and YQ performed the AFM experiments. SG performed AFM image analysis. PS acquired funding. YQ and **JHK** prepared the manuscript. All authors commented on the manuscript. YQ and **JHK** contributed equally to the work.

In addition to the acknowledgments in the published manuscript, we would like to acknowledge Alena Khmelinskaia's contribution to this work for first proposing the idea of accelerating DNA origami cross-linking by the use of low-complexity sequences, which she and Beatrice Ramm used in a distinct manuscript prepared around the same time [205], which we were unaware of at the time of publication.

The following was published as part of a special issue of Journal of Physical Chemistry B dedicated to William E. Moerner, a pioneer of single-molecule imaging whose work laid important foundations for the methods employed in this work.

published in

The Journal of Physical Chemistry B (2021)

THE JOURNAL OF PHYSICAL CHEMISTRY B
A JOURNAL OF THE AMERICAN CHEMICAL SOCIETY

pubs.acs.org/JPCB Article

Design Features to Accelerate the Higher-Order Assembly of DNA Origami on Membranes

Published as part of The Journal of Physical Chemistry virtual special issue "W. E. Moerner Festschrift".

Yusuf Qutbuddin,[§] Jan-Hagen Krohn,[§] Gereon A. Brüggenthies, Johannes Stein, Svetozar Gavrilovic, Florian Stehr, and Petra Schwille*

Cite This: *J. Phys. Chem. B* 2021, 125, 13181−13191 Read Online

ACCESS | Metrics & More | Article Recommendations | Supporting Information

ABSTRACT: Nanotechnology often exploits DNA origami nanostructures assembled into even larger superstructures up to micrometer sizes with nanometer shape precision. However, large-scale assembly of such structures is very time-consuming. Here, we investigated the efficiency of superstructure assembly on surfaces using indirect cross-linking through low-complexity connector strands binding staple strand extensions, instead of connector strands binding to scaffold loops. Using single-molecule imaging techniques, including fluorescence microscopy and atomic force microscopy, we show that low sequence complexity connector strands allow formation of DNA origami superstructures on lipid membranes, with an order-of-magnitude enhancement in the assembly speed of superstructures. A number of effects, including suppression of DNA hairpin formation, high local effective binding site concentration, and multivalency are proposed to contribute to the acceleration. Thus, the use of low-complexity sequences for DNA origami higher-order assembly offers a very simple but efficient way of improving throughput in DNA origami design.

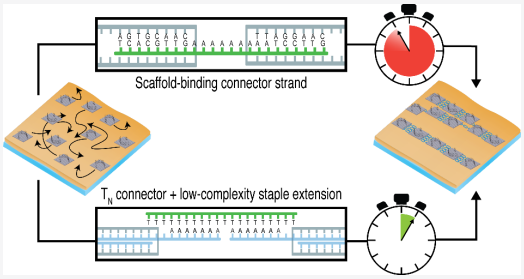

INTRODUCTION

Over the past 15 years, the development of DNA origami technology led to huge advances in the field of structural DNA nanotechnology, as it allows straightforward construction of large and complex nanostructures.[1] This is obtained by forcing long single-stranded DNA (ssDNA) "scaffold" strands into programmed conformations using many short "staple" strands. Diverse structures are possible, and multiple site-specific functionalizations can be introduced into a single structure with few-nanometer resolution.[2,3] Applications include single-molecule observation of chemical reactions,[4] positioning of nanoparticles for nanophotonics,[5] design of sensitive and specific biosensors,[6] and many others. Recent examples of DNA origami nanostructures designed in our lab include benchmark targets for single-molecule method development,[7] curved nanostructures to deform membranes,[8] or nanostructures serving as passive cargo to study transport processes in reaction−diffusion systems.[9]

The structural complexity allowed by the DNA origami technology is essentially limited by the length of the scaffold strand, typically 7−8 kb bacteriophage genomes. Even with cutting-edge strategies to increase the scaffold length up to 10 kb and modify it for different applications,[10,11] it is still challenging to produce DNA origami in sizes above 100 nm with high yield. To arrive at larger structures, the very first publication of the DNA origami technology already introduced the idea of cross-linking origami "monomer" particles into higher-order structures.[1] Nowadays, quite large and complex higher-order DNA origami structures ("superstructures") are being used for nanometer-precise positioning of structures over micrometer scales,[12,13] molecular "tubing" systems for linear transport of cargo,[14] or the encapsulation of cargo that itself is tens of nanometers in diameter.[15]

There are multiple strategies for assembling DNA origami superstructures. The most common ones exploit direct DNA−DNA binding, either sticky-end hybridization[16] or blunt-end stacking.[17] We focus on sticky-end hybridization strategies in the present manuscript: First, as sticky-end hybridization exploits Watson−Crick base pairing, the association is specific and programmable.[12] Second, sticky-end hybridization can be induced in a time-controlled manner by first preparing samples from DNA origami monomers and then cross-linking them by adding "connector strands".[18] Notably, programmability and

Received: August 31, 2021
Revised: November 13, 2021
Published: November 24, 2021

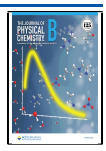

https://doi.org/10.1021/acs.jpcb.1c07694
J. Phys. Chem. B 2021, 125, 13181−13191

The Journal of Physical Chemistry B pubs.acs.org/JPCB Article

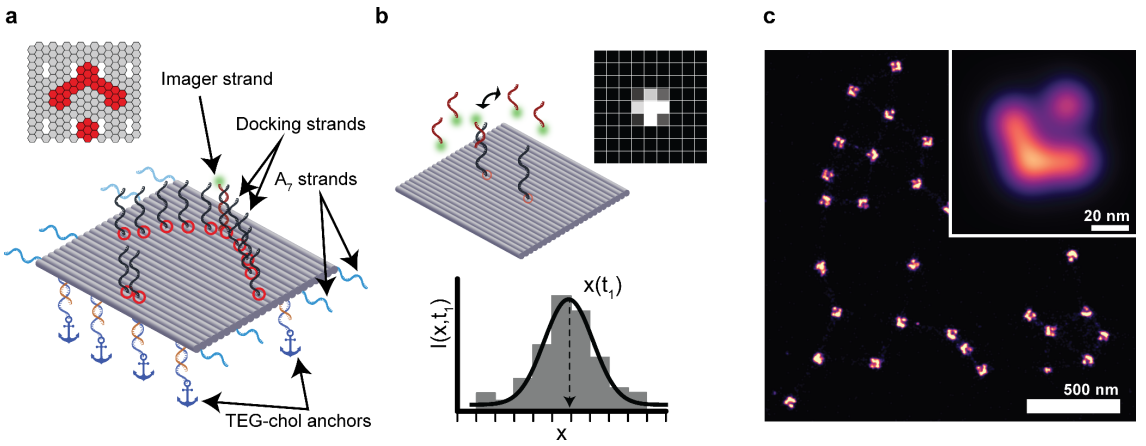

Figure 1. Design of DNA origami nanostructure used in this study. (a) Design schematic (elements not to scale). A 24-helix bundle is functionalized with a 36 docking sites for imager strands. Only a subset of these is shown for clarity, the Picasso Design[26] schematic in the corner shows the true arrangement. Additionally, the particle is functionalized for membrane binding (orange extensions binding dark-blue "anchor" sequences) and lateral extensions for linear cross-linking (light-blue). (b) DNA-PAINT super-resolution imaging. Imager strands reversibly bind to the docking sites on the particle, successively highlighting them and allowing their super-resolved position determination. (c) Experimental DNA-PAINT data from surface-immobilized DNA origami particles, with arrows shapes clearly resolved on many particles. Inset shows an average image from 32 901 particles.

time control are in principle also possible with blunt-end stacking but are more restricted.[17,19] Sticky-end hybridization is typically performed by two alternative approaches: One option is to directly prepare one origami species with staple strands that are extended with sticky ends binding to sequences in another origami, either directly in the scaffold, or in staple extensions.[12,20] Alternatively, to control the timing of association, one can prepare ssDNA stretches on the origami nanostructures and later add separate connector strands to bind and cross-link those ssDNA stretches *in situ*.[16,18] Here we will address the latter strategy (Figure 2), as DNA superstructure assembly with time-controlled onset is valuable for synthetic biology applications, such as mimicking cytoskeleton assembly in order to probe the response of *in vitro* reconstituted proteins to changes in their environment. Time control is also accessible through photoactivation schemes,[21] but this requires additional functionalization of oligomers. We aimed for a radically simple design for time-controlled DNA origami superstructure assembly, avoiding multistep assemblies,[12,14] special buffer requirements,[19] or non-DNA functionalizations.[21]

To allow time-controlled formation of DNA origami superstructures, the effective association rates after reaction initiation should be as high as possible. Past studies of DNA origami superstructures were often quite unsatisfactory in this regard, usually requiring incubation times in the order of 1 h or more,[22] up to overnight incubation.[16,23] Several ways to accelerate association have been identified. One option is multivalent binding between origami monomers to facilitate nucleation.[20,24] Specifically, for origami in 2D systems, increasing DNA origami monomer diffusion coefficients by adding monovalent cations and/or depositing particles on a fluid lipid bilayer rather than on a solid support accelerates assembly.[18,19,23] Additional acceleration comes from precisely matched and rigid geometries of the associating staple extensions to accelerate transition from monovalent binding nucleation to multivalent full binding.[20] Importantly, at least in solution, association rates for DNA origami dimerization reach values comparable to typical association rates for free DNA oligonucleotides.[20] This indicates that increasing effective association rates of the hybridization reaction itself may yield an additional gain in DNA origami superstructure assembly speed. With this idea in mind, we reasoned that recent developments toward increasing hybridization on-rates in DNA point accumulation for imaging in nanoscale topography (DNA-PAINT) microscopy could be transferred to accelerate DNA origami superstructure assembly.[25]

DNA-PAINT (Figure 1b) super-resolution microscopy is an implementation of single-molecule localization microscopy (SMLM) in which fluorophore-conjugated "imager strand" oligonucleotides reversibly bind to "docking sites" on the structure of interest. With low concentrations of imager strands, only a sparse random subset of docking sites is labeled at each time point, allowing their imaging in the single-molecule regime. Acquisition of thousands of frames and subsequent emitter point spread function fitting allows reconstruction of a super-resolved map of docking site coordinates.[26−28] Recent improvements in DNA-PAINT acquisition speed focus on improved docking site design. Specifically, docking sites with low-complexity sequences, i.e., repeats of a short sequence motif such as $[CTC]_N$, were found to be superior: These offer a large number of overlapping imager strand binding sites and thus increase the effective association rates for imager strand binding.[25] The same strategy can also be used in single-particle tracking (SPT) of sparse sets of DNA origami particles.[28] In this case, a long docking strand and a high concentration of imager strands yield unusually long tracks due to continuous replacement of bleached imager strands, circumventing photobleaching limitations to track duration.[29]

We thus set out to characterize two different sticky-end-based DNA origami superstructure assembly approaches in a lipid membrane-anchored 2D system. We use fluorescence techniques including single-particle tracking (SPT), DNA-PAINT, and image correlation analysis, complemented by atomic force microscopy (AFM), to characterize the assembly kinetics and the resulting structures. To this end, we employ a simple, stochastically assembling DNA origami superstructure based on

https://doi.org/10.1021/acs.jpcb.1c07694
J. Phys. Chem. B 2021, 125, 13181−13191

rectangular monomers.[1,26] We functionalized this DNA origami with staple extensions for cross-linking using low-complexity sequence connector strands to assemble superstructures *in situ* rather than preforming them in solution. We demonstrate assembly kinetics that are 1 order of magnitude faster than more traditional approaches by using low-complexity sequence connector strands. We discuss effects contributing to the acceleration, in particular the influence of length of the used sticky end. Our results provide useful insights for future experiments that require rapid cross-linking of DNA origami superstructures.

MATERIALS AND METHODS

Unless specified otherwise, chemicals were purchased from Sigma-Aldrich/Merck. DNA oligonucleotide sequences can be found in the Supporting Information.

Buffer Compositions. DNA origami folding buffer: 12.5 mM $MgCl_2$, 10 mM tris, 1 mM EDTA, pH 8.0. Buffer A: 100 mM NaCl, 10 mM tris, pH 8.0. Buffer B: 10 mM $MgCl_2$, 5 mM tris, 1 mM EDTA, pH 8.0. Buffer D: 140 mM NaCl, 7.5 mM $MgCl_2$, 20 mM tris, 0.75 mM EGTA, pH 7.6. SLB formation buffer: 150 mM KCl, 5 mM $MgCl_2$, 25 mM tris, pH 7.5. SLB washing buffer: 150 mM KCl, 25 mM tris, pH 7.5. AFM imaging buffer: 40 mM $MgCl_2$, 5 mM tris, pH 7.5.

Origami Folding and Purification. DNA origami were designed using Picasso Design software,[26] and modified using caDNAno.[30] Scaffold DNA (p7249, tilibit nanosystems, 10 nM in folding buffer) was mixed with a 10-fold molar excess of unmodified staple strands or staple strands with extensions for tetraethyleneglycol−cholesterol (TEG-chol)-anchoring to membranes. Staple strands with DNA-PAINT docking site extensions, the adapter sequence for the "tracking handle", or A_7 cross-linking extensions were added in a 100-fold molar excess. The folding reaction was performed via melting for 5 min at 80 °C and temperature ramping from 60 to 4 °C over 3 h. The folded origami were PEG-purified by two cycles of dilution (1:1 in folding buffer containing additional 15% *w*/*v* PEG-8000 (89510) and 250 mM NaCl), centrifugation (30 min, 17 900 rcf, 4 °C), and resuspension (in folding buffer, 30 min, shaking at 30 °C). DNA origami solutions were stored at −20 °C until use. Before use, DNA origami solutions were diluted with dilution factors adjusted differently for different sample types, typically on the order of 1:20 relative to the concentration obtained after PEG purification.

Surface-Immobilization of DNA Origami. Liquid chambers were assembled from coverslips (22 × 22 mm^2, no. 1.5, Marienfeld) and microscopy slides (Menzel-Gläser) using double-sided sticky tape (Scotch Transparent 665, Conrad) as a spacer. Chambers (ca. 20 μL volume) were passivated with biotinylated BSA (A8549; 1 mg/mL in buffer A, 3 min), washed with 40 μL of buffer A, and functionalized with streptavidin (S888, Thermo Fisher, 0.5 mg/mL in buffer A, 3 min). After washing with 40 μL buffer A and 40 μL buffer B, DNA origami were washed in (20 μL, in buffer B, 6 min). After incubation, unbound origami were washed out with 80 μL of buffer B. Finally, samples were washed with 40 μL of imaging solution (buffer D with imager strands and POCT oxygen scavenger) and sealed in an air-tight container with two-component epoxy glue (Toolcraft Epoxy Transparent, Conrad). The POCT oxygen scavenger consisted of 20 μg/μL catalase (P4234), 0.26 μg/μL pyranose oxidase (C40), 1 μg/μL trolox (238813), and 0.8% *w*/*w* glucose.

Supported Lipid Bilayer (SLB) Preparation and Membrane-Tethering of DNA Origami. SLBs were formed via vesicle fusion. Lipids dissolved in chloroform were mixed in glass vials, and after solvent evaporation under N_2 flow, the lipids were resuspended in SLB formation buffer to 4 μg/μL. The obtained large multilamellar vesicle suspensions were then sonicated (Bransonic 1510, Branson) until the solutions were clear. These small unilamellar vesicle (SUV) solutions were either used immediately or stored at −20 °C and re-sonicated before use. For fluorescence imaging of SLBs, sample chambers were assembled from cut 0.5 mL reaction tubes glued (NOA 68, Norland) onto ethanol- and water-rinsed coverslips and cured under 365 nm UV light exposure for 20 min. Immediately before use, chambers were surface-etched with oxygen plasma (30 s, 0.3 mbar, Zepto, Diener Electronics). Next, 75 μL of diluted SUV suspension (ca. 0.5 μg/μL in SLB formation buffer) were added into prewarmed (37 °C) chambers and incubated for 5 min, during which SLBs formed. After formation, SLBs were washed with 2 mL of SLB washing buffer, followed by 600 μL of buffer B. After the sample cooled to room temperature, the supernatant was replaced with 100 μL of 10 nM TEG-chol anchor oligonucleotide solution (buffer B, 3 min), followed by washing with 200 μL buffer B. Next, 100 μL of DNA origami solution was added (buffer B, 6 min), and the sample was washed with 200 μL of buffer B, followed by 200 μL of buffer D, and finally flushed twice with 200 μL of each imaging solution in buffer D with POCT. SLBs used in fluorescence experiments consisted of DOPC with 1 mol % biotinyl-cap-DOPE (both Avanti Polar Lipids) and 0.01 mol % Atto655-DOPE (ATTO-TEC). The biotin functionalization was not exploited in generating the data shown in this manuscript. SLBs for AFM imaging consisted of DOPC with 0.1 mol % Atto655-DOPE and were prepared on coverslips (22 mm diameter, no. 1, Marienfeld) in dedicated sample chambers for liquid-phase AFM (JPK). Atto655-DOPE was used to locate and quality-check membranes but not for generation of the data shown here. For preparation of SLBs for AFM, the same protocol was followed with the reagent volumes scaled up 2- to 3-fold compared to the chambers used for fluorescence imaging.

Total Internal Reflection Fluorescence Microscopy. Fluorescence microscopy was performed at a custom inverted microscope described in detail in a previous publication.[31] Light from a solid-state laser (561 nm, DPSS-System, MPB) was intensity-adjusted using a half-wave plate and a polarizing beam splitter (WPH05M-561 and PBS101, THORLABS). The beam passed through a refractive beam-shaping device (piShaper 6_6_VIS, AdlOptica) to create a flat illumination profile. To achieve evanescent-field illumination, the beam excentrically entered the oil immersion objective lens (100× NA 1.49 UAPON, Olympus). Fluorescence emission was collected by the same objective and filtered through suitable band-pass filters (605/64, AHF Analsentechnik) before detection on a CMOS camera (Zyla 4.2, Andor). During acquisitions, the temperature was stabilized at 23 °C (H101-CRYO-BL, Okolab), and *z*-positioning of the sample was stabilized via a piezo stage (Z-INSERT100, Piezoconcept and CRISP, ASI). The camera was operated with the open source acquisition software μManager[32] and images were acquired with 2 × 2 $pixel^2$ binning and field of view cropping to the central 700 × 700 (prebinned) pixels to achieve an effective pixel width of 130 nm and a field of view matching the circular flat illumination profile ca. 130 μm in diameter.

https://doi.org/10.1021/acs.jpcb.1c07694
J. Phys. Chem. B 2021, 125, 13181−13191

The Journal of Physical Chemistry B pubs.acs.org/JPCB Article

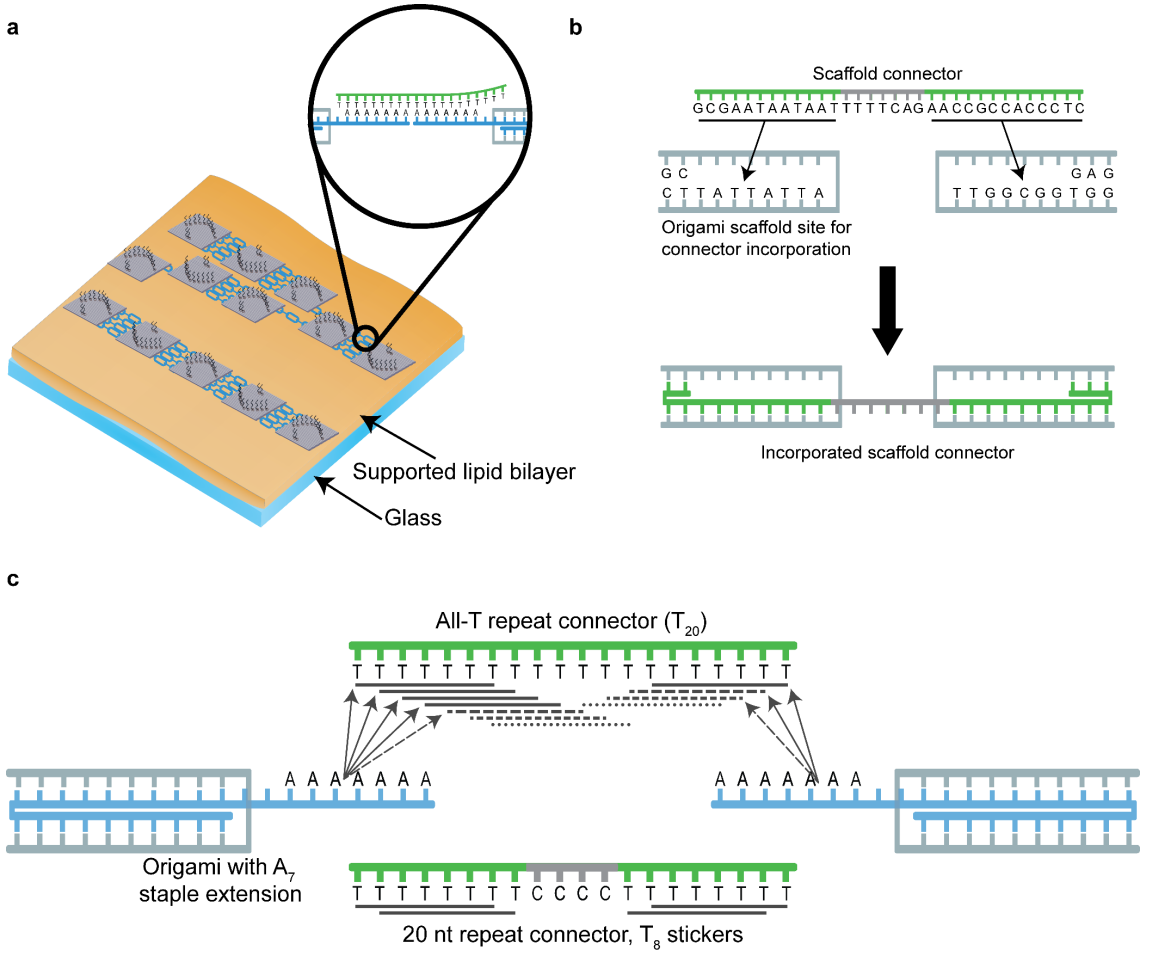

Figure 2. Schematic of DNA origami cross-linking kinetics on membranes. (a) Cross-linking geometry. Cross-linking sites are distributed on the DNA origami such that linear assemblies are expected, but with repeat connectors branching is also possible. (b) Scaffold connectors directly bind scaffold loops of two DNA origami particle, yielding highly site-specific assembly. (c) Repeat connectors bind the DNA origami indirectly via A_7 staple extensions. Depending on the design of the connector strand, many binding reading frames are available for the A_7.

Details for Different Acquisition Strategies. DNA-PAINT Microscopy. DNA origami nanostructures were functionalized with 5xR1 docking sites.[25] The imaging solution contained 1.25 nM $R1_{6nt}$-Cy3B imager strands. Illumination intensity was set to ca. 30 $\mu W\ \mu m^{-2}$. A total of 10 000 images per data set were acquired at a frame rate of 20 Hz.

Single Particle Tracking. DNA origami with a 20 nucleotide (nt) adapter sequence were deposited on membranes. A $[TCT]_{38}$ "tracking handle" docking site analogous to that described by Stehr et al.[29] was quasi-irreversibly recruited to the origami via the adapter complement: During DNA origami deposition, 10 nM tracking-handle−adapter conjugate were additionally present. To ensure a sparse subset of labeled DNA origami nanostructures suitable for SPT, a low density of tracking-handle-coupled particles was diluted in a 20-fold excess of unlabeled DNA origami particles, i.e., the same DNA origami, except without the adapter sequence. The imaging solution contained 10 nM $R5\_S2_{8nt}$-Cy3B imager strands. Illumination intensity was set to ca. 20 $\mu W\ \mu m^{-2}$. A total of 10 000 images per data set were acquired at a frame rate of 20 Hz.

Imaging for Correlation Analysis. DNA origami nanostructures were functionalized with 5xR1 docking sites,[25] which were quasi-irreversibly labeled through 4 min incubation with 10 nM $R1_{18nt}$-Cy3B. The imaging solution did not contain imager strands. Connector strands were added at 250 nM immediately before start of acquisition (ca. 10 s delay, limited by speed of pipetting and closing of microscope stage incubation chamber). A total of 300 images were acquired at a frame rate of 30 Hz at each time point along the cross-linking observation. The laser was shuttered between observation time points. Illumination intensity was set to ca. 2 $\mu W\ \mu m^{-2}$.

Fluorescence Image Analysis. Processing parameters for all fluorescence experiments are listed in Table S1.

DNA-PAINT Microscopy. Image stacks were processed using Picasso software.[26] Picasso Addon[7] was used for automation. The Python software can be found on Github (https://github.com/schwille-paint). The general pipeline started with Picasso

https://doi.org/10.1021/acs.jpcb.1c07694
J. Phys. Chem. B 2021, 125, 13181−13191

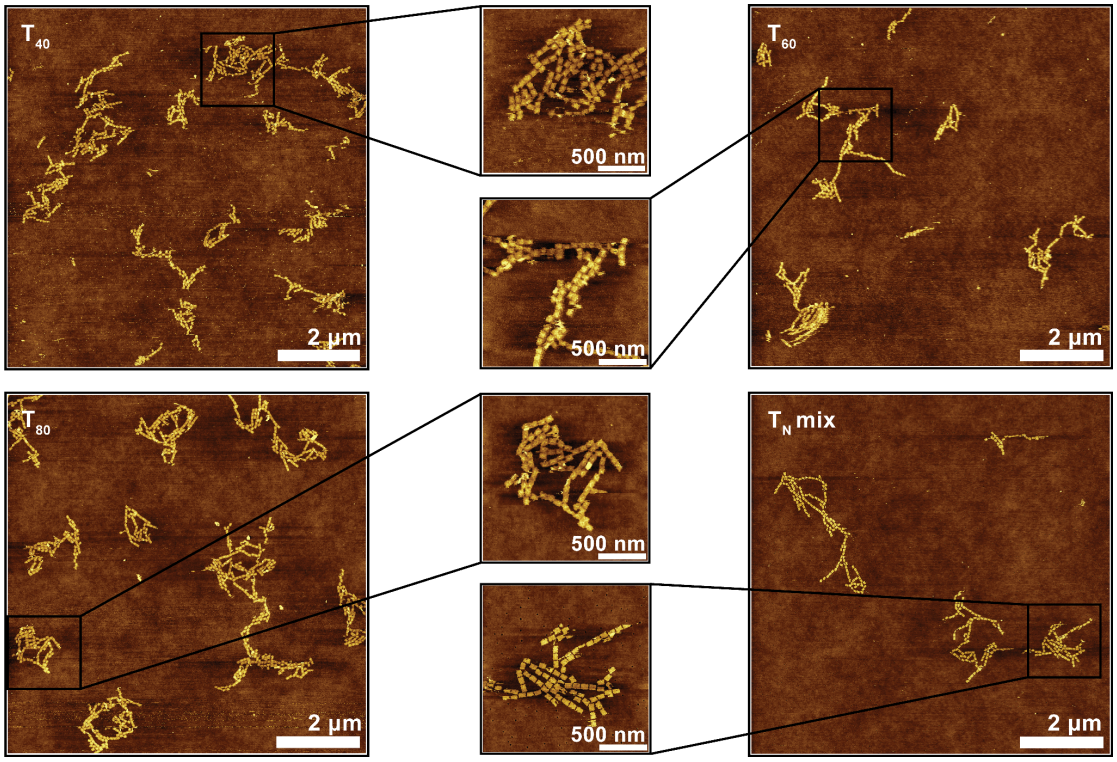

Figure 3. AFM characterization of DNA origami superstructures, showing conditions which yielded high-quality images. Additional conditions are shown in Figure S3. All images were acquired after 2 h incubation with 250 nM of the specified connector strand. The T_N mix is 50 nM each T_{14}, T_{20}, T_{40}, T_{60}, and T_{80}. The color-coded height scale in all panels is 6 nm.

Localize to pick and localize emitters, followed by Picasso Render for drift correction (RCC). In the case of biotin/streptavidin-immobilized origami, particles were manually picked in Picasso Render, followed by automated picking of similar particles and drift correction from picked particles. The average image from many immobilized DNA origami nanostructures was created using Picasso's Average3 module.

Single-Particle Tracking. The analysis pipeline started with localization in Picasso Localize as in the case of SMLM. Subsequent steps used the "SPT" package, which is also available via the above-mentioned GitHub page, for linking of localizations into tracks and mean-squared displacement analysis.

Correlation Analysis of Cross-Linking Kinetics. Image stacks were analyzed using a custom Python script, which is included in the Supporting Information. A detailed explanation of the analysis can be found in the Supporting Information, including a description of the simulations performed to test the accuracy of the analysis.

Atomic Force Microscopy. Measurements were performed on a JPK Nanowizard 3. The AFM images were taken in QI (quantitative imaging) mode using BioLever Mini BL-AC40TS-C2 cantilevers (Olympus). The set point force was 0.25−0.35 nN, acquisition speed 66.2 μm s^{-1}, Z-range 106 nm; 10 × 10 μm^2 fields of view were acquired with a 15 nm pixel size. Images were first processed in JPKSPM Data Processing (JPK, v6.1.142) performing a line-wise second-degree polynomial leveling followed by another second-degree polynomial leveling with limited data range (0% lower limit, 70% upper limit). Subsequent plane leveling, third-degree polynomial row alignment and scar correction were performed in Gwyddion (v2.58, http://gwyddion.net/).

RESULTS AND DISCUSSION

Simple DNA Origami Design for Cross-Linking Studies. To study DNA origami cross-linking, we first designed a suitable monomer structure. We reasoned that the use of a well-characterized modular structure would be most convenient and thus opted for a flat rectangular grid origami used in a number of previous single-molecule fluorescence studies.[7,25,29,33,34] On this monomer structure, we arranged 36 DNA-PAINT docking sites in the shape of an arrow. This design challenges the resolution in DNA-PAINT imaging and allows reading out the orientation of the origami on the surface (Figure 1). DNA-PAINT imaging of individual DNA origami particles immobilized on a glass surface via biotin−streptavidin anchoring indeed revealed the expected arrow pattern with high yield (Figure 1c).

We then functionalized the "bottom" side of the origami structure with staple extensions to bind it to supported lipid bilayer membranes (SLBs) via complementary TEG-chol-coupled oligonucleotides. Only two opposing lateral edges of the DNA origami were further functionalized for cross-linking into higher-order assemblies, aiming for linear chains rather than tilings, as the latter might be more difficult to distinuish from unspecific clustering (Figure 2a). In all cross-linking experiments described in this manuscript, each DNA origami edge

https://doi.org/10.1021/acs.jpcb.1c07694
J. Phys. Chem. B 2021, 125, 13181−13191

The Journal of Physical Chemistry B pubs.acs.org/JPCB Article

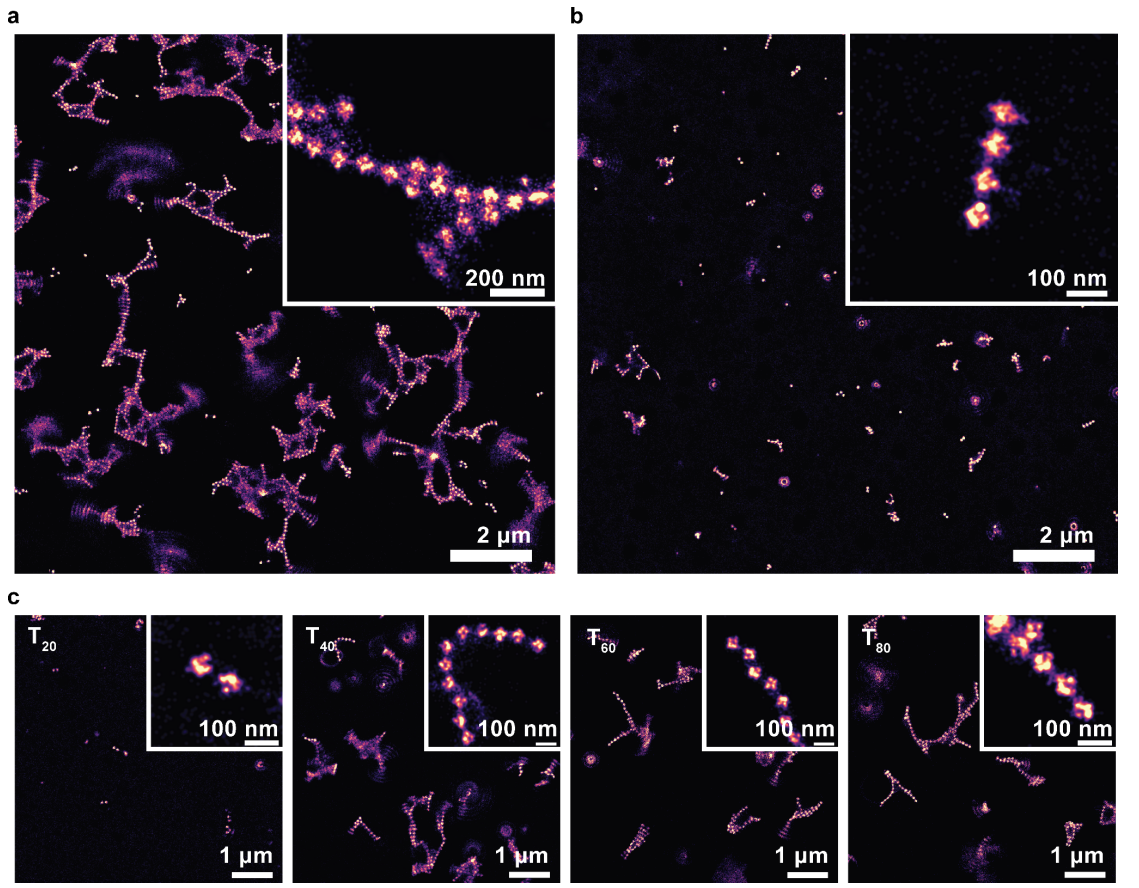

Figure 4. DNA-PAINT characterization of DNA origami superstructures cross-linked with different connector strands. (a) T_N repeat connector mix containing T_{14}, T_{20}, T_{40}, T_{60}, and T_{80} at 50 nM each (30 min incubation). (b) Scaffold connectors (250 nM total concentration, 20 h). (c) Individual repeat connectors (250 nM, 30 min).

participating in the association was designed to bind four connector strands. The DNA origami design exposes no blunt ends of DNA duplexes to avoid uncontrolled association via base stacking. Figure 2 gives a schematic summary of the DNA origami cross-linking strategies. One strategy that we employed has been frequently reported before.[16,18,23] Here, DNA origami nanostructures are cross-linked via connector strands that are essentially staple strands which incorporate into both monomers simultaneously (Figure 2b). For concision, we will call these "scaffold connectors". The other strategy is to incorporate modified staples into the DNA origami that carry extensions for indirect binding of connector strands to the DNA origami. We reasoned that DNA origami superstructure assembly could be accelerated through a connector strand design analogous to the above-mentioned high-on-rate docking site design[25,29,33] used for example in DNA-PAINT, i.e., the use of low-complexity sequences to increase the effective association rate (Figure 2c). We opted for short stretches of a single nucleotide species, specifically A_7 as an extreme case of such a low-complexity sequence. The connector strands were simply oligo-T sequences. These connector strands will be referred to as "repeat connectors". We note that we did not optimize our structure for highly specific assembly geometries. Instead, we aimed for a simple system that would serve as a model system for characterizing the assembly process itself. Thus, a stochastically assembling design was chosen in which also the shape of the formed structures would reveal the action of the connector strands in super-resolution imaging. With the basic origami design and cross-linking strategies at hand, we proceeded to create higher-order DNA origami assemblies on fluid membranes.

Repeat Connectors Are a Viable Option for Superstructure Assembly. We first characterized the structures of our cross-linked DNA origami structures using AFM to confirm the possibility of forming superstructures with desired geometry using repeat connectors. For AFM imaging, we prepared DNA origami samples on fluid SLBs and cross-linked them for 2 h using all-T repeat connectors of different lengths (T_{14}, T_{20}, T_{40}, T_{60}, T_{80}, or a mixture of all of these referred to as T_N mix). Before imaging, we exchanged the buffer, increasing the Mg^{2+} concentration from 7.5 to 40 mM to decrease mobility of the preformed structures for better AFM image quality. When using repeat connectors, ≥40 nt in length, high-quality images showing the expected formation of extended filaments were obtained which agree with the linear assembly geometry dictated by design (compare Figures 3 and 2). However, we saw hardly

https://doi.org/10.1021/acs.jpcb.1c07694
J. Phys. Chem. B 2021, 125, 13181−13191

any differences between different lengths ≥ 40 nt. Small oligomers formed by shorter repeat connector strands yielded lower quality images, suggesting that these led to hardly any superstructure formation within 2 h. In fact, the structures that we obtained with repeat connectors rather looked like unspecific association due to the high Mg^{2+} concentration (Figure S3). We did see some lateral assembly as well: As all cross-linking staple extensions have the same A_7 sequence and only differ by orientation of 3′- or 5′-ends, there is no strict specificity regarding the orientation of neighboring DNA origami monomers within the superstructure. This allows branching of linear assemblies, which leads to the formation of the observed 2-dimensional superstructures. We observed this branching somewhat less frequently when using scaffold connectors, which are site-specific in their binding to DNA origami and thus suppress branching (Figure S3). The presence of some branching even in this setting suggests Mg^{2+} unspecific association. Overall, the AFM data suggests that using long repeat connectors allows to cross-link DNA origami superstructures efficiently, albeit with trade-offs in specificity. However, there was no obvious difference between the different repeat connectors that efficiently cross-linked the DNA origami structures. In our AFM experiments, pushing of DNA origami structures by the AFM tip forced us to strongly increase the Mg^{2+} concentration, which led to unspecific association. Thus, at least with lengths ≥40 nt, repeat connectors do facilitate formation of DNA origami superstructures. To characterize the structures in more detail under origami-typical buffer conditions, we employed single-molecule fluorescence imaging.

Repeat Connectors Form Stable Superstructures Faster than Scaffold Connectors. Before acquiring super-resolution images of our samples, we used SPT to characterize particle mobility prior to cross-linking in the imaging buffer used for all following fluorescence microscopy experiments, containing 7.5 mM Mg^{2+} and 140 mM Na^{+}. SPT showed that our TEG-chol-anchored DNA origami particles diffused freely on the SLBs with a diffusion coefficient of ca. 0.2 $\mu m^2\ s^{-1}$ (Figure S4). However, upon addition of connector strands, we observed a strong decrease in mobility, indicating superstructure formation. A large fraction of particles was practically immobilized 30 min after addition of a mixture of oligo-T connector strands to A_7-functionalized origami (Figure S5). We reasoned that these may in fact be sufficiently immobilized for DNA-PAINT-based structural characterization using an accelerated acquisition protocol following Strauss and Jungmann,[25] which reduces the acquisition time to ca. 8 min. SMLM has been successfully applied to samples with slow but non-negligible motion such as live cells before, albeit with trade-offs between acquisition time and resolution.[35,36]

Even with that accelerated acquisition, we were unable to resolve any structures in DNA-PAINT imaging without cross-linking (Figure S6a). However, we were able to resolve large DNA origami superstructures on the membrane after cross-linking for only 30 min with the T_N repeat connector mixture (Figure 4a). Notably, in all our AFM and DNA-PAINT experiments, the connector strand solution had been replaced with connector strand-free imaging buffer before acquisition. This means that the observed assemblies were rather stable and did not undergo rapid dissociation/reassociation dynamics and, in particular, that the assemblies were not dependent on stabilization by the high Mg^{2+} concentration in the AFM imaging buffer. This confirms that the use of short A_7 sticker sequences combined with multivalent cooperative binding is sufficient for association of stable superstructures. In fact, the branching of oligomers seen in AFM and confirmed by SMLM suggests that our A_7 cross-linking extensions are too long for efficient "self-healing" of association sites into "ideal" association geometries.[12,37] We saw similar results when using scaffold connectors, but much longer incubation times were needed before high-quality imaging was possible: Compare Figure 4b acquired after 20 h to Figure S7 acquired after 2 h. This is in line with previous publications using scaffold connectors to cross-link DNA origami into 2D systems.[18,23] Each scaffold connector first needs to bind to its unique binding site on a DNA origami nanoparticle and then to the appropriate binding site on a second particle, requiring the DNA origami monomers to collide in the correct mutual orientation. Even after 20 h, only rather small assemblies were found. Thus, repeat connectors allowed assembly within less than 1 h, while scaffold connectors seemed quite unsatisfying regarding throughput of the experiment.

Although the image resolution in DNA-PAINT on membranes was lower than that in the image of origami directly immobilized on glass, we achieved resolution down to the 10 nm scale even on membranes. The resolution was limited by residual motion on the time scale of the acquisition, as demonstrated by the blurred clouds of localizations in various positions of the image. The orientation of some DNA origami monomers within the context of the superstructures was visible in the SMLM images, giving access to some information about the geometry in association. When repeat connectors are used, both parallel and antiparallel arrow orientations in neighboring particles are seen, which is obviously another consequence of the lack of site specificity in repeat connector binding. This is in stark contrast to the images obtained using scaffold connectors, which yield assemblies specifically with parallel orientation (Figure 4b). Notably, DNA-PAINT imaging of DNA origami deposited in a 3-fold higher density, but not exposed to connector strands, yielded low-resolution images of very different structures (Figure S6b). This confirms that despite the compromises in association geometry specificity when using repeat connectors, the retrieved superstructures are products of hybridization-based, connector strand-dependent association.

Finally, we compared superstructures formed by different lengths of all-T connector strands using DNA-PAINT imaging (Figure 4c). T_{14} (not shown) or T_{20} repeat connectors showed almost no cross-linking within 30 min, supporting the idea that assembly seen with AFM was mostly unspecific due to the high Mg^{2+} concentration. As in AFM, we saw little difference between the different all-T connectors of lengths ≥ 40 nt. From our DNA-PAINT experiments, we could thus confirm the connector strand-driven association of our DNA origami superstructures, and that long repeat connectors yield faster assembly than scaffold connectors. Motivated by these findings, we decided to characterize more quantitatively the differences between assembly kinetics of scaffold and repeat connectors, in order to obtain a mechanistic understanding of these differences.

Quantification and Mechanisms of Assembly Acceleration. In the next experiments, we set out to determine characteristic time scales for DNA origami higher-order assembly under different conditions. We opted for an image correlation analysis-based read-out of oligomerization (see Supplementary Note and Figure S1). The calculated correlation parameter, reporting the amplitude of temporal fluorescence fluctuations, increases as the particles associate into higher-order assemblies: Fluorescence fluctuations are larger when few bright particles diffuse through a pixel than many dim ones do. Later,

https://doi.org/10.1021/acs.jpcb.1c07694
J. Phys. Chem. B 2021, 125, 13181−13191

The Journal of Physical Chemistry B pubs.acs.org/JPCB Article

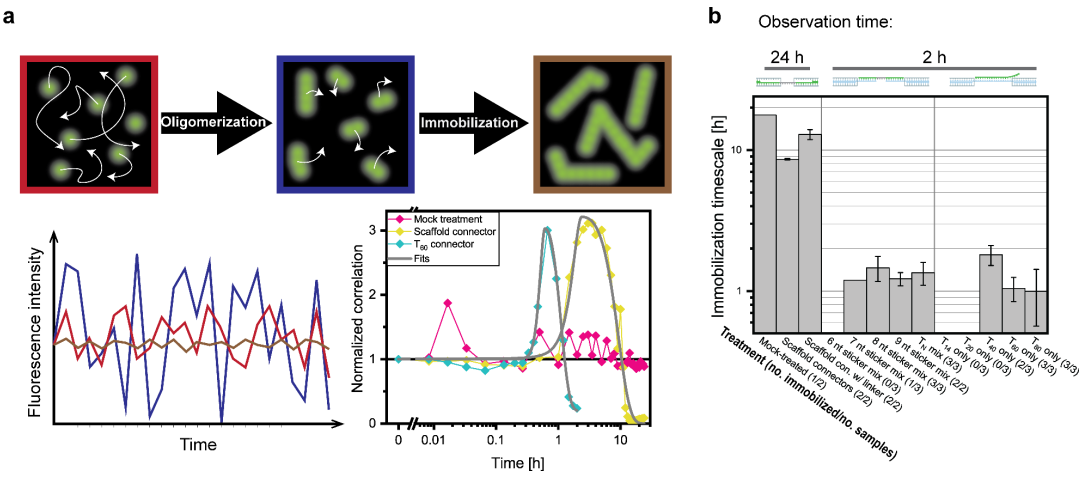

Figure 5. Correlation analysis of cross-linking kinetics. (a) Illustration and example data of correlation analysis. At the beginning of the experiments, monomers diffuse rapidly, creating moderate fluorescence fluctuations (red image and fluorescence intensity trace). As oligomerization begins, effectively fewer brighter particles are observed, increasing fluctuation amplitudes at unchanged average intensity (blue). As oligomerization progresses, yielding large, immobile particles, fluctuations become negligible (brown). The time traces of correlation parameter change show two examples of traces quite clearly undergoing these phases within observation time, and a buffer-treated negative control. (b) Kinetics of DNA origami higher-order assembly measured through image correlation analysis (mean ± s.d.). See the main text for details about the different conditions. Numbers in parentheses refer to the number of data sets for which an assembly time scale could be fitted compared to the number of data sets acquired for this condition. One of the mock-treated samples did show clear immobilization, which we attribute to unspecific sample degradation.

the correlation parameter falls to zero or a low baseline value, as the assemblies become so large that they are essentially immobile during the 10 s observation: Immobile particles yield an approximately constant signal over time (Figure 5a). The correlation analysis was found to be sensitive to oligomerization and immobilization in simulations of different ratios of mono- and oligomers (Figure S2). Additional advantages for long-term observation of the overall evolution of the sample are lower illumination intensities and the fact that in contrast to SMLM and AFM, this analysis captures the entire ensemble of particles rather than selectively showing immobile assemblies. Thus, image correlation analysis provided a convenient aggregate readout for higher-order assembly kinetics, from which we derived characteristic time scales of immobilization as a surrogate for assembly of DNA origami superstructures (Figure 5b). For these experiments, the spatial arrangement of docking sites previously used for DNA-PAINT plays no role (ca. 50 nm pattern width vs ca. 200 nm spatial resolution). Instead, we created bright particles through quasi-irreversible binding of multiple long $R1_{18nt}$-Cy3B imager strands to the full length of the docking site.[38] We systematically compared cross-linking by a variety of connector strands under otherwise constant conditions. These included the previously used scaffold connectors with and without short flexible linkers between the binding sites and all-T repeat connectors of lengths 14, 20, 40, 60, and 80 nt. In addition, we included mixtures of repeat connectors of all lengths, but with inserted oligo-C spacers that do not bind the oligo-A extensions, thus tuning the "sticker" length (i.e., number of binding reading frames) without changing the overall length of the connector strands (Figure 2c). The results are compiled in Figure 5b for comparison, but they will now be discussed sequentially.

Assembly kinetics were observed following addition of connector strands for either 24 h (scaffold connectors and negative controls) or 2 h (repeat connectors). Confirming the findings from DNA-PAINT imaging, very long incubation times in the order of 10 h were needed to create fully assembled structures using scaffold connectors. Adding a short flexible linker sequence to the scaffold connectors did not strongly affect the association kinetics. If anything, it slowed down association, which may be explained by the findings of Zenk et al.[20] that larger flexibility of connector binding sites can be detrimental to association.

We then characterized the repeat connectors with total lengths of 14, 20, 40, 60, and 80 nt. First, we looked at cross-linking kinetics for mixtures of repeat connectors with internal oligo-C stretches and terminal oligo-T stickers. Oligo-T sticker lengths varied from 6 nt (shorter than the A_7 docking site) to 9 nt (three binding reading frames). Using repeat connector mixtures for cross-linking, we saw a strong acceleration in association kinetics for sticker lengths of ≥7 nt. Within the 2 h acquisition time, we did not see any notable changes in the fluctuation data for 6 nt stickers, and for 7 nt stickers, only one out of three samples showed immobilization. Increasing the oligo-T sticker length at the end of the repeat connectors to 8 or 9 nt yielded robust assembly within <2 h, demonstrating the desired acceleration. These sticker lengths offer 2 or 3 reading frames for the A_7 binding partner, respectively, meaning that the data is entirely consistent with our idea of multiple reading frames accelerating binding. Another cause for acceleration is the same effect that is the cause for the reduced orientation specificity observed by nanoscale imaging: Repeat connectors can bind various positions on DNA origami nanoparticles, reproducing the effect of multivalent binding previously reported.[20,24] Time-resolved analysis of cross-linking kinetics thus confirms an order-of-magnitude acceleration in assembly dynamics by using our repeat connector strategy, as compared to our scaffold connector strategy.

Interestingly, no further acceleration of superstructure assembly was seen by using a mixture of all-T connector strands

https://doi.org/10.1021/acs.jpcb.1c07694
J. Phys. Chem. B 2021, 125, 13181−13191

of different lenths ("T_N mix" in Figure 5b) compared to those with 8 or 9 nt stickers. We hoped to find an explanation for this effect by comparing different lengths of all-T connector strands. The longer all-T repeat connectors accelerated assembly compared to shorter ones. While Zenk et al.[20] argued that increasing connector strand flexibility (i.e., length) can be detrimental to binding, here the increased length comes with an increase in the number of binding sites. We did not see immobilization within 2 h using T_{14} or T_{20} connectors. This suggests an explanation for the fact that using a mix of different all-T connectors did not further accelerate assembly relative to connectors with 9 nt stickers: The inefficient $T_{14,20}$ connectors likely competed with the more efficient $T_{40,60,80}$ connectors. The low efficiency of $T_{14,20}$ connectors may be explained by the fact that their short sequences cause A_7 docking sites to compete for overlapping binding sites on the same connector strand, which is clearly detrimental for cross-linking. This competition is suppressed in repeat connectors with internal oligo-C stretches and less relevant in long all-T ones.

Obviously, by comparing scaffold connectors to repeat connectors only consisting of oligo-T stretches, we looked at two extremes in a broad spectrum of thinkable cross-linker designs: one entirely optimized for assembly speed and the other entirely for specificity. Intermediate strategies would allow different trade-offs between these parameters. For example, one could combine oligo-A staple strand extensions with oligo-G staple extensions, creating two orthogonal cross-linking systems. These could also be combined through connectors concatenating oligo-T stretches and oligo-C stretches to link an oligo-A functionalized DNA origami face to an oligo-G functionalized one. This would increase specificity in assembly geometry, unlikely to result in antiparallel association of our DNA origami monomers. Repeats of 2 or 3 nt sequence motifs further increase the number of orthogonal motifs available for cross-linking,[25] but the number of binding reading frames will decrease rapidly with increasing motif length. Notably, such 2 nt motifs, albeit without repeats, were used previously to create very large DNA origami superstructures[12] with high specificity in assembly geometry. However, this specific formation of large structures required a multistep assembly that is slow and is not easily transferred to the *in situ* assembly in which we were interested.

Finally, an additional mechanism that likely contributes to the acceleration of binding using low-complexity sequences is the absence of internal hairpins from oligo-T or A_7 sequences. Hairpin formation can strongly reduce effective on-rates.[33,34] Due to sequence constraints from direct binding to the scaffold strand, hairpin formation could not be abolished completely in the design of the scaffold connectors used in this study according to the prediction by NUPACK.[39] One might thus consider high-complexity, yet hairpin-free, docking site extensions. While sequence design will become very challenging with increasing numbers of desired orthogonal sequences and the speed gain will likely remain modest compared to what our work demonstrates, such an approach remains highly attractive regarding specificity. In any case, our recommendation for designing rapidly cross-linking sequences for DNA origami superstructures is to avoid direct binding of connector strands to the scaffold and instead use staple extensions, designed with the lowest possible sequence complexity sufficient to ensure the required specificity.

CONCLUSIONS

In this work, we compared different design features to optimize assembly kinetics of higher-order DNA origami structures. A significant acceleration was achieved by cross-linking DNA origami indirectly via low sequence complexity connector strands binding to staple strand extensions, instead of direct binding of high-complexity sequences to loops in the scaffold DNA. We postulate two effects to contribute to the increased speed: The presence of multiple binding reading frames increases the effective local concentration of binding sites, and thus the effective association rate, and the used low-complexity sequences prevent the formation of hairpins. Using modifications of the strategy will allow multiple orthogonal sequences, increasing association specificity, with some trade-off in experimental throughput. This quite simple and generic approach to accelerate DNA origami superstructure assembly should prove useful to increase throughput of experiments in the field and to benefit experiments that require time-controlled assembly.

ASSOCIATED CONTENT

Supporting Information

The Supporting Information is available free of charge at https://pubs.acs.org/doi/10.1021/acs.jpcb.1c07694.

Methods, image correlation analysis workflow, simulations to assess sensitivity of image correlation analysis to oligomerization and immobilization, AFM results, example of single particle tracking results for monomeric DNA origami particles on DOPC SLBs, DNA-PAINT imaging of non-cross-linked and incompletely cross-linked DNA origami nanostructures, image analysis parameters, oligonucleotide sequences for DNA origami design, additional references (PDF)

MATLAB and Python scripts used for simulation and analysis of cross-linking kinetics (ZIP)

AUTHOR INFORMATION

Corresponding Author

Petra Schwille − *Department of Cellular and Molecular Biophysics, Max Planck Institute of Biochemistry, D-82152 Martinsried, Germany;* orcid.org/0000-0002-6106-4847; Email: schwille@biochem.mpg.de

Authors

Yusuf Qutbuddin − *Department of Cellular and Molecular Biophysics, Max Planck Institute of Biochemistry, D-82152 Martinsried, Germany;* orcid.org/0000-0003-0054-0608

Jan-Hagen Krohn − *Department of Cellular and Molecular Biophysics, Max Planck Institute of Biochemistry, D-82152 Martinsried, Germany; Exzellenzcluster ORIGINS, D-85748 Garching, Germany;* orcid.org/0000-0002-7383-3535

Gereon A. Brüggenthies − *Department of Cellular and Molecular Biophysics, Max Planck Institute of Biochemistry, D-82152 Martinsried, Germany*

Johannes Stein − *Department of Cellular and Molecular Biophysics, Max Planck Institute of Biochemistry, D-82152 Martinsried, Germany;* orcid.org/0000-0002-1335-1120

Svetozar Gavrilovic − *Department of Cellular and Molecular Biophysics, Max Planck Institute of Biochemistry, D-82152 Martinsried, Germany*

https://doi.org/10.1021/acs.jpcb.1c07694
J. Phys. Chem. B 2021, 125, 13181−13191

Florian Stehr − *Department of Cellular and Molecular Biophysics, Max Planck Institute of Biochemistry, D-82152 Martinsried, Germany*

Complete contact information is available at: https://pubs.acs.org/10.1021/acs.jpcb.1c07694

Author Contributions

[§]Y.Q. and J.-H.K. contributed equally to this work.

Funding

Open access funded by Max Planck Society.

Notes

The authors declare no competing financial interest.

■ ACKNOWLEDGMENTS

We thank H. G. Franquelim and L. Babl for useful discussions and H. G. Franquelim for help with AFM acquisitions. Y.Q., J.-H.K., and S.G. acknowledge support from the International Max Planck Research School for Molecular and Cellular Life Sciences (IMPRS-LS). J.S. and F.S. acknowledge support from Graduate School of Quantitative Bioscience Munich (QBM). All authors acknowledge support from the Center for Nano Science (CeNS). J.-H.K. received funding from the Deutsche Forschungsgemeinschaft (DFG, German Research Foundation) under Germany's Excellence Strategy, EXC-2094−390783311. Y.Q. received funding from the European Union's Horizon 2020 research and innovation programme under the Marie Skłodowska-Curie grant agreement no. 859416.

■ ABBREVIATIONS

AFM: Atomic force microscopy
DNA-PAINT: DNA point accumulation for imaging in nanoscale topography
FCS: Fluorescence correlation spectroscopy
SLB: Supported lipid bilayer
SMLM: Single-molecule localization microscopy
SPT: Single-particle tracking
ssDNA: Single-stranded DNA
SUV: Small unilamellar vesicle
TEG-chol: Tetraethyleneglycol−cholesterol

■ REFERENCES

(1) Rothemund, P. W. K. Folding DNA to create nanoscale shapes and patterns. *Nature* **2006**, *440*, 297−302.
(2) Wang, P.; Meyer, T. A.; Pan, V.; Dutta, P. K.; Ke, Y. The beauty and utility of DNA origami. *Chem.* **2017**, *2*, 359−382.
(3) Dey, S.; Fan, C.; Gothelf, K. V.; Li, J.; Lin, C.; Liu, L.; Liu, N.; Nijenhuis, M. A. D.; Saccà, B.; Simmel, F. C.; et al. DNA origami. *Nat. Rev. Methods Primers* **2021**, *1*, 13.
(4) Voigt, N. V.; Tørring, T.; Rotaru, A.; Jacobsen, M. F.; Ravnsbæk, J. B.; Subramani, R.; Mamdouh, W.; Kjems, J.; Mokhir, A.; Besenbacher, F.; et al. Single-molecule chemical reactions on DNA origami. *Nat. Nanotechnol.* **2010**, *5*, 200−203.
(5) Kuzyk, A.; Schreiber, R.; Fan, Z.; Pardatscher, G.; Roller, E.-M.; Högele, A.; Simmel, F. C.; Govorov, A. O.; Liedl, T. DNA-based self-assembly of chiral plasmonic nanostructures with tailored optical response. *Nature* **2012**, *483*, 311−314.
(6) Selnihhin, D.; Sparvath, S. M.; Preus, S.; Birkedal, V.; Andersen, E. S. Multifluorophore DNA origami beacon as a biosensing platform. *ACS Nano* **2018**, *12*, 5699−5708.
(7) Stein, J.; Stehr, F.; Schueler, P.; Blumhardt, P.; Schueder, F.; Mücksch, J.; Jungmann, R.; Schwille, P. Toward absolute molecular numbers in DNA-PAINT. *Nano Lett.* **2019**, *19*, 8182−8190.
(8) Franquelim, H. G.; Khmelinskaia, A.; Sobczak, J.-P.; Dietz, H.; Schwille, P. Membrane sculpting by curved DNA origami scaffolds. *Nat. Commun.* **2018**, *9*, 811.
(9) Ramm, B.; Goychuk, A.; Khmelinskaia, A.; Blumhardt, P.; Eto, H.; Ganzinger, K. A.; Frey, E.; Schwille, P. A diffusiophoretic mechanism for ATP-driven transport without motor proteins. *Nat. Phys.* **2021**, *17*, 850−858.
(10) Bush, J.; Singh, S.; Vargas, M.; Oktay, E.; Hu, C.-H.; Veneziano, R. Synthesis of DNA origami scaffolds: current and emerging strategies. *Molecules* **2020**, *25*, 3386.
(11) Engelhardt, F. A. S.; Praetorius, F.; Wachauf, C. H.; Brüggenthies, G.; Kohler, F.; Kick, B.; Kadletz, K. L.; Pham, P. N.; Behler, K. L.; Gerling, T.; et al. Custom-size, functional, and durable DNA origami with design-specific scaffolds. *ACS Nano* **2019**, *13*, 5015−5027.
(12) Tikhomirov, G.; Petersen, P.; Qian, L. Fractal assembly of micrometre-scale DNA origami arrays with arbitrary patterns. *Nature* **2017**, *552*, 67−71.
(13) Aghebat Rafat, A.; Pirzer, T.; Scheible, M. B.; Kostina, A.; Simmel, F. C. Surface-Assisted Large-Scale Ordering of DNA Origami Tiles. *Angew. Chem., Int. Ed.* **2014**, *53*, 7665−7668.
(14) Stömmer, P.; Kiefer, H.; Kopperger, E.; Honemann, M. N.; Kube, M.; Simmel, F. C.; Netz, R. R.; Dietz, H. A synthetic tubular molecular transport system. *Nat. Commun.* **2021**, *12*, 4393.
(15) Sigl, C.; Willner, E. M.; Engelen, W.; Kretzmann, J. A.; Sachenbacher, K.; Liedl, A.; Kolbe, F.; Wilsch, F.; Aghvami, S. A.; Protzer, U.; et al. Programmable icosahedral shell system for virus trapping. *Nat. Mater.* **2021**, *20*, 1281−1289.
(16) Jungmann, R.; Scheible, M.; Kuzyk, A.; Pardatscher, G.; Castro, C. E.; Simmel, F. C. DNA origami-based nanoribbons: assembly, length distribution, and twist. *Nanotechnology* **2011**, *22*, 275301.
(17) Woo, S.; Rothemund, P. W. K. Programmable molecular recognition based on the geometry of DNA nanostructures. *Nat. Chem.* **2011**, *3*, 620−627.
(18) Kocabey, S.; Kempter, S.; List, J.; Xing, Y.; Bae, W.; Schiffels, D.; Shih, W. M.; Simmel, F. C.; Liedl, T. Membrane-assisted growth of DNA origami nanostructure arrays. *ACS Nano* **2015**, *9*, 3530−3539.
(19) Woo, S.; Rothemund, P. W. K. Self-assembly of two-dimensional DNA origami lattices using cation-controlled surface diffusion. *Nat. Commun.* **2014**, *5*, 4889.
(20) Zenk, J.; Tuntivate, C.; Schulman, R. Kinetics and thermodynamics of Watson−Crick base pairing driven DNA origami dimerization. *J. Am. Chem. Soc.* **2016**, *138*, 3346−3354.
(21) Suzuki, Y.; Endo, M.; Yang, Y.; Sugiyama, H. Dynamic Assembly/Disassembly Processes of Photoresponsive DNA Origami Nanostructures Directly Visualized on a Lipid Membrane Surface. *J. Am. Chem. Soc.* **2014**, *136*, 1714−1717.
(22) Suzuki, Y.; Endo, M.; Sugiyama, H. Lipid-bilayer-assisted two-dimensional self-assembly of DNA origami nanostructures. *Nat. Commun.* **2015**, *6*, 8052.
(23) Kempter, S.; Khmelinskaia, A.; Strauss, M. T.; Schwille, P.; Jungmann, R.; Liedl, T.; Bae, W. Single particle tracking and super-resolution imaging of membrane-assisted stop-and-go diffusion and lattice assembly of DNA origami. *ACS Nano* **2019**, *13*, 996−1002.
(24) Jiang, S.; Yan, H.; Liu, Y. Kinetics of DNA tile dimerization. *ACS Nano* **2014**, *8*, 5826−5832.
(25) Strauss, S.; Jungmann, R. Up to 100-fold speed-up and multiplexing in optimized DNA-PAINT. *Nat. Methods* **2020**, *17*, 789−791.
(26) Schnitzbauer, J.; Strauss, M. T.; Schlichthaerle, T.; Schueder, F.; Jungmann, R. Super-resolution microscopy with DNA-PAINT. *Nat. Protoc.* **2017**, *12*, 1198−1228.
(27) Jungmann, R.; Steinhauer, C.; Scheible, M.; Kuzyk, A.; Tinnefeld, P.; Simmel, F. C. Single-molecule kinetics and super-resolution microscopy by fluorescence imaging of transient binding on DNA origami. *Nano Lett.* **2010**, *10*, 4756−4761.
(28) von Diezmann, L.; Shechtman, Y.; Moerner, W. E. Three-dimensional localization of single molecules for super-resolution imaging and single-particle tracking. *Chem. Rev.* **2017**, *117*, 7244−7275.

https://doi.org/10.1021/acs.jpcb.1c07694
J. Phys. Chem. B 2021, 125, 13181−13191

(29) Stehr, F.; Stein, J.; Bauer, J.; Niederauer, C.; Jungmann, R.; Ganzinger, K.; Schwille, P. Tracking single particles for hours via continuous DNA-mediated fluorophore exchange. *Nat. Commun.* **2021**, *12*, 4432.
(30) Douglas, S. M.; Dietz, H.; Liedl, T.; Högberg, B.; Graf, F.; Shih, W. M. Self-assembly of DNA into nanoscale three-dimensional shapes. *Nature* **2009**, *459*, 414−418.
(31) Stehr, F.; Stein, J.; Schueder, F.; Schwille, P.; Jungmann, R. Flat-top TIRF illumination boosts DNA-PAINT imaging and quantification. *Nat. Commun.* **2019**, *10*, 1268.
(32) Edelstein, A. D.; Tsuchida, M. A.; Amodaj, N.; Pinkard, H.; Vale, R. D.; Stuurman, N. Advanced methods of microscope control using μManager software. *Journal of Biological Methods* **2014**, *1*, No. e10.
(33) Schickinger, M.; Zacharias, M.; Dietz, H. Tethered multi-fluorophore motion reveals equilibrium transition kinetics of single DNA double helices. *Proc. Natl. Acad. Sci. U. S. A.* **2018**, *115*, No. E7512.
(34) Schueder, F.; Stein, J.; Stehr, F.; Auer, A.; Sperl, B.; Strauss, M. T.; Schwille, P.; Jungmann, R. An order of magnitude faster DNA-PAINT imaging by optimized sequence design and buffer conditions. *Nat. Methods* **2019**, *16*, 1101−1104.
(35) Biteen, J. S.; Thompson, M. A.; Tselentis, N. K.; Bowman, G. R.; Shapiro, L.; Moerner, W. E. Super-resolution imaging in live Caulobacter crescentus cells using photoswitchable EYFP. *Nat. Methods* **2008**, *5*, 947−949.
(36) Shroff, H.; Galbraith, C. G.; Galbraith, J. A.; Betzig, E. Live-cell photoactivated localization microscopy of nanoscale adhesion dynamics. *Nat. Methods* **2008**, *5*, 417−423.
(37) Tikhomirov, G.; Petersen, P.; Qian, L. Programmable disorder in random DNA tilings. *Nat. Nanotechnol.* **2017**, *12*, 251−259.
(38) Woehrstein, J. B.; Strauss, M. T.; Ong, L. L.; Wei, B.; Zhang, D. Y.; Jungmann, R.; Yin, P. Sub−100-nm metafluorophores with digitally tunable optical properties self-assembled from DNA. *Science Advances* **2017**, *3*, No. e1602128.
(39) Zadeh, J. N.; Steenberg, C. D.; Bois, J. S.; Wolfe, B. R.; Pierce, M. B.; Khan, A. R.; Dirks, R. M.; Pierce, N. A. NUPACK: Analysis and design of nucleic acid systems. *J. Comput. Chem.* **2011**, *32*, 170−173.

https://doi.org/10.1021/acs.jpcb.1c07694
J. Phys. Chem. B 2021, 125, 13181−13191

5

Measuring Partition Coefficients of In Vitro Biomolecular Condensates Using Fluorescence Correlation Spectroscopy

Liquid-liquid phase separation is of interest as a widespread organizing principle for compartmentalization and regulation in extant life, as a tool for synthetic biology, and as a candidate mechanism for protocell formation at the origin of life. Many physical parameters of condensates are of interest to understanding the properties of these structures, and how to engineer them for different applications (Figure 5.1).

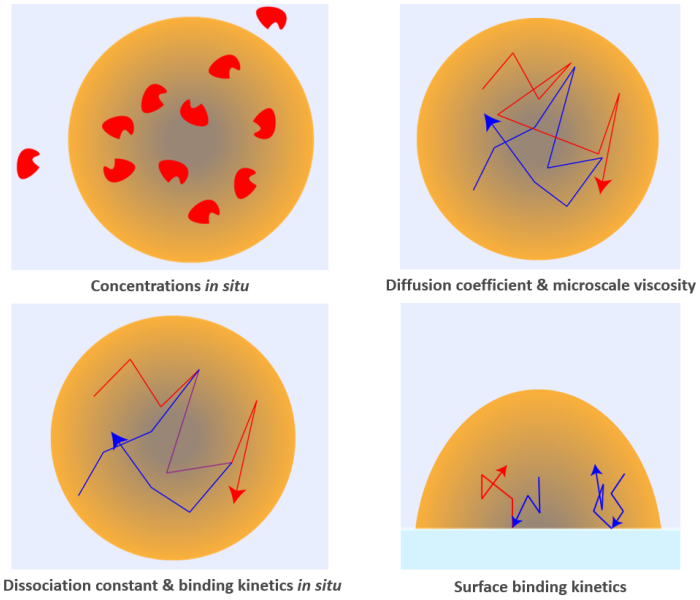

Figure 5.1. Parameters of interest in studying LLPS. The schematic illustrates some of the physicochemical parameters and processes of interest in studying liquid-liquid phase separation that are at least in principle accesible using Fluorescence Correlation Spectroscopy.

FCS gives access to many parameters of interest in the context of studying liquid-liquid phase separation (see Section 2.4): Diffusion coefficients as a readout of viscosity and polymer entanglement, concentrations in dense and dilute phases and thus binodals and partition coefficients, conformational kinetics of involved poly-

mers, and binding kinetics, to name a few [147,149,160,206]. Besides standard single-spot FCS [207–212], FCS techniques employed to study condensates cover STED-FCS to probe mobility over short length scales [213], and various scanning FCS schemes such as circle-scanning FCS [214] and ultrafast axial scanning FCS [215]. Scanning FCS techniques have two important advantages over standard single-spot confocal FCS that are relevant in studying liquid-liquid phase separation:

Firstly, scanning the beam means that bleaching and triplet-state build-up are reduced by illuminating each spot repeatedly for short times [216]. Particles in condensates typically diffuse slowly within the environment that is densely packed with polymer chains. Thus, statically illuminating the same spot for a long time in single spot FCS leads to pronounced build-up of dark-state populations like triplet-state or nonfluorescent isomers. This happens less in scanning FCS as the molecules are given time to relax into the ground state in the "stroboscopic" illumination scheme. Triplet-state transitions often precede bleaching [217], which is why scanning FCS can be favorable in samples prone to bleaching.

Secondly, the scan pattern introduces fixed and known length and time scales into the FCS acquisition which are less affected by spherical aberration than the shape of the PSF. Therefore, scanning FCS techniques are more robust in estimating diffusion coefficients in environments of nonideal refractive index, where spherical aberration is hard to avoid [214, 218]. Condensate droplets are such an environment, with the high polymer density increasing the refractive index [219]. Structured Illumination Microscopy (SIM), an imaging technique that notoriously sensitive to optical aberrations [220], highlights the effect as seen in Figure 5.2: SIM tends to amplify high-frequency noise in featureless areas like the inside of condensate droplets, but in the example, the refraction at the droplet boundary added an imprint from the illumination pattern into the image (appearing as stripes). Such refractive index mismatch also distorts FCS data heavily [221, 222], which in past FCS studies of particle mobility in crowded environments – similar to those within condensate droplets – has been misinterpreted as anomalous diffusion [222, 223].

With these issues in mind, single spot FCS seems nonideal for studying physical chemistry of liquid-liquid phase separation. However, it also remains the simplest and often most accessible FCS technique, that is best-known in the user community. Thus, we believed that a study to establish best practices for performing single-spot FCS on condensates would be help of value.

We used simple and well-characterized model condensates prepared from poly-L-lysine and uridine triphosphate (UTP) [224] to explore protocols for performing FCS experiments. We realized that the issue of condensates acting as micro-lenses can be circumvented *via* centrifugation protocols that merge microscopic droplets into macroscopic condensate mass that forms a dome on a coverslip, or even fully spans a coverslip sandwich. When this is combined with careful surface passivation of the coverslip to avoid unwanted interactions of the condensate constituents with the surface [225,226], this approach yields rather robust experimental conditions. Even then, the dense phase of a condensate still has an increased refractive index compared to water [219]. Here, we find that correct adjustment of the correction collar is critical, and the experimenter should be careful to double-check for deviations between the dense and dilute phase. Figure 6.1 illustrates the effect that the correction collar has on FCS data with a typical high-performance water immersion objective (60x NA 1.2

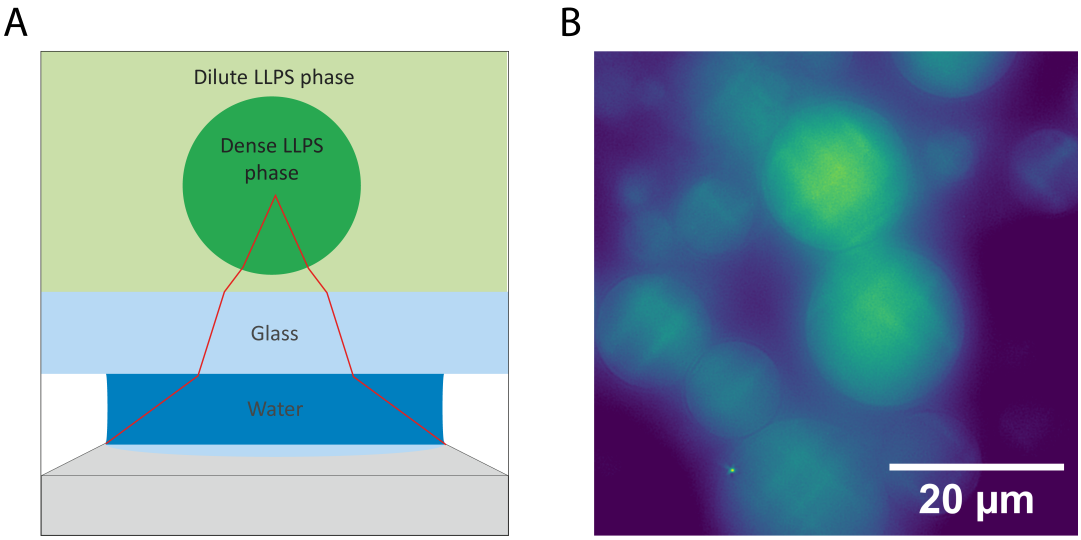

Figure 5.2. Refractive index mismatch. **A**: Schematic of a phase-separated sample on a microscope, with marginal rays of the illumination illustrated in red. The dense phase droplet has an increased refractive index, creating one more refracting interface in th beam path that must be corrected, or avoided altogether. **B**: Experimental data of Lattice Structured Illumination Microscopy on phase separated droplets formed from poly-L-lysine (100-mer) and UTP containing fluorescently labelled oligonucleotides (GAGGAGGA-3'-Atto655), highlighting artifacts from refraction at the condensates.

UPlanApo water immersion, Olympus) [227–230]. While the refractive index increment between dilute solution and dense condensate does not usually require a large adjustment of the correction collar, the figure illustrate that deviations (and sample-to-sample heterogeneity) can be signifcant.

Regarding data analysis, we found that a number of artifacts that commonly occur when performing single-spot FCS measurements in condensates can be recognized and at least partially corrected in the data. This somewhat relaxes the experimental challenge if suitable software is available. Thus, we developed a software tool for exactly this purpose, that also covers a few other artifacts beyond those typically relevant in condensates. The artifacts themselves and the software are discussed in the context of liquid-liquid phase separation in the following, and more generally and in more technical detail in section 8.1.

We compiled our insights into a protocol chapter covering best practices for sample preparation, for measurements, and for data analysis, which is presented in the following. Of note, not long before publication, another protocol chapter with similar aims but different emphasis was published by other authors [212]. As an application example for detailled discussion, we focused on the determination of partition coefficients, a parameter commonly of interest in characterizing liquid-liquid phase-separation due to its direct connection to the thermodynamics of the phase separation process and the recruitment of "guest" particles into the condensate.

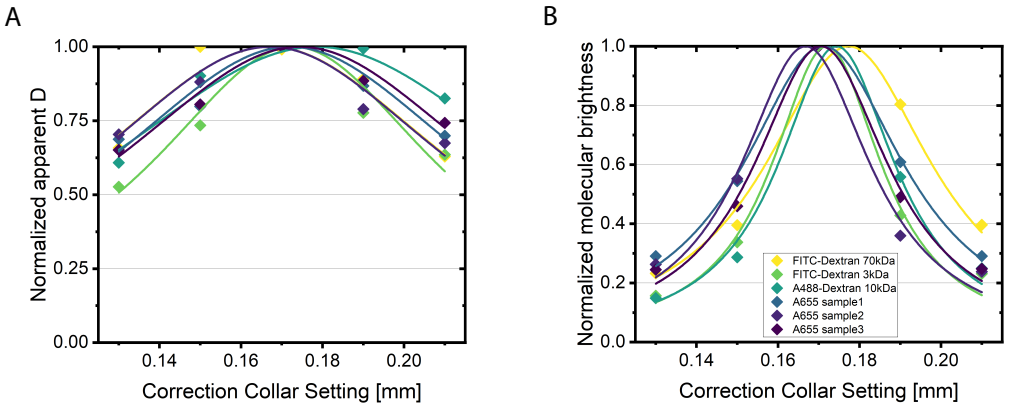

Figure 5.3. Correction Collar in FCS. Shown are apparent normalized diffusion coefficients (inverse of diffusion time, **A**) and normalized molecular brightness (**B**) as a function of correction collar setting in six different condensate samples containing a few different fluorescent labels. Lines are fits with Lorentzian profiles and are meant as a guide to the eye.

Measuring Partition Coefficients of In Vitro Biomolecular Condensates Using Fluorescence Correlation Spectroscopy

Jan-Hagen Krohn, Leon Babl, Lise Isnel, Yusuf Qutbuddin, Petra Schwille*

Author contributions:

PS, LB, and **JHK** conceived the project. **JHK**, LB, and LI performed experiments. **JHK** and YQ developed software. PS, **JHK**, and LB acquired funding. **JHK** prepared the manuscript. All authors commented on the manuscript.

published in

Remus T. Dame (ed.): Bacterial Chromatin. Methods and Protocols. Methods in Molecular Biology, volume 2819 (2024)

Reprinted from Krohn et al. 2024 [2] with permission from Springer Nature.

Chapter 21

Measuring Partition Coefficients of In Vitro Biomolecular Condensates Using Fluorescence Correlation Spectroscopy

Jan-Hagen Krohn, Leon Babl, Lise Isnel, Yusuf Qutbuddin, and Petra Schwille

Abstract

Liquid–liquid phase separation is a widespread organizing principle of live cells, including, for example, the spatiotemporal organization of bacterial chromatin. The biophysics of phase-separating systems is often studied in vitro to avoid the complexity of the live-cell environment and facilitate application of advanced biophysical methods. One attractive method for measuring, e.g., partition coefficients, in such systems is fluorescence correlation spectroscopy (FCS). FCS circumvents some of the limitations of the widespread confocal laser scanning microscopy image-based measurements. Here, we describe how to perform partition coefficient measurements in biological phase-separating systems. Our protocol details typical workflows for the preparation of in vitro reconstituted condensates, FCS data acquisition, and subsequent data analysis, including corrections of some common artifacts. Our recommendations should help avoid many pitfalls of partition coefficient determination in these challenging systems.

Key words Phase separation, Concentration, Reconstitution, Confocal microscopy

Abbreviations

ACF	Autocorrelation function
CLSM	Confocal laser scanning microscopy
FCS	Fluorescence correlation spectroscopy
FLCS	Fluorescence lifetime correlation spectroscopy
LLPS	Liquid–liquid phase separation
PLL	Poly-L-lysine
SNR	Signal-to-noise ratio
SPAD	Single-photon avalanche photodiode
TCSPC	Time-correlated single-photon counting
UTP	Uridine triphosphate

Remus T. Dame (ed.), *Bacterial Chromatin: Methods and Protocols*, Methods in Molecular Biology, vol. 2819,
https://doi.org/10.1007/978-1-0716-3930-6_21,

1 Introduction

A variety of membraneless organelles form through liquid–liquid phase separation (LLPS). The growing awareness of LLPS in cell biology has led to significant interest into the formation, regulation, and biophysics of these cellular substructures [1]. The biological functions of such membraneless organelles are tightly linked to the material properties of, and partitioning of molecules into, dense droplets [2, 3]. Liquid-like condensates often emerge from the interaction of proteins with nucleic acids, prominent examples being the eucaryotic nucleolus [4], stress granules [5], or the bacterial partition complex [6, 7]. While most previous studies of membraneless organelles have focused on eukaryotes, evidence is accumulating for LLPS in bacterial cytoplasm as well [8]. Many bacterial condensates form within, or close to, the nucleoid [7, 9–11]. However, bacterial cells are much smaller in size than eukaryotes, making in vivo characterization of these condensates challenging. Combinations of in vitro reconstitution and super-resolution microscopy methods have begun to reveal the underlying principles of bacterial phase separation. Similar to eukaryotic condensates, bacterial membraneless organelles are highly dynamic and tightly regulated [6, 7, 10]. These cellular substructures can dissolve and reform upon environmental stress or cellular signals, allowing spatiotemporal control of various cellular processes.

In vitro reconstitution studies of biomolecular condensates have highlighted two aspects of condensate formation as particularly important for their functionality: the difference in molecular mobility inside vs. outside of the condensate, and the partitioning, i.e., up-concentration or exclusion, of molecules between the dense phase and the surrounding dilute phase [12, 13]. The key descriptor of partitioning is the ratio of a solute's concentration inside the condensate droplet over the concentration in the surrounding dilute phase, known as the partition coefficient P. Partitioning of nucleic acids, proteins, or small molecules can be highly selective, allowing for rigorous control of the condensate composition [13]. Up-concentration of proteins and their substrates inside condensates can enhance reaction rates, nucleate the formation of mesoscopic assemblies, and even build hierarchical structures fulfilling complex biochemical tasks [4, 12, 14].

The partition coefficient is most frequently measured using confocal laser scanning microscopy (CLSM) images, simply using image grayscale ratios as estimates of concentration ratios. However, besides possible bias from optical aberrations, this assay can be distorted by changes in dark-state fractions and fluorescence quantum yields between the dense and dilute phases.

A complementary approach is fluorescence correlation spectroscopy (FCS) [15–17]. In a typical FCS measurement, a confocal

microscope is used to record fluorescence fluctuations in steady state with high time resolution. These fluorescence fluctuations over time are then statistically analyzed via their so-called autocorrelation function (ACF). The ACF $G(\tau)$ is calculated as

$$G(\tau) = \frac{\langle \delta F(t) \delta F(t+\tau) \rangle_t}{\langle F(t) \rangle^2} \quad (1)$$

with measured intensity data over time $F(t)$, time average $\langle \ldots \rangle$, fluorescence fluctuation $\delta F(t) = F(t) - \langle F(t) \rangle$, and lag time τ. The ACF is closely related to the signal variance, but while the variance is a single number reporting only the strength of signal fluctuations, the ACF represents their shape over time. Thus, the shape of the ACF can be used to retrieve kinetics of processes such as diffusion or fluorophore blinking. In addition to kinetics, particle concentrations can be determined from the amplitude of the ACF: small concentration fluctuations yield stronger signal fluctuations at low average concentration than at high average concentration. Measuring concentrations from the ACF amplitude is independent of the dye's quantum yield and thus allows true particle number counting. In addition, fluorophore blinking, which can also change the apparent concentration measured by CLSM, can often be directly corrected in FCS by fitting the ACF shape. Using the sample's fluorescence signal in a very different manner than CLSM, FCS-based concentration measurements are therefore complementary to ones based on CLSM and circumvent some of their limitations. Nonetheless, both CLSM and FCS are often possible on the same instrument. Thus, FCS is highly attractive for measuring concentrations, i.e., partition coefficients, in regions of interest in which dye photophysics may be altered—such as the distinct phases of a phase-separating sample. However, FCS is strongly influenced by signal drift, for example, due to photobleaching [18], and optical artifacts such as spherical aberration due to refractive index mismatch, which can inflate the size of the observation volume and thus lead to overestimation of concentrations [19]. These require special attention when measuring in biomolecular condensates.

In this chapter, we explain a workflow for confocal FCS-based measurement of partition coefficients in LLPS systems under controlled in vitro conditions. Note that in this chapter, we keep the explanations focused on a single well-defined target readout by restricting ourselves to the determination of partition coefficients using FCS, ignoring the characterization of particle dynamics. However, the very same data acquired following the protocol described here can also be used, e.g., for the determination of diffusion coefficients. While we describe measurements on simple model coacervates formed from poly-L-lysine (PLL) and uridine triphosphate (UTP) [20], the same protocols apply for other LLPS systems. Transferring these protocols for condensates formed from

DNA-binding proteins is straightforward, except for the specific idiosyncrasies of one's protein of interest regarding, for example, protein stability or condensate ageing. We begin by giving recommendations on sample preparation for in vitro LLPS studies, including coverslip passivation and condensate formation. Next, we describe the acquisition and analysis of confocal FCS data for partition coefficient measurements in condensates. Finally, we comment on a few more advanced data analysis techniques that we find helpful for addressing the specific challenges of FCS in LLPS systems.

2 Materials

One should aim for the highest possible purity in all chemicals, especially the condensate constituents and fluorescent dyes, as FCS is a highly sensitive near single-molecule technique and can be significantly compromised by background from impurities.

1. Coverslips (e.g., 22 mm × 22 mm, 170 μm thickness, high precision).
2. PTFE racks and sharp tweezers for coverslip handling.
3. Glass Petri dishes.
4. Oven (90 °C).
5. Sonication bath.
6. N_2 gas line.
7. Plasma chamber equipped with O_2 gas supply.
8. Ethanol (absolute).
9. Deionized water.
10. 0.5 M NaOH solution .
11. Acetone (water-free).
12. mPEG-5kDa-triethoxysilane.
13. DMSO (water-free).
14. Spacers for coverslip sandwich-based sample chamber assembly (e.g., Grace BioLabs SecureSeal Imaging spacers).
15. Condensate constituents. Used here: PLL 100-mer (e.g., from Alamanda Polymers) and UTP (e.g., from Jena Bioscience).
16. 1 M Tris–HCl stock solution, pH 7.5.
17. MilliQ water (or higher purity).
18. Fluorescently labelled particles: To be chosen to suit your biochemical system and microscope. Used here: Atto655-carboxylate and Alexa Fluor 647-carboxylate as simple model compounds.

19. FCS-compatible microscope: FCS requires a confocal fluorescence microscope capable of recording fluorescence intensity time traces with high time resolution and single-molecule sensitivity. There are many options for (commercial or home built) FCS-compatible systems. This manuscript is based on experiments performed at a PicoQuant MicroTime200 microscope with minor customizations. For reference, we describe the key components of our system and the rationale of their use. We typically excite fluorescence using laser pulse trains with a repetition rate of 40 MHz. Lower repetition rates allow higher information content for fluorescence lifetime-based analysis [21], while higher repetition rates or continuous-wave excitation improves signal-to-noise ratio and reduces excitation saturation effects. The objective is crucial for FCS: A high numerical aperture, preferably >1, is required. The lens immersion medium should be matched to the sample refractive index to minimize spherical aberration from refractive index mismatch. Water and aqueous buffers, including the dilute phase of many LLPS systems, have refractive indices close to 1.34. Condensate dense phase has a higher refractive index. Finally, the objective must offer good aberration correction including an adjustable correction collar (*see* **Note 1**). We typically use either Olympus 60× NA 1.2 UPlanApo water immersion or Olympus 40× NA 1.25 UPlanSApo silicon oil immersion objectives. In the detection path, besides spectral filtering using suitable dichroic mirrors and bandpass filters, the fluorescence emission is spatially filtered through a suitably sized confocal pinhole. We use a panel of exchangeable pinholes, picking for each experiment one with radius close to $\frac{5\lambda M}{2\pi NA}$ with peak emission wavelength λ, objective magnification M, and objective numerical aperture NA [22]. Finally, photons are detected by single-photon avalanche photodiodes (SPADs) and subsequently time tagged and digitized using a TCSPC card with 80-ns digitization time. Depending on the experiment, we sometimes use only one SPAD, but, if possible, we prefer to use a 50/50 neutral beam splitter to split the signal onto two SPADs (*see* **Note 2**). Our combination of lasers, detectors, and time-tagging electronics yields an overall time resolution in the order of 500 ps, which is sufficient for analyzing fluorescence lifetimes of many widespread dyes. The TCSPC capability together with pulsed excitation allows for fluorescence lifetime correlation spectroscopy (FLCS, *see* **Note 3**) unmixing of data. A three-axis piezo scanner allows precise positioning of the sample and scanning for image acquisition. Neither TCSPC nor imaging capabilities are strictly required for FCS analysis of condensates, but both are extremely helpful. If no fluorescence lifetime information is desired, a time resolution close to 1 μs is enough for most FCS applications.

3 Methods

3.1 Coverslip Passivation

Dense-phase droplets of LLPS systems tend to wet coverslip surfaces, which can cause problems for microscopy-based in vitro studies of condensates. FCS analysis usually assumes that there are no barriers to molecular motion close to the observation volume. If coverslip surface wetting flattens the droplet to an extent not much larger than the observation volume, this will distort measured correlation functions and bias estimated parameters. Even more importantly, depletion of molecules due to binding at the coverslip surface will reduce concentrations, introducing additional errors. Thus, we recommend thorough passivation of coverslips, for which we prefer polyethylene glycol (PEG) functionalization. PEGylation of coverslips is performed following this protocol based on [23] (*see* **Note 4**).

1. Place coverslips in a PTFE rack and rinse them twice with absolute ethanol and then twice with deionized water.
2. Blow-dry using pressurized air or N_2.
3. Place clean and dry coverslips in plasma chamber and etch with oxygen plasma (*see* **Note 5**).
4. Sonicate coverslips in 0.5 M NaOH solution for 30 min.
5. Rinse coverslips in deionized water at least twice.
6. Sonicate coverslips in deionized water for 5 min.
7. Rinse coverslips twice in acetone.
8. Sonicate coverslips in acetone for 5 min.
9. To prepare PEGylation solution, dissolve ca. 10 mg of mPEG-triethoxysilane in 30 µL DMSO per two coverslips. Brief sonication of the solution helps dissolve mPEG-triethoxysilane clumps.
10. Blow-dry coverslips.
11. Sandwich 30 µL drops of PEGylation solution between two coverslips each and place in a Petri dish.
12. Incubate for 15 min at 90 °C in an oven.
13. Wash with large amounts of deionized water.
14. Blow-dry and store dry until use.

3.2 Condensate Production and Sealing

Typically, the phase-separating solution will form droplets within seconds after mixing of components. To ensure homogeneity of concentrations throughout the sample, we prefer to mix the constituents in two non-phase-separating solutions at doubled concentration and then mix those at equal volumes. If large volumes of condensate solution can be produced, FCS experiments can be made much more reproducible by centrifuging the phase-separated

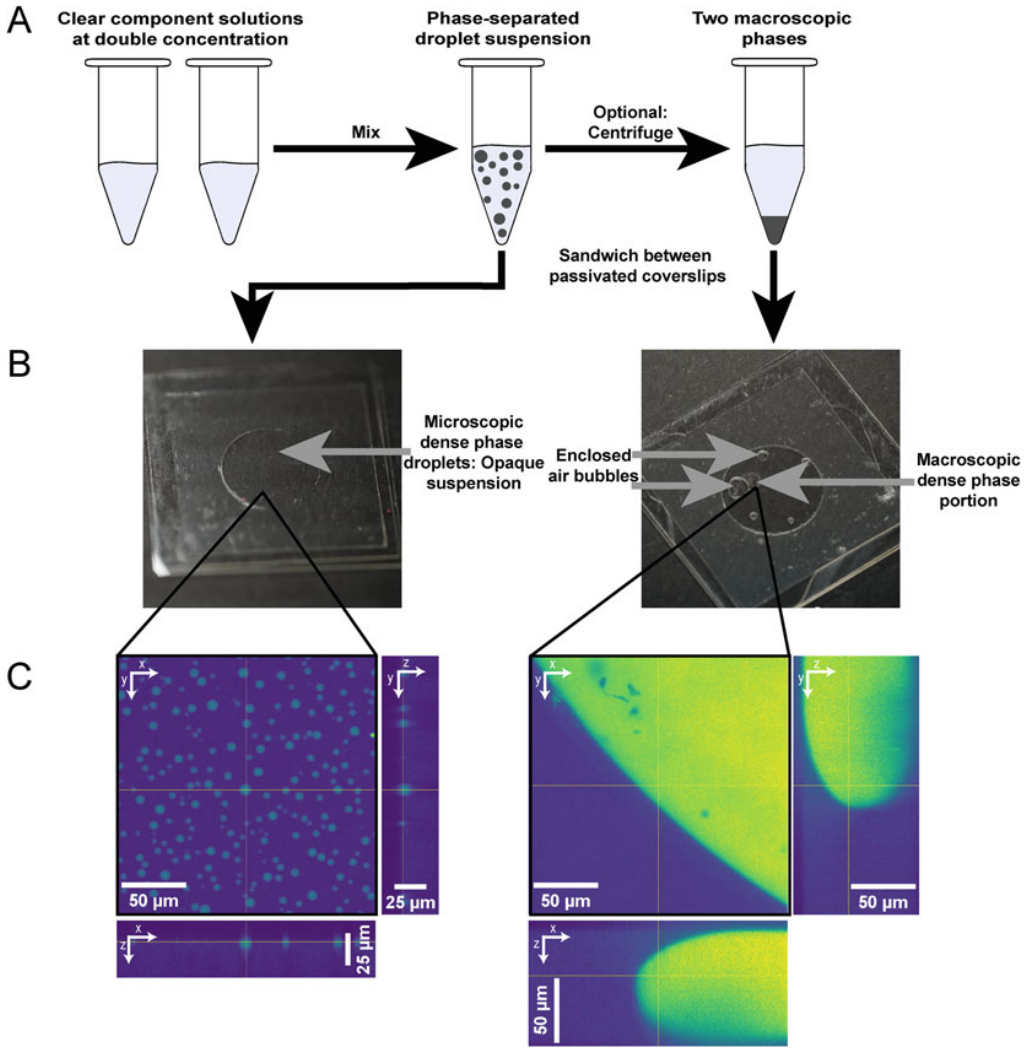

Fig. 1 Overview over the sample preparation workflow. (**a**) Schematic two- or three-step preparation of phase-separated solution. (**b**) Macroscopic images of samples prepared in two ways. (**c**) Spinning-disk confocal microscopy 3D images of phase separation in the two types of samples. "Conventionally" prepared samples contain rather small droplets in a macroscopically homogeneous suspension. Centrifugation yields macroscopic phase separation with structures that are homogeneous on a scale of many micrometers

solution to fuse all dense-phase droplets into a single macroscopic drop (*see* **Note 6**). The steps of condensate production and the resulting sample morphologies are illustrated in Fig. 1.

1. Mix condensate constituents, buffer, and fluorescent compound at twice the desired final concentrations. As an example, to get a condensate formed from 60 µM PLL and 1.5 mM UTP in 20 mM Tris–HCl buffer, containing 5 nM of the fluorescent compound, mix (*see* **Note 7**):

Solution 1: 120 μM PLL 100-mer, 20 mM Tris–HCl, pH 7.5.

Solution 2: 3 mM UTP, 10 nM fluorescent compound, 20 mM Tris–HCl, pH 7.5

2. Transfer equal volumes of solutions 1 and 2 to a protein low-binding tube and mix quickly and thoroughly.
3. Pipet the droplet suspension (or a dense-phase pellet obtained from centrifugation, *see* **Note 6**) into a suitable sample chamber and seal. We recommended a coverslip sandwich-based chamber with spacers that create a cavity enclosing ca. 10 μL of solution.

3.3 Optical Alignment and Calibration for FCS

Before performing any FCS measurements on the sample of interest, it is strongly recommended to adjust, or at least check, the optical alignment of the system in the beginning of every experiment day. Thus, we begin the description of FCS data acquisition with the adjustment and calibration procedure, before proceeding to the data acquisition itself.

1. Dilute a fluorescent dye to ca. 1–10 nM in water or aqueous buffer (*see* **Note 8**), and place the sample on the microscope.
2. Use fluorescence signal from the dye solution to align the optics, in particular, the pinhole, of the FCS-capable microscope, following system-specific procedures (*see* **Note 9**).
3. Acquire calibration FCS data using the dye solution under conditions as close as possible to the conditions of the actual measurement (*see* **Note 10**).
4. Fit the correlation function derived from the calibration data using a model for single-component three-dimensional diffusion (Eq. 2, possibly Eq. 3, see below) to judge alignment quality. Follow **steps 1** and **2** in Subheading 3.5, which many FCS data acquisition programs offer directly at the microscope. Use the fit parameters to judge the quality of the system alignment, and if needed repeat **steps 2–4** (*see* **Note 11**).

3.4 FCS Data Acquisition

Data acquisition for confocal FCS in essence means positioning a static diffraction-limited confocal observation volume in a region of interest within your sample and measuring the fluctuating fluorescence signal over time. Thus, we emphasize details that we found important when doing measurements on LLPS samples. The experimental setup is illustrated in Fig. 2.

1. Mount the condensate sample onto the microscope.
2. If the sample has not been centrifuged and contains microscopic droplets, wait a few minutes to allow droplets to settle.
3. If possible, acquire one or multiple fluorescence images to inspect the brightness and spatial organization of the sample, and identify suitable positions for FCS acquisition (*see* **Note 1**).

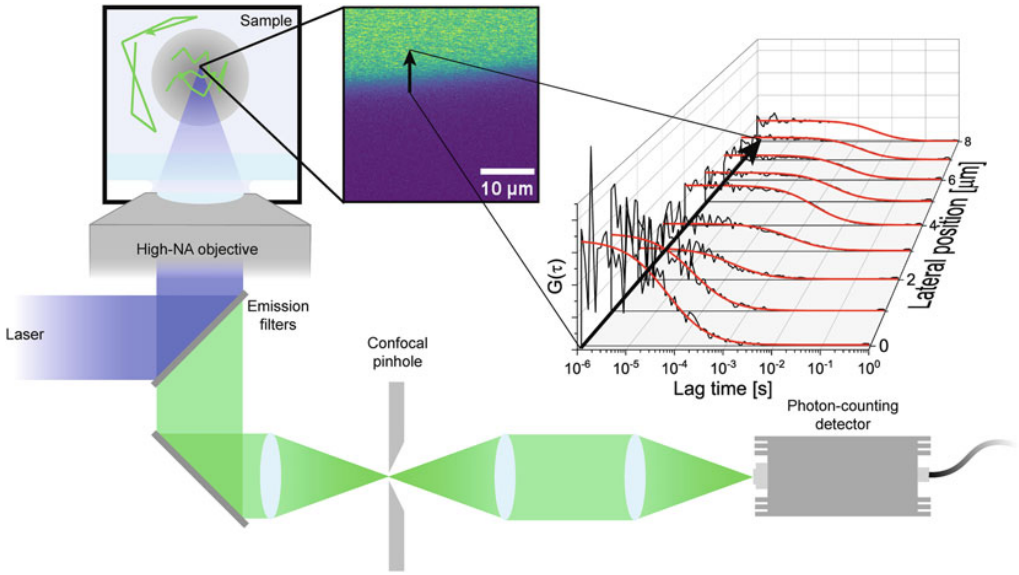

Fig. 2 Overview of experimental setup. Schematically shown is an FCS-capable microscope on which a phase-separated sample is mounted. Confocal imaging of that sample reveals a strong contrast between dense- and dilute-phase samples in intensity, a clear sign of partitioning of the molecule between the two phases. Performing FCS acquisitions at different spots immediately reveals the transition between the two phases

4. If you are not yet familiar with the sample composition, perform test measurements in both the dilute phase and the dense phase to (1) confirm that both phases have fluorophore concentrations suitable for FCS (as a rough orientation, look for ACF amplitude $G_0 \geq 0.01$ *see* Eq. 2, although measurements outside that regime can also be possible), but fluorescence signal clearly above background level, and (2) find an excitation power level that yields sufficient signal-to-noise ratio (SNR) for stable data fitting within an acceptable acquisition time while keeping bleaching levels low, ideally not noticeable (*see* **Note 10**).
5. Acquire FCS data in the dilute phase. As fluorescent particle concentrations often are low in the dilute phase, long measurement times may be needed to compensate low signal levels, and background characterization is particularly important.
6. Acquire FCS data in the dense phase. Check if readjusting the correction collar to the higher refractive index in the condensate dense phase is necessary by maximizing the molecular brightness (*see* **Note 1**). Observe the measurement closely, as especially small droplets can move away during the measurement.

7. Repeat **steps 3**, **5**, and **6** in multiple regions of interest.
8. Repeat **steps 1**–*7* in all relevant samples. Make sure to include a blank sample without any fluorescent dye to characterize background signal (*see* Subheading 3.6).

3.5 Basic FCS Data Analysis for Partition Coefficient Determination

There are many tools available for data analysis in FCS, but they generally follow the same principles. FCS-capable commercial microscope systems usually come with software capable of performing **steps 1** and **2**, and various free software tools do the same. **Steps 3** and **4** can be performed with any spreadsheet calculation program. We will not be specific about any particular software here, but we will instead describe the general steps that should be easy to perform in any FCS software and the standard fit models. Some useful data corrections will be described in the following sections. The steps of the general data analysis are illustrated in Fig. 3.

1. Calculate ACF of the data according to Eq. 1, possibly applying suitable corrections (*see* Subheadings 3.6, 3.7, and 3.8). The correlation function calculation should include an estimation of the uncertainty of the experimental correlation function (*see* **Note 12**).
2. Fit the data with an appropriate model using nonlinear least squares fitting routines such as the Levenberg–Marquardt method. The uncertainties of the experimental correlation function should be used for weighted fitting. The typical fit model for a single molecule species diffusing in three dimensions is [17]

$$G(\tau) = G_0 \frac{1}{1+\frac{\tau}{\tau_D}} \sqrt{\frac{1}{1+\frac{\tau}{S^2\tau_D}}} + G_\infty \qquad (2)$$
$$G_0 = \frac{\gamma}{\langle N \rangle}$$

$\langle N \rangle$ is the average molecule number in the observation volume and thus proportional to the concentration. It is the key parameter of interest when measuring partition coefficients and can be retrieved directly from the ACF amplitude G_0. γ is a factor relating to observation volume shape but not size. In practice, it rarely matters as long as it is kept constant, typically at $\frac{1}{\sqrt{8}}$, or 1, depending on the definition of the observation volume used to interpret $\langle N \rangle$. The diffusion time $\tau_D = \frac{r^2}{4D}$ reports on the molecular mobility via the diffusion coefficient D and the lateral observation volume width r. S is the ratio of observation volume size along the optical axis over r. S should be determined from calibration ACFs and subsequently fixed in fitting. G_∞ is the offset at long τ and should ideally be 0. However, as,

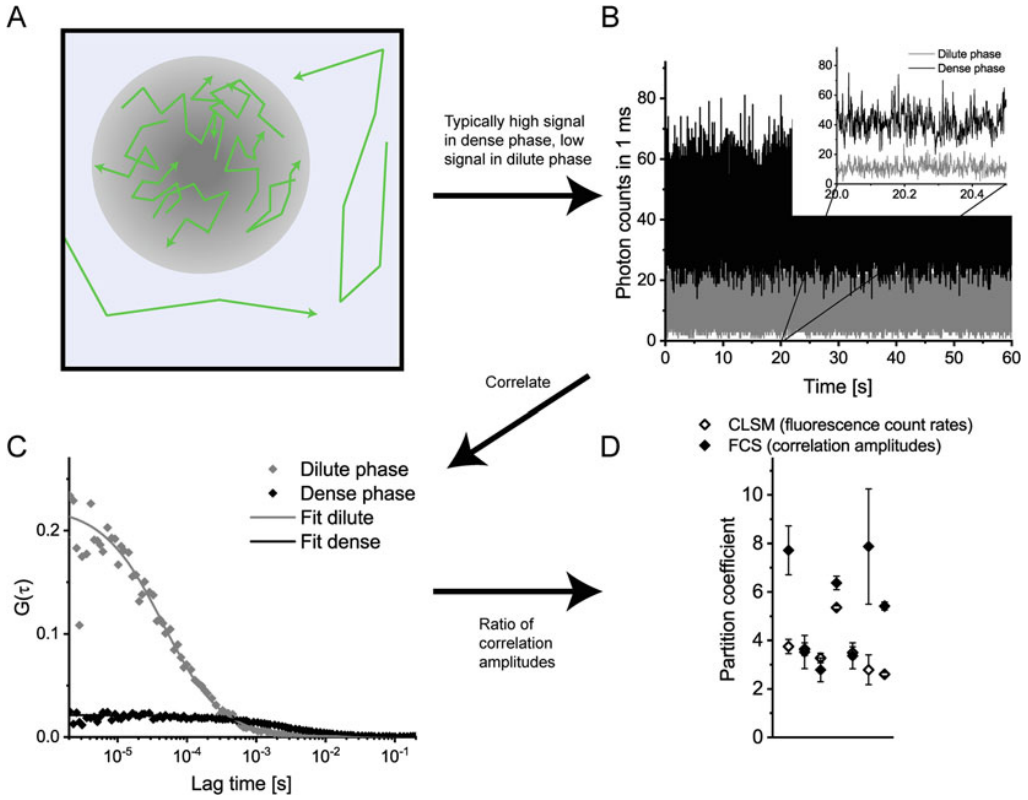

Fig. 3 Overview of data analysis. (**a**) Schematic of the sample composition. Typically, the dense phase contains a high concentration of slow-moving particles, while the dilute phase contains a low concentration of highly mobile particles. (**b**) The raw data is fluctuating fluorescence signal traces, with different properties in dense and dilute phases. (**c**) Autocorrelating the fluorescence traces reveals different decay times and concentrations. (**d**) Performing multiple measurements and calculating a ratio of mean correlation amplitudes yields a single partition coefficient per sample. Shown are results from multiple samples, including both the results from FCS analysis and those from the raw fluorescence traces mimicking CLSM image-based estimates. These results somewhat differ as both techniques are biased by different processes in the sample in different ways

in real experimental data, it rarely is precisely 0, fit quality can improve significantly by fitting G_∞ freely. G_∞ should remain small compared to G_0, though. Often, the fluorophore will exhibit significant blinking at short timescales. This blinking can affect correlation amplitudes and should be taken into account during fitting by modifying the above expression:

$$G(\tau) = G_0 \frac{1 - F_B + F_B \cdot exp(-\frac{\tau}{\tau_B})}{1 - F_B} \frac{1}{1 + \frac{\tau}{\tau_D}} \sqrt{\frac{1}{1 + \frac{\tau}{S^2 \tau_D}}} + G_\infty \quad (3)$$

with dark-state fraction F_B and characteristic blinking time τ_B. The other parameters have the same meaning as above. Sometimes the data is not adequately described by free motion with a

single diffusion coefficient. In that case one can consider extending these simple models to two-species mixture models or anomalous motion models [17]. However, the need to use multicomponent or anomalous motion models indicates rather complex behavior of the sample or even experimental artifacts. Unless such behavior is expected from your system, the results from these fits should be interpreted with caution.

3. Discard outliers. Cutoff values can be defined based on different criteria. What cutoff values to use depends on the overall signal quality. Our typical criteria are as follows: (1) The goodness of fit achieved with physically plausible fit models, where we often define a simple cutoff value for the reduced χ^2 of the weighted fit. However, we also visually inspect the fit residuals for systematic trends, where we do not rely on automation and cutoffs on a single number. (2) The values of $\langle N \rangle$ and τ_D compared to the respective median value of all measurements on the same sample. If an ACF looks like an outlier toward unusually high values in both of these parameters simultaneously, this is a typical sign of optical aberrations, for example, from an ill-adjusted correction collar or from refraction at a dense-dilute phase boundary. (3) The absolute value of the ratio G_∞/G_0. G_∞ values far from 0 typically result from bleaching or sample signal drift during the measurement.
4. Due to the relation of correlation amplitudes to concentrations, the partition coefficient in a given sample is calculated as a simple ratio of ACF amplitudes:

$$P = \frac{c_{dense}}{c_{dilute}} = \frac{\langle N_{dense} \rangle}{\langle N_{dilute} \rangle} = \frac{G_{0,dilute}}{G_{0,dense}} \tag{4}$$

We prefer to first average over all fit values obtained in the same sample for $G_{0,\,\mathrm{dilute}}$ and $G_{0,\,\mathrm{dense}}$, respectively, and then recalculate a single P for that sample as a ratio of means. However, if there is significant spatial heterogeneity or evolution of the sample over time, other averaging schemes make more sense. Note that as only ratios of ACF amplitudes are needed to calculate P, this measurement is more robust than the measurement of absolute concentrations using FCS, which requires accurate knowledge of the absolute observation volume size.

3.6 Background Correction

In the following Subheading 3.6, 3.7, and 3.8, we will describe a few data corrections that that we find particularly useful for FCS in LLPS systems. Here we assume the use of an FCS system performing single-photon counting data acquisition and allowing software correlation, rather than the use of a hardware correlator. If a hardware correlator is used, some steps as described here have to be modified or may even be impossible. At https://github.com/Janhagenkrohn/FCS_Fixer, we provide software for automated

FCS data processing using, among others, the corrections described here. Firstly, every measurement contains some level of background signal originating, for example, from detector dark current or sample autofluorescence. In FCS, the presence of background unrelated to the signal of interest reduces the ACF amplitude G_0. However, when measuring partition coefficients, G_0 is the key parameter. Thus, it is important to know and correct the impact of background. There are two options for this.

1. A simple method for background removal in FCS is to acquire background data from an unlabeled control sample and correct the correlation via:

$$G(\tau)_{corrected} = G(\tau)_{measured}\left(\frac{\langle F(t)\rangle_{measured}}{\langle F(t)\rangle_{measured} - \langle F(t)\rangle_{background}}\right)^2 \quad (5)$$

   This correction can be implemented either by multiplying the ACF itself, as a part of the fit model, or as a post-processing correction of the fitted G_0 values. An example for the effect of background and the impact of its correction using this strategy is shown in Fig. 4a.

2. FLCS (*see* **Note 3**) is powerful for subtracting background that is detected with random ("flat") TCSPC pattern, which includes, for example, detector dark counts, ambient light, and afterpulses (see below). FLCS can even correct background from sample autofluorescence or scattered light, which come with their own characteristic TCSPC patterns. This requires reference measurements to characterize the background TCSPC pattern(s), which must be quite distinct from the fluorescence signal of interest. Different from the ACF amplitude correction described above, FLCS can correct not only static but also fluctuating background. The practical workflow depends in detail on the software used, for which multiple options are available.
   (a) Acquire, if possible, high SNR reference TCSPC data from the fluorophore of interest within the condensate environment. Keep in mind that both conjugation of the dye to another molecule and the environment (e.g., dense phase vs. dilute phase) are likely to alter the photophysics, i.e., the TCSPC pattern, of the fluorophore. This step is not required if only correction of flat background is desired.
   (b) Perform a pattern-matching fit of the reference pattern to the data to determine the contribution of the TCSPC pattern of interest to the total signal. For correcting flat background alone, it will suffice to perform a reference-

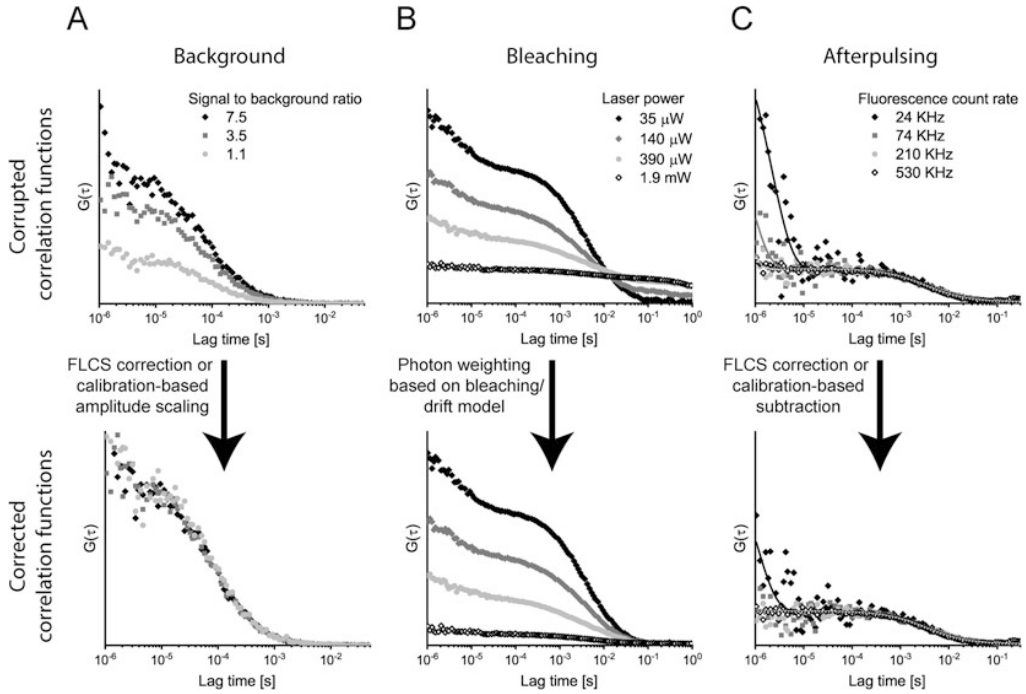

Fig. 4 Helpful data corrections**.** Shown are comparisons of artifact-corrupted and corrected ACFs. (**a**) Background can severely change the amplitude, which can occur especially in the dilute phase. (**b**) Bleaching creates distortions at long lag times, which also distort amplitude fitting. The shown example data was acquired at quite high laser power, but with slower-moving particles, this can become significant already at much lower laser powers. (**c**) Afterpulsing distorts short timescales and is most important when analyzing strongly blinking dyes. It is more severe for low correlation amplitudes and low fluorescence count rates. Due to the limited signal-to-noise ratio in the shown example for afterpulsing, fits curves have been added as a guide to the eye

free fit to determine what fraction of the data belongs to an exponentially decaying fluorescence signal and which fraction to a flat background.

(c) From the fit, recalculate the FLCS filter functions (photon weights) and use these filter functions to calculate a background-free ACF.

(d) Fit the FLCS ACF as described above. Usually, no specialized fit models are needed.

3.7 Bleaching Correction

Bleaching is often significant in dense-phase droplets. Some condensates are not truly liquid and have a significant immobile fraction of molecules that will be bleached away during the FCS acquisition. If the condensate droplet in which one measures is small, and exchange with the surrounding dilute phase is slow, even a fully mobile particle pool can be slowly depleted. Bleaching

should be experimentally minimized as much as possible, as the bleaching correction of an ACF will always remain imperfect. Nevertheless, bleaching correction can help make sense of otherwise unusable data. We use a method that uses the same photon weights used for FLCS. In this case, rather than unmixing different contributions to the signal, time-dependent weights $w(t)$ are used to correct the fluorescence intensity $F(t)_{\text{bleachcorr}} = F(t)_{\text{measured}}\ w(t)$ such that while $F(t)_{\text{measured}}$ shows both fast fluctuations of interest and a slower trend representing the bleaching depletion, $F(t)_{\text{bleachcorr}}$ contains only the fast fluctuations. Figure 4b shows ACFs corrupted by bleaching to varying degrees and the correction using the photon weighting method.

1. Fit a coarsely binned representation of $F(t)_{\text{measured}}$ with an exponential or polynomial bleaching model $b(t)$. We usually use a polynomial fit, choosing the degree of the polynomial model automatically based on the F-test for goodness of fit improvement with increasing degree.
2. The weighting function $w(t)$ is obtained from $b(t)$ as

$$w(t) = \sqrt{\frac{b(0)}{b(t)}} + \left(1 - \sqrt{\frac{b(t)}{b(0)}}\right) \tag{6}$$

   with $b(0)$ as a signal level at the beginning of the measurement. This expression ensures that not only the fluorescence intensity but also its variance is flattened on long timescales [18].
3. Calculate the ACF with an FLCS correlation algorithm, weighting the photons with $w(t)$. For combination with FLCS-based background correction, simply multiply each photon's weight from background correction with that from bleaching correction.
4. Fit the FLCS ACF as described above. Usually, no specialized fit models are needed.

3.8 Afterpulsing Correction

If measurements are performed using a single detector rather than a "pseudo-cross-correlation" setup (*see* **Note 2**), afterpulsing may appear as a significant ACF distortion at short timescales. It may be possible to fit the data only at longer lag times that are unaffected by afterpulsing, but this depends on both instrument and sample. Especially if blinking is to be analyzed, afterpulsing often cannot be ignored, and different data correction strategies exist.

1. FLCS (*see* above and **Note 3**) can eliminate afterpulsing efficiently, as afterpulses usually contribute to the flat background in the TCSPC data. The protocol is exactly as described above for removal of "flat" background. In fact, both are done simultaneously. Examples of afterpulsing-corrupted ACFs and their correction using calibrated subtraction are shown in Fig. 4c.

2. Applicable in every FCS system, even without TCSPC detection, is calibrated subtraction of afterpulsing. Afterpulsing follows quite reproducible patterns, which can be calibrated, predicted, and subtracted.
   (a) Perform an FCS measurement of a static signal such as backscattered light from a glass–air interface. Be careful about appropriate choices of filter and laser power to achieve sufficient counts without risking damage to the detector.
   (b) Calculate the ACF of that static signal. This ACF should show only the correlation arising from the afterpulses.
   (c) Fit an afterpulsing model to the calibration data. In our experience, the afterpulsing characteristic in the ACF can be approximated with this expression:

$$G_{AP}(\tau) = \frac{A_1 exp(-\frac{\tau}{\tau_{AP,1}}) + A_2 exp(-\frac{\tau}{\tau_{AP,2}})}{(1 + A_1\tau_{AP,1} + A_2\tau_{AP,2})\langle F(t)\rangle_{measured}} \quad (7)$$

   Determine the time constants $\tau_{AP,\,1/2}$ and the amplitudes $A_{1/2}$ from the afterpulse calibration data. Note that for every detector, an independent set of these four parameters must be calibrated. $\langle F(t)\rangle_{\text{measured}}$ is the measured count rate containing both fluorescence and afterpulsing. $A_{1/2}$ are in frequency units, so keep track of the units in calculations.
   (d) Use Eq. 9 with the calibration parameters and the average count rate $\langle F(t)\rangle_{\text{measured}}$ of the measurement as input to predict the afterpulsing pattern of the ACF of any measurement at that detector. In our experience, in a stable lab environment, the same calibration of the afterpulsing parameters can be used for data correction for months.

4 Notes

1. The correction collar of a microscope objective is a means of correcting spherical aberration. It allows adapting the optical path to deviations in coverslip thickness and in refractive index, such as the increased refractive index of condensate dense phase. We prefer to readjust the correction collar between measurements in the dense phase and in the dilute phase based on the molecular brightness measured in the region of interest or at least confirm that the deviation is negligible.
2. FCS acquisitions can be performed in different detector configurations. Regarding detector type, SPADs are most common, and their use is assumed throughout this chapter. Further, one can use a single detector or a beam splitter

followed by a pair of detectors. Following photon detection, SPADs occasionally produce spurious signals known as afterpulses. As this follows very characteristic patterns, afterpulsing tends to appear as a strong distortion in the ACF of the fluorescence signal of a single SPADs. Using two detectors offers a solution: As afterpulses are uncorrelated between two detectors, they do not appear in a cross-correlation function from the same signal split onto two detectors. Otherwise, such a "pseudo-cross-correlation" function is equivalent to the ACF. The disadvantage of such a setup is the need for two redundant detectors, making the instrument more complex and/or reducing spectral multiplexing capabilities.

3. Fluorescence lifetime correlation spectroscopy (FLCS) uses TCSPC information to assign a probability for each photon to belong to each out of a set of signal species, such as the desired fluorescence signal, which arrives with a certain pattern on the nanosecond time scale, or the background arriving at a random time point on the nanosecond scale. These probabilities are then used to assign statistical weights to the photons during the ACF calculation that allows calculation of "species ACFs." The downside is that FLCS requires dedicated software as well as a fluorescence lifetime measurement-capable FCS system, which may not be available to every lab. The theory of FLCS is somewhat more complex than that of conventional FCS, and for further information we refer the reader to explanations given by other authors [24, 25].
4. The described PEGylation protocol is based on alkoxysilane chemistry used in many contexts for coverslip functionalization. There are many partially exchangeable alkoxysilane functionalization protocols in the literature, which may work equally well for the purpose described here. The protocol should cover the basic steps of (1) cleaning the coverslip surface, (2) chemically activating it by creating exposed Si–OH moieties, (3) removing residual water, (4) immersing the surface in low-water alkoxysilane solution, usually at elevated temperature, and (5) washing with water to hydrolyze unreacted alkoxysilane moieties.
5. We typically perform plasma treatment in 0.1–0.3 mbar O_2 atmosphere for 30 s, at ca. 50% power setting in a Diener electronic Zepto plasma chamber, but this will depend on the equipment available. Make sure that the coverslips are truly dry before inserting them into the plasma chamber, otherwise water vapor will perturb the plasma treatment.
6. We frequently centrifuge our samples to enrich the dense phase for easier FCS experiments. Centrifugation of the phase-separated sample will collapse the dense-phase droplets into a

single larger dense-phase portion, which can be a few microliters in volume. This can be pipetted into the sample chamber to create a single large dense-phase domain rather than many small droplets. Centrifugation can be performed, for example, for 15 min at 17900 rcf, at a temperature at, or slightly above, room temperature to avoid dissolution of the dense-phase pellet after centrifugation. While requiring a lot of condensate constituent material, measurements in such macroscopic portions have a few advantages: (1) Positioning of the confocal observation volume for FCS acquisition in a macroscopic dense phase drop is trivial, even without a CLSM reference image. Generally, out of centrifugation or reference image acquisition, at least one is required for reproducible FCS experiments. (2) There are no artifacts from thermal motion of the droplet itself. (3) Molecular dynamics are not altered by proximity to the condensate phase boundary. (4) While microscopic dense-phase droplets themselves can act as micro-lenses and distort the confocal observation volume, the macroscopic drop adheres directly to the coverslip and thus circumvents the additional optical interfaces at phase boundaries.

7. The PLL and UTP concentrations given are chosen to maximize the yield of dense-phase volume under our conditions. Assuming UTP to be on average fourfold negatively charged at pH 7.5, and PLL 100-mer approximately 100-fold positively charged, 25 UTP molecules charge-neutralize one PLL molecule and hence their concentration ratio. Given the concentration ratio, the absolute concentration was chosen based on an empirical concentration screen read out via optical density measured in a photometer and visual inspection in transmitted-light microscopy.
8. The calibration dye must be spectrally similar to the dye to be measured in the phase-separating system. Further desirable properties for the calibration dye are high brightness, photostability, and low blinking. Knowing the dye diffusion coefficient is essential for calibration of the absolute observation volume size. The latter is needed for measuring absolute concentrations or diffusion coefficients in FCS, and recommended in general to ensure reproducibility, but not strictly required for the partition coefficient measurements described here.
9. The daily optical alignment routine should at least include alignment of the confocal pinhole and objective correction collar, if only to experimentally confirm that the performance has not deteriorated since the last use.
10. Fluorescence excitation saturation effects can have a strong influence on effective observation volume size [26]. Staying at low power levels also reduces dye blinking, allowing simpler,

more robust, fit models in data analysis (Eq. 2 rather than Eq. 3). Thus, if possible, calibrations and measurements should be performed at low laser power. In an equilibrium sample like a simple dye solution, increasing signal-to-noise ratio by increasing measurement time is usually to be preferred over increasing laser power. We usually use powers in the order of 1–2 μW at the objective back pupil. Scaling of signal-to-noise ratio (SNR) in FCS with acquisition parameters is somewhat complex in detail but follows simple trends. When setting up an experiment, we use the following three rules of thumb for orientation [27]:

1. Independent of the other parameters, SNR increases with the square root of acquisition time.
2. At very low fluorophore concentrations ($G_0 \gg 1$), the signal-to-noise ratio scales approximately with the square root of particle concentration, but for $G_0 \lesssim 1$, further increase in concentration will have no noticeable effect on SNR.
3. The ACF consists essentially of two regimes of lag times, defined loosely by the molecular brightness $\varepsilon = G_0\langle F(t)\rangle_t$. At short lag times $\tau \ll \varepsilon^{-1}$, typical for the time scales of blinking effects and diffusion of small particles in the dilute phase, SNR will increase linearly with ε. Here, increasing the laser power to increase molecular brightness can increase SNR dramatically, at the cost of saturation and bleaching. For long lag times $\tau \gg \varepsilon^{-1}$, typical for the slow diffusion kinetics in the dense phase of condensates even at moderate laser powers, increasing ε further has no notable effect on SNR, making further increase in laser power useless.

11. There are different ways to judge the alignment quality from the ACF fit. First and foremost, the fit quality should be high, with the reduced χ^2 of a weighted fit close to 1 and no systematic trend in the fit residuals. If this is not the case, make sure that you understand the reason for the mismatch and, if possible, fix the issue. Once you do obtain good fits, inspect the fit parameters: The diffusion time τ_D is proportional to the squared width of the observation volume in the *xy* plane, and generally, the shorter the diffusion time, the better the alignment is. The observation volume aspect ratio S will also decrease with improved alignment and in our experience tends to be a more sensitive indicator than τ_D. When performing FCS using typical objectives with numerical aperture around 1.2, we generally consider $S \leq 6$ a threshold for acceptable alignment. Note that with poor alignment or low signal-to-noise ratio in the calibration data, the fit will usually return high, practically random, numbers for S. The molecular

brightness $\varepsilon = G_0\langle F(t)\rangle_t$ is another quite sensitive indicator of alignment quality and will increase for better alignment. We mostly rely on ε as a real-time readout while performing the alignment and on S to confirm alignment quality when analyzing higher signal-to-noise ratio calibration data.

12. There are different methods of calculating the uncertainty of the ACF. The first method is to theoretically estimate it from the ACF itself [28]. The second, more empirical, option is to estimate it from multiple shorter measurement or to cut a single long measurement into pieces [29]. The latter option is to be preferred for sufficient measurement times. If the measurement time is short, bootstrapping of photon time tags also yields a good empirical estimate for uncertainty at short lag times but does not perform well at long lag times.

Acknowledgments

This research was supported by the Excellence Cluster ORIGINS which is funded by the Deutsche Forschungsgemeinschaft (DFG, German Research Foundation) under Germany's Excellence Strategy (EXC-2094 – 390783311) (JHK), by the Max Planck School Matter to Life supported by the German Federal Ministry of Education and Research (BMBF) in collaboration with the Max Planck Society (LB), and by the European Union's Horizon 2020 research and innovation program under the Marie Skłodowska-Curie grant agreement no. 859416 (YQ). JHK and YQ acknowledge support by IMPRS-ML.

References

1. Hyman AA, Weber CA, Jülicher F (2014) Liquid-liquid phase separation in biology. Annu Rev Cell Dev Biol 30:39–58. https://doi.org/10.1146/annurev-cellbio-100913-013325
2. Hondele M, Sachdev R, Heinrich S et al (2019) DEAD-box ATPases are global regulators of phase-separated organelles. Nature 573:144–148. https://doi.org/10.1038/s41586-019-1502-y
3. Jegers C, Franzmann TM, Hübner J et al (2022) A conserved and tunable mechanism for the temperature-controlled condensation of the translation factor Ded1p. bioRxiv 20221011511767
4. Feric M, Vaidya N, Harmon TS et al (2016) Coexisting liquid phases underlie nucleolar subcompartments. Cell 165:1686–1697. https://doi.org/10.1016/j.cell.2016.04.047
5. Protter DSW, Parker R (2016) Principles and properties of stress granules. Trends Cell Biol 26:668–679. https://doi.org/10.1016/j.tcb.2016.05.004
6. Guilhas B, Walter J-C, Rech J et al (2020) ATP-driven separation of liquid phase condensates in bacteria. Mol Cell 79:293–303.e4. https://doi.org/10.1016/j.molcel.2020.06.034
7. Babl L, Giacomelli G, Ramm B et al (2022) CTP-controlled liquid–liquid phase separation of ParB. J Mol Biol 434:167401. https://doi.org/10.1016/j.jmb.2021.167401
8. Azaldegui CA, Vecchiarelli AG, Biteen JS (2021) The emergence of phase separation as an organizing principle in bacteria. Biophys J 120:1123–1138. https://doi.org/10.1016/j.bpj.2020.09.023

9. Ladouceur A-M, Parmar BS, Biedzinski S et al (2020) Clusters of bacterial RNA polymerase are biomolecular condensates that assemble through liquid–liquid phase separation. Proc Natl Acad Sci USA 117:18540–18549
10. Ramm B, Schumacher D, Harms A et al (2022) A phase-separated biomolecular condensate nucleates polymerization of the tubulin homolog FtsZ to spatiotemporally regulate bacterial cell division. bioRxiv. https://doi.org/10.1101/2022.09.12.507586
11. Gupta A, Joshi A, Arora K et al (2023) The bacterial nucleoid-associated proteins, HU, and Dps, condense DNA into context-dependent biphasic or multiphasic complex coacervates. J Biol Chem 104637. https://doi.org/10.1016/j.jbc.2023.104637
12. Peeples W, Rosen MK (2021) Mechanistic dissection of increased enzymatic rate in a phase-separated compartment. Nat Chem Biol 17:693–702. https://doi.org/10.1038/s41589-021-00801-x
13. Nott TJ, Craggs TD, Baldwin AJ (2016) Membraneless organelles can melt nucleic acid duplexes and act as biomolecular filters. Nat Chem 8:569–575. https://doi.org/10.1038/nchem.2519
14. Wiegand T, Hyman AA (2020) Drops and fibers - how biomolecular condensates and cytoskeletal filaments influence each other. Emerg Top Life Sci 4:247–261. https://doi.org/10.1042/ETLS20190174
15. Magde D, Elson E, Webb WW (1972) Thermodynamic fluctuations in a reacting system—measurement by fluorescence correlation spectroscopy. Phys Rev Lett 29:705–708. https://doi.org/10.1103/PhysRevLett.29.705
16. Elson EL (2013) Brief introduction to fluorescence correlation spectroscopy. In: Tetin SY (ed) Meth Enzymol. Elsevier, pp 11–41
17. Wohland T, Maiti S, Macháň R (2020) An introduction to fluorescence correlation spectroscopy. IOP Publishing
18. Ries J, Chiantia S, Schwille P (2009) Accurate determination of membrane dynamics with line-scan FCS. Biophys J 96:1999–2008. https://doi.org/10.1016/j.bpj.2008.12.3888
19. Enderlein J, Gregor I, Patra D et al (2005) Performance of fluorescence correlation spectroscopy for measuring diffusion and concentration. ChemphysChem 6:2324–2336. https://doi.org/10.1002/cphc.200500414
20. Fisher RS, Elbaum-Garfinkle S (2020) Tunable multiphase dynamics of arginine and lysine liquid condensates. Nat Commun 11:4628. https://doi.org/10.1038/s41467-020-18224-y
21. Köllner M, Wolfrum J (1992) How many photons are necessary for fluorescence-lifetime measurements? Chem Phys Lett 200:199–204. https://doi.org/10.1016/0009-2614(92)87068-Z
22. Hess ST, Webb WW (2002) Focal volume optics and experimental artifacts in confocal fluorescence correlation spectroscopy. Biophys J 83:2300–2317. https://doi.org/10.1016/S0006-3495(02)73990-8
23. Gidi Y, Bayram S, Ablenas CJ et al (2018) Efficient one-step PEG-Silane passivation of glass surfaces for single-molecule fluorescence studies. ACS Appl Mater Interfaces 10:39505–39511. https://doi.org/10.1021/acsami.8b15796
24. Böhmer M, Wahl M, Rahn H-JSSS et al (2002) Time-resolved fluorescence correlation spectroscopy. Chem Phys Lett 353:439–445. https://doi.org/10.1016/S0009-2614(02)00044-1
25. Gregor I, Enderlein J (2007) Time-resolved methods in biophysics. 3. Fluorescence lifetime correlation spectroscopy. Photochem Photobiol Sci 6:13–18. https://doi.org/10.1039/B610310C
26. Nagy A, Wu J, Berland KM (2005) Characterizing observation volumes and the role of excitation saturation in one-photon fluorescence fluctuation spectroscopy. J Biomed Opt 10:044015. https://doi.org/10.1117/1.1991860
27. Kask P, Günther R, Axhausen P (1997) Statistical accuracy in fluorescence fluctuation experiments. Eur Biophys J 25:163–169. https://doi.org/10.1007/s002490050028
28. Koppel DE (1974) Statistical accuracy in fluorescence correlation spectroscopy. Phys Rev A 10:1938–1945. https://doi.org/10.1103/PhysRevA.10.1938
29. Wohland T, Rigler R, Vogel H (2001) The standard deviation in fluorescence correlation spectroscopy. Biophys J 80:2987–2999. https://doi.org/10.1016/S0006-3495(01)76264-9

6

Fluorescence correlation spectroscopy for particle sizing: A notorious challenge

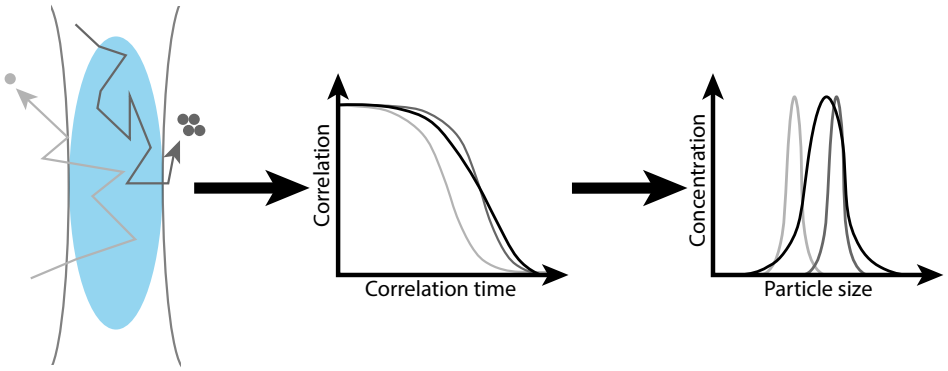

Figure 6.1. Particle sizing using FCS. Diffusion coefficients of particles depend on particle size. Therefore, an average particle size can be estimated from the correlation time approximating the average residence time of particles in the observation volume (small particles in light grey, larger particles in dark grey). However, for a mixture of particle sizes, the shape of the correlation function changes (black), which should allow to estimate a distribution of particle sizes, rather than just an average.

To understand biomolecular self-organization, studying binding kinetics of the underlying self-assembly processes is critical. For example, cytoskeleton filaments and their bacterial homologs often participate in the spatio-temporal organisation of functional protein machineries, like FtsZ as a central factor in the organization of the bacterial cell division machinery [99]. However, often, the protein filaments themselves are no passive scaffold. Instead, their dynamic reorganization is part of the self-organization process.

Yet, quantitatively characterizing self-assembly is a challenging task in many cases:

Many self-assembly processes, including the above-mentioned filament-forming proteins, are stochastic in the sense that there is no fixed monomer number up to which the self-assembly proceed. Instead, a broad distribution of oligomer sizes is observed. The mean, width, and/or shape of the distribution may then change in response to the conditions under which the self-assembly happens.

Characterizing the distribution of oligomer sizes in a self-assembling system is a challenging task for which many methods exist, but no general method of choice [231–233]. Fluorescence correlation spectroscopy in principle is expected be a powerful method for the purpose: The diffusion time depends on particle size, with the relation given by the Stokes-Einstein equation (Eq. 2.10) or other equations linking particle size and diffusion coefficient (*e.g.*, Eq. 2.11). At least for well-behaved systems, the shape of the ACF is predictable given knowledge of the point spread function geometry, with amplitude and diffusion time as the only free parameters which affect the ACF entirely indepedently. Given these facts, one should be able to fit a multi-species mixture model where the relative amplitude of each species corresponds to the relative concentration. However, in practice, the power of FCS as usually performed is rather limited for characterizing multi-species mixtures, for multiple reasons.

In the following chapter, we reviewed various aspects of FCS methodology that are relevant to characterization of polydisperse systems, such as self-assembling proteins. We aimed to understand why FCS remains underused for this purpose, discussing from a historical perspective of FCS emerging from the concept of Dynamic Light Scattering (DLS) [234–236], the limitations that were encountered, and the (partial) solutions that have been proposed to tackle those. We brought together various relevant insights that are otherwise scattered in the literature with the two-fold aim of helping prospective users understand what to keep in mind when trying to use FCS to characterize self-assembling proteins or similar systems, and to give developers an overview of the different ideas that have been established and are waiting to be implemented into a joint user-friendly framework.

Fluorescence correlation spectroscopy for particle sizing: A notorious challenge

Jan-Hagen Krohn, Adam Mamot, Nastasja Kaletta, Yusuf Qutbuddin, Petra Schwille*

Author contributions:

PS and **JHK** conceived the project. **JHK**, AM, and NK performed experiments. **JHK** and YQ developed software. **JHK** prepared the manuscript. All authors commented on the manuscript.

The following was published as part of a special issue of Biophysical Journal dedicated to Watt W. Webb, whose lab, among many other achievements, pioneered the development of Fluorescence Correlation Spectroscopy.

published in

Biophysical Journal (2025)

Reprinted from Krohn et al. 2025 [3] with permission from Elsevier

Please cite this article in press as: Krohn et al., Fluorescence correlation spectroscopy for particle sizing: A notorious challenge, Biophysical Journal (2025), https://doi.org/10.1016/j.bpj.2025.03.017

Biophysical Journal
Biophysical perspective

Biophysical Society

Fluorescence correlation spectroscopy for particle sizing: A notorious challenge

Jan-Hagen Krohn,[1,2] Adam Mamot,[1] Nastasja Kaletta,[1] Yusuf Qutbuddin,[1] and Petra Schwille[1,2,*]
[1]Department of Cellular and Molecular Biophysics, Max Planck Institute of Biochemistry, Martinsried, Germany and [2]Exzellenzcluster ORIGINS, Garching, Germany

ABSTRACT In many quantitative investigations of biological systems, including, e.g., the study of biomolecular interactions, assembly and disassembly, aggregation, micelle and vesicle formation, or drug encapsulation, accurate determination of particle sizes is of key interest. Fluorescence correlation spectroscopy (FCS), with its exceptional sensitivity for molecular diffusion properties, has long been proposed as a valuable method to size small, freely diffusible particles with superior precision. It is conceptually related to the more widespread particle sizing technique dynamic light scattering (DLS) but offers greater selectivity and sensitivity due to the use of fluorescence rather than scattered light. However, in spite of these apparent advantages, FCS has never become established as a biophysical routine for particle sizing. This is due to the fact that sensitivity can, under certain conditions, indeed be disadvantageous, as it renders the technique error prone and overly susceptible to signal disturbances. Here, we discuss the systematic challenges, as well as the advances made over the past decades, to employing FCS in polydisperse samples. The problematic role of large particles, a common issue in DLS and FCS, and the effect of fluorescent labeling are discussed in detail, along with strategies for respective error mitigation in experiments and data analysis. We expect this overview to guide future users in successfully applying FCS to their particle sizing problems in the hope of fostering a more widespread and routine use of FCS-based technology.

CORRELATION SPECTROSCOPY USING SCATTERED LIGHT AND FLUORESCENCE

Particle sizing is an extremely common challenge in (bio) physical chemistry. In polymer science, the size of a particle is a key parameter for understanding both the properties of the polymer and its interaction with other particles (1–4). Changes in particle size are a convenient readout for complex formation of two or more molecules in biochemistry, e.g., ligand binding or protein-protein association/aggregation (5–9). For nanoparticle-based drug carriers, monitoring the carrier size is considered important for targeting drug distribution in the body and for their uptake by target cells (10,11).

As for any other problem, there is no universal method of choice for all particle sizing applications. Many methods are available, with their specific strengths and weaknesses (12,13). One approach is to physically fractionate particles by size, followed by a secondary readout such as UV absorbance. Analytical ultracentrifugation is a powerful approach to fractionate particles based on sedimentation in solution, which can be interpreted based on well-established theories of hydrodynamics (11). (Micro)fluidic approaches like asymmetric flow field fractionation separate particles by exploiting predictable relations between flow velocity profiles, particle diffusion coefficients, and resulting distributions of particles within the channel (14,15). Among the more direct approaches, nanoscale imaging, e.g., by electron microscopy, is an obvious choice for image-based characterization of particle size and shape but generally suffers from low throughput (14,16). Other single-particle approaches include tunable resistive pulse sensing, in which particles passing through a microscopic pore transiently reduce electrolyte currents, which are converted into particle volume estimates (17), or nanoparticle tracking analysis, another image-based technique in which diffusing particles are imaged with high time resolution to extract particle sizes from particle mobility (13).

Perhaps the most widespread technique, particularly popular for combining simple and fast measurements with typically high signal/noise ratios, is dynamic light scattering (DLS) (18–20). In DLS, laser light elastically scattered at

Submitted January 3, 2025, and accepted for publication March 20, 2025.

*Correspondence: schwille@biochem.mpg.de

Jan-Hagen Krohn's present address is Institute for Experimental Immunology and Bioimaging and IMCES Imaging Center Essen, University Hospital Essen, Essen, Germany

Editor: Elizabeth Rhoades.

https://doi.org/10.1016/j.bpj.2025.03.017

Please cite this article in press as: Krohn et al., Fluorescence correlation spectroscopy for particle sizing: A notorious challenge, Biophysical Journal (2025), https://doi.org/10.1016/j.bpj.2025.03.017

moving particles is statistically analyzed in time through the intensity autocorrelation function (ACF):

$$G(\tau) = \frac{\langle I(t)I(t+\tau)\rangle_t}{\langle I(t)\rangle_t^2}. \quad (1)$$

The temporal profile of the ACF represents the characteristic profiles of all processes that change the detected intensity. In essence, it reflects on the probability for a signal fluctuation that had been observed at an arbitrary time point t to persist until a later time point $t+\tau$. For homodisperse systems and at low noise levels, the ACF reveals the diffusion coefficient D of the particles via the time constant of an exponential decay. Similar to the other diffusion-based techniques mentioned above, DLS exploits the fact that D depends on the particle size, where the Stokes-Einstein equation describes the relation for (approximately) spherical particles with hydrodynamic radius r_H:

$$D = \frac{k_B T}{6\pi\eta r_H}, \quad (2)$$

with solvent viscosity η. Obviously, not every particle is spherical, and nonspherical particles of the same volume have different diffusion coefficients than spherical ones (21). Alternative models exist to replace Eq. 2 for other particle shapes, for example, that of elongated cylinders (22,23). By extending the models used in the analysis of DLS data to describe a multi-species mixture with a range of diffusion coefficients D_j, one can also characterize a distribution of particle sizes. This allows using DLS to quantify not only particle suspensions of a single particle size, but also polydisperse ones that display a range of particle sizes, at least in principle.

The time-correlation concept underlying DLS is generic and has been successfully used using other contrast methods besides scattered light, including, but not limited to, fluorescence emission (24,25). The latter approach, known as fluorescence correlation spectroscopy (FCS), is the focus of this article. Here, laser light is used to excite fluorescent dyes attached to a particle of interest, and the fluorescence emission is correlated and analyzed in time analogous to the scattered laser light intensity in DLS. ACFs recorded in FCS from suitable samples also primarily report on diffusion dynamics, like those in DLS. Also, similarly to DLS, the FCS ACF for a multi-species mixture containing a range of diffusion coefficients for the respective species j in FCS is generally described by three key parameters: the species-wise diffusion time $\tau_{D,j}$, the particle number $\langle N_j\rangle$, and the molecular brightness ε_j:

$$G(\tau) = \gamma \sum_{j=1}^{j_{max}} G_{0,j} g_{D,j}(\tau), \quad (3a)$$

$$G_{0,j} = \frac{\langle N_j\rangle {\varepsilon_j}^2}{\left(\sum_{j=1}^{j_{max}} \langle N_j\rangle \varepsilon_j\right)^2}, \text{and} \quad (3b)$$

$$g_{D,j}(\tau) = \frac{1}{1+\frac{\tau}{\tau_{D,j}}} \frac{1}{\sqrt{1+\frac{\tau}{S^2\tau_{D,j}}}}, \quad (3c)$$

where the usually confocal observation volume is described by its width in the xy plane w_{xy}, by the aspect ratio $S = w_z/w_{xy}$, and by the shape factor $\gamma = const. \approx 0.354$. w_{xy} enters the model implicitly through $\tau_{D,j}$ via the mean-squared displacement $\langle {\Delta_j}^2\rangle$ in the Einstein-Smoluchowski equation: ${w_{xy}}^2 = \langle {\Delta_j}^2\rangle = 4D_j\tau_{D,j}$.

The overall correlation amplitude is proportional to the inverse of the total particle number, meaning that FCS also probes absolute particle concentrations, as long as the size of the observation volume is known. If background levels are significant even in confocal detection, then the evaluation of absolute concentrations requires correction of the background, which distorts the correlation amplitude (26). Depending on the hardware and software available, one can either employ techniques like fluorescence lifetime correlation spectroscopy (27) or explicitly correct for the amplitude if the background level if known (25,26,28). Of note, for especially low signal/background ratios, the correlation amplitude increases with increasing total particle number rather than being inversely related. Thus, without appropriate correction, this relation is not always trivial.

In spite of the obvious conceptual similarities and a superior signal to the background level, FCS remains less routinely used for particle sizing than DLS. The purpose of this article is first to discuss the key limitations, i.e., the particular challenges FCS faces for particle sizing applications. We also highlight what advances have been made and offer an overview of various considerations to make in such experiments. We will focus on the analysis of polydisperse samples, i.e., samples that are not adequately described by a single particle size. As both FCS and DLS generally determine particle sizes indirectly via the diffusion coefficients using Eq. 2 or similar relations, we will not strictly distinguish between particle size measurements and diffusion coefficient measurements. We start by discussing some practical reasons why one would be interested in using FCS as an alternative to DLS in the first place. We then emphasize challenges that are specific to FCS. In the remaining sections, we address how fluorescent labeling affects the interpretation of FCS data acquired for particle sizing, followed by a short treatise on advances in experiments and data processing. While the technical considerations are generic in nature, we will focus on (self-assembling) proteins and other biomolecules.

Please cite this article in press as: Krohn et al., Fluorescence correlation spectroscopy for particle sizing: A notorious challenge, Biophysical Journal (2025), https://doi.org/10.1016/j.bpj.2025.03.017

What advantages do we expect from FCS over DLS?

While built on the same conceptual basis, FCS and DLS have different strengths and weaknesses in practice. The first obvious differences is the use of fluorescent labeling in FCS. Fluorescent labeling has the advantage of a very high signal/background ratio. With contemporary high-performance fluorescent dyes and modern detector technology, discriminating a single fluorescent molecule's signal over the (usually solute) background from ca. 10^{10} molecules within a 1 fL observation volume has become possible on systems of all major commercial manufacturers of confocal microscopes. This specificity allows performing FCS routinely in complex environments that would hardly allow meaningful DLS measurements, such as intact cells (29,30) or even organisms (31).

Further, the single-molecule sensitivity also allows FCS to be performed with very low sample concentrations and volumes (29). Another obvious advantage of using fluorescent labeling lies in multi-color experiments, namely fluorescence cross correlation spectroscopy (FCCS) (32). FCCS distinguishes signal fluctuations that are (cross) correlated between two signal channels from single-channel fluctuations. The former indicate molecular complex formation, the latter unbound particles. While not typically used as a particle sizing technique, FCCS is a valuable extension for studying exactly what components interact to form a particle.

Besides these obvious strengths of fluorescence as a readout, there are more subtle advantages to FCS. FCS is applicable to practically any particle that is large enough to attach a fluorescent dye without significantly altering the particle dynamics. What constitutes a "significant alteration" has to be decided and checked in suitable control experiments on a case-by-case basis. Typically, attaching a synthetic dye to a protein of interest adds ca. 1 kDa molecular mass, a fluorescent protein tag, or a self-labeling protein tag ca. 10–30 kDa (33). If labeling limitations are a serious concern, then DLS may be preferred. However, DLS may struggle to detect small particles over the background, especially if the particles are not dissolved in simple buffers: the contrast from scattered light scales sharply with the particle volume. However, the limit of detection in DLS depends on multiple factors (18). Thus, although the required attachment of a fluorophore seems to be a conceptual limitation, FCS is a particularly attractive technique for studying small particles or complex environments but also to add specificity in samples of unknown composition.

What keeps us from routinely using FCS for dispersity characterization?

In spite of these obvious methodological advantages, FCS is not used very frequently for particle sizing. A first, trivial reason is perhaps found in history: DLS is significantly older than FCS. While the concept of FCS was proposed in the 1970s (24), the technique reached maturity only in the 1990s following technical breakthroughs in confocal microscopy (5,34) and is still marketed mostly as an optional add-on to confocal imaging platforms. In contrast, DLS has been commercialized since the late 70s and is nowadays performed in affordable benchtop systems (an outline of the early history of DLS can be found, for example, in (20) and for FCS in (35,36)). Thus, FCS is lagging behind in endorsement by the community and by instrument manufacturers by about two decades.

Furthermore, the required use of fluorophores creates complications beyond the added effort of attaching fluorophores to the particles of interest. While the specificity of fluorescence is an enormous advantage, one should not confuse the high signal/background ratio with a high signal/noise ratio. In contrast to elastic scattering, the excitation/emission photocycle of fluorescence is a saturable process under realistic measurement conditions. Therefore, one cannot arbitrarily increase the signal/noise ratio in any fluorescence technique by increasing the laser power. In addition, saturation tends to introduce artifacts: in FCS in particular, saturating the photocycle can lead to an overestimation of particle sizes (37,38).

Photochemical side processes of the photocycle can lead to off switching of the fluorophore. Reversible off switching ("blinking") mostly makes data interpretation more complicated (39). Irreversible off switching ("photobleaching") has rather complex consequences: photobleaching leads to a compromised signal/noise ratio, introduces artificial additional slow-diffusing kinetics into the ACF, and/or leads to an overestimation of diffusion coefficients, i.e., underestimation of particle sizes (28,40). While the first two effects of photobleaching can be controlled or compensated rather easily, the underestimation of particle sizes due to photobleaching often remains cryptic unless controlled via an experimental laser power series and is especially severe for large, slow-moving particles.

In principle, particle size overestimation due to fluorescence saturation and particle size underestimation due to photobleaching always counteract each other. In practice, their balance is system specific and hard to predict, and the safe option is to perform experiments at low laser power where both effects remain negligible, albeit at the cost of reduced signal/noise ratio.

Fluorescence emission can also change in response to the local environment of the particle, and one should be careful about photophysical processes possibly affecting the measured diffusion dynamics. The increasingly widespread combination of FCS with time-correlated single-photon counting helps to detect and correct such effects through the measurement of accompanying changes in fluorescence lifetime (41).

As none of these limitations apply to the scattered light used in DLS, interpretation of DLS data seems more robust.

Please cite this article in press as: Krohn et al., Fluorescence correlation spectroscopy for particle sizing: A notorious challenge, Biophysical Journal (2025), https://doi.org/10.1016/j.bpj.2025.03.017

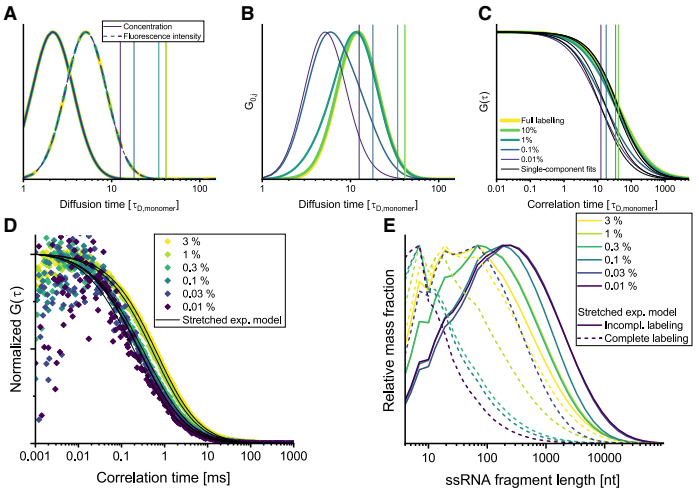

FIGURE 1 Effect of fluorescent labeling efficiency on FCS signal. (*A–C*) Theoretical curves illustrating effects of changing labeling efficiency. (*A*) Simulated lognormal particle concentration and relative fluorescence signal over particle size. (*B*) Resulting species-wise correlation function amplitudes. (*C*) Obtained correlation functions with fits with Eqs. 3a, 3b, and 3c. Vertical lines in (*A*)–(*C*) indicate fitted diffusion times. (*D and E*) Experimental results from broad distributions of single-stranded RNA (ssRNA) fragment lengths with similar size distributions but different stochastic labeling efficiencies (compare also Fig. S2). (*D*) Experimental ACFs. (*E*) Reconstructed concentration profiles over particle size. Analysis was repeated with and without correction of labeling effect. Irregular distribution shape features at low fragment lengths are discretization artifacts. The smaller overall size in the 3% labeled sample compared to the others is consistent with gel electrophoresis (compare Fig. S2).

However, caveats about similar effects resulting from local heating effects and internal dynamics within particles have been raised for DLS (19).

Besides these rather practical issues, there are further challenges that are specific to the use of FCS for the characterization of polydisperse samples and are of a more conceptual nature. Here, progress can be made by improving the strategy of FCS data acquisition and analysis as described in further sections.

Why are large particles such a problem and how can they be dealt with?

A challenge that is common to both FCS and DLS and deserves explicit mention is an overrepresentation of large particles in the data. In DLS, the amplitude of a particle species in the intensity correlation function scales with the square of the particle mass. Similarly, in FCS, the species amplitude usually scales with the square of the particle brightness (Eqs. 3a, 3b, and 3c). While this scaling is predictable, it is unfavorable for many applications for two reasons: firstly, the bias of the correlation function toward large particles makes it hard to capture the particle number distribution of polydisperse samples. It also strongly biases analysis strategies based on single-species approximations toward larger species. Secondly, these large particles are often rare and, therefore, weakly sampled in the experimental data. This obscures the dynamics of interest below high noise levels.

Different, to some degree complementary approaches can be taken to obtain data that are more representative of the large number of smaller particles in the sample. A first, obvious, and widespread approach is to discard data that show signal "bursts" from especially bright particles. This approach is very established and powerful, and different partially or fully automated strategies are available (42–44). Such "burst removal" performs well for the characterization of low-disperse systems with the occasional formation of unwanted aggregates. However, for intrinsically polydisperse systems, the decision of what is a desired signal and what is undesired remains somewhat arbitrary, posing a severe risk of distorting the results and rendering them useless.

A strategy frequently applied by FCS experimenters when working with disperse self-assembling systems is to dilute fluorescently labeled monomers in an excess of unlabeled ones (8,45,46). This incomplete labeling reduces the average brightness of large particles and the noise they introduce into the data. While this strategy is successful, it has an often-overlooked side effect (47). Consider a system in which the number of fluorophore moieties within a particle scales linearly with particle mass, which is realistic for many self-assembling systems. If we assume that the fluorescence quantum yield of fluorophores is independent of particle size and that every monomer has a stoichiometry-independent probability p to carry a fluorophore moiety, the normalized (to $\epsilon_{monomer}$) brightness of a j-mer oligomer species is characterized by a binomial distribution with average relative brightness jp (Fig. 1 *A*) but also, and easily overlooked, variance $jp(1-p)$. Inserting this into Eq. 3b and following the calculations in (47) yields

$$G_{0,j,p} = \frac{\langle N_j\rangle j^2\left(1+\frac{1-p}{jp}\right)}{\left(\sum_{j=1}^{j_{max}}\langle N_j\rangle j\right)^2}. \quad (4)$$

Please cite this article in press as: Krohn et al., Fluorescence correlation spectroscopy for particle sizing: A notorious challenge, Biophysical Journal (2025), https://doi.org/10.1016/j.bpj.2025.03.017

For $p \ll \frac{1}{j+1}$, the numerator is proportional to j rather than j^2 as implied by Eq. 3b. In other words, the limited labeling efficiency not only reduces the noise caused by rare large particles but also shifts the weights with which different complex sizes are measured in FCS altogether (Fig. 1, *B* and *C*). While Eq. 4 is based on strong assumptions, it will often serve as a reasonable approximation (Fig. 1 *E*). Related effects of concentrations and brightness have been investigated in some detail in experiments on micelles (46). In that study, the concentrations of both the micelle constituent and the fluorescent label were systematically varied. This allowed to understand both the self-assembly kinetics of the micelles and the impact of labeling in the system. The experimental data from sparsely labeled detergent micelles supported analysis using assumptions analogous to those underlying Eq. 4. However, this work also presents considerations about the case of changing quantum yields with label density.

Another issue that arises with increasing particle sizes is that Eqs. 3a, 3b, 3c, and 4 implicitly assume that particles are small compared to the observation volume. Simply speaking, Eqs. 3a, 3b, and 3c only consider center-of-mass movement of particles, but for bigger particles, the center of mass leaving the observation volume does not mean that the entire particle left the observation volume. Particle sizes significantly exceeding ca. $w_{xy}/5$ lead to significant distortions of the effective diffusion time and particle number (48,49). A simple correction for particles of moderate size is to scale the effective beam waist parameter as $w^2_{xy,eff} = 1 + r^2$ with particle radius r. $\tau_{D,j}$ and $\langle N_j \rangle$ then both increase by the same factor (48,49). Note that r, strictly speaking, refers to the spatial distribution of fluorophores in the particle, for which the hydrodynamic radius r_H may or may not be a good approximation. (49) contains more accurate expressions for the large-particle correction, considering different particle shapes.

Experimental avenues beyond single-spot confocal FCS

Nowadays, FCS is mostly performed on confocal microscopes due to the convenience of its implementation in commercial instruments, with small and relatively well-defined detection volumes. As mentioned above, confocal microscopes from all major manufacturers offer adequate platforms for traditional single-spot confocal FCS measurements. However, besides the single-spot FCS acquisition that most of our discussion focuses on, other FCS concepts exist that promise to be especially attractive for particle sizing applications.

In single-spot FCS, deviations from the assumed Gaussian detection volume will lead to stretched decay patterns in the ACF that are easily confused with polydispersity (50). To increase the robustness of analysis, it is desirable to observe diffusion over fixed length scales that are robust against detection volume shape deviations. This has been part of the motivation behind the development of multifocus FCS approaches like dual-focus FCS (51,52). Dual-focus FCS was the method of choice in a study pushing the limits of sensitivity to mass changes upon protein-ligand binding in FCS (6).

A further extension of this concept is scanning FCS, which also increases particle throughput by sampling a larger volume without a large increase in the confocal detection volume (47,53). The concept of scanning FCS allows many different scanning modes regarding geometry and timescales. Raster image correlation spectroscopy (RICS) is very attractive for the analysis of polydisperse samples, as it samples a range of spatial and temporal scales in a single dataset (54–56). Given that the scan parameters in RICS are generally adaptable to the diffusion coefficients of the sample, an experimental approach globally analyzing RICS data from multiple scan speeds is likely to be of particular value for the analysis of disperse mixtures (57).

In addition, one may wonder whether the regular pixel grid usually employed in RICS and similar approaches is the most efficient grid for spatiotemporal diffusion analysis (55). Following the principles of pair correlation function analysis (35,58,59), a set of observation volumes could be engineered for optimal information content given the question at hand. Besides established implementations in scanning confocal systems and more recent advances exploiting array detectors (58,59), it will be interesting to explore what developments toward ultrafast laser scanning microscopes can contribute here (60–62).

Besides these ideas toward increased precision of FCS-based particle sizing, another interesting aspect is that of FCS automation. Another reason why FCS applications lag behind DLS is that nowadays, DLS is routinely and quickly performed with compact cuvette spectrometers or even plate reader systems. In contrast, the performance of FCS in confocal microscopes requires instrumentation that is expensive, physically large, and relatively complex in operation. This need not be the case. Using concepts that are widespread in automated high-throughput/high-content image acquisition, workflows and dedicated devices suitable for automated FCS acquisition have been developed, which effectively operate as plate readers and even automatically recognize cells as regions of interest for measurements (63–66). Alternatively, a cuvette-based FCS spectrometer was reported that exploits advances in objective lens design to go beyond measurements through standard-thickness coverslips (67). FCS hardware has reached technical maturity to the point of allowing highly automated apparatuses that strip away most of the complexity of standard confocal microscopy. Further efforts, also by commercial manufacturers, to implement and spread turn-key apparatuses for a nonexpert user community would be of great value.

Please cite this article in press as: Krohn et al., Fluorescence correlation spectroscopy for particle sizing: A notorious challenge, Biophysical Journal (2025), https://doi.org/10.1016/j.bpj.2025.03.017

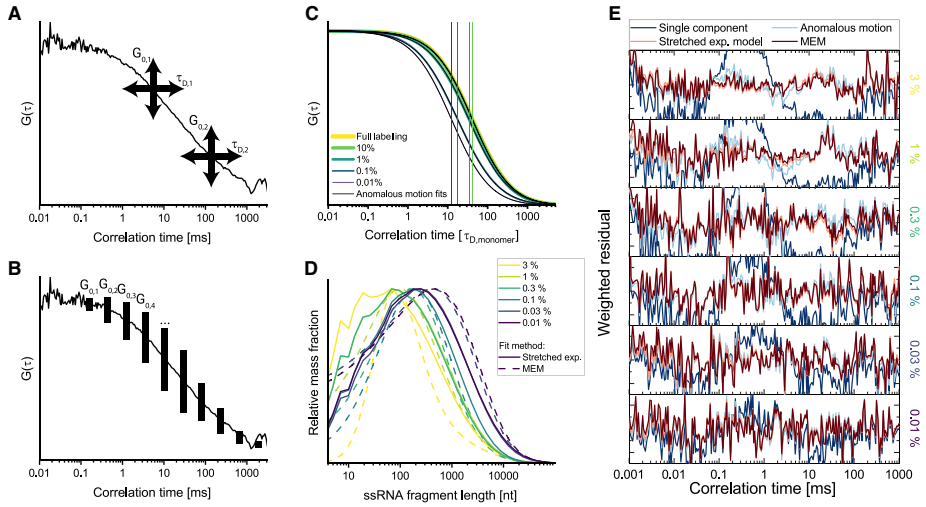

FIGURE 2 Analysis strategies for FCS of polydisperse samples. (*A*) Illustration of conventional two-component FCS fitting that attempts to find amplitude and diffusion time for each component. (*B*) Illustration of method of histograms fitting, with fixed array of diffusion times and optimization of associated amplitudes. (*C*) Same theoretical ACFs as in Fig. 1 *C* but fitted with Eqs. 5a and 5b. Vertical lines are fitted diffusion times. (*D*) Same as Fig. 1 *E* but comparing resulting particle size distributions between fits using the maximum entropy method (MEM) and a stretched-exponential model (based on Eq. 4) of concentration over particle size. (*E*) Fit residuals for the fits that (*B*) is based on, as well as fits with Eqs. 3a, 3b, and 3c with a single component and with Eqs. 5a and 5b.

How to make the most of available data?

For the analysis of a polydisperse system, a naive approach would be to evaluate Eqs. 3a, 3b, and 3c or 4, with many j-mer species up to a cutoff stoichiometry j_{max}. This would, however, require estimating a parameter number reaching or even surpassing the number of data points in an experimentally determined ACF. That is impossible in practice, especially given that successive data points in the ACF are strongly correlated and show few distinctive features. In this section, we will briefly discuss strategies for dealing with FCS data from disperse samples.

The first obvious solution is to determine only a single average value. However, the interpretation of this average is nontrivial due to the brightness dependence of amplitudes. The vertical lines in Fig. 1, *A*–*C*, illustrate the average diffusion time estimated by the single-component fits in comparison to the ground-truth distributions. The estimated diffusion time changes with labeling efficiency but under no circumstances is representative of the particle number distribution (Fig. 1 *A*) or particle mass distribution (equals fluorescence intensity distribution in Fig. 1 *A*). Fig. 1 *D* shows single-component FCS model fits (Eqs. 3a, 3b, and 3c with $j_{max} = 1$), which display visible mismatch for some curves. An alternative is to modify Eq. 3c with an anomalous diffusion model ($\langle\Delta^2\rangle = 4\Gamma\tau^{\alpha}$) such that

$$G_{anom}(\tau) = G_0 \frac{1}{1+\left(\frac{\tau}{\tau_D}\right)^{\alpha}} \frac{1}{\sqrt{1+\frac{1}{S^2}\left(\frac{\tau}{\tau_D}\right)^{\alpha}}} \text{ and} \quad (5a)$$

$$\tau_D = \left(\frac{{w_0}^2}{4\Gamma}\right)^{\frac{1}{\alpha}}, \quad (5b)$$

with transport coefficient Γ, anomalous diffusion coefficient α, and amplitude G_0. Originally intended to describe FCS data for non-Brownian motion inside living cells, the model allows the fit to adapt to deviations from the assumption of "random walk characterized by a single diffusion coefficient in an open Gaussian-shaped detection volume" (29,50,68). Obviously, a polydisperse sample violates this assumption. Analyzing the example in Fig. 1 *C* with Eqs. 5a and 5b with $\alpha < 1$ improves the fits, but the change in τ_D compared to fitting with Eqs. 3a, 3b, and 3c was negligible (below 1% difference; Fig. 2 *C*). Note that for real data including noise, Eqs. 3a, 3b, 3c, 5a, and 5b can return significantly different diffusion times. Considering other factors besides dispersity affect α (50,68), anomalous motion models should generally only be used as an empirical approximation if no better model is available.

Two-component approximations are another popular analysis strategy. Here, the diffusion coefficient of one species, for example, the monomer, should be known and fixed

Please cite this article in press as: Krohn et al., Fluorescence correlation spectroscopy for particle sizing: A notorious challenge, Biophysical Journal (2025), https://doi.org/10.1016/j.bpj.2025.03.017

in the fitting. Two-component models (Eqs. 3a, 3b, and 3c with $j_{max} = 2$) have the same, or even greater, difficulties in interpretation as single-component approximations. Thus, while single- or two-component diffusion or anomalous diffusion models can be used to quantify trends in data from polydisperse samples, one should be cautious about what the average represents.

When going beyond single-component approximations, one encounters the issue that the ACF alone is not sufficient to distinguish differences in $\langle N_j \rangle$ from differences in ε_j (Eqs. 3a, 3b, and 3c). Some assumption must generally be made about these two parameters. One possible assumption is that all particles are of equal brightness, a trivial case in which ε_j disappears from the calculation. While for some systems, this is justified, for many, this assumption is unphysical. A better approach is often that described in the previous section, considering labeled monomer units within the oligomer particle (Eq. 4). When combining this with assumptions about the link of particle size ($\tau_{d,j}$ as a function of j) and brightness ε_j as mentioned before, this drastically reduces the number of model parameters. For example, one can combine the before-discussed impact of labeling (Eq. 4) with models of particle mobility, such as Eq. 2, to arrive at

$$\frac{\tau_{d,j}}{\tau_{d,monomer}} = \left(\frac{\varepsilon_j}{\varepsilon_{monomer}}\right)^{\frac{1}{3}} = j^{\frac{1}{3}}. \tag{6}$$

This scaling is different for other models of particle shape, of course (22,23). In that case, by determining $\tau_{d,monomer}$ from control measurements, one can reduce the model to $\langle N_j \rangle$, being the only remaining parameter to determine for each species. One can then fit $\langle N_j \rangle$ using the "method of histograms" (69): this approach uses a regular-spaced array of $\tau_{d,j}$ (considering associated bin widths) and optimizes an array of associated amplitudes as opposed to diffusion times and amplitudes (Fig. 2, *A* and *B*). That way, one only needs to estimate $\langle N_j \rangle$ for a relatively modest-sized subset of particle sizes. For robust results, this is combined with suitable fit constraints, e.g., non-negativity of amplitudes, and with methods to exploit the fact that for most polydisperse systems, no sharp jumps in the profile of concentration over particle size are expected. There are at least two different techniques to ensure a smooth profile of $G_{0,j}$. Firstly, one can regularize the fit without specific assumptions about the underlying distribution via a modified cost function that penalizes unphysically spiky profiles of $\langle N_j \rangle$ using, for example, the maximum entropy method (70) or minimization of the squared second derivative (71). These and similar approaches have been successfully introduced into FCS (68,69,72–75). A downside is that these methods require very high signal/noise ratios (Figs. 2 *D* and 1 *D*, note the skewed distributions at low labeling efficiency). Also, secondary analysis of the obtained particle size distribution is required for quantitative interpretation. As a simpler alternative, we can force the distribution of $\langle N_j \rangle$ to follow a predefined profile over stoichiometry with tuneable parameters, such as Gaussian, lognormal, or stretched-exponential functions. This allows us to describe the entire distribution with a small number of parameters (three for the mentioned functions). In some cases, such fits can offer a direct link to physical models of self-assembly (2). In our experience, the use of regularization techniques offered no notable advantage over the use of parameterized models (Fig. 2 *D*), in agreement with previous reports (72,76). Suitable parameterized models and the maximum entropy method or minimization of the squared second derivative fits typically yield similar quality of fit and overall similar distributions, and parameterized models handle data of limited signal/noise ratio more robustly (Fig. 2, *D* and *E*).

Another option is the use of alternative data analysis frameworks besides ACF fitting, such as photon counting histograms and related approaches (36,77,78). These methods use other representations of the fluctuation signal besides the ACF. Their key advantage over ACF fitting is that they can discriminate changes in $\langle N_j \rangle$ or ε_j, thus removing ambiguity in the fitting. While these methods have proven their value, they generally come with increased computational cost compared to ACF fitting, especially when many species must be evaluated. Thus, they tend to encounter practical limitations in use on data from polydisperse systems.

Outlook: From ACF fitting to neural networks?

Particle sizing of polydisperse samples is a challenging problem and probably will remain one for the foreseeable future. Nonetheless, since the inception of FCS in the 1970s, the FCS community has introduced many concepts into experiments and analysis that are tremendously useful for the task. An exciting avenue for such a challenge is obviously the recent progress in machine learning, especially convolutional neural networks (CNNs). A few recent papers explored the capabilities that machine learning brings into FCS (43,79,80). Besides applications for artifact removal, specifically for the above-mentioned burst removal problem (43), of key interest are papers that report the use of machine learning for parameter estimation in FCS (79,80). The good understanding of the physical basis of FCS was exploited to generate large amounts of realistic training data *in silico* based on random walk simulations. Different models were trained to analyze ACFs previously calculated using traditional approaches (CNN in (79) or gradient boosting models in (80)) or to analyze the raw data directly (CNN in (79)). Good results could be obtained from significantly shortened acquisition times. Remarkably, the CNN utilizing raw data compensated experimental artifacts that it was not explicitly trained to deal with (79). ACF-based analysis and related frameworks are essentially data compressions that emphasize patterns of interest but also discard a lot of

Please cite this article in press as: Krohn et al., Fluorescence correlation spectroscopy for particle sizing: A notorious challenge, Biophysical Journal (2025), https://doi.org/10.1016/j.bpj.2025.03.017

information. Machine learning techniques utilizing the raw data can retrieve and exploit information that is lost in the ACF calculation. Similar ideas of exploiting uncompressed raw data have been developed in Bayesian statistics frameworks (81,82). Analysis of uncompressed data promises to overcome many of the difficulties of ACF-based analysis, as discussed above. Fortunately, simulations incorporating various aspects of the physics of FCS allow us to generate a large body of training data for such models (83,84).

To conclude, while FCS is, for many practical reasons, still not the primary method of choice for routine particle sizing, it performs quite well when some of the major error sources can be routinely dealt with, as demonstrated by a number of referenced studies. That these improvements have not yet been widely implemented and standardized in FCS routines is regrettable but understandable due to the persistent lack of affordable turnkey instrumentation. We argue that, particularly with respect to the immense potential of implementing machine learning in FCS data analysis, the time has come for instrument developers to revisit FCS as an easily accessible technology that opens fully new perspectives on a fast and widely applicable large-scale analysis of molecular sizes. With respect to the omics era, particle sizes and diffusion coefficients are highly valuable complementary parameters to map the dynamic proteome and interactome on a cell-wide scale—comprehensive dynamic information being the next big challenge in our holistic understanding of living systems.

ACKNOWLEDGMENTS

This work was supported by funding by the Deutsche Forschungsgemeinschaft (DFG, German Research Foundation) under Germany's Excellence Strategy – EXC-2094 – 390783311. We would like to thank Béla Frohn, Martin Spitaler, and the Imaging Facility team (all MPI of Biochemistry, Martinsried) and Don C. Lamb (Ludwig Maximilians University Munich) for helpful discussions. We dedicate this work to the memory of Watt W. Webb, whose pioneering contributions to a large selection of biophysical methods, including FCS, have left a lasting impact on our scientific community.

DECLARATION OF INTERESTS

The authors declare no competing interests.

SUPPORTING REFERENCES

References (85–88) appear in the supporting material.

SUPPORTING MATERIAL

Supporting material can be found online at https://doi.org/10.1016/j.bpj.2025.03.017.

REFERENCES

1. Xu, G., J. Yang, and J. Zhao. 2018. Molecular weight dependence of chain conformation of strong polyelectrolytes. *J. Chem. Phys.* 149:163329.
2. Schaeffel, D., S. Yordanov, …, K. Koynov. 2015. Fluorescence Correlation Spectroscopy in Dilute Polymer Solutions: Effects of Molar Mass Dispersity and the Type of Fluorescent Labeling. *ACS Macro Lett.* 4:171–176.
3. Wei, M.-T., S. Elbaum-Garfinkle, …, C. P. Brangwynne. 2017. Phase behaviour of disordered proteins underlying low density and high permeability of liquid organelles. *Nat. Chem.* 9:1118–1125.
4. Holyst, R., A. Bielejewska, …, S. A. Wieczorek. 2009. Scaling form of viscosity at all length-scales in poly(ethylene glycol) solutions studied by fluorescence correlation spectroscopy and capillary electrophoresis. *Phys. Chem. Chem. Phys.* 11:9025–9032.
5. Schwille, P., F. Oehlenschläger, and N. G. Walter. 1996. Quantitative Hybridization Kinetics of DNA Probes to RNA in Solution Followed by Diffusional Fluorescence Correlation Analysis. *Biochemistry.* 35:10182–10193.
6. Sarkar, A., A. Sharma, …, M. Kumbhakar. 2020. Binding Constant Determined from the Angstrom-Scale Change in Hydrodynamic Radius of Transferrin upon Binding with Europium Using Dual-Focus Fluorescence Correlation Spectroscopy. *J. Phys. Chem. Lett.* 11:1148–1153.
7. Hanlon, A. D., M. I. Larkin, and R. M. Reddick. 2010. Free-Solution, Label-Free Protein-Protein Interactions Characterized by Dynamic Light Scattering. *Biophys. J.* 98:297–304.
8. Novo, M., S. Freire, and W. Al-Soufi. 2018. Critical aggregation concentration for the formation of early Amyloid-β (1–42) oligomers. *Sci. Rep.* 8:1783.
9. Guillén-Boixet, J., A. Kopach, …, T. M. Franzmann. 2020. RNA-Induced Conformational Switching and Clustering of G3BP Drive Stress Granule Assembly by Condensation. *Cell.* 181:346–361.e17.
10. Theek, B., M. Baues, …, T. Lammers. 2018. Histidine-rich glycoprotein-induced vascular normalization improves EPR-mediated drug targeting to and into tumors. *J. Contr. Release.* 282:25–34.
11. Cinar, G., J. I. Solomun, …, I. Nischang. 2022. Nanoparticle sizing in the field of nanomedicine: Power of an analytical ultracentrifuge. *Anal. Chim. Acta.* 1205:339741.
12. Caputo, F., R. Vogel, …, L. Calzolai. 2021. Measuring particle size distribution and mass concentration of nanoplastics and microplastics: addressing some analytical challenges in the sub-micron size range. *J. Colloid Interface Sci.* 588:401–417.
13. Bell, N. C., C. Minelli, …, A. G. Shard. 2012. Emerging Techniques for Submicrometer Particle Sizing Applied to Stöber Silica. *Langmuir.* 28:10860–10872.
14. Vezočnik, V., K. Rebolj, …, E. Žagar. 2015. Size fractionation and size characterization of nanoemulsions of lipid droplets and large unilamellar lipid vesicles by asymmetric-flow field-flow fractionation/multi-angle light scattering and dynamic light scattering. *J. Chromatogr. A.* 1418:185–191.
15. Wang, Y., C. W. Cuss, and W. Shotyk. 2020. Application of asymmetric flow field-flow fractionation to the study of aquatic systems: Coupled methods, challenges, and future needs. *J. Chromatogr. A.* 1632:461600.
16. Mahl, D., J. Diendorf, …, M. Epple. 2011. Possibilities and limitations of different analytical methods for the size determination of a bimodal dispersion of metallic nanoparticles. *Colloids Surf. A Physicochem. Eng. Asp.* 377:386–392.
17. Vogel, R., G. Willmott, …, M. Trau. 2011. Quantitative Sizing of Nano/Microparticles with a Tunable Elastomeric Pore Sensor. *Anal. Chem.* 83:3499–3506.
18. Hassan, P. A., S. Rana, and G. Verma. 2015. Making Sense of Brownian Motion: Colloid Characterization by Dynamic Light Scattering. *Langmuir.* 31:3–12.
19. Fischer, K., and M. Schmidt. 2016. Pitfalls and novel applications of particle sizing by dynamic light scattering. *Biomaterials.* 98:79–91.
20. Stetefeld, J., S. A. McKenna, and T. R. Patel. 2016. Dynamic light scattering: a practical guide and applications in biomedical sciences. *Biophys. Rev.* 8:409–427.

Please cite this article in press as: Krohn et al., Fluorescence correlation spectroscopy for particle sizing: A notorious challenge, Biophysical Journal (2025), https://doi.org/10.1016/j.bpj.2025.03.017

21. Chen, L., H. Zhu, and H. Cui. 2017. A study of the Brownian motion of the non-spherical microparticles on fluctuating lattice Boltzmann method. *Microfluid. Nanofluidics.* 21:54.
22. Tirado, M. M., and J. G. De La Torre. 1979. Translational friction coefficients of rigid, symmetric top macromolecules. Application to circular cylinders. *J. Chem. Phys.* 71:2581–2587.
23. Löwen, H. 1994. Brownian dynamics of hard spherocylinders. *Phys. Rev. E.* 50:1232–1242.
24. Magde, D., E. Elson, and W. W. Webb. 1972. Thermodynamic Fluctuations in a Reacting System—Measurement by Fluorescence Correlation Spectroscopy. *Phys. Rev. Lett.* 29:705–708.
25. Wohland, T., S. Maiti, and R. Macháň. 2020. An Introduction to Fluorescence Correlation Spectroscopy. IOP Publishing.
26. Koppel, D. E. 1974. Statistical accuracy in fluorescence correlation spectroscopy. *Phys. Rev.* 10:1938–1945.
27. Enderlein, J., and I. Gregor. 2005. Using fluorescence lifetime for discriminating detector afterpulsing in fluorescence-correlation spectroscopy. *Rev. Sci. Instrum.* 76:033102.
28. Krohn, J.-H., L. Babl, …, P. Schwille. 2024. Measuring Partition Coefficients of In Vitro Biomolecular Condensates Using Fluorescence Correlation Spectroscopy. *In* Bacterial Chromatin: Methods and Protocols. R. T. Dame, ed Springer US, New York, NY, pp. 455–475.
29. Schwille, P., J. Korlach, and W. W. Webb. 1999. Fluorescence correlation spectroscopy with single-molecule sensitivity on cell and model membranes. *Cytometry.* 36:176–182.
30. Kim, S. A., K. G. Heinze, and P. Schwille. 2007. Fluorescence correlation spectroscopy in living cells. *Nat. Methods.* 4:963–973.
31. Ries, J., S. R. Yu, …, P. Schwille. 2009. Modular scanning FCS quantifies receptor-ligand interactions in living multicellular organisms. *Nat. Methods.* 6:643–645.
32. Schwille, P., F. J. Meyer-Almes, and R. Rigler. 1997. Dual-color fluorescence cross-correlation spectroscopy for multicomponent diffusional analysis in solution. *Biophys. J.* 72:1878–1886.
33. Dean, K. M., and A. E. Palmer. 2014. Advances in fluorescence labeling strategies for dynamic cellular imaging. *Nat. Chem. Biol.* 10:512–523.
34. Rigler, R., Ü. Mets, …, P. Kask. 1993. Fluorescence correlation spectroscopy with high count rate and low background: analysis of translational diffusion. *Eur. Biophys. J.* 22:169–175.
35. Digman, M. A., and E. Gratton. 2011. Lessons in Fluctuation Correlation Spectroscopy. *Annu. Rev. Phys. Chem.* 62:645–668.
36. Elson, E. L. 2013. 40 Years of FCS. *In* Methods in Enzymology. S. Y. Tetin, ed Elsevier, pp. 1–10.
37. Gregor, I., D. Patra, and J. Enderlein. 2005. Optical Saturation in Fluorescence Correlation Spectroscopy under Continuous-Wave and Pulsed Excitation. *ChemPhysChem.* 6:164–170.
38. Nagy, A., J. Wu, and K. M. Berland. 2005. Observation Volumes and γ-Factors in Two-Photon Fluorescence Fluctuation Spectroscopy. *Biophys. J.* 89:2077–2090.
39. Widengren, J., Ü. Mets, and R. Rigler. 1995. Fluorescence correlation spectroscopy of triplet states in solution: a theoretical and experimental study. *J. Phys. Chem.* 99:13368–13379.
40. Widengren, J., and R. Rigler. 1996. Mechanisms of photobleaching investigated by fluorescence correlation spectroscopy. *Bioimaging.* 4:149–157.
41. Günther, J.-P., M. Börsch, and P. Fischer. 2018. Diffusion Measurements of Swimming Enzymes with Fluorescence Correlation Spectroscopy. *Acc. Chem. Res.* 51:1911–1920.
42. Ries, J., M. Bayer, …, P. Schwille. 2010. Automated suppression of sample-related artifacts in Fluorescence Correlation Spectroscopy. *Opt. Express.* 18:11073–11082.
43. Seltmann, A., P. Carravilla, …, D. Waithe. 2024. Neural network informed photon filtering reduces fluorescence correlation spectroscopy artifacts. *Biophys. J.* 123:745–755.
44. Margineanu, A., S. De Feyter, …, J. Hofkens. 2007. Complexation of Lipofectamine and Cholesterol-Modified DNA Sequences Studied by Single-Molecule Fluorescence Techniques. *Biomacromolecules.* 8:3382–3392.
45. Reija, B., B. Monterroso, …, S. Zorrilla. 2011. Development of a homogeneous fluorescence anisotropy assay to monitor and measure FtsZ assembly in solution. *Anal. Biochem.* 418:89–96.
46. Yu, L., M. Tan, …, T. Wohland. 2006. Determination of critical micelle concentrations and aggregation numbers by fluorescence correlation spectroscopy: Aggregation of a lipopolysaccharide. *Anal. Chim. Acta.* 556:216–225.
47. Petersen, N. O. 1986. Scanning fluorescence correlation spectroscopy. I. Theory and simulation of aggregation measurements. *Biophys. J.* 49:809–815.
48. Starchev, K., J. Zhang, and J. Buffle. 1998. Applications of Fluorescence Correlation Spectroscopy— Particle Size Effect. *J. Colloid Interface Sci.* 203:189–196.
49. Wu, B., Y. Chen, and J. D. Müller. 2008. Fluorescence Correlation Spectroscopy of Finite-Sized Particles. *Biophys. J.* 94:2800–2808.
50. Kalwarczyk, T., K. Kwapiszewska, …, R. Holyst. 2017. Apparent Anomalous Diffusion in the Cytoplasm of Human Cells: The Effect of Probes' Polydispersity. *J. Phys. Chem. B.* 121:9831–9837.
51. Brinkmeier, M., K. Dörre, …, M. Eigen. 1999. Two-Beam Cross-Correlation: A Method To Characterize Transport Phenomena in Micrometer-Sized Structures. *Anal. Chem.* 71:609–616.
52. Dertinger, T., V. Pacheco, …, J. Enderlein. 2007. Two-Focus Fluorescence Correlation Spectroscopy: A New Tool for Accurate and Absolute Diffusion Measurements. *ChemPhysChem.* 8:433–443.
53. Ries, J., S. Chiantia, and P. Schwille. 2009. Accurate Determination of Membrane Dynamics with Line-Scan FCS. *Biophys. J.* 96:1999–2008.
54. Digman, M. A., R. Dalal, …, E. Gratton. 2008. Mapping the Number of Molecules and Brightness in the Laser Scanning Microscope. *Biophys. J.* 94:2320–2332.
55. De Mets, R., A. Delon, …, I. Wang. 2020. Dynamic range and background filtering in raster image correlation spectroscopy. *J. Microsc.* 279:123–138.
56. Longfils, M., N. Smisdom, …, A. Sărkkă. 2019. Raster Image Correlation Spectroscopy Performance Evaluation. *Biophys. J.* 117:1900–1914.
57. Gröner, N., J. Capoulade, …, M. Wachsmuth. 2010. Measuring and imaging diffusion with multiple scan speed image correlation spectroscopy. *Opt. Express.* 18:21225–21237.
58. Scipioni, L., L. Lanzanó, …, E. Gratton. 2018. Comprehensive correlation analysis for super-resolution dynamic fingerprinting of cellular compartments using the Zeiss Airyscan detector. *Nat. Commun.* 9:5120.
59. Slenders, E., M. Castello, …, G. Vicidomini. 2021. Confocal-based fluorescence fluctuation spectroscopy with a SPAD array detector. *Light Sci. Appl.* 10:31.
60. Karpf, S., C. T. Riche, …, B. Jalali. 2020. Spectro-temporal encoded multiphoton microscopy and fluorescence lifetime imaging at kilohertz frame-rates. *Nat. Commun.* 11:2062.
61. Deguchi, T., P. Bianchini, …, M. Duocastella. 2020. Volumetric Lissajous confocal microscopy with tunable spatiotemporal resolution. *Biomed. Opt. Express.* 11:6293–6310.
62. Katona, G., G. Szalay, …, B. Rózsa. 2012. Fast two-photon in vivo imaging with three-dimensional random-access scanning in large tissue volumes. *Nat. Methods.* 9:201–208.
63. Wood, C., J. Huff, …, W. Wiegraebe. 2011. *In* Fluorescence Correlation Spectroscopy as Tool for High-Content-Screening in Yeast (HCS-FCS), J. Enderlein, Z. K. Gryczynski, and R. Erdmann, eds SPIE, p. 79050H.
64. Wachsmuth, M., C. Conrad, …, J. Ellenberg. 2015. High-throughput fluorescence correlation spectroscopy enables analysis of proteome dynamics in living cells. *Nat. Biotechnol.* 33:384–389.

Please cite this article in press as: Krohn et al., Fluorescence correlation spectroscopy for particle sizing: A notorious challenge, Biophysical Journal (2025), https://doi.org/10.1016/j.bpj.2025.03.017

65. Fu, X., Y. Song, …, C. I. Richards. 2020. High-throughput fluorescence correlation spectroscopy enables analysis of surface components of cell-derived vesicles. *Anal. Bioanal. Chem.* 412:2589–2597.
66. Hartmann, A., K. Sreenivasa, …, M. Schlierf. 2023. An automated single-molecule FRET platform for high-content, multiwell plate screening of biomolecular conformations and dynamics. *Nat. Commun.* 14:6511.
67. Sahoo, B., T. B. Sil, …, K. Garai. 2018. A Fluorescence Correlation Spectrometer for Measurements in Cuvettes. *Biophys. J.* 115:455–466.
68. Tsekouras, K., A. P. Siegel, …, S. Pressé. 2015. Inferring Diffusion Dynamics from FCS in Heterogeneous Nuclear Environments. *Biophys. J.* 109:7–17.
69. Starchev, K., J. Buffle, and E. Pérez. 1999. Applications of Fluorescence Correlation Spectroscopy: Polydispersity Measurements. *J. Colloid Interface Sci.* 213:479–487.
70. Skilling, J., and R. K. Bryan. 1984. Maximum entropy image reconstruction: general algorithm. *Mon. Not. Roy. Astron. Soc.* 211:111–124.
71. Provencher, S. W. 1982. A constrained regularization method for inverting data represented by linear algebraic or integral equations. *Comput. Phys. Commun.* 27:213–227.
72. Pal, N., S. Dev Verma, …, S. Sen. 2011. Fluorescence Correlation Spectroscopy: An Efficient Tool for Measuring Size, Size-Distribution and Polydispersity of Microemulsion Droplets in Solution. *Anal. Chem.* 83:7736–7744.
73. Pánek, J., L. Loukotová, …, P. Štěpánek. 2018. Distribution of Diffusion Times Determined by Fluorescence (Lifetime) Correlation Spectroscopy. *Macromolecules.* 51:2796–2804.
74. Sengupta, P., K. Garai, …, S. Maiti. 2003. Measuring Size Distribution in Highly Heterogeneous Systems with Fluorescence Correlation Spectroscopy. *Biophys. J.* 84:1977–1984.
75. Xue, L., S. Jin, …, T. Ito. 2022. Investigation of Molecular Diffusion at Block Copolymer Thin Films Using Maximum Entropy Method-Based Fluorescence Correlation Spectroscopy and Single Molecule Tracking. *J. Fluoresc.* 32:1779–1787.
76. Goertz, V., N. Dingenouts, and H. Nirschl. 2009. Comparison of Nanometric Particle Size Distributions as Determined by SAXS, TEM and Analytical Ultracentrifuge. *Part. Part. Syst. Char.* 26:17–24.
77. Chen, Y., J. D. Müller, …, E. Gratton. 1999. The Photon Counting Histogram in Fluorescence Fluctuation Spectroscopy. *Biophys. J.* 77:553–567.
78. Skakun, V. V., A. V. Digris, and V. V. Apanasovich. 2014. Global Analysis of Autocorrelation Functions and Photon Counting Distributions in Fluorescence Fluctuation Spectroscopy. *In* Fluorescence Spectroscopy and Microscopy: Methods and Protocols. Y. Engelborghs and A. J. W. G. Visser, eds Humana Press, Totowa, NJ, pp. 719–741.
79. Tang, W. H., S. R. Sim, …, T. Wohland. 2024. Deep learning reduces data requirements and allows real-time measurements in imaging FCS. *Biophys. J.* 123:655–666.
80. Quiblier, N., J.-M. Rye, …, H. Berry. 2024. Enhancing Fluorescence Correlation Spectroscopy with Machine Learning for Advanced Analysis of Anomalous Diffusion. Preprint at: *arXiv*. https://doi.org/10.48550/ArXiv.2407.12382.
81. Jazani, S., I. Sgouralis, …, S. Pressé. 2019. An alternative framework for fluorescence correlation spectroscopy. *Nat. Commun.* 10:3662.
82. Tavakoli, M., S. Jazani, …, S. Pressé. 2020. Pitching Single-Focus Confocal Data Analysis One Photon at a Time with Bayesian Nonparametrics. *Phys. Rev. X.* 10:011021.
83. Woringer, M., I. Izeddin, …, H. Berry. 2020. Anomalous Subdiffusion in Living Cells: Bridging the Gap Between Experiments and Realistic Models Through Collaborative Challenges. *Front. Physiol.* 8:134.
84. Waigh, T. A., and N. Korabel. 2023. Heterogeneous anomalous transport in cellular and molecular biology. *Rep. Prog. Phys.* 86:126601.
85. Kohyama, S., A. Merino-Salomón, and P. Schwille. 2022. In vitro assembly, positioning and contraction of a division ring in minimal cells. *Nat. Commun.* 13:6098.
86. Mansour, F. H., and D. G. Pestov. 2013. Separation of long RNA by agarose–formaldehyde gel electrophoresis. *Anal. Biochem.* 441:18–20.
87. Peulen, T.-O., K. Hemmen, …, K. G. Heinze. 2025. tttrlib: modular software for integrating fluorescence spectroscopy, imaging, and molecular modeling. *Bioinformatics.* 41:btaf025.
88. Steinbach, P. J., K. Chu, …, R. D. Young. 1992. Determination of rate distributions from kinetic experiments. *Biophys. J.* 61:235–245.

7

FCS-based Characterization of FtsZ-ZapD Interaction

This chapter will describe my contributions to a study led by Adrián Merino-Salomón, published as a reviewed preprint in eLife [4].

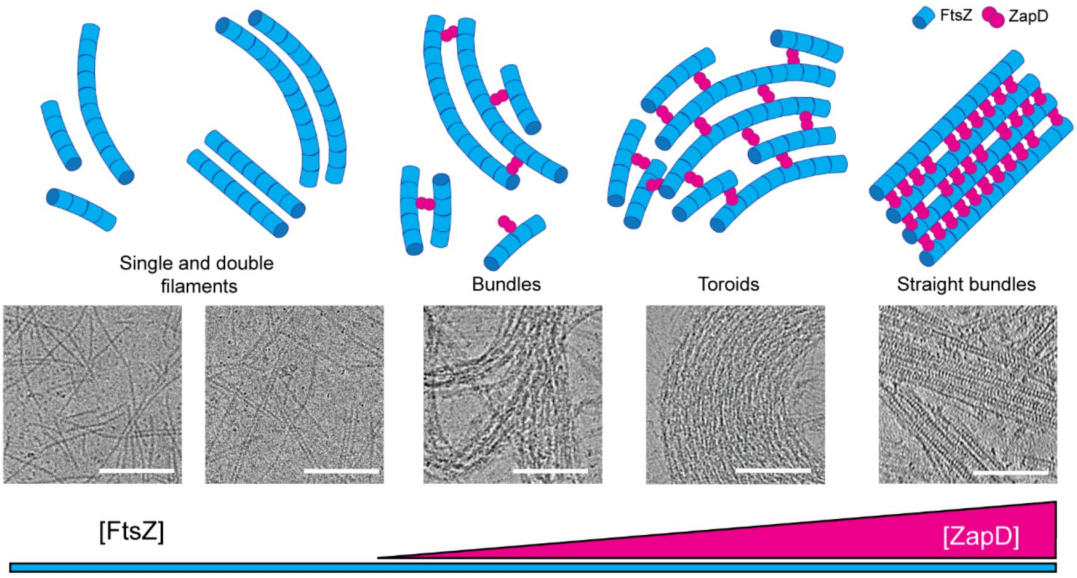

Figure 7.1. Effect of ZapD on FtsZ assembly *in vitro*. The schematic and representative electron micrographs illustrate how with increasing concentration of ZapD protein compared to FtsZ, the FtsZ protofilaments assemble into differently-shaped structures. Scale bars: 100 nm. Reprinted from Merino-Salomón et al. eLife 2025 [4] under Creative Commons Attribution License.

The protein FtsZ is a filament-forming protein and one of the key players in bacterial cell division. It is homologous to eukaryote tubulin proteins, and self-assembles into linear filaments in the presence of guanidine triphosphate (GTP). In the absence of GTP, FtsZ is thought to form only small oligomers. Preceding cell division for example in *E. coli* cells, FtsZ forms a ring-like structure in mid-cell known as the Z ring, which contracts during scission. The exact role of FtsZ in this process, and how the protein executes its function, remains poorly understood. The importance of FtsZ is emphasized by its long list of interaction partners. At the same time, the complex,

often functionally redundant, interactions also make the study of FtsZ function difficult. Among the proteins interacting with FtsZ are membrane-anchored proteins like FtsA and ZipA, but also proteins binding to FtsZ multivalently which thereby cross-link FtsZ filaments into larger assemblies [99]. Presumably, these interactions, together with the suppression of FtsZ assembly away from midcell by the MinCDE system and SlmA, ensure a densely packed ring-shaped functional Z ring assembly.

In this study, we were interested in studying molecular details of the interaction of FtsZ with the cross-linking protein ZapD. ZapD forms symmetic homodimers. Such a dimer can then bind two FtsZ protofilaments, cross-linking them into a bundle. Cryo-electron microscopy and tomography were used to study the structure of superstructures resulting from this higher-order assembly. Consistent with previous work, FtsZ itself formed relatively short filaments, which were cross-linked into higher-order assemblies. The morphology of these superstructures varied depending on the concentration of ZapD (Figure 7.1). Of particular interest are the observed toroids, which may relate to the native Z ring structure. Fluorescence correlation spectroscopy, among other techniques, was used to gain insight into biophysical properties of the interaction. The results will be summarized in the following.

7.1 Materials and Methods

Protein purification and labelling were carried out by A. Merino-Salomón following the methods described in reference [4]. Samples for FCS measurements were freshly prepared ca. 2 min before the start of the measurement. Each sample contained FtsZ and/or ZapD at varying concentrations, with one of the proteins doped with $100nM$ labelled protein (FtsZ-Atto488 or ZapD-Atto647N, respectively). Beta-casein-passivated coverslips were used to enclose the solution in coverslip sandwiches like those described in the protocol of Chapter 5.

FCS measurements were carried out on a PicoQuant MicroTime 200 confocal microscope equipped with a water immersion objective with correction collar (UPlanApo 60x NA 1.2, Olympus). Fluorescence from FtsZ-Atto488 or ZapD-Atto647N were excited with picosecond pulsed diode lasers operated at 483 nm or 636 nm, respectively. Laser pulse repetition rates were 20 MHz or 26.7 MHz, with average power in the order of $1 - 2\mu W$ at the objective back pupil. Detected photons were collected though suitable bandpass filters with transmission bands 520/35 or 670/90 and split onto two avalanche photodiodes (Excelitas SPCM-AQRH-14-TR) using either neutral 50/50 beam splitter or a polarizing beam splitter. Photon signals were digitized and time-tagged using a TimeHarp 260Nano TCSPC module (PicoQuant). Information on fluorescence lifetime obtained that way was used for data quality monitoring during measurement, and for automated background removal in computational post-processing (see Section 8.1.3). For some analyses, fluorescent bursts and other transient deviations in the ACF were automatically detected and removed using the tools described in Section 8.1.3, for other measurements this could be ignored. Exported ACFs are technically cross-correlation functions between the two channels (average of forward and backward cross-correlation). Fits were performed using the software tool described in Section 8.3, typically using a single discrete species approximation. Data shown in the publication [4] are based on earlier stages of development of these software tools, this section reports results obtained from re-analysis

with later software version, although the differences are small.

Time-resolved fluorescence anisotropy information concurrently acquired in some measurements did not reveal useful information beyond what was revealed by plate-reader based steady-state anisotropy assays with higher signal-to-noise ratio [4] and was therefore ignored in further analysis.

7.2 Results and Discussion

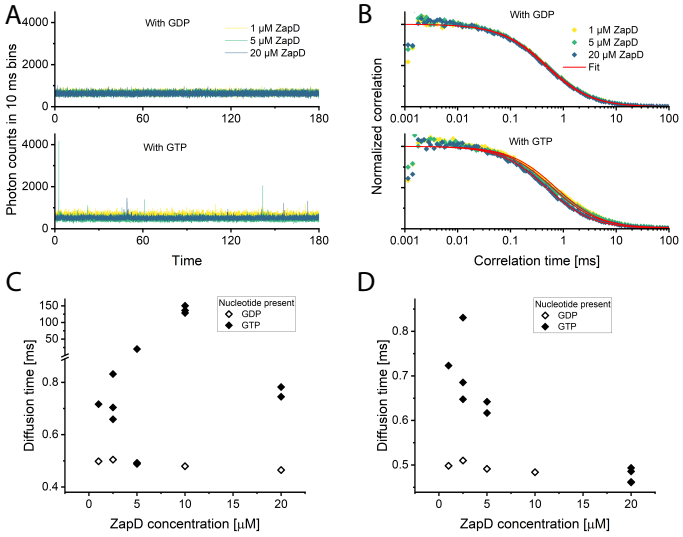

Figure 7.2. ZapD diffusion in presence of active and inactive FtsZ. $5\mu M$ FtsZ were mixed with varying concentrations of ZapD protein and $50\mu M$ of either GDP or GTP. **A**: Fluorescence time traces. Note the shift in mean intensity for ZapD concentration $\geq 5\mu M$ in presence of GTP, although the amount of added protein was kept constant. **B**: ACFs with single-component fits. **C**: Fitted average diffusion times. **D**: Same as C, but from data subjected to removal of fluorescent bursts.

For the insights of this study based on cryo electron microscopy, cryo electron tomography, and a few other complementary techniques, the reader is referred to the publication [4]. To complement the electron microscopy results, FtsZ protein and ZapD protein were mixed *in vitro* and diffusion kinetics were observed to confirm cross-linking. Cross-linking is expected to lead to an increase in effective particle size, and therefore diffusion time. An increase in average molecular brightness is also expected in pricinple, although the change may remain below noise levels given practical considerations (see below).

We first observed the dynamics of labelled ZapD protein in presence of FtsZ. Labelled ZapD should undergo a strong change in diffusion time when the ZapD dimer binds an FtsZ oligomer. $5\mu M$ FtsZ were mixed with ZapD at varying concentrations. Atto647N-conjugated protein was diluted in an excess of unlabelled ZapD, primarily to achieve correlation amplitudes suitable for high-quality FCS acquisition. The results are shown in Figure 7.2, with measurements performed both in the presence of GDP, and in the presence of GTP. Focusing on the fluorescence time traces in panel

A, two observations are made: Firstly, in presence of GTP and ZapD concentration $\geq 5\mu M$, fluorescent bursts are visible, confirming that the labelled ZapD gets incorporated into large particles which are absent without GTP and also at low ZapD concentration. This is also confirmed by an obvious shift in diffusion time in presence of ZapD and GTP visible in the ACFs shown in panel B.

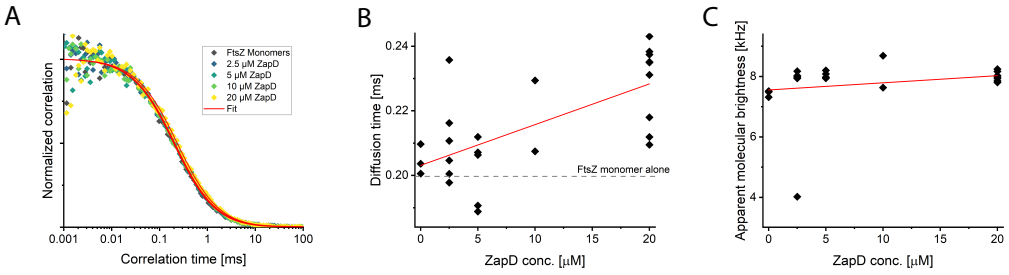

Figure 7.3. FtsZ diffusion kinetics with changing ZapD concentration. $5\mu M$ FtsZ were mixed with varying concentrations of ZapD protein and $50\mu M$ GDP. **A**: ACFs with single-component fits. **B**: Fitted average diffusion times. The diffusion time of the FtsZ monomer was measured in an independent batch, explaining the difference of the reference line from the mean at $0\mu M$ ZapD. The red line is an (unweighted, unconstrained) linear fit. **C**: Apparent molecular brightness over ZapD concentration with linear fit.

However, the ZapD concentration dependence of the diffusion time shift seems counterintuitive, with increasing ZapD concentration leading first to longer, then to shorter diffusion times (Figure 7.2 C). According to the assumed function of ZapD, one would expect higher ZapD concentration to lead to more cross-linking of FtsZ, and therefore monotonously longer diffusion time. This is explained by the second observation in panel A: The average count rate decreases in the presence of GTP and high ZapD concentrations. The reason is probably that while large cross-linked filament bundles did form, they rapidly grew to a size at which they precipitated. Thus, the measurement was strongly biased towards the still-mobile small particles, and this bias increased with increasing ZapD concentration. This is confirmed by an analysis in which bright bursts from large particles have been removed before autocorrelation function calculation. In that case, the fitted diffusion times, and hence apparent particle sizes, decrease practically monotonously with increasing ZapD concentration (Figure 7.2 D). This observation discouraged us from continuing measurements under GTP-containing conditions where FtsZ filaments were formed.

Turning to measurements performed with labelling of FtsZ itself, we found that when titrating ZapD into a mixture of labelled and unlabelled FtsZ ($5\mu M$ total), there was indeed a slight but visible ZapD-dependent increase in diffusion time (Figure

7.3). This may be surprising given that these measurements were performed in presence of GDP, not GTP. This demonstrates that binding of FtsZ and ZapD is not strictly dependent on FtsZ activation. However, as can be seen clearly in Figure 7.3, the signal to noise ratio of the results remained low, and diffusion time shifts small. We could not detect any notable shift in apparent molecular brightness either (Figure 7.3 C). This is due to the fact that labelled FtsZ-Atto488 was diluted in a 50-fold excess of unlabelled FtsZ. Considering that FtsZ did not form filaments under the conditions of the experiment, multivalently labelled oligomers made up only a negligible fraction of the particles observed, and thus average molecular brightness did not reveal any useful information.

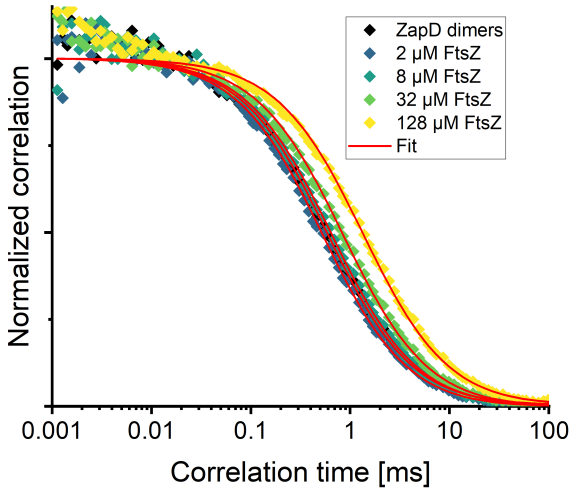

Figure 7.4. ACFs of ZapD in presence of FtsZ. $5\mu M$ ZapD were mixed with varying concentrations of FtsZ protein without additional nucleotide. ACFs were calculated without removal of fluorescent bursts, and fitted with single-component diffusion models. Blinking was ignored in these fits.

In the last set of experiments, we returned to observation of fluorescent signal from ZapD-Atto655. We observed the dynamics without addition of nucleotide, which due to the protein purification strategy corresponds to measurements in the presence of low GDP levels. When adding different amounts of FtsZ protein, we were able to obtain data of high signal to noise ratio that could easily be interpreted quantitatively (Figure 7.4). Fitting the data with a simple one-component model, we saw an increase in diffusion time that was well-described by a typical expression for steady-state binding kinetics (Eq. 2.15). We found an EC_{50} of $43.8 \pm 6.0\mu M$ for the binding of ZapD to FtsZ, although these values should be taken with caution as no clear saturation of binding at high concentrations is visible in the obtained data (Figure 7.5 A).

While the extrapolated diffusion time saturation of $1.6 \pm 0.1ms$ is quantitatively unreliable, the longest experimentally observed diffusion time at the higest FtsZ concentration of $128\mu M$ was $1.32 \pm 0.04ms$ (mean ± SD from 5 samples), three times longer than that of the ZapD dimer. In the approximation of a spherical particle following the Stokes-Einstein equation (Eq. 2.10), this would imply a ca. 80-fold dif-

ference in particle mass. As the other extreme, in a linear filament model (Eq. 2.11) one obtains an approximately 7-fold mass increase. It should be kept in mind that these numbers are firstly inaccurate as they are based on unrealistic particle shape descriptions and ignore the hetero-oligomer character of the FtsZ-ZapD assembly, and secondly biased towards large particles as they are derived from singles-species approximations (see Section 6). Nonetheless, they emphasize the formation of complexes that are far larger than the ternary complex of a ZapD dimer and an FtsZ monomer.

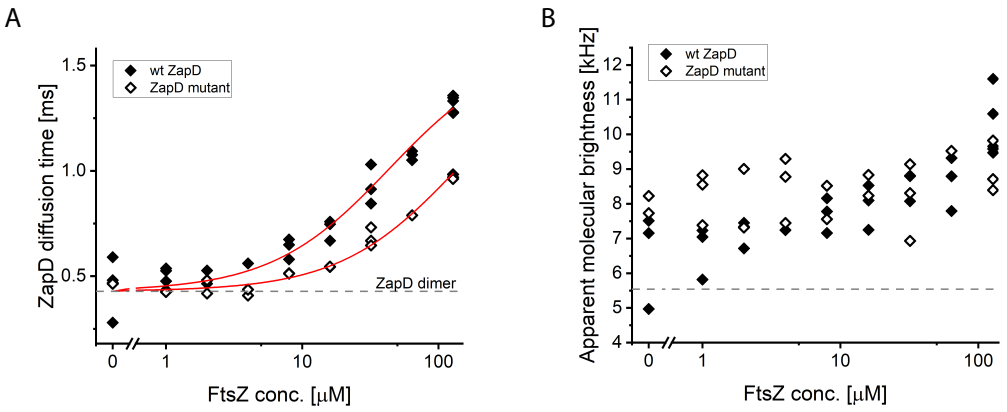

Figure 7.5. ZapD dynamics in presence of varying FtsZ concentration. $5\mu M$ ZapD were mixed with varying concentrations of FtsZ protein without additional nucleotide. Shown are (**A**) average diffusion times and (**B**) apparent molecular brightness determined from FCS analysis without removal of bright bursts. Fits in A are with an expression analogous to Eq. 2.15, with minimum diffusion time in absence of FtsZ fixed at $428\mu s$, and extrapolated maximum diffusion time fitted globally for both wt ZapD and ZapD mutant at $1.6 \pm 0.1ms$. For wt ZapD, the fit estimated an EC_{50} of $43.8 \pm 6.0\mu M$ and for ZapD mutant $138 \pm 17\mu M$.

In the same experiment, we also looked at a mutated variant of ZapD (Figure 7.5). This variant shows a partial defect in dimer formation due to a triple mutant in the homodimerization interface (R20A, R113A, H140A). As ZapD dimers are thought to cross-link FtsZ filaments by binding of each ZapD subunit to one FtsZ filament, the mutant is expected to be deficient in FtsZ cross-linking. Partial defects in this function were confirmed through various techniques such as turbidity measurements and analytical ultracentrifugation [4]. FCS analysis of this mutant showed a clear reduction in FtsZ binding, with an estimated EC_{50} of $138 \pm 17\mu M$ and an observed diffusion time of $972 \pm 11\mu s$ at $128\mu M$ FtsZ (mean ± SD from 3 samples). This more than 2-fold increase over the ZapD dimer diffusion time of $428\mu s$ still indicates higher-order complex formation, albeit with reduced efficiency.

7.3 Summary

We studied the self-assembly of FtsZ filaments and the effect of ZapD using fluorescence correlation spectroscopy and other techniques. Biochemically, the FCS results confirm the results of other techniques: ZapD binds directly to FtsZ, with increasing ZapD concentration leading to larger assemblies, far larger than what would be expected for a hypothetical oligomer of one ZapD dimer binding one FtsZ monomer. This remains true for the partially dimerization-deficiant mutant, but the apparent particle sizes are reduced. Notable here is the finding that the FtsZ-ZapD interaction does not require GTP. If ZapD can cross-link FtsZ proteins irrespective of their nucleotide state, this raises the question of how ZapD influences FtsZ treadmilling dynamics: Can it stabilize the GDP-bound decaying end? Can it prevent a GDP-bound monomer from diffusing away after release from a filament? Of course, due to the experimental challenges we did not quantify the affinity in to GTP-bound FtsZ, so the possibility remains that while the interaction with FtsZ-GDP is detectable, it is weak overall.

From a technical point of view, we compare results from different experiment designs that give some insight complementary to what is described in Chapter 6: We obtained more robust results if we labelled not FtsZ itself, but ZapD. Labelling the filament-associated protein rather than the filament-forming protein, and increasing the concentration of the latter, we created a contrast between a condition in which ZapD dimers were present to one in which the majority of the ZapD protein was recruited to FtsZ oligomers, possibly forming cross-linked higher-order assemblies. In contrast, when labelling FtsZ and titrating ZapD, we likely saturated the loading of FtsZ with ZapD, possibly even suppressing oligomerization. While ultimately both strategies of observation are viable, our experiments suggest that to obtain a yes/no answer to confirm or refute interaction, labelling the filament-associated protein is the better option for systems like the one studied here. Alternatively, one can of course label both and perform fluorescence cross-correlation spectroscopy, although the balance between higher-order structure formation and labelling efficiency is likely to complicate interpretation of such data.

8 Scientific software

While performing the work that has been described in the previous chapters, I developed or modified a number of software tools for scientific image analysis and time-resolved spectroscopy. The following sections describe the conceptual basis and some technical and applicative details of some of the more generic tools that are likely to be useful beyond the described projects. The tools described here are all available *via* GitHub.

8.1 Automated artifact correction in FCS

Fluorescence correlation spectroscopy (FCS) is a technique that can be used to measure many parameters that are of interest in biophysics, as discussed in previous chapters (see Section 2.7 and preceding Results and Discussion chapters). However, as was also mentioned in previous chapters, FCS is also notoriously sensitive to a number of different artifacts. These stem from a variety of different sources, some sample-related, some instrument-derived. Besides stemming from different sources, the artifacts common in FCS also differ in whether or not they can be detected and corrected based on the data alone, or not. A number of authors have contributed valuable ideas for automated suppression of specific artifacts whose presence can be determined from the raw data. This chapter reviews a non-exhaustive list of such artifacts, and describes the algorithms for highly automated suppression of these artifacts combined in the Python software tool "FCS_Fixer". The example figures shown throughout the chapter show plots automatically generated by the FCS_Fixer software during data processing, documenting the intermediate results of various processing steps. The dataset used is an example dataset from the experiments of FtsZ and ZapD binding described in Section 7. Figure 8.1 shows the example data without application of any filters. FCS_Fixer is now in routine use for FCS applications in the Department of Cellular and Molecular Biophysics at the MPI for Biochemistry, and is available via GitHub under https://github.com/Janhagenkrohn/FCS_Fixer.

8.1.1 Contributions

JHK conceived the software. **JHK** wrote the software with input from Yusuf Qutbuddin and Lise Isnel (LI). **JHK** and LI tested software on experimental data.

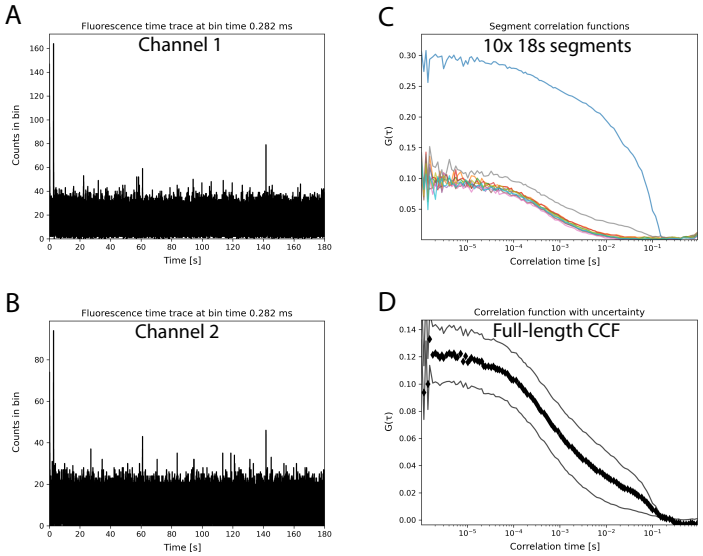

Figure 8.1. Correlation without data corrections applied. A, B: Raw fluorescence time traces for two channels in one measurement. The channels are largely equivalent for the purpose of the experiment, with signal being splitted by polarization. The bin width of $282\mu s$ was chosen automatically by the software. **C**: The three-minutes measurement is split into 10 segments of equal length, which are then individually cross-correlated between the channels to calculate the uncertainty (envelope in D) [237]. The segments also highlight the heterogeneity of the signal throughout the acquisition time. **D**: Cross-correlation function calculated from the full-length data. The large uncertainty and the seemingly biphasic decay again confirm the heterogeneity of the data that complicates analysis.

8.1.2 Software Concept

The overall design of the software is guided by the following principles:

- Automation: A number of data correction algorithms are provided to be usable with little user interaction beyond specifying the raw data to use. All correction methods are based on statistical criteria to adapt the processing parameters to the data, with hyperparameters chosen empirically to work satisfyingly on many datasets. Overriding the statistical methods for parameter choice is possible in many cases, although this will often require custom scripts. In addition, the tool is written for batch processing of many input files with the same parameters.

- Modularity: These different data corrections are implemented into a single common framework to allow using them in arbitrary combinations and sequence. For this reason, the software is built around the open-source package tttrlib [238] which offers many routines useful for this purpose. tttrlib also ensures compatibility with many formats of time-tagged time-resolved photon counting data (*e.g.*, PicoQuant .ptu format, Becker-Hickl .spc format, and others).

- Transparency: Results are automatically written into files at many intermediate steps of the processing in a manner that makes transparent for the human

user how the correction algorithms interacted with the data. The intermediate results are generally written in pairs of a figure in Portable Network Graphics (.png) format for visual inspection and corresponding numeric data in Comma-Separated Value (.csv) format for detailed inspection and further processing for example in spreadsheet calculation programs.

8.1.3 Artifacts and Correction strategies

BACKGROUND

Besides the fluorescence signal of interest, various kinds of background can corrupt the data. Some of these will exhibit their own characteristic time correlations, others appear uncorrelated in time. In general, the effect of background on the ACF is understood by revisiting the defition of the FCS ACF, decomposing the measured signal $F(t)$ into desired signal $F_{true}(t)$ and background $B(t)$:

$$G(\tau) = \frac{\langle F_{true}(t) F_{true}(t+\tau)\rangle}{\langle F_{true}(t) + B(t)\rangle^2} + \frac{\langle B(t) B(t+\tau)\rangle}{\langle F_{true}(t) + B(t)\rangle^2} \tag{8.1}$$

Uncorrelated background with negligible $\langle B(t)B(t+\tau)\rangle$ may originate for example from scattered laser light bleeding through the filters, or thermal dark counts of the detector. If the background fluctuates with characteristic time scales within the measurement window, $\langle B(t)B(t+\tau)\rangle$ may be significant. Such a situation can originate from various sources. In live cells, autofluorescence from flavins and other molecules can be significant [239]. In multi-color experiments like FCCS, spectral cross-talk between different fluorescent dyes is a frequent issue [162]. On the instrumental side, depending on the detector technology chosen, afterpulses can follow true photon detections with characteristic time delays [240].

Besides experimental optimization to suppress these and other background sources, correction methods for some of thesetypes of background are available in post-processing of the data. Different types of background require, and allow, different treatments.

For background that is uncorrelated on the time scales of interest, the second term of the righthand side of Eq. 8.1 is close to zero. In that case, the only distortion introduced by the presence of background is a reduction in the correlation amplitude (increased denominator in the $F_{true}(t)$ correlation term). In that case, one obtains [241]:

$$G(\tau) = \frac{\langle F_{true}(t) F_{true}(t+\tau)\rangle}{\langle F_{true}(t)\rangle^2} + \left(1 + \frac{\langle B(t)\rangle^2}{\langle F_{true}(t)\rangle^2}\right)^{-1} \tag{8.2}$$

Thus, one can correct the data to obtain the desired $G_{true}(\tau)$ with known $\langle B(t)\rangle$ and with $F(t) = F_{true}(t) + B(t)$:

$$G_{true}(\tau) = \frac{\langle F(t) F(t+\tau)\rangle}{\langle F(t)\rangle^2}\left(1 + \frac{\langle B(t)\rangle^2}{(\langle F(t)\rangle - \langle B(t)\rangle)^2}\right) \tag{8.3}$$

This background correction strategy works with measurement of $\langle B(t)\rangle$ through a control measurement without the fluorophore label of interest. However, it works well if and only if the background counts are uncorrelated on the time scales of interest, and it requires a reference for the background level. Therefore, it is not trivial to

perform in a fully automated manner, but it is simple to perform later on as it is only a correction to the correlation amplitude. Thus, it is not part of FCS_Fixer.

The is no general method to deal with fluctuating autofluorescence background, and one may have to analyze the ACFs based on explicit multi-component models using Eq. 8.1 with both $\langle B(t)\rangle$ and $\langle B(t)\,B(t+\tau)\rangle$ determined from reference measurements. However, often, autofluorescence stems from many dim particles rather than few bright ones, meaning that the amplitude of the background term in Eq. 8.1 may be small enough to allow a static-background approximation. Depending on what reference measurements are permitted by the experimental setup, such background may also be removed by fluorescence lifetime correlation spectroscopy (FLCS) unmixing, which is explained below.

Spectral cross-talk is another possible source of fluctuating background especially in multi-color experiments. It can be minimized *via* so-called Pulsed Interleaved Excitation (PIE) [242]. In the PIE scheme, picosecond- or nanosecond-scale pulsed lasers fire in an interleaved manner with fixed time delays, which is typically combined with the use of multiple detection channels. This allows extreme suppression of cross-talk by gating photons to be used in analysis in time and detection channel. All tools implemented in FCS_Fixer fully support the use of arbitrary user-defined PIE gating strategies. Weighting factors in some calculations that depend on fluorescence count rate or on duty cycle of observation are automatically adapted to the gating strategy used.

CORRELATED BACKGROUND FROM DETECTOR AFTERPULSES

Background from afterpulsing can be corrected using two strategies that are both implemented in FCS_Fixer. The first strategy solves Eq. 8.1 for the expression of afterpulsing [240,243]. The occurrence of afterpulses is a stochastic process, and generally, the probability for an afterpulse decreases with increasing lag time τ after the initial photon (if one ignores dead time effects). The lag time-dependent afterpulsing probability $\alpha(\tau)$ usually is described simply as a sum of exponentials:

$$\alpha(\tau) = \sum_i A_i \exp\left(-\frac{\tau}{\tau_{AP,i}}\right) \tag{8.4}$$

Note that here, $\alpha(\tau)$ is not defined as a normalized probability density function. Instead, the time integral yields the conditional probability $P_{AP} \leq 1$ of detecting an afterpulse at some time point after detection of a photon:

$$\begin{aligned} P_{AP} &= \int_0^\infty \alpha(\tau)\,d\tau \\ &= \sum_i A_i \tau_{AP,i} \end{aligned} \tag{8.5}$$

The ACF $G(\tau)$ in general is proportional to the number of correlated pulse pairs detected at a given τ. For afterpulsing, this number is just $\langle B(t)\,B(t+\tau)\rangle = \langle F_{true}(t)\rangle\alpha(\tau)$:

$$G(\tau) = \frac{\langle F_{true}(t)\,F_{true}(t+\tau)\rangle}{\langle F(t)\rangle^2} + \frac{\langle F_{true}(t)\rangle\alpha(\tau)}{\langle F(t)\rangle^2} \tag{8.6}$$

Considering $\langle F(t)\rangle = \langle F_{true}(t)\rangle + \langle F_{true}(t)\rangle P_{AP}$, this becomes:

$$G(\tau) = \frac{\langle F_{true}(t)\, F_{true}(t+\tau)\rangle}{\langle F(t)\rangle^2} + \frac{\alpha(\tau)}{\langle F(t)\rangle(1+P_{AP})} \tag{8.7}$$

Note that Eq. 8.4 defining $\alpha(\tau)$ contains all parameters in this model apart from the count rate $\langle F(t)\rangle$, which can obviously be determined automatically from the data. The parameters characterizing $\alpha(\tau)$ are fairly stable for a given detector if the conditions of operation remain stable. Therefore, $\alpha(\tau)$ be determined from calibration measurements that exhibit negligible fluorescence fluctuations on the time scale of afterpulsing and then repeatedly used for data correction for an extended period of time. Suitable for calirbation in practice are for example laser light backscattered or reflected at static structures, or fluorescence from slow-diffusing particles labelled with a negligibly blinking dye like lipid vesicles labelled with ATTO655.

FCS_Fixer performs afterpulsing correction based on Eqs. 8.4, 8.5, and 8.7 given a set of calibrated detector parameters for a biexponential approximation to Eq. 8.4, *i.e.*, four calibration parameters per detector. Figure 4C in Chapter 5 shows example measurements acquired at vastly different count rates before and after application of the afterpulsing calibration. At the lowest count rate (highest amplitude of the afterpulsing artifact, compare Eq. 8.7), the correction is not perfect, but clearly, under all conditions it strongly reduces the artifacts. Note that the detector parameters used in correction had been calibrated ca. two years before the measurement, confirming the stability of the calibration, at least for the detector model used here (Excelitas Technologies SPCM-AQRH series).

Correction of fluctuating background using fluorescence lifetime correlation spectroscopy

Afterpulse correction can also be performed using fluorescence lifetime correlation spectroscopy (FLCS) [244–246]. This strategy works for many kinds of uncorrelated background, and also for correlated background from ambient light and other sources that are unrelated to the (pulsed) excitation laser. When using TCSPC detection, such background appears as a flat pattern on the nanosecond time scale. Afterpulsing follows photon detection with a characteristic time delay and therefore is not truly independent from the excitation laser. However, the finite detection electronics dead time (usually tens of nanoseconds for classical TCSPC acquisition schemes) and the relatively long time scales of afterpulsing (up to microseconds) mean that on the nanosecond time scales inspected in TCSPC, it does mostly appear as a flat pattern independent from the laser. Thus, assuming that $F_{true}(t, i_\mu)$ stems from an excited state population that decays over nanosecond-scale (discrete) micro time i_μ with normalized pattern $p_F(i_\mu)$ while the corresponding background pattern $p_B(i_\mu)$ is flat over micro time, one can decompose $F(t, i_\mu)$ as:

$$\begin{aligned} F(t, i_\mu) &= F_{true}(t)\, p_F(i_\mu) + B(t)\, p_B(i_\mu) \\ &= F_{true}(t)\, p_F(i_\mu) + B(t)\, \frac{t_{\mu bin}}{t_{rep}} \end{aligned} \tag{8.8}$$

with TCSPC bin time $t_{\mu bin}$ and laser repetition time t_{rep}. Decomposing a measured $F(i_\mu)$ TCSPC dataset according to Eq. 8.8 is a simple task that can be per-

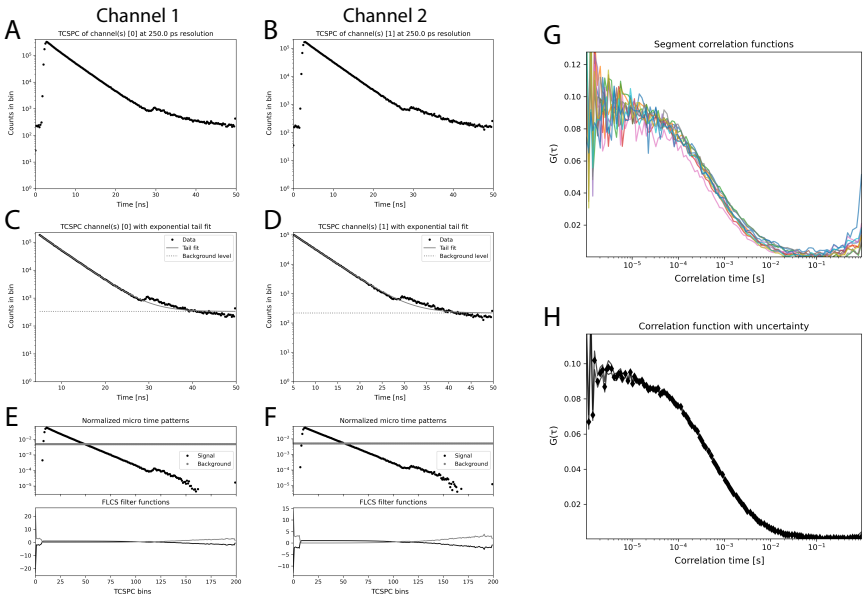

Figure 8.2. Background removal using FLCS. A, B: Raw channel-wise TCSPC histograms. The secondary peak at approx. $30ns$ stems from early afterpulses detected directly after the electronic dead time of the time tagging electronics. **C, D**: Tail fits approximate the backgroud level. In this case, the fit is slightly misled by the afterpulses, but suffices as a close approximation. **E, F**: Normalized signal patterns and FLCS filter functions calculated for signal and background, respectively. **G, H**: As background levels are relatively low in this example, the change in the correlation function is small. These figures are automatically generated by the software when running FLCS background correction.

formed for example *via* (Poisson-)weighted nonlinear regression. Technically, the TCSPC histogram is an integral of Eq. 8.8 over t, but assuming a stationary system to treat $F\left(t, i_\mu\right)$ and $F\left(i_\mu\right)$ equivalently is generally not an issue.

For automated FLCS-based background removal in FCS_Fixer, a tail fit with a monoexponential model for $p_F\left(i_\mu\right)$ is performed, by default using all data $\geq 2\ ns$ after the peak of the TCSPC data. This tail fit is used to estimate $B\left(t\right)$. $F_{true}\left(t\right)$ and $p_F\left(i_\mu\right)$ are then recalculated from the data by subtracting the determined $B\left(t\right)$.

Decomposing the data using Eq. 8.8 is in principle enough to perform a correction of uncorrelated background as mentioned above. However, FLCS goes one step further in use the knowledge of the all terms in Eq. 8.8 to resolve even fluctuating, correlated background, as encountered with afterpulsing. To this end, filter functions $f_F\left(i_\mu\right)$ and $f_B\left(i\mu\right)$ are constructed such that:

$$\begin{aligned} F_{true}\left(t\right) &= \sum_{i_\mu} F\left(t, i_\mu\right) f_F\left(i_\mu\right) \\ B\left(t\right) &= \sum_{i_\mu} F\left(t, i_\mu\right) f_B\left(i\mu\right) \end{aligned} \tag{8.9}$$

For calculating $f_F\left(i_\mu\right)$ and $f_B\left(i\mu\right)$ based on Eqs. 8.8 and 8.9, a convenient method based on matrix manipulations has been proposed by Enderlein and co-workers for photon counting data [247]:

$$f_k\left(i_\mu\right) = \left(\left[\hat{M} \cdot diag\left(F\left(i_\mu\right)^{-1}\right) \cdot \hat{M}^T\right] \cdot \hat{M} \cdot diag\left(F\left(i_\mu\right)^{-1}\right)\right)_{i\mu,k} \tag{8.10}$$

with index k iterating over signal contributions (true signal F or background B), matrix $\hat{M}$ containing the normalized TCSPC patterns $\hat{M}_{i_\mu,k} = p_k\left(i_\mu\right)$, and $diag\left(F\left(i_\mu\right)^{-1}\right)$ as diagonal matrix containing the inverse of the elements of the TCSPC histogram. When the "true fluorescence signal" filter function $f_F\left(i_\mu\right)$ is used for a weighted correlation function calculation, $G_{true}\left(\tau\right)$ is obtained:

$$G_{true}\left(\tau\right) = \frac{\sum_{i_\mu}\sum_{j_\mu}\langle F\left(t, i_\mu\right) f_F\left(i_\mu\right) F\left(t+\tau, j_\mu\right) f_F\left(j_\mu\right)\rangle}{\left[\sum_{i_\mu}\langle F\left(t, i_\mu\right) f_F\left(i_\mu\right)\rangle\right]^2} \tag{8.11}$$

In FCS_Fixer, FLCS is available in two ways. Firstly, the above-mentioned automated background estimation from TCSPC data is combined with calculation (Eq. 8.10) and application (Eq. 8.11) of FLCS filters to automatically correct background with flat TCSPC pattern. Note the use of this correction overwrites and replaces the use of calibration-based afterpulsing correction as explained above, to avoid overcompensation. Secondly, the user can supply the built-in functions with TCSPC patterns for signal and background for example from reference measurements or from multi-component analysis in other software tools, to determine species filters and use these to calculated cleaned-up ACFs corrected also for fluctuating background with non-flat TCSPC patterns. The latter is not automated and requires some custom high-level code, though.

SIGNAL BURSTS

Another common artifact in FCS are high-intensity "bursts" from large aggregates etc. [248–250]. Such bursts are a frequent observation in intrinsically polydisperse systems. Chapter 6 contains a rather detailed discussion of the phenomenon, and why it is an issue in FCS, which will not be repeated here. As mentioned in Chapter 6, multiple strategies for automated correction are available, including Deep Learning-based tools [250]. FCS_Fixer uses a relatively simple strategy which is based on heuristic traditional statistics, but that we found to yield useful results on a broad variety of input data.

For this data correction, a fluorescence time trace needs to be constructed. In FCS_Fixer, the bin width of the time trace is automatically chosen in an attempt to represent data from vastly different fluorescence count rates meaningfully without user intervention (Figure 8.3 A). To this end, first, an ACF is calculated from the uncorrected photon counts, and force-fitted with a two-component three-dimensional diffusion model (see Eqs. 2.26 and 2.30, nelgecting the impact of particle brightness brightness ε). If the two component fit fails for some reason, a single-component model is used instead. A (discrete) fluorescence time trace $F\left(i\right)$ is then constructed from the data with the smallest bin width t_{bin} that fulfils three criteria:

- $t_{bin} \geq \tau_{diff}$ with τ_{diff} from the diffusion fit (in the case of a two-component model, the shorter of the two τ_{diff} is used)

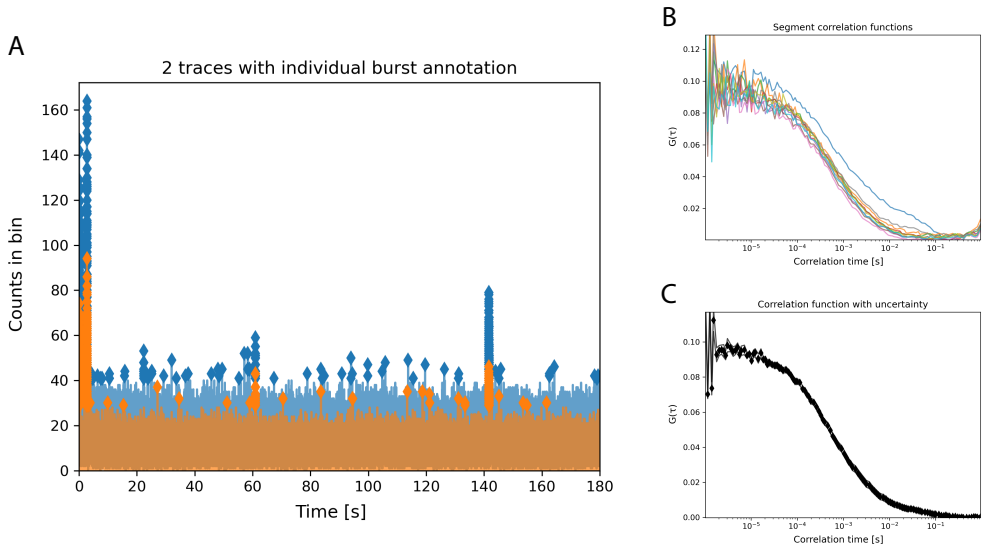

Figure 8.3. Removal of fluorescent bursts. Compare Figure 8.1. **A**: Fluorescence time traces with annotation of fluorescent bursts (diamond symbols). For cross-correlation function calculation, a logical OR operation is applied to discerd time points in which either of the two fluorescence channels was annotated as "burst". **B**: The segment correlation functions now exhibit much smaller, albeit still significant, distortions. **C**: The full-length cross-correlation function looks almost like that of a single species, except for a slight additional conpoment on the scale of tens of milliseconds. These figures are automatically generated by the software when running burst removal.

- t_{bin} is long enough such that $\langle F\,(i)\rangle \geq 10$ photons or another, user-defined lower bound
- $t_{bin} \geq 100\ \mu s$ or another, user-defined lower bound

The use of criterion 1 can also be switched off by the user in case it does not perform robustly on the data at hand. In the next step, the fluorescence time trace needs to be binarized into "burst" and "non-burst". To this end, a simple cutoff number of photons T_F per bin is applied:

$$\begin{aligned} F\,(i) > T_F &: bin\ i\ is\ burst \\ F\,(i) \leq T_F &: bin\ i\ is\ not\ burst \end{aligned} \tag{8.12}$$

T_F could in principle be chosen by the user, but we opted for a strategy that choses the threshold based on a statistical criterion inspired by statistical hypothesis testing. The reasoning here is to consider the data as essentially a two-species mixture consisting of a baseline fluctuating at a relatively low intensity, which contains the signal of interest, and of occasional unwanted high-intensity bursts. Then, given an approximate description of the distributions of photon counts per bin (effectively the photon counting histogram PCH [192]) in the baseline, one can calculate a confidence interval for deciding whether or not a given photon count stemming from the baseline

signal is plausible. The challenge here is to construct such a description of the baseline PCH without contributions from the high-intensity bursts.

We opted to combine moment statistics-based description with a quantile statistics-based description. Specifically, we assume an approximately Gaussian distribution in the baseline PCH. The Gaussian distribution is clearly inaccurate, especially at low numbers of bright particles, but works well enough for the intended purpose. The Gaussian distribution has two parameters of interest: The mean μ_G and the standard deviation σ_G. These are then obtained by assuming that the observed median of the time trace approximates μ_G, and the 84th percentile of the time trace approximates $\mu_G + \sigma_G$, as would be the case for a truly Gaussian distribution. That way, the brightest 16 % of $F(i)$ are ignored, making this approach outlier-resistant while still considering the majority of the data.

Next, to obtain T_F from the Gaussian approximation, a false-positive burst detection probability α_T is considered. α_T is adjusted from the set target $\alpha_{T,set}$ for the number of bins n_{bins} in trace $F(i)$ to attenuate effects from different bin sizes (bin numbers, equivalently) using Šidák's method:

$$\alpha_T = 1 - (1 - \alpha_{T,set})^{\frac{1}{n_{nbins}}} \tag{8.13}$$

Note that the actual false-positive burst detection probability is much higher than α_T, even with Šidák's correction, as the PCH has a more pronounced tail towards high photon counts than the Gaussian approximation. Thus, the algorithm will over-threshold most datasets and annotate more bursts than required. Some degree of over-thresholding is intended, as false-positively discarding a handful modest fluctuations leads to smaller distortions of the ACF than false-negatively ignoring a burst does. The default is $\alpha_{T,set} = 0.02$, but this value can be adapted by the user, where a higher value means higher sensitivity in burst detection, but also increased signal loss due to false-positive thresholding.

With the Gaussian described by μ_G and σ_G and the corrected false-positive burst detection probability α_T determined, T_F can now be calculated by inverting the complementary error function of a standard normal distribution $erfc^{-1}$:

$$T_F = \mu_G + \sigma_G \, erfc^{-1}(\alpha_T) \tag{8.14}$$

After thresholding and burst annotation, the bursts are excised and updated photon arrival times are calculated to close the gaps left by excision to avoid artifacts from sudden intensity drops. Figure 8.3 B and C in comparison to Figure 8.1 C and D show the impact. Note that "excising" bursts does not refer to discarding of photons, but rather creation of a Boolean mask of which photons to keep and which not, meaning that the process is reversible in calculation, should that be required. Similarly, the updated time tags are a corrected copy, while the original data remains unaltered, facilitating for example multiple subsequent analysis runs on the same data. This may for example be of interest for FCCS applications where only one channel is prone to exhibiting bursts, in which case different burst removal masks may be used for the channel-wise ACFs and the cross-correlation function.

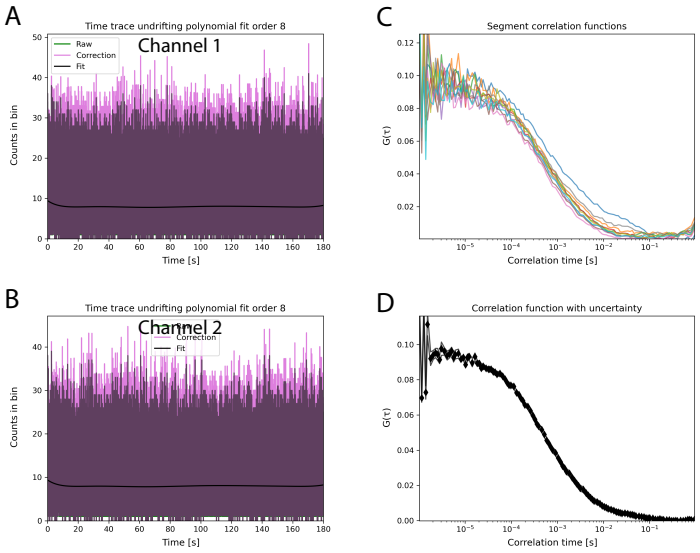

Figure 8.4. Correction of bleaching (insignificantly affected dataset) Compare Figures 8.1 and 8.3. Note that the example dataset does not show significant bleaching dynamics. A more severly impacted dataset is found in Figure 4 of Section 5. **A, B**: Fluorescence time traces with polynomial fits, and after correction. Due to the absence of bleaching, the change is small. **C, D**: The segment correlation functions and full-length cross-correlation function show no added distortions despite use of an unnecessary "overcorrection". These figures are automatically generated by the software when running bleaching correction.

BLEACHING

Photobleaching can distort FCS data in two ways, as discussed in more detail Chapter 5 and in Section 8.2. Here, we are interested in the continuous decrease of fluorescence intensity due to depletion of molecules. This effect is especially pronounced when measuring in confined volumes like cells or giant unilamellar vesicles, when observing slow-diffusing particles, and when using high-power excitation. Under such conditions, the average fluorescence intensity drops over time. The process under study is then no longer stationary, and the ACF is distorted especially at long time scales. It should be noted that when dealing with such bleaching artifacts, the brightness of individual molecules remains the same, only the number of molecules is no longer stationary. Figure 8.4 shows an example of the automatically generated figures of the bleaching correction performed by FCS_Fixer on a dataset weakly affected by bleaching. Figure 4 B in Chapter 5 shows correction results of more severely affected ACF examples.

As a first step of the practical implementation of bleaching correction in FCS_Fixer (based on [189]), a fluorescence time trace $F(i)$ is constructed using the same strategy as described above for the burst removal, including the same automatic bin width choice. This trace is subsequently fitted with a series of simple polynomial models:

$$F_{model}^{(k)}(i) = a_0 + \sum_{m=1}^{k} a_m t_i^m \tag{8.15}$$

with polynomial degree $k \leq 10$, discrete time t_i, and polynomial coefficients a_m. Each fit is perfomed as a weighted least-squares minimization with weights based on an assumed Poisson distribution of photon counts per bin. k is incrementally increased up to the maximum of 10, or until two consecutive increments in k did not increase the goodness of fit as judged based on F-tests with significance threshold $\alpha_{F-test} = 0.05$. This procedure allows the model for $F^{(k)}_{model}(i)$ to adapt flexibly to data with arbitrary bleaching kinetics by using relatively high k where needed, while generally avoiding overfitting by limiting k to what is statistically justified. Note that the example shown in Figure 8.4 is fitted with a relatively high-degree (8) polynomial, which did not introduce notable distortions either.

Other approaches for generating $F^{(k)}_{model}(i)$ not implemented in FCS_Fixer include models using (multi-)exponential decays or smoothing operations using for example Gaussian kernel filters. Exponential models are physically better justified than a polynomial model, but less generic in adapting to arbitrary date. We decided to prioritize a generic nature of the model. Kernel filter smoothing has the disadvantage that the filter acts locally over a characteristic user-defined time scale, and therefore may distort the ACF at those time scales.

With the fitted model $F^{(k)}_{model}(i)$ at hand, the bleaching kinetics in the time trace $F(i)$ can be compensated. In FCS_Fixer, this is done on a single photon basis. The expression for that is:

$$f_{bleachcorr}(t) = \sqrt{\frac{F^{(k)}_{model}(0)}{F^{(k)}_{model}(t)}} + \left(1 - \sqrt{\frac{F^{(k)}_{model}(t)}{F^{(k)}_{model}(0)}}\right) \tag{8.16}$$

where $f_{bleachcorr}(t)$ are photon-wise weights calculated based on analogous to those obtained through Eq. 8.10. They can be used to calculate corrected ACFs like in the same manner as those of FLCS (Eq. 8.11).

Using FLCS and bleaching correction simultaneously is also possible by following a pipeline of:

1. Calculate a bleaching correction
2. Construct a bleaching-corrected TCSPC histogram by summing $f_{bleachcorr}$ rather than counting photons
3. Calculate FLCS filter functions from the bleaching-corrected TCSPC histogram
4. Calculate ACF using Eq. 8.11, using the product of FLCS weights and bleaching correction weights as effective photon weights

This pipeline is automatically performed as part of the default pipeline in FCS_Fixer processing if both bleaching correction and FLCS correction are activated at the same time.

FOCUS DRIFT AND MEMBRANE UNDULATIONS

A different experimental scenario that can yield non-stationary $F(t)$ very similar to the effect of bleaching occurs if tries to measure on a membrane that is not static during the measurement time [251]. Membrane undulations will also lead to changes in

average fluorescence intensity over time, and these will distort the ACF in hard-to-predict ways. This effect is particularly strong in live cells that often actively move their plasma membrane as part of normal cell mobility. However, it is also often an issue even when measuring on stable membranes without active dynamics as thermal drift in the microscope hardware and the sample can move the focus in unwanted ways. The strategy used for bleaching correction in FCS_Fixer also works well for straightening out such drift dynamics and suppressing the resulting artifacts in the ACF. It should be kept in mind though that the correction is not entirely accurate as it makes the assumption met by bleaching dynamics that the number of molecules changes while the molecular brightness does not. Thus, in this case the correction can often be used to correct fitted correlation times (although some bias will remain [252]), but should be used with a lot of caution when it comes to analysis of correlation amplitudes.

OTHER NON-STATIONARY DYNAMICS

FCS_Fixer contains another correction algorithm that is designed to generically deal with temporary anomalies in the observed dynamics, proposed by Ries and co-workers [249] and implemented in FCS_Fixer with minor adaptations. The algorithm splits the photon data into a number of segments and calculates a segment ACF $G_i(\tau_k)$ for each segment i (with discrete lag times τ_k). The default segment length is 1/10 of the total acquisition time, or 5 times the longest queried correlation time, whichever is longer. The shortest correlation time queried in this correlation operation is 100 μs by default, to avoid noisy short lag times that would distort the results.

Then, the algorithm iteratively determines how consistent the segment ACFs are with each other:

1. Iterating over i, compare each $G_i(\tau_k)$ to the average of all other segments $\bar{G}(\tau_k) = \frac{1}{i_{max}-1}\sum_{j=1}^{i_{max}} G_{j\neq i}(\tau_k)$
   (a) Optional, used by default: Find a linear scaling factor a to minimize the sum of squared deviations $\sum_{k=1}^{k_{max}}\left(aG_i(\tau_k) - \bar{G}(\tau_k)\right)^2$. The purpose of this step is to emphasize ACF shape deviations rather than amplitude changes.
   (b) For each $G_i(\tau_k)$, store mean-square error $MSE_i = \frac{1}{k_{max}}\sum_{k=1}^{k_{max}}\left(aG_i(\tau_k) - \bar{G}(\tau_k)\right)^2$
2. Discard the segment with the highest MSE_i, storing information about i and MSE_i
3. Repeat steps 1 and 2 with the remaining segments, until only two segments are left
4. Find the smallest MSE_{min} at which a segment was discarded at step 2, obtain a threshold mean-square error $MSE_T = 2.5\ MSE_{min}$ where the scaling factor can be changed by the user
5. Identify the last-discarded segment that was discarded with $MSE_i \geq MSE_T$, label this and all earlier-discarded segments as segments to excise
6. Excise segments and collapse the gaps analogously to the excision of signal bursts described above

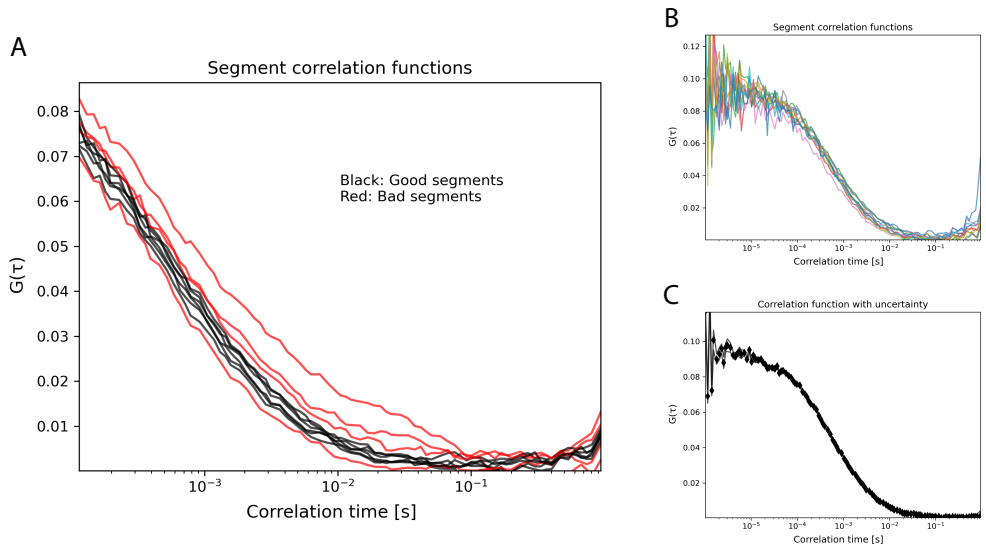

Figure 8.5. Removal of other artifacts affecting the correlation function. Compare Figure 8.1 to 8.4. **A**: Segment correlation functions are overlaid and color-coded to indicated which segments passed the filter, and which were discarded. **B**: The segment correlation functions recalculated after removal seem essentially stationary now. Note that the total duration of the measurement is shortened after discarding 4 out of 10 segments, and thus the 10 segments are now 6 seconds long each. Therefore, correlation function distortions at long lag times appear more pronounced than before that stem from the correlation function calculation itself [253]. **C**: The artifact that was still seen on the $100ms$ time scale in Figure 8.3 C is now gone. As the full-length correlation function is calculated from a concatenated long time trace, rather than as the average of the curves in panel B, it does not show significant artifacts from the shortening. These figures are automatically generated by the software when running removal of segments with anomalous correlation function.

This routine can be used towards the end of a processing pipeline as one more method to identify and remove artifacts that the other algorithms that are based on inspection of the fluorescence time trace and TCSPC histogram representations of the data did not pick up.

8.1.4 Summary

FCS_Fixer is a tool that allows extracting high-quality FCS data from raw data of varying quality. It automates correction of background, afterpulse correlation, signal bursts, bleaching, and other temporary distortions of the correlation function, in most cases performing well without any user input. In addition, the software leaves open interfaces for custom scripts that modifiy the data pipeline. It serves as a routine tool for relaxing the data quality requirements on the experiment side, in order to facilitate analysis of experimentally challenging systems.

8.2 Automated FCS at lipid membranes using z-scan FCS

As mentioned in section 8.1 about artifacts in FCS and their software-based correction, membrane undulations or focus drift are a serious concern when performing FCS measurements on lipid membranes such as supported lipid bilayers or giant unilamellar vesicles. FCS is a frequently-used technique to characterize molecular mobility or concentrations within membranes. However, motion of the membrane relative to the observation volume introduces a change in overall fluorescence intensity. This change in intensity has a number of effects that impact essentially all parameters to be estimated in FCS, and it introduces an additional slow time scale into the observed ACF [251, 252].

In fact, when performing FCS on membranes, another issue complicates the measurements, even if the relative positions of membrane and observation volume are stable: The point spread function, and thus the observation volume, is not actually the three-dimensional Gaussian ellipsoid that is frequently used as approximation in calculations (Figure 8.6). It is rather hourglass-shaped. Displacing a membrane that is oriented in the xy plane away from the waist of the observation volume along the optical axis (z) will therefore lead not only to decreased molecular brightness, but also increase the membrane area probed by the measurement. In the approximation of Gaussian beam propagation, the change in the observation area over z position, proportional to the square of the local beam radius $w(z)$, is a parabola [39]:

$$\begin{aligned} I(r,z) &= I_0 \frac{w_0^2}{w(z)^2} \exp\left(-\frac{2r^2}{w(z)^2}\right) \\ w(z)^2 &= w_0^2 \left(1 + \left(\frac{\lambda_{laser} z}{\pi n w_0^2}\right)^2\right) \end{aligned} \tag{8.17}$$

where $r^2 = x^2 + y^2$ characterizes the displacement from the beam axis. Even small displacements of the observation volume from the beam waist can lead to significant distortions of the data, and due to the symmetry of the parabola along z, this artifact not only is an added source of random noise, but it biases the data towards apparently reduced molecular brightness, increased concentration, and reduced diffusion coefficients [252, 254].

A few strategies have been proposed to deal with this issue. These strategies have in common that they introduce an additional length scale besides the point spread function size into the measurement. Examples are dual-focus FCS where two observation volumes are placed at a known distance [180, 181], pair correlation function analysis as a generalization of the dual-focus FCS concept [182], and scanning FCS techniques that move the observation volume in a known scan pattern [218]. All these have intrinsic length scales that negligibly change with defocus from the membrane. Therefore, by concentrating on motion over these known scales in analysis, these techniques allow suppressing the effect of defocus on membrane FCS.

Another powerful but simple strategy is z-scan FCS [252, 257, 258] (Figure 8.7). In z-scan FCS, a series of conventional single-spot FCS measurements is performed at the same position within the xy plane perpendicular to the optical axis, but at varying z positions. The reasoning is that when using a suitable model describing the change

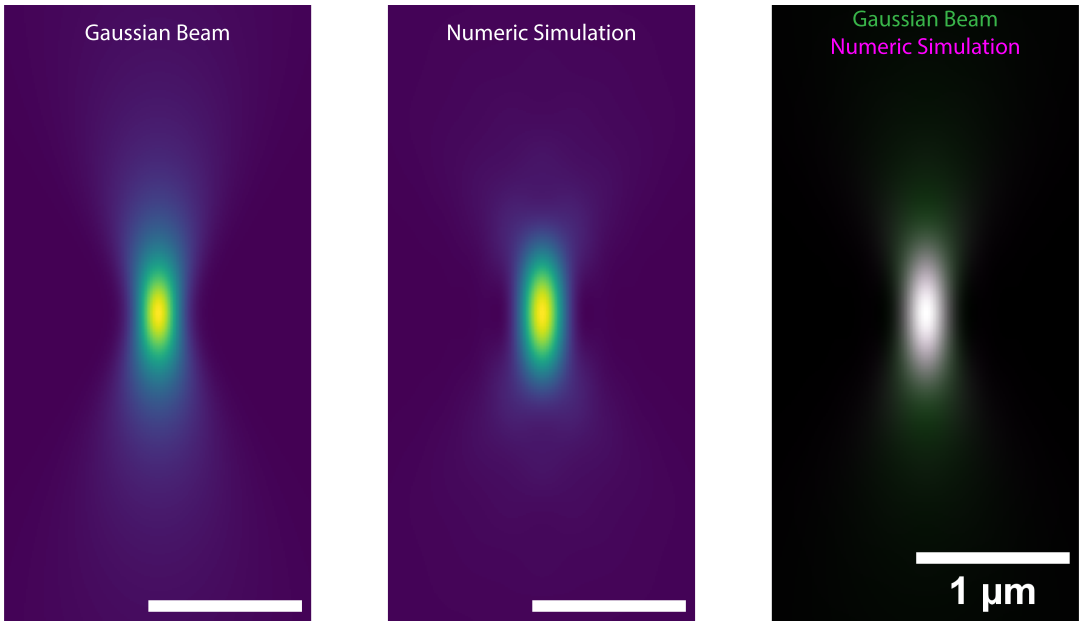

Figure 8.6. Point Spread Function Models. Shown are calculations of theoretical Point Spread Functions for a 488 nm laser and an objective with $NA = 1.2$ in water ($n = 1.34$) using either a Gaussian beam model (left, Eq. 8.17), or a numeric integration scheme suited for simulation of high-NA illumination (middle, [40,41]). The numeric simulation was calculated using MATLAB code written by Kareem Elsayad, modified by Hannah S. Heil and by me (Katrin G. Heinze lab, IMP Vienna and University of Würzburg) [255,256]. In the right, an overlay is shown to highlight differences.

of the observation area over z position, such as the above-mentioned Gaussian beam propagation approximation, one can link the subsequent measurements over z to essentially interpolate the "true" values at optimal focus positioning from a fit.

Strengths of z-scan FCS are the high signal to noise ratio that can be achieved even at low laser powers in contrast to scanning FCS approaches that suffer from a relatively low duty cycle of observation, and the relatively simple execution at many FCS-ready confocal microscopes. Additionally, at least in theory, z-scan FCS with data analysis using the Gaussian beam propagation model allows calibration-free analysis, as the beam divergence determines the beam waist diameter w_0 (see Eq. 8.17). As the beam divergence can be estimated from z-scan FCS data (from the changes of apparent diffusion time and particle number over z), so can w_0. Therefore, the data can be directly interpreted in terms of the diffusion coefficient $D = 4w_0^2/\tau_{diff,0}$ with diffusion time at the beam waist $\tau_{diff,0}$. In practice, due to possible mismatch between theory and experiment, for example due to spherical aberration, it may be better to interpret $\tau_{diff,0}$ in terms of a previously calibrated w_0. In that case, z-scan FCS still helps avoid artifacts from defocus.

8.2.1 Contributions

JHK and Yusuf Qutbuddin (YQ) conceived the workflow and software. **JHK** established the experimental workflow. **JHK** wrote the software with contributions from YQ.

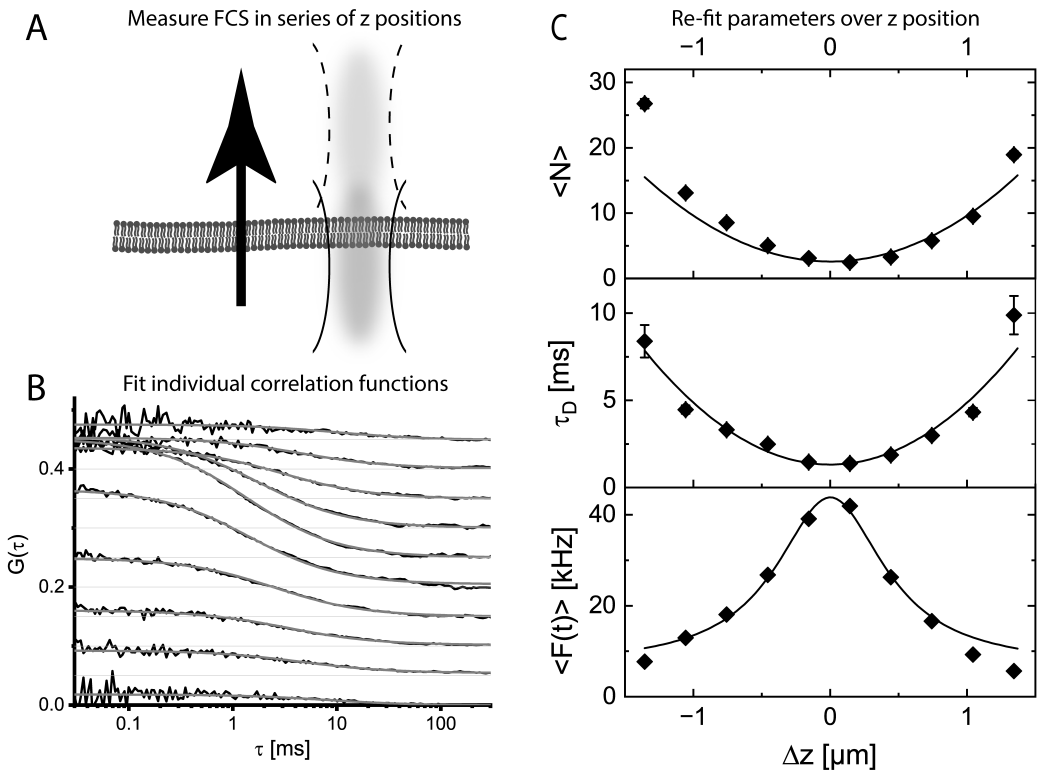

Figure 8.7. z-Scan FCS. A Schematic illustration of z-scan acquisition concept. A series of single-spot FCS acquisitions is performed at different focus depth around the membrane. **B** Each single-spot measurement is correlated and the resulting ACF fitted with a 2D diffusion model (Eq. 8.18). Example data is from a GUV (lipid mole fractions 7 DOPC : 3 DOPG : 10^{-4} Atto565-DOPE; prepared *via* swelling on PVA [259]). ACFs are shown with added offsets for clarity. **C** Re-fitting of parameters determined from individual fits to Eqs. 8.19 where $\Delta z = z - z_0$. In this example, the fitted key parameters were $w_0 = 0.283 \pm 0.018\ \mu m$, $\tau_{diff,0} = 1.32 \pm 0.29\ \mu ms$, $\langle N_0 \rangle = 2.60 \pm 0.19$, and $\varepsilon = \langle F_{max} \rangle / \langle N_0 \rangle = 16.8 \pm 1.6\ kHz$.

8.2.2 Software Concept

We developed a robust workflow for z-scan FCS for use at the Zeiss LSM980 confocal microscopy platform that is currently frequently used for FCS in the Department of Cellular and Molecular Biophysics at Max Planck Institute of Biochemistry. Some steps in the workflow use custom software, which is publicly available under https://github.com/Janhagenkrohn/z_Scan_FCS. The software consists of four separate scripts of which in principle at least three could be joined into a single one. While this may seem inconvenient, it was a conscious design choice to keep the software modular and interoperable with other tools used in our and other labs for related applications through writing of intermediate files in common formats (in particular, exporting ACFs into, and importing them from, csv files in the format for "Krisine" software [163, 260] also used by the other tools described in this Chapter). The software is built to strip away most of the complex manual interventions in z-scan FCS acquisition and analysis, allowing the experimenter to focus on the dynamics to be measured rather than the details of the experimental process.

8.2.3 Workflow and Software

Acquisition

The first step after localizing the sample is the acquisition of a single reference image of the region of interest in conventional confocal microscopy. This is no different from common workflows for performing conventional single-spot FCS in samples where positioning of the observation volume is critical, such as live cells or giant unilamellar vesicles [8, 261].

The second step uses the tool for definition of points of interest that is built into the ZEISS ZEN software for operating the microscope is then used to select one or multiple points in the xy plane to measure. The user then targets all previously defined positions and updates the z-position associated with each xy position as close as possible to the intensity maximum. This is most conveniently done using the "Verify" tool in the ZEN graphical user interface.

A custom Python script written for use as macro in ZEN software is used next. The macro defines a series of z positions around each specified point of interest, where the previously defined reference point becomes the center point of the z-scan. The user can choose three parameters: The z spacing between points within a z-scan is typically set in the range of 200 nm to 300 nm. Denser sampling increases robustness of the analysis, but also increases measurement time and photodamage to the sample. The range of the z-scan, typically 1.5 µm to 3 µm, is a trade-off between on the one hand the capture range over which the z-scan re-analysis will find the beam waist, and on the other hand measurement time. Using a large z-scan range, and therefore capture range, is particularly useful if many xy positions are to be targeted in a single automated measurement run. In that case, using a large z-scan range increases robustness against slow thermal drift. Finally, the user can choose the scan pattern, where they have a choice between scans from the bottom upward or from the top downward, as well as more unusual scan patterns that are rarely used. The macro also writes a csv file that records metadata about each single measurement (*i.e.*, every xyz position) that is needed for analysis later.

Once all positions have been defined, automated execution all the full set of measurements can be started. The workflow allows in principle an arbitrary number of xy positions to be targeted in a single automated measurement run, and the positions need not strictly be within a single confocal scan field of view. For practical purposes, we find that usually up to ca. 10 xy positions can be measured in a single measurement run under typical conditions, limited typically by evaporation of immersion water.

Data Analysis

ACFs are calculated from raw photon arrival time data using custom software written in MATLAB. The correlation script is conceptually similar to the automated artifact correction software ("FCS_Fixer") described in section 8.1, but adapted to the raw data format of the LSM980 platform. Out of the corrections implemented in FCS_Fixer, only calibration-based afterpulsing correction and bleaching/drift correction are implemented as the ones that we found to be most significant for our z-scan FCS applications. There is no link between successive measurements in a z-scan at

this point of data analysis. Otherwise, the calculations underlying data correction and ACF calculation are comparable to those described in the corresponding subsections of Section 8.1.

After calculation and export of ACFs, a custom Python script is used to fit the ACFs individually. A few models are available. The most useful one in many applications is the model for two-dimensional diffusion in a Gaussian observation area, with an arbitrary offset G_∞ to the ACF:

$$G(\tau) = \frac{\gamma}{\langle N \rangle} \frac{1}{1 + \frac{\tau}{\tau_{diff}}} + G_\infty \tag{8.18}$$

with shape factor $\gamma = 0.5$. The script is written to recognize, and iterate over, all ACFs within one measurement series with little user input beyond one or multiple directories to search for ACFs, and a naming pattern by which to recognize the files to use. The fit results from all individual ACFs are compiled into a single table for further analysis and written into a csv file.

In the final step of the analysis, the z-scan data is re-analyzed to exploit the added information provided by the z-scan. To this end, another custom Python script is used that uses the metadata file written earlier together with the ACF fit results to first sort all data as required, separating the data associated with different z-scans within one acquisition series. If the measurement consisted of multiple z-scan FCS acquisitions performed at different positions, the software will analyze all of them sequentially. For each z-scan, a global fit of three parameters over z position is performed:

$$\begin{aligned} \langle N(z) \rangle &= \langle N_0 \rangle \left(1 + A_P (z - z_0)^2\right) \\ \tau_{diff}(z) &= \tau_{diff,0} \left(1 + A_P (z - z_0)^2\right) \\ \langle F(z) \rangle &= \langle F_{min} \rangle + \frac{(\langle F_{max} \rangle - \langle F_{min} \rangle) A_L}{(z - z_0)^2 + A_L} \end{aligned} \tag{8.19}$$

where $\langle N(z) \rangle$ and $\tau_{diff}(z)$ are taken from the fits with Eq. 8.18, while $\langle F(z) \rangle$ is the average fluorescence count rate in each measurement. A_P is a scaling factor for the parabolas which is expressed through, and initialized at, a theoretical value combining the Abbe resolution limit as estimate for the beam waist diameter w_0 with a Gaussian beam propagation (compare Eq. 8.17):

$$\begin{aligned} A_{P,theory} &= \left(\frac{\lambda_{laser}}{\pi n w_0^2}\right)^2 \\ &= \left(\frac{4NA^2}{\pi n \lambda_{laser}^2}\right)^2 \end{aligned} \tag{8.20}$$

with refractive index $n \approx 1.34$ and objective numerical aperture NA. w_0, and through it A_P, is fitted to the data rather than fixed at the theoretical value to accommodate deviations between theory and experiment, such as deviation from Gaussian beam propagation (Figure 8.6) and aberrations. A_L is a similar to A_P, but serves as

half-width parameter for the Lorentzian peak function used for $\langle F(z)\rangle$, and is also fitted freely (initialized at 1 μm^2).

The parameters $\langle N_0\rangle$, $\langle F_{min}\rangle$, $\langle F_{max}\rangle$, z_0, A_P, w_0, and D are optimized by a global fit of all three observables to minimize:

$$\begin{aligned} COST = \sum_i & \left(\frac{\langle N_{model}(z_i)\rangle - \langle N_{data}(z_i)\rangle}{\sigma_{N,i}} \right)^2 \\ & + \left(\frac{\tau_{diff,model}(z_i) - \tau_{diff,data}(z_i)}{\sigma_{\tau,i}} \right)^2 \\ & + \left(\frac{\langle F_{model}(z_i)\rangle - \langle F_{data}(z_i)\rangle}{\sigma_{F,i}} \right)^2 \end{aligned} \tag{8.21}$$

where uncertainties $\sigma_{N,i}$ and $\sigma_{\tau,i}$ are, if possible, directly retrieved from uncertainties in the fits of individual ACFs. In case this information is not available, as a backup the software will assume $\sigma_{N,i} = \langle N_{data}(z_i)\rangle$ and $\sigma_{\tau,i} = \tau_{diff,data}(z_i)$. For the fluorescence count rate, $\sigma_{F,i} = \sqrt{\langle F_{data}(z_i)\rangle t_{ac}}$.

Often, the fitted parameters do not follow the model well at larger z displacements from the beam waist (Figure 8.7 C), which is not surprising given the limited accuracy of the Gaussian beam model (Figure 8.6). Thus, the model is best applied to a limited data range around the center position z_0. For that reason, the software automatically performs a series of fits to determine an optimal data range to use. After fitting the full set of data points, the data point that is furthest away from the current estimate for z_0 is discarded. Then, the remaining data points are used for a new fit, another data point far from z_0 is discarded, and the procedure is repeated until only five z positions are left, which is treated as the minimum data range. For each of these fits, the sum of relative uncertainties U of all fitted parameters is calculated:

$$U = \frac{\sigma_{\langle N_0\rangle}}{\langle N_0\rangle} + \frac{\sigma_D}{D} + \frac{\sigma_{\langle F_{min}\rangle}}{\langle F_{min}\rangle} + \frac{\sigma_{\langle F_{max}\rangle}}{\langle F_{max}\rangle} + \frac{\sigma_{A_L}}{A_L} + \frac{\sigma_{w_0}}{w_0} + \frac{\sigma_{z_0}}{z_{max} - z_{min}} \tag{8.22}$$

where $z_{max} - z_{min}$ is the scan range of the z-scan acquisition. U is used as a goodness of fit parameter. Out of the series of fits performed with different data ranges, the one with the smallest U is used as the result to report. This fit is then exported to csv files for further processing, and to a png graphic showing the fit with Eq. 8.19.

8.2.4 Summary

The established workflow offers a convenient implementation of z-scan FCS at a current generation commercial confocal microscope platform as a means of acquiring robust membrane FCS data without concerns about limited accurary of observation volume positioning. The workflow combines built-in features of the commercial system with custom software extensions for z-scan FCS-specific features. With the current MATLAB dependence, the software cannot be considered fully open-source. However, the MATLAB-dependent code is in principle easily exchanged with other tools that perform similar functions. For many labs, the tool should offer convenient access to z-scan FCS as-is.

8.3 Fitting of FCS data from polydisperse systems

FCS responds to different parameters that correlate with the size of a particle. Firstly, there is obviously the diffusion time, *i.e.*, diffusion coefficient, which depends on particle size and shape (Eqs. 2.10, 2.11, and others). Additionally, there is the dependence of particle brightness on the stoichiometry of the particle. These relations are discussed in more detail in chapter 6. In this section, a software tool for fitting FCS data pre-processed for example with FCS_Fixer software (see Section 8.1) with models for polydisperse systems is described. This software was used in exploratory studies that formed the basis of parts of Chapter 6.

8.3.1 Contributions

JHK designed and wrote software. The algorithms for regularizion fitting (Maximum-Entropy Method, CONTIN, see below) are extensions of code that had originally been drafted by Yusuf Qutbuddin.

8.3.2 Software Concept

The Python software was designed with the intention to modularly embed many tools expected to be useful for FCS analysis of polydispere systems into a common framework, in a manner that would allow the user to exchange and/or combine modules of the analysis with few keywords in code. The key to achieving this was to extensively use the "lmfit" Python package [262] to define constraints and links between model parameters, and build model evaluation and cost function as a hierarchical model with easily exchangeable functions.

8.3.3 Software: Model

PARAMETERS

The model always evaluates one or multiple discrete species, defined as described in Chapter 6. The parameters describing each species are:

- The diffusion time τ_{diff}.
- The average particle number $\langle N \rangle$.
- The molecular brightness ε.
- The oligomer stoichiometry j. The molecular brightness of oligomer species j is always $\varepsilon_j = j\varepsilon_1$.
- The labelling efficiency p_{label}, *i.e.*, the probability that a given monomer carries a fluorophor. If no explicit consideration of labelling efficiency is desired, this is left at $p_{label} = 1$. This value usually is supplied by the user and fixed at the same value for all species. Figure 8.8 illustrates the impact.
- A more technical species-wise parameter is the stoichiometry binwidth parameter d_j, which is used to evaluate an arbitrarily (for example logarithmically) spaced subset of oligomer species $j \in J_e$ as representative for the entire ensemble of species.

- $\langle N \rangle$ and p_{label} are present twice for each species, once as "population-level" parameter and once as "observation-level" parameter. This is relevant for the "incomplete-sampling" fitting strategy, which is explained below. For conventional fitting, without treatment of incomplete sampling, "population-level" parameter and "observation-level" parameters are constrained to have the same value and their distinction does not matter.

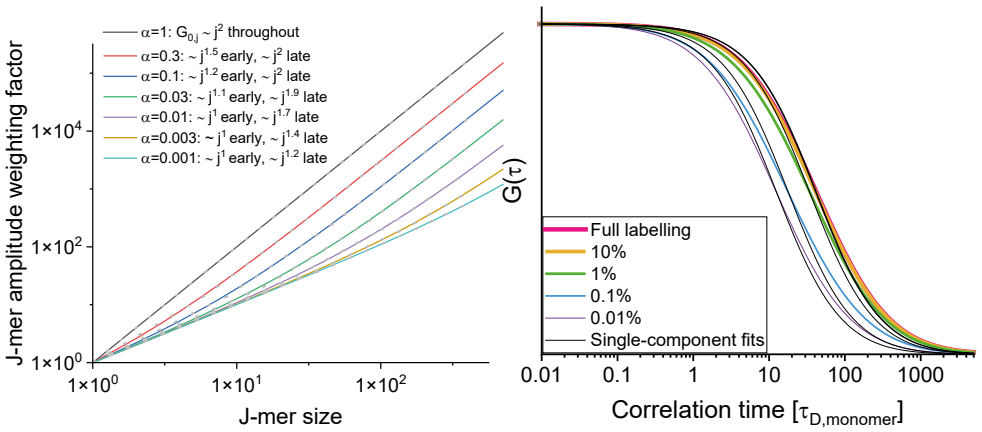

Figure 8.8. Effect of labelling efficiency on the ACF. The labelling efficiency here is called α, different from the main text. Shows are relative species-wise correlation function weights (relative to the monomer, without concentration profile effects). Curves have been fitted (grey dots) to approximately determine effective scaling exponents at small and high j. In the right, an example is shown of how the ACF of a given concentration profile changes with labelling efficiency.

Next, there are a number of parameters that characterize the ensemble as a whole. Firstly, there are categorical parameters to choose between different model assumptions. The "oligomer type" specifies the model to describe the scaling of τ_{diff} with j. This means that by querying a discrete set of stoichiometries J_e, the set of τ_{diff} values to evaluate is also defined if only the monomer diffusion time $\tau_{diff,1}$ is given. Some examples are (Figure 8.9):

- Spherical empty shell or random coil polymer in good solvent (Stokes-Einstein equation with particle surface area proportional to particle mass):

$$\tau_{diff,j} = \tau_{diff,1} j^{1/2} \tag{8.23}$$

- Spherical dense particle or collapsed polymer in poor solvent (Stokes-Einstein equation with particle volume proportional to particle mass):

$$\tau_{diff,j} = \tau_{diff,1} j^{1/3} \tag{8.24}$$

- Simple stiff filament [55–57]:

$$\tau_{diff,j} = \tau_{diff,1} \frac{2j}{2ln(j) + 0.632 + 1.165j^{-1} + 0.1j^{-2}} \tag{8.25}$$

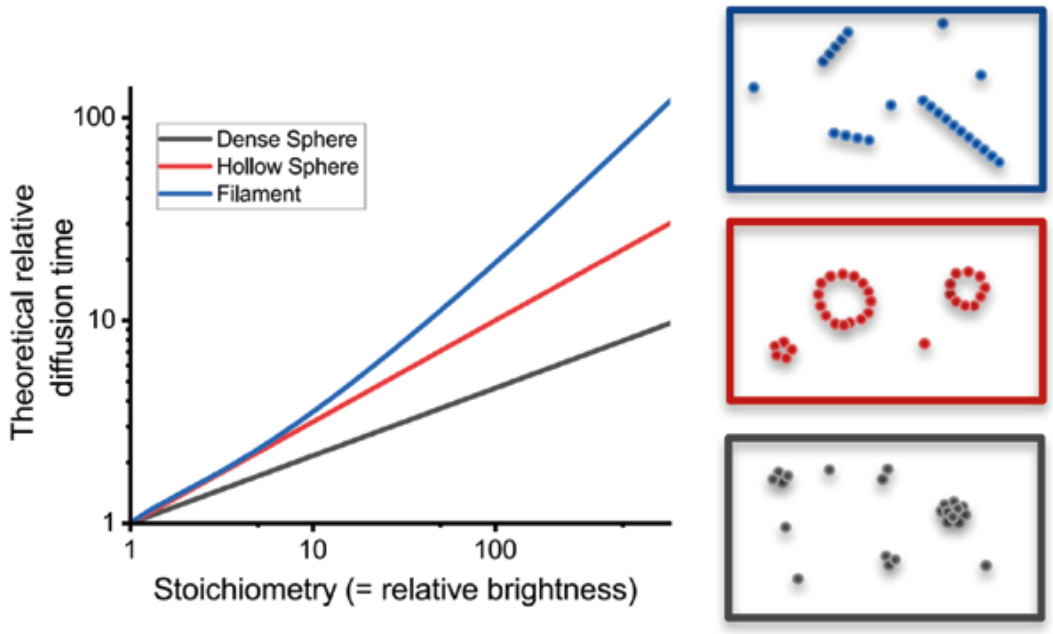

Figure 8.9. Diffusion time scaling for different particle types. The plots correspond to the expressions for diffusion time change over stoichiometry enumerated in the main text (Eqs. 8.23 to 8.25).

- There is also a "naive" model which uses no physically plausible scaling. It is mostly intended for fitting of one or a few discrete species, without constraining assumptions about the relations of ε, and τ_{diff}.

Using these models together with the above-mentioned link of ε_j to j dramatically reduces the complexity of the optimization to that of determining ε_1, $\tau_{diff,1}$, and the concentration profile $\langle N_j \rangle$. There are different functions to choose from that specify a general shape for $\langle N_j \rangle$. The implemented examples are different three-parameter functions with amplitude A, position parameter a, and shape parameter b:

- Gaussian peak:

$$\langle N_j \rangle = A x_j d_j \exp\left(-\frac{1}{2}\left(\frac{j-a}{b}\right)^2\right) \tag{8.26}$$

- Lognormal peak:

$$\langle N_j \rangle = \frac{A x_j d_j}{j} \exp\left(-\frac{1}{2}\left(\frac{ln(j)-ln(a)}{ln(b)}\right)^2\right) \tag{8.27}$$

- Stretched-exponential decay profile:

$$\langle N_j \rangle = A x_j d_j \exp\left(-\left(ja\right)^b\right) \tag{8.28}$$

- Gamma distribution:

$$\langle N_j \rangle = A x_j d_j j^{(a-1)} \exp\left(-bj\right) \tag{8.29}$$

where x_j is an additional variable that ensures that, while Eqs. 8.26-8.29 always refers to the oligomer particle concentrations $\langle N_j \rangle$, the distribution function can depending on user choice refer to:

- the oligomer particle number distribution ($x_j = 1$). This is also always used when the "naive" particle size scaling model is selected.
- to the monomer fraction in each species j ($x_j = j^{-1}$), which is equivalent to mass fraction distribution over j.
- or to the amplitude distribution ($x_j = j^{-2}$ without consideration of incomplete labelling, or $x_j = j^{-2}\left(1 + \frac{1-p_{label}}{jp_{label}}\right)^{-1}$ with consideration of labelled-particle fraction).

In addition to the above-mentioned parameters characterizing particles within a distribution of oligomer sizes, it is also possible to add further discrete species to the model, with flexible choice of which parameters to fix or fit. This can for example be used to describe the background signature of freely diffusing unconjugated fluorescent dye.

Additional, miscellaneous parameters:

- Blinking in the ACF is treated through a stretched-exponetial model similar to Eq. 8.28 with off-state fraction F_{blink}, blinking time scale τ_{blink} and stretch factor β_{blink}. The user can choose whether to fit the blinking term, or assume no blinking. In that case $F_{blink} = 0$, while τ_{blink} and β_{blink} are fixed at dummy values. Blinking kinetics are assumed to be the same for all species.
- A constant offset in the ACF G_∞ can be fitted. For certain settings, this is automatically fixed to 0 though, as otherwise the fitting would become numerically instable.
- The detection volume aspect ratio $S = \frac{w_0}{z_0}$, which is a fixed, user-supplied metadata parameter.
- If PCH data is to be included in fitting, a parameter F with $0 \leq F \leq 1$ buffers deviations between the real data and the assumption of an ideal Gaussian point spread function [263]. Additionally, a parameter Q fixed by the user is introduced that characterizes the size of the reference volume for PCH evaluation such that $V_{ref} = QV_{eff}$ with effective observation volume $V_{eff} = \pi^{3/2} w_0^2 z_0$ [263].

EVALUATION

The same parameters can be evaluated in different ways: Given a set of parameters, one can calculate an FCS ACF, Photon Counting (Multiple) Histograms (PC(M)H [194, 195]), and/or the average count rate.

The model evaluation for FCS is rather simple and based on standard expressions for FCS, adapted to consider the effect of distribution bin width and labelling efficiency. Figure 8.10 shows a simplified scheme of the concept underlying the model evaluation.

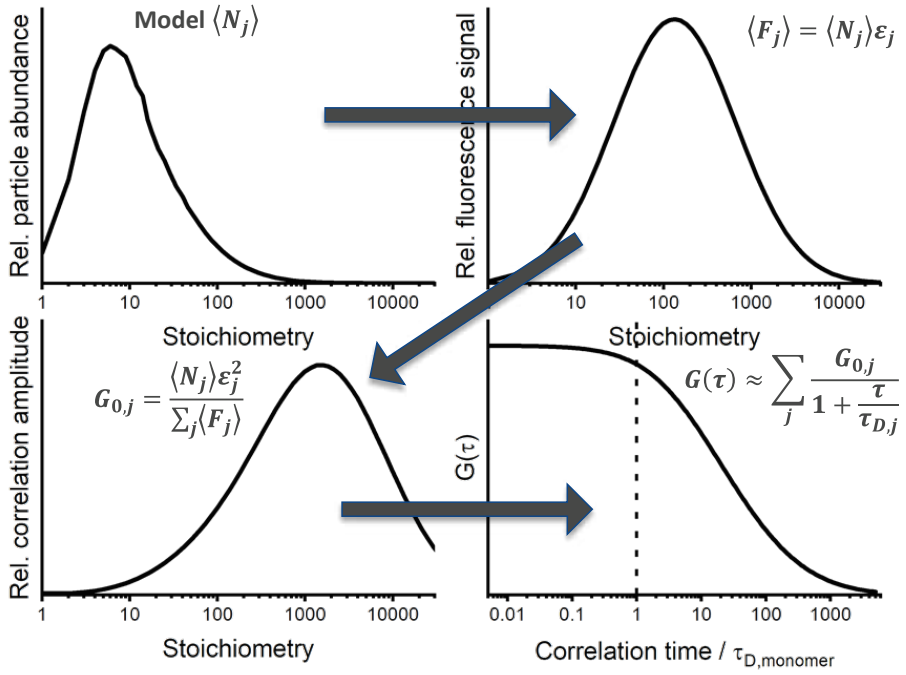

Figure 8.10. Basic model hierarchy. At the lowest level, the model considers a distribution of particle numbers over stoichiometries. The molecular brightness $\varepsilon_j \propto j$ is then condsidered to determine the species-wise signal level for evaluation of average count rates and PCH if needed. Species binning and labelling efficiency are also considered at this step, but omitted from the figure. The same information is also sufficient to predict the species-wise correlation amplitudes. Finally, considering links between stoichiometry and diffusion coefficient, the species-wise diffusion times are calculated and the ACF evaluated. For brevity, the two-dimensional expression of the ACF time-dependence is shown.

$$
\begin{aligned}
G(\tau) &= \gamma G_{mobility} G_{blinking} + G_\infty \\
G_{mobility} &= \frac{\sum_{j \in J_e} g_{diff,j}(\tau) \langle N_j \rangle d_j \varepsilon_j^2 \left(1 + \frac{1-p_{label}}{j p_{label}}\right)}{\left[\sum_{j \in J_e} \langle N_j \rangle d_j \varepsilon_j\right]^2} \\
g_{diff,j}(\tau) &= \frac{1}{1 + \frac{\tau}{\tau_{diff,j}}} \sqrt{\frac{1}{1 + \frac{\tau}{\tau_{diff,j} S^2}}} \\
G_{blinking} &= 1 + \frac{F_{blink}}{1 - F_{blink}} \exp\left(-\left(\frac{\tau}{\tau_{blink}}\right)^{\beta_{blink}}\right)
\end{aligned}
\tag{8.30}
$$

with $\gamma = 2^{-3/2}$ for 3D diffusion.

PC(M)H model evaluation is a multi-step procedure [263]. Firstly, the probability for $n_{h\nu}$ photon counts within bin time t_{bin} is evaluated for a single particle residing at a random position within the observation volume, given molecular brightness ε. The range of queried $n_{h\nu}$ is matched to the range of experimentally observed photon

counts. Using the 3D Gaussian approximation for the observation volume shape that is commonly used in FCS, this becomes:

$$p_j^{(1)}(n_{hv}) = \frac{1}{n_{hv}! Q\sqrt{\pi}} \int_0^\infty \gamma\left(n_{hv}, t_{bin}\varepsilon_j \exp\left(-2x^2\right)\right) dx \tag{8.31}$$

where the integral over the incomplete gamma function $\gamma(\ldots)$ is evaluated numerically. However, it was pointed out that the 3D Gaussian approximation does not work well for PCH [263]. Instead, a simple correction has been proposed that summarizes the non-Gaussian PSF shape features through an additional fit parameter F:

$$p_{j,corr}^{(1)}(n_{hv}) = \frac{p_j^{(1)}(n_{hv})}{(1+F)^2} + \begin{cases} 2^{-\frac{3}{2}} Q^{-1} t_{bin}\varepsilon_j F & n_{hv} = 1 \\ 0 & n_{hv} > 1 \end{cases} \tag{8.32}$$

In practice, $p_{j,corr}^{(1)}(0)$ is calculated as $p_{j,corr}^{(1)}(0) = 1 - \sum_{n_{hv}>0} p_{j,corr}^{(1)}(n_{hv})$ Next, given the current estimate of particle number $\langle N_j \rangle$ (considering stoichiometry bin width d_j), a probability mass distribution $p(N)$ of N_{trial} particles being in the reference volume at any given time is calculated based on a Poisson distribution with expectation value $\lambda = \langle N_{j,PCH} \rangle = 2^{\frac{3}{2}} Q d_j \langle N_j \rangle$.

$$p(N_{trial}) = \text{Poisson}\left(k = N_{trial}, \lambda = \langle N_{j,PCH} \rangle\right) \tag{8.33}$$

The highest N_{trial} to evaluate is chosen such that $N_{trial,max} \geq 2$ and $\sum_{N_{trial}} p(N_{trial}) > 1 - T_P$ with precision cutoff T_P. The same range of relevant N_{trial} is now also used to extend the single-particle PCH (Eq. 8.32 to N_{trial}-particle PCHs though repeated self-convolutions:

$$p_{j,corr}^{(N_{trial})}(n_{hv}) = \begin{cases} \delta_{n_{hv}}, & N_{trial} = 0 \\ p_{j,corr}^{(1)}(n_{hv}), & N_{trial} = 1 \\ p_{j,corr}^{(1)}(n_{hv}) \underset{N_{trial}\ terms\ total}{\otimes \ldots \otimes} p_{j,corr}^{(1)}(n_{hv}), & N_{trial} > 1 \end{cases} \tag{8.34}$$

where Kroneker delta $\delta_{n_{hv}}$ expresses the fact that if $N_{trial} = 0$, no photons can be detected:

$$\delta_{n_{hv}} = \begin{cases} 1, & n_{hv} = 0 \text{t} \\ 0, & n_{hv} > 0 \end{cases} \tag{8.35}$$

The actual PCH for species j $\Pi_j(n_{hv})$ is then a weighted sum over all the N_{trial}-particle PCHs:

$$\Pi_j(n_{hv}) = \sum_{N_{trial}} p(N_{trial}) p_{j,corr}^{(N_{trial})}(n_{hv}) \tag{8.36}$$

When there is mixture of different species to evaluate $J_e = \{j_1, \ldots, j_{max}\}$, the overall PCH $\Pi(n_{hv})$ is the convolution of the independently evaluated species-wise PCHs.

$$\Pi(n_{hv}) = \Pi_{j_1}(n_{hv}) \otimes \ldots \otimes \Pi_{j_{max}}(n_{hv}) \tag{8.37}$$

The calculation described so far assumes that the bin time t_{bin} is much shorter than the time scale of diffusion, and neglects blinking. For PCMH analysis, *i.e.*, PCH

analysis with varied bin time t_{bin}, these are explicitly corrected considered through t_{bin}-dependent corrections to ε_j and $\langle N_j \rangle$ based on [194,195]:

$$\begin{aligned} \langle N_{j,app} \rangle (t_{bin}) &= \frac{\langle N_j \rangle}{\Lambda_{diff}(t_{bin})\,\Lambda_{blink}(t_{bin})} \\ \varepsilon_{j,app}(t_{bin}) &= \varepsilon_{j,app}\Lambda_{diff}(t_{bin})\,\Lambda_{blink}(t_{bin}) \end{aligned} \tag{8.38}$$

with diffusion correction term:

$$\begin{aligned} \Lambda_{diff}(t_{bin}) &= \frac{4S\tau_{diff,j}}{t_{bin}^2 a_1}\left[a_3\left(\tau_{diff,j}+t_{bin}\right)+a_1\tau_{diff,j}\left(S-a_2\right)\right] \\ a_1 &= \sqrt{S^2-1} \\ a_2 &= \sqrt{S^2+\frac{t_{bin}}{\tau_{diff,j}}} \\ a_3 &= tanh^{-1}\left(a_1\frac{a_2-S}{1+S\left(a_2-1\right)}\right) \end{aligned} \tag{8.39}$$

and blinking correction term:

$$\begin{aligned} \Lambda_{blink}(t_{bin}) &= 1+ \\ &\frac{2F_{blink}\tau_{blink,eff}}{t_{bin}\left(1-F_{blink}\right)}\left(1-\frac{\tau_{blink,eff}}{t_{bin}}\left(1-\exp\left(-\frac{t_{bin}}{\tau_{blink,eff}}\right)\right)\right) \\ \tau_{blink,eff} &= \tau_{blink}\Gamma\left(1+\frac{1}{\beta_{blink}}\right) \end{aligned} \tag{8.40}$$

where average blinking time $\tau_{blink,eff}$ of the stretched exponential profile is used for simplicity.

Incomplete labelling in PCH is evaluated by iteration over all possible number of labels (*i.e.*, $\varepsilon = \{\varepsilon_1, 2\varepsilon_1, \cdots, j\varepsilon_1\}$) for each j-mer species. Here, the monomer labelling probability p_{label} is used to predict the average particle numbers of different brightnesses *via* a binomial distribution:

$$\langle N_{j,\varepsilon=k\varepsilon_1} \rangle = \langle N_j \rangle \binom{k}{j} p_{label}^k \left(1-p_{label}\right)^{j-k} \tag{8.41}$$

Finally, in addition to ACF and PCH, the average count rate $\langle F_{model} \rangle$ is evaluated by considering concentrations, molecular brightnesses, blinking, and labelled monomer fractions:

$$\langle F_{model} \rangle = \sum_j \langle N_j \rangle d_j \varepsilon_j p_{label} \tag{8.42}$$

8.3.4 Software: Cost function and optimization

The fit is performed by minimizing a negative logarithmic likelihood function NLL using the Nelder-Mead algorithm [264]. In general, the NLL used consists of a number of additive terms that can be used or not, or exchanged between different likeli-

hood models, depending on the fit settings. This choice is motivated as a generalization of the global minimization strategy for FCS and PCH data in [195,265], and justified as a joint probability of the different observables given a trial model (although we recognize that the different observables are not entirely independent, and a more rigorous treatment may require consideration of their dependencies):

$$NLL = \frac{NLL_{FCS}}{DoF_{FCS}} + \frac{NLL_{PCH}}{DoF_{PCH}} + NLL_{ACR} + NLL_{is} \tag{8.43}$$

NLL_{FCS} is a simple weighted sum of residual squares (WLSQ) for the comparison of the current ACF model to the ACF data:

$$NLL_{FCS} = \frac{1}{2}\sum_i \left(\frac{G_{model}(\tau_i) - G_{data}(i)}{\sigma\left[G_{data}(i)\right]} \right)^2 \tag{8.44}$$

where the factor $1/2$ reflects the scaling between negative logarithmic likehood and weighted sum of residual squares for a Gaussian-distributed variable, and i describes iteration over data points in the experimental ACF.

The likelihood function for PC(M)H fitting is available in two variants depending on user choice, either as a weighted least-squares approximation, or as an explicit evaluation of the binomial probability distribution (considering that the normalized PCH is just a probability mass function for detection of n_{hv} photons per bin):

- WLSQ:

$$NLL_{PCH} = \frac{1}{2}\sum_{n_{hv}} \frac{\left[\Pi_{model}(n_{hv})\, N_{hv} - \Pi_{data}(n_{hv})\right]^2}{\Pi_{data,abs}(n_{hv})} \tag{8.45}$$

- Binomial:

$$\begin{aligned} NLL_{PCH} = \sum_{n_{hv}} & -\Pi_{data,abs}(n_{hv})\, ln\left(\Pi_{model}(n_{hv})\right) \\ & -\left(N_{hv} - \Pi_{data,abs}(n_{hv})\right) ln\left(1 - \Pi_{model}(n_{hv})\right) \end{aligned} \tag{8.46}$$

where $N_{hv} = \sum_{n_{hv}} \Pi_{data,abs}(n_{hv})$ is the total number of considered photons, and $\Pi_{data}(n_{hv})$ is the experimentally obtained non-normalized PCH. In the case of PCMH analysis, the NLL_{PCH} for all evaluated bin times are summed. The degrees of freedom DoF_{FCS} and DoF_{PCH} for normalization are obtained from counting the contributing data points, and the local free parameters relevant only to the respective function:

$$\begin{aligned} DoF_{FCS/PCH} = N\left[\text{datapoints in ACF/PCH}\right] - 1 \\ - N\left[\text{free local parameters for ACF/PCH}\right] \end{aligned} \tag{8.47}$$

NLL_{ACR} is an additional likehood function term that serves as a soft constraint to match the estimated concentrations and molecular brightnesses to the average count rate. It can be either a weighted least-squares term, or a Poisson likelihood term:

- WLSQ:

$$NLL_{ACR} = \frac{t_{ac}}{2} \frac{\left[\langle F_{model}\rangle - \langle F_{data}\rangle\right]^2}{\langle F_{data}\rangle} \tag{8.48}$$

- Poisson:

$$NLL_{ACR} = -t_{ac}\left[\langle F_{data}\rangle ln\left(\langle F_{model}\rangle t_{aq}\right) + \langle F_{model}\rangle\right] \tag{8.49}$$

NLL_{is} is an additional likelihood term describing "incomplete sampling", *i.e.*, deviations between population-level concentrations and observation-level concentrations. During measurement duration t_{ac}, the signal at any time will stem from a number of particles that is Poisson-distributed around a population mean $\langle N_{pop}\rangle$.

$$P\left(N_{obs,tot}\right) = \text{Poisson}\left(k = N_{obs,tot}, \lambda = \langle N_{pop}\rangle \frac{t_{ac}}{\tau_{diff,j}}\right) \tag{8.50}$$

The total number $N_{obs,tot}$ of particles with diffusion time τ_{diff} observed during the entire acquisition will then also be Poisson-distributed, and the observation-level mean particle number will follow that:

$$\langle N_{obs}\rangle \approx N_{obs,tot}\frac{\tau_{diff,j}}{t_{ac}} \tag{8.51}$$

Generally, interpretation of FCS data assumes that $\langle N_{obs}\rangle = \langle N_{pop}\rangle$, which is reasonable for large $N_{obs,tot}$ given the properties of the Poisson distribution:

$$\frac{\sigma\left[\langle N_{obs}\rangle\right]}{\langle N_{obs}\rangle} \approx \frac{\sigma\left[N_{obs,tot}\right]}{N_{obs,tot}} \propto \frac{1}{\sqrt{\langle N_{pop}\rangle \frac{t_{ac}}{\tau_{diff,j}}}} \tag{8.52}$$

But clearly, for rare events entering the data analysis with a small $N_{obs,tot}$ this uncertainty can be significant. This insufficient sampling of events with long $\tau_{diff,j}$ and/or small $\langle N_{pop}\rangle$ is one of the reasons for the failure of FCS in treating rare particle species correctly in conventional data analysis (see Chapter 6). In analysing a multi-species mixture such as what is typically observed in self-assembling systems, these considerations are true for each occurring species independently, meaning that it is perfectly possible and expected for some species to be well-represented in the data while others are not. This is what the incomplete sampling fitting strategy tries to take into account by explicitly distinguishing population-level and observation-level concentrations. Effectively, the model is a hierarchical model in which $\langle N_{j,pop}\rangle$ is constrained by one of the above-mentioned distribution models while $\langle N_{j,obs}\rangle$ is in principle fitted freely for every evaluated j, but constrained to fluctuate within a reasonable interval around $\langle N_{j,pop}\rangle$ *via* NLL_{is}:

- WLSQ:

$$NLL_{is} = \frac{t_{ac}}{2}\sum_{j\in J_e}\frac{d_j}{\tau_{diff,j}}\frac{\left[\langle N_{j,pop}\rangle - \langle N_{j,obs}\rangle\right]^2}{\langle N_{j,pop}\rangle} \tag{8.53}$$

- Poisson:

$$\begin{aligned} NLL_{is} = \sum_{j\in J_e} d_j \Bigg[& \langle N_{j,obs}\rangle \frac{t_{ac}}{\tau_{diff,j}} ln\left(\langle N_{j,pop}\rangle \frac{t_{ac}}{\tau_{diff,j}}\right) \\ & -\langle N_{j,pop}\rangle \frac{t_{ac}}{\tau_{diff,j}} - ln\left(\Gamma\left(\langle N_{j,obs}\rangle \frac{t_{ac}}{\tau_{diff,j}}\right) + 1\right)\Bigg] \end{aligned} \tag{8.54}$$

with gamma function $\Gamma(\ldots)$. In case incomplete sampling and incompltete labelling are considered, the likelihood function iterates not only over J_e, but also over all possible nonzero numbers of labels (*e.g.*, for $j = 3$, one label, two labels, and three labels are considered), calculaing their respective frequencies based on binomial distributions. In doing so, p_{label} is assumed to be constant and fixed, though. There is also the option of extending NLL with another term to allow deviations of the species-wise observation-level p_{label}, fluctuating around the user-specified population-level parameter. However, this fitting strategy is computationally prohibitively expensive and gave no practical added value, and will therefore not be described here further.

8.3.5 Regularized fitting

The methods described in the previous section assume the use of few-parameter functions like lognormal or stretched exponential to describe a particle size distribution. However, there are also other techniques available that make no *a priori* assumptions about the shape of the distribution to be reconstructed other than the fact that the distribution is smooth. These methods, mentioned in Chapter 6, include Maximum Entropy Method (MEM, [266–268]), "CONTIN" fitting [269–271], and other analogous approaches [272]. The "FCS_Spectrum" software also allows replacing the use of parametric distribution models with these optimization methods, with little change to the rest of the model structure and evaluation.

In general, to use a regularization fit in "FCS_Spectrum", first, a Gaussian distribution fit with some simplifications to accelerate evaluation is performed to get a first reasonable estimate of concentrations. The result of that fit is then used as the basis for the regularization fit. The key of the regularization fit from the technical point of view is a modified iteration scheme dueing minimization. At each iteration, the gradient in residuals is calculated based on weighted residuals:

$$\nabla Q(j) = \frac{2\gamma}{i_{max}} \sum_i g_{diff,j}(\tau_i) \frac{G_{model}(\tau_i) - G_{data}(i)}{\sigma^2 [G_{data}(i)]} \tag{8.55}$$

with $g_{diff,j}(\tau_i)$ as in Eq. 8.30. Note that Eq. 8.55 only works directly if the target of regularization (see below) is the species-wise correlation amplitude, and labelling efficiency $p_{label} = 1$. In other cases, other, somewhat more cumbersome expressions for the gradients need to be used.

In addition, the gradients for the regularization term of choice are calculated:

- MEM cost:
$$S = -\sum_{j \in J_e} a(j) \, ln(a(j)) \tag{8.56}$$
- MEM gradient:
$$\nabla S(j) = -1 - ln(a(j)) \tag{8.57}$$
- CONTIN cost:
$$S = -\sum_{j \in J_e} (2a(j) - a(j-1) - a(j+1))^2 \tag{8.58}$$

- CONTIN gradient:

$$\begin{aligned}\nabla S\left(j\right) = -[12a\left(j\right) - 8\left(a\left(j-1\right) + a\left(j+1\right)\right) \\ +2\left(a\left(j-2\right) + a\left(j+2\right)\right)]\end{aligned} \tag{8.59}$$

where $a\left(j\right)$ is the normalized weight of the distribution on which the smoothness regularization operates ($\sum_{j\in J_e} a\left(j\right) = 1$). Similarly to the use of distribution function models, $a\left(j\right)$ can be set to represent amplitude fractions, mass fractions, or particle number fractions. S is not explicitly evaluated in calculation, only the (directly calculated) gradients $\nabla S\left(j\right)$ are required. From ∇Q and $\nabla S\left(j\right)$, the update of $a\left(j\right)$ is calculated:

$$\begin{aligned}a_{new}\left(j\right) &= a_{old}\left(j\right) + \Delta a + 0.1\Delta a_{old} \\ \Delta a &= 2\cdot 10^{-4} a_{old}\left(j\right)\left(\frac{|\nabla Q|}{|\nabla S|L}\nabla S\left(j\right) - \frac{1}{2}\nabla Q\left(j\right)\right)\end{aligned} \tag{8.60}$$

with regularization weight (Lagrange multiplier) L, which will be mentioned again later, increment Δa, and vertical bars denoting magnitude of the respective vector. Δa_{old} is Δa from the previous iteration.

After a single update of $a\left(j\right)$ based on Eqs. 8.55-8.60, the global amplitude of the correlation function (total particle concetration) is optimized based on weighted-least-squares minimization of Eq. 8.44. Next, if other model parameters are freely fitted besides concentation parameters, a single iteration of Nelder-Mead optimization of the other model parameters based on Eq. 8.43 is performed, where also PCH and/or average count rate can be considered. Then, a single iteration round is complete, and gradients in ACF residuals and regularization functions are calculated again. This loop terminates after an iteration limit is reached, or until the test parameter described in [273] falls below the threshold:

$$TEST = \frac{1}{2}\sum_{j\in J_e}\left(\frac{\nabla Q\left(j\right)}{|\nabla Q|} - \frac{\nabla S\left(j\right)}{|\nabla S|}\right)^2 < 0.1 \tag{8.61}$$

The optimization begins with regularization weight $L = 20$. The purpose of L is to balance the weight between goodness of fit and model smoothness (enforced by regularization term) to achieve a parsimoneous fit within the limits allowed by the data. The iteration strategy described so far is the inner loop of a nested iteration strategy. The outer loop aims to update L until a good trade-off between goodness of fit and smoothness is found. If the goodness of fit parameter in the last iteration was outside the range of $[1; 1.3]$, the fit is considered either over- or underfitted. The optimization terminates if the fit is within the plausible range, or if for 3 (outer) iterations relative changes in both goodness of fit and L were within 1%. Otherwise, L is updated and the inner iterations resumed:

$$L_{new} = L_{old}\frac{|\nabla Q_{new}|}{|\nabla S_{new}|}\left(\frac{|\nabla Q_{old}|}{|\nabla S_{old}|}\right)^{\frac{1}{3}} \tag{8.62}$$

where $|\nabla Q_{old}/S_{old}|$ denoting the magnitudes of vectors at the time of the previous evaluation of Eq. 8.62 ($|\nabla Q_{old}/S_{old}| = 1$ in first evaluation).

8.3.6 Application example: Real-time quantification of RNA digestion

As a simple application example to discuss some aspects of the use of the model, the analysis of data from ssRNA samples to track degradation in real time will be shown here. ssRNA samples were produced by Adam Mamot using *in vitro* transcription similar to what is described in the Appendix to Chapter 6, but following a protocol that produced a single target length of 928 nucleotides unless specified otherwise. FCS measurements were performed also performed as described in the Appendix.

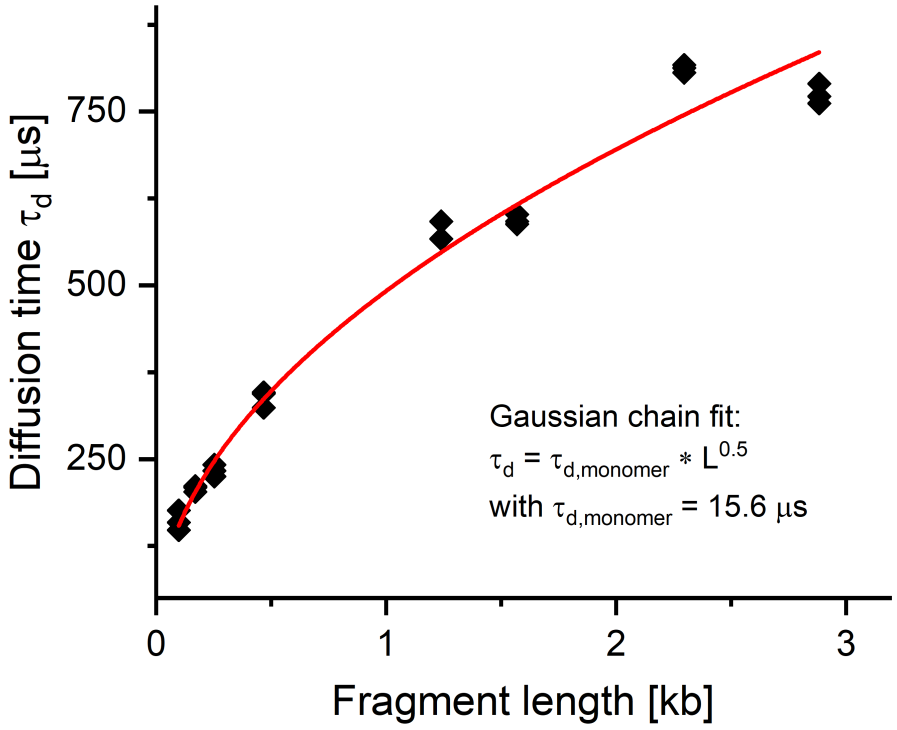

Figure 8.11. Calibrating particle size scaling. A series of single-size ssRNAs was measured in FCS and analyzed with conventional single-species fits. The diffusion times could be fitted well with a simple model for a Gaussian-chain polymer in good solvent, with $\tau_d \propto j^{0.5}$. Measurements were performed at 23°C.

In a first set of measurements, a series of ssRNA fragments of different sizes were measured to determine the scaling of diffusion time with RNA fragment length (Figure 8.11). Consistent with the common assumption that the persistence length of single stranded nucleic acid filaments is in the order of one or a few nanometers (not much more than ten nucleotides) [274], we could describe the data well with a model assuming $\tau_d \propto j^{0.5}$, corresponding to a random coil polymer in good solvent. This is not a trivial result for ssRNA due to the tendency of ssRNA to fold onto itself into complex secondary structures. We thus found an extrapolated monomer diffusion time of $15.6\ \mu s$ under the experimental conditions given. Note that this is an extrapolated value meant for coarse description of ssRNA fragments of length $>> 1\ nt$. Therefore, the short diffusion time that would be implausible for a free nucleotide

(shorter than what is usually found for free fluorescent dyes) is neither surprising, nor invalidating the model.

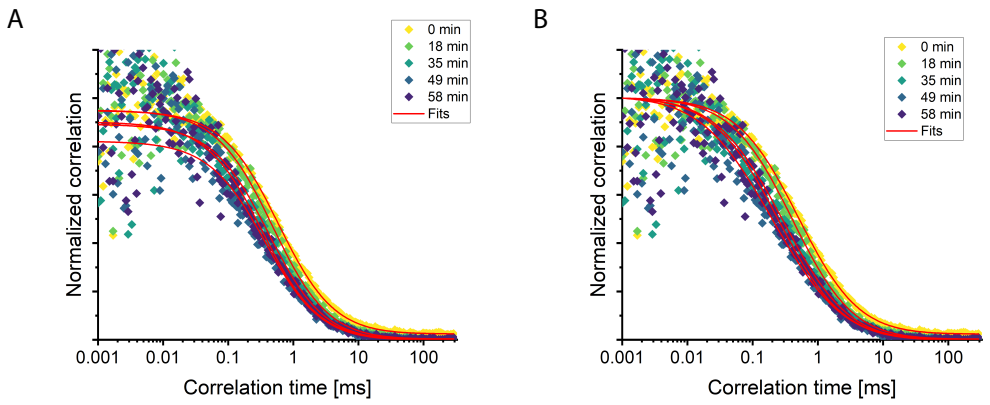

Figure 8.12. FCS observation of ssRNA digest. ssRNA diffusion ACFs from a series of 90 seconds measurements over one hour starting with a 928 nt long fragment under digestion with RNase R. Only five ACFs out of the time series are shown for clarity. **A**: ACFs with fits using a conventional single-species model. **B**: ACFs with fits using a lognormal size distribution model as described in the main text. Measurements were performed at 37°C.

We then measured ssRNA samples that initially had a single size, but were slowly digested after addition of $2\ \mu l$ of the exonuclease RNase R solution (Ribonuclease R, Biosearch Technologies) to a total volume $50\mu l$. Using the previously calibrated particle size scaling, we estiamted fragment length distributions from FCS data acquired during digestion. To do this, ACFs were exported using FCS_Fixer software (Section 8.1) with automated FLCS-based background removal. ACFs were then fitted assuming a lognormal distribution of particle number fractions over fragment length (Figure 8.12). The fraction of labelled nucleotides was explicitly considered. Figure 8.12 also shows conventional single-component fits for comparison.

The choice of particle number distribution (as opposed to amplitude fractions or mass fractions, see above) was empirically motivated based on which model yielded good fit results. The use of a lognormal distribution rather than the alternatives was based on the fact that the lognormal distribution is rather generic in nature and works well for many different datasets. In contrast, the Gaussian function tends to yield too-narrow distributions with the logarithmically spaced array of diffusion times queried, whereas the Gamma distribution is numerically instable on some datasets. The stretched-exponential model finally is a model with very different shape that is physically unjustified in this sample. Note that artifacts from discretization and stoichiometry binwidth consideration distort the histograms in Figure 8.13 at short fragment lengths. The fact that the distributions do not match the initial size of 928 nt well is likely explained by the fact that the calibration data (Figure 8.11) and the digestion data (Figure 8.13) were acquired at different temperatures.

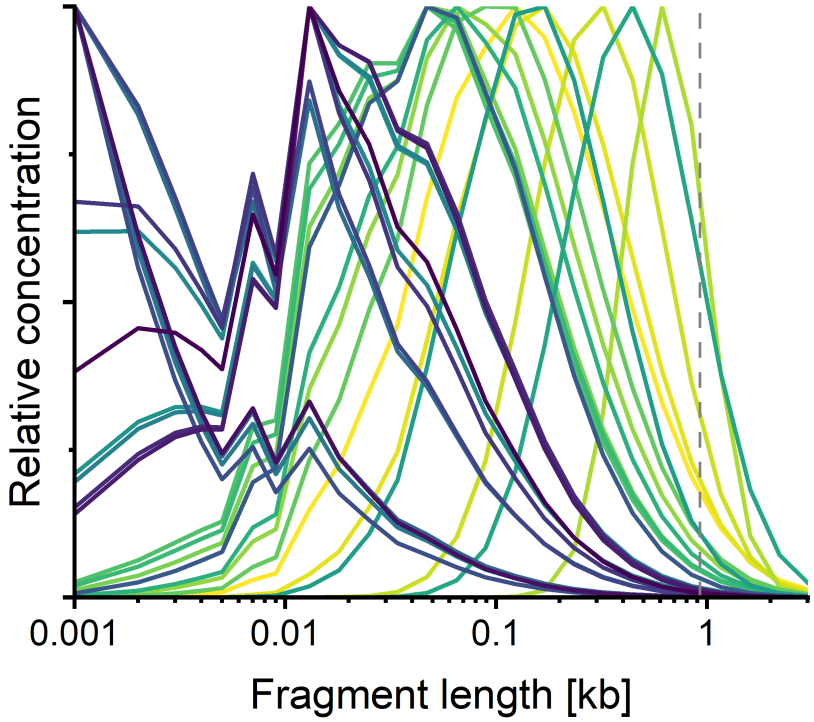

Figure 8.13. Fragment length distributions during ssRNA digestion. ssRNA particle number distributions reconstructed from the fits in Figure 8.12 Grey dotted line marks the 928 nt fragment size before digest. Yellow lines are early measurements, purple lines late measurements.

Using the obtained distributions, one can now obtain the average fragment size. Averaging can be done according to different weighting schemes: Weighting by particle number fraction, weighting by mass fraction, or weighting by ACF amplitude fraction ("z-average" [234]). All thres averages can be recalculated from the same fit result. Results are shown in Figure 8.14 A. Obviously, the z-average results are implausible with seemingly increasing particle size over time. Such instable behavior of the z-average statistics is often seen in this software for fitting, if the original distribution in fitting is defined on particle numbers or mass fractions. The particle number weighted or mass weighted distribtuions yield more robust results, and decay over time towards smaller fragments as expected. These two can then be used to recalculate the polydispersity index $PDI = \langle j \rangle_{mass} / \langle j \rangle_{number}$, which is shown in Figure 8.14 B. The increase in PDI over time is the expected observation as not all ssRNA particles will be digested at the same time. Rather, the digest is a stochastic process that is expected to proceed through a phase of high dispersity before reaching a final, fully digested state. From FCS data alone it is hard to tell whether this final state was reached due to the low weight of monomers in the overall ACF (see Chapter 6) and the fact that the fitting of a parametric distribution restricted to $j \geq 1$ is not ideal for analyzing a monomers-dominated sample. The PDI in the earliest measurements is clearly > 1, although the undigested ssRNA should show $PDI = 1$. This is a bias

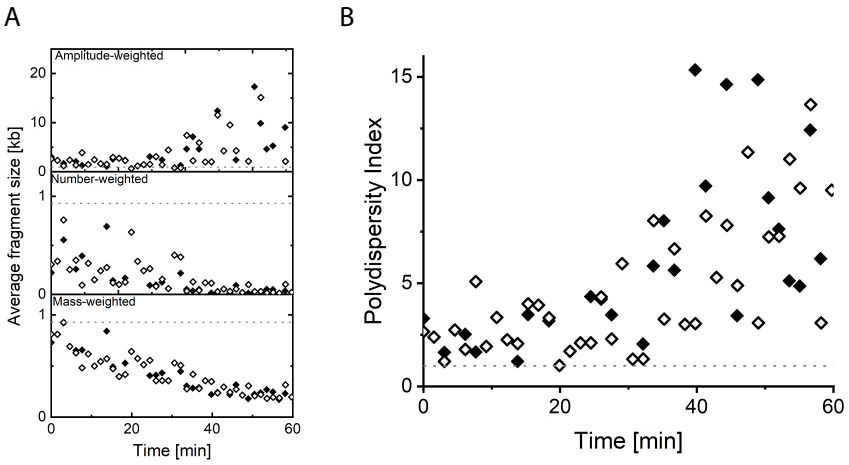

Figure 8.14. Average fragment lengths over time. **A**: Changes in average fragment length over time for two samples (indicated by symbols), with averages over the distributions in Figure 8.13 calculated with weighting by particle number fraction, by mass fraction, or by ACF amplitude fraction. **B**: Polydispersity index recalculated from particle number fraction weighted and mass fraction weighted average framgent sizes.

of the model strategy as $PDI = 1$ would indicate a delta function-like distribution, but the lognormal distribution used is constrained to have a non-vanishing standard deviation.

8.3.7 Summary

The described software "FCS_Spectrum" offers a flexible and extendable framework for complex fitting FCS data based on generic descriptions. Various different descriptions of size distributions in polydisperse particle mixtures allow the user to try out a broad range of models on a dataset, with scripts for batch processing and parallel computing available for upscaling available. Overall, the software remains in an experimental state with some parameter configurations still leading to unexpected behavior. However, it is a starting point for development of a truly general FCS modelling framework. Of note, alternative frameworks have been proposed that omit the data crompression of ACF or PCH calculation, based for example on Baysian modelling frameworks [275] or on deep learning models [276]. It will be interesting to see which approach will become widespread in the future. Data compression-free techniques have the advantage of being able use more information present in the raw data, but the disadvantage of unfavorable scaling of computation time for longer acquisitions. Thus, different niches may form for compression-based and compressionless analysis techniques, depending on the signal to noise ratio and acquisition time feasible for a given system of interest.

9
Summary and outlook

The previous chapters described various applications and method improvements, mostly of FCS, for the study of self-organization and related processes in bottom-up synthetic biology.

We used single-molecule fluorescence imaging, in particular DNA-PAINT, to characterize the higher-order self-assembly of DNA origami nanoparticles upon addition of cross-linking connector strands. Here, we found an assembly strategy that is much faster than widespread strategies, at the cost of specificity. This strategy continues being used in other studies combining the DNA origami with other tools of synthetic biology like phase separating membranes and pattern-forming proteins [198, 204]. Exciting future work here may be the combination with filament-forming proteins to shape dynamic hydrid DNA origami/protein cortices on membranes. With DNA origami being much larger "monomer" particles than the monomers of filament-forming proteins, one could imagine the DNA nanostructures serving as the rigid structural element, while protein filaments could act as the active element with faster turnover of binding/unbinding. The approaches described in this thesis could be used directly for detailled characterization of structure and dynamics of such networks. Largely unused in the published work reprinted in Chapter 4 remained the orientation information on origami particles. The origami particles were designed to carry an arrow pattern in DNA-PAINT imaging (Figure 1 of Chapter 4), which was mostly used as a resolution benchmark. However, this or other patterns (*e.g.* an asymmetric three-dots pattern [277]) could also be used to detect and quantitatively analyze the orientation of origami particles. This may reveal interesting details about the interaction of specific faces of the origami with protein filaments or pattern-forming proteins: DNA origami typically expose DNA helix ends on some faces but not on others, and edge functionalizations and geometry effects are expected to further change such interactions.

We explored the feasibility of FCS in LLPS, and the issues that should be routinely considered. Optimization of sample geometry to avoid unnecessary refracting interfaces is helpful to improve data quality - although depending on the system of interest, it may not always be possible. With concentrations of particles of interest often high in the dense phase and extremely low in the dilute phase, accurately characterizing background especially in the dilute phase can be critical if concentrations are of interest. Bleaching artifacts on the other hand need to be considered especially in the dense phase. With these insights at hand, it will be interesting to

study in particular phase-separating systems that are out of thermodynamic equilibrium [278, 279]. While scanning FCS techniques can circumvent some of the issues mentioned here [214], this "self-calibrating" approach to scanning FCS sacrifices some spatial resolution. The optimizations described here for single-spot FCS will also be valuable for scanning FCS schemes in which the scanning serves to parallelize readout at multiple positions [174]. That way, spatially resolved information about the condensate dynamics can be retrieved. This should be of great interest for more detailled microrheology of spatially inhomogeneous droplets [90,280]. Precisely these inhomogemeous condensates are likely to be of interest as eary protocell candidates.

Discussing the application of FCS for particle sizing, especially in polydisperse systems, we offer insights into a number of complementary concepts in experiment design and data analysis. Many useful ideas exist, but remain to be integrated into a common framework comparable to what is established in commercial DLS instruments. We develop a prototype for such a general analysis framework with the "FCS_Spectrum" Python software, and hope that the FCS community will follow our recommendations in streamlining FCS-based particle sizing experiments in complex settings.

Overall, we believe that the contribution of our work to the scientific community is in bringing together a number of ideas for time-resolved fluorescence spectroscopy and single-molecule microscopy that existed disconnected in the scientific literature. We developed these ideas further, and standardized protocols, for application to the specific challenges of self-organizing biomimetic systems of interest to the bottom-up synthetic biology community. We hope that the insights we gained will be of use to future researchers in the field who want to obtain high-quality time-resolved fluorescence microscopy data from fascinating but challenging systems.

Part III

Appendix

A
Appendix to Chapter 4

Supplementary Information
Design Features to Accelerate the Higher-Order Assembly of DNA Origami on Membranes

Yusuf Qutbuddin,[†,¶] Jan-Hagen Krohn,[†,‡,¶] Gereon A. Brüggenthies,[†] Johannes Stein,[†] Svetozar Gavrilovic,[†] Florian Stehr,[†] and Petra Schwille*[,†]

†*Department of Cellular and Molecular Biophysics, Max Planck Institute of Biochemistry, Am Klopferspitz 18, D-82152 Martinsried, Germany*

‡*Exzellenzcluster ORIGINS, Boltzmannstr. 2, D-85748 Garching, Germany*

¶*Equal contribution*

E-mail: schwille@biochem.mpg.de

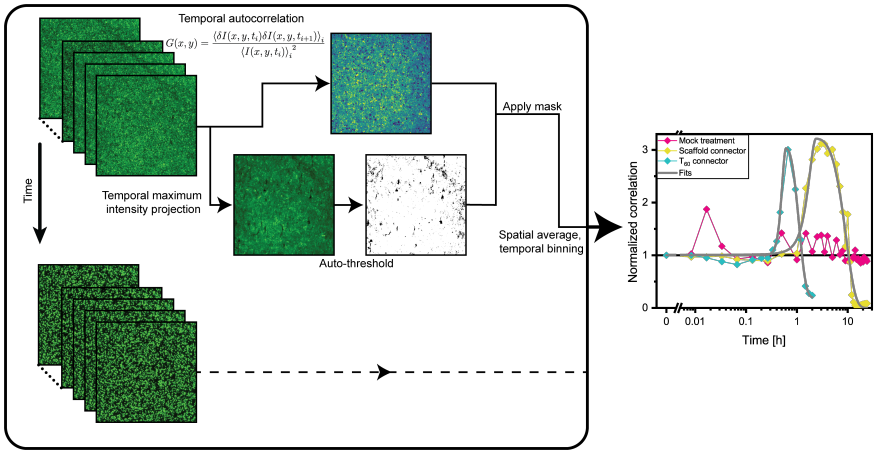

Figure S1: Image correlation analysis workflow. An acquisition consists of a series of blocks with a few hundred frames each. From each acquisition block, a correlation image and a thresholded mask (e.g., to remove membrane defects from the analysis) are calculated, and from these a single average correlation parameter is calculated, which serves as an estimate of the autocorrelation amplitude. This value is calculated independently for each bock in an acquisition, and the (normalized) trace of correlation amplitude over time is fitted to extract a characteristic timescale of immobilization. The right panel shows three example traces from different conditions with asymmetric Gaussian fits.

In this section, will first describe the workflow for our image correlation analysis, followed by an explanation of the underlying concept. Our correlation analysis is based on the following autocorrelation expression:

$$G(x,y) = \frac{\langle \delta I(x,y,t_i) \delta I(x,y,t_{i+1}) \rangle_i}{\langle I(x,y,t_i) \rangle_i^{\,2}} \tag{S1}$$

with frame-wise pixel greyscale $I(x,y,t_i)$, greyscale fluctuation $\delta I(x,y,t_i) = I(x,y,t_i) - \langle I(x,y,t_i) \rangle_i$ and $\langle ... \rangle_i$ as averaging over parameter i, here (discrete) time. This expression was applied to the time-dependent greyscale of every image pixel within each 10 s acquisition block. Further, a temporal maximum intensity projection (MIP) of the 10 s image stack was calculated and automatically thresholded to eliminate positions in which no particles

were present throughout the acquisition block, e.g., membrane defects. Autocorrelation values $G(x, y)$ from pixels within the mask from MIP thresholding were averaged to yield a single correlation value $G(j)$ characterizing the entire acquisition block j. The correlation values for a given experiment consisting of multiple 10 s blocks were then normalized as $G_n(j) = G(j)/G(j = 1)$. To extract characteristic timescales, the retrieved curves were fitted in OriginPro (2019b, OriginLab, unweighted Levenberg-Marquardt fit) with an asymmetric Gaussian function:

$$G_n(j) = \begin{cases} 1 + A_1 \cdot e^{\left[\frac{-ln2(t_j - t_0)^2}{T^2_{\frac{1}{2},rise}}\right]} & for\ t_j \leq t_0 \\ G_\infty + A_2 \cdot e^{\left[\frac{-ln2(t_j - t_0)^2}{T^2_{\frac{1}{2},drop}}\right]} & for\ t_j > t_0 \end{cases} \tag{S2}$$

with $A_2 = 1 + A_1 - G_\infty$. A_1 and G_∞ characterize amplitude and asymptote of $G_n(j)$, respectively, and t_0 is the peak position. $T_{\frac{1}{2},rise}$ and $T_{\frac{1}{2},drop}$ are peak half-widths for rising and falling edge of the correlation change. Reported values in Figure 5b are $t_0 + T_{\frac{1}{2},drop}$ as overall timescale of immobilization (i.e., drop in correlation). The use of a Gaussian function is rather arbitrary, motivated by its simplicity and the fact that no other model was found to yield notably better fits to the shapes of the traces.

The correlation analysis used to characterize cross-linking kinetics is a simplified implementation of the concept of fluorescence correlation spectroscopy (FCS), in particular temporal image correlation spectroscopy (TICS).[1] We will not review that theory in detail but only explain how the correlation parameter shown in Figure 5 relates to oligomerization and immobilization. Details can be found in the FCS literature, e.g. refs. 2, 3, and 4. In FCS/TICS, fluorescence intensity time traces are analyzed through an expression closly resembling Equation S1:

$$G(\tau) = \frac{\langle \delta F(t) \delta F(t + \tau) \rangle_t}{\langle F(t) \rangle_t^{\ 2}} \tag{S3}$$

with time-resolved fluorescence signal $F(t)$ and correlation lag time τ. The autocorrelation parameter $G(x, y)$ determined in our image correlation analysis serves as an estimate of the

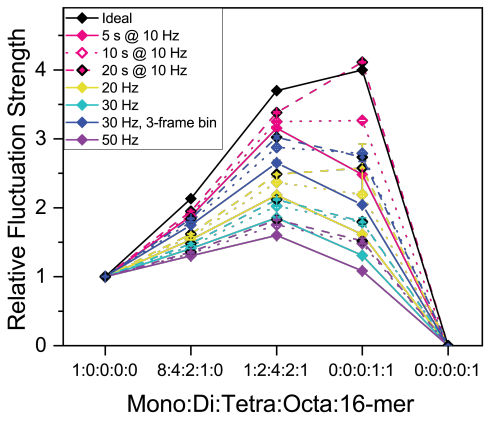

Figure S2: Simulations to assess sensitivity of image correlation analysis to oligomerization and immobilization. 16-mers are immobile in these simulations, their increasing fraction decreases the fluctuation amplitude. Symbol types and linestyles indicate acquisition block duration, colors indicate frame rate. Black line is the prediction according to Equation S6.

correlation amplitude G_0, which in simple settings directly yields the number of particles in the observation volume:

$$G_0 = \lim_{\tau \to 0} G(\tau) = \frac{1}{\langle N(t) \rangle_t} \tag{S4}$$

which is true if one assumes the number of particles in the observation volume over time $N(t)$ to be Poisson-distributed and $F(t) = \varepsilon N(t)$, i.e. all particles to be described by the same brightness parameter ε. This relation is true independent of the specific value of ε, and independent of the diffusion coefficient.

Now consider a mixture of fluorescent signals from multiple species A with distinct brightnesses, e.g., different oligomerization states, as well as a static signal contribution from an immobilized particle fraction S:

$$F(t) = \varepsilon_S N_S + \sum_A \varepsilon_A N_A \tag{S5}$$

Assuming a Poisson-distributed $N_A(t)$ as before and that the different species do not interact, G_0 becomes:

$$G_0 = \frac{\sum_A {\varepsilon_S}^2 \langle N_A(t) \rangle_t}{[\varepsilon_S N_S + \sum_A \varepsilon_A \langle N_A(t) \rangle]^2} \tag{S6}$$

Fluctuations in the signal from S only originate from shot noise, which is temporally uncorrelated and thus eliminated from the analysis by estimating G_0 from nonzero correlation times (extrapolation of $\lim_{\tau \to 0} G(\tau)$ in FCS, one-frame temporal lag in our analysis). As a consequence, immobilization of particles manifests as a drop in G_0: S contributes only to the denominator of the correlation function. Thus, increasing the number of immobile particles (fraction S) while decreasing the number of mobile particles (fractions A) will decrease the numerator of G_0, but leave the denominator unchanged. On the other hand, G_0 increases with progress of oligomerization. To understand this, one has to remember that producing e.g. one dimer particle consumes two monomer particles. This means that with progress of association, the overall number of particles will decrease. Further, the different oligomer species contribute to G_0 with different weights given by their squared brightness ${\varepsilon_A}^2$, which increases with higher oligomer stoichiometry. Therefore, a moderate number of large oligomers will overwhelm the correlation signal from a large number of monomers or small oligomers: The correlation amplitude will indicate a small overall particle number (i.e., large G_0).

We employed simple Monte-Carlo simulations to test the sensitivity of this analysis for oligomerization and immobilzation. Simulations of near-single-molecule imaging acquisitions were performed using custom software written in MATLAB (R2020b, The MathWorks). A strongly simplified system that yields data similar to that experimentally observed was simulated: A constant number of $5{\cdot}10^5$ particles were split into user-defined factions of monomers, dimers, tetramers, octamers, and 16-mers. The simulated field of view was equal in size to that of the experimental acquisitions expanded in each direction by 10 %. Particles were placed with random positions and orientations in the simulated area. Then, a random walk simulation with periodic boundary condition was performed. In each one-frame time step,

particles were displaced by Gaussian-distributed random distances in both x and y, each with 0 mean and standard deviation $\sqrt{2D[pixel^2 \cdot frame^{-1}]}$. The diffusion coefficient of monomers was assumed to be 0.1 μm^2 s^{-1}, similar to the experimentally observed value (Figure S4). Oligomer diffusion coefficients were assumed to be the monomer diffusion coefficient divided by the oligomer stoichiometry as a simple model of decreasing mobility with increasing oligomer size. 16-mers were fully immobile, representing the immobilized fraction. Rotational motion was neglected. After completion of the random walk simulation, localizations in the added 10 % edge were discarded to create a field of view equal comparable to the experiments. From the frame-wise center of mass positions and the orientations, images of linear oligomers were then generated with Gaussian-shaped point spread functions with resolution similar to the experiments. Poisson-distributed photon shot noise and realistic values for Poisson-distributed fluorescent background, camera offset and Gaussian-distributed readout noise were applied to create image stacks comparable to the experimental ones. Simulations were performed in blocks of 20 s, and each condition (oligomer fractions, frame rate) was simulated three times. For simulations of shorter acquisitions times, the 20 s simulations were cropped, so that finally for 20 s acquisitions three simulations per condition were analyzed, for 10 s acquisitions six, and for 5 s acquisitions twelve.

Comparing the simulation results to predictions according to Equation S6 (Figure S2), we see that with 10 Hz frame rate and 20 s observation time, we almost perfectly retrieve the theoretical values. Lower exposure times per frame and shorter acquisitions seem to yield data less sensitive particularly to association, presumably mainly due to signal-to-noise ratio limitations. Binning three successive frames of the 30 Hz simulations into a single frame (i.e., reducing time resolution to 100 ms without otherwise changing the data content) restores some of the sensitivity, again suggesting that signal-to-noise ratio is the main limitation. As our experimental data had been acquired at 30 Hz frame rate with 300 frames (10 s) blocks, we decided to post-bin our experimental data the same way.

Note that increase of the correlation amplitude due to oligomerization and its decrease

due to immobilization can happen at the same time, and the correlation amplitude G_0 (or $G(x, y)$) alone is not sufficient to dissect them. Even if one constrains the oligomer brightness to increase linearly with stoichiometry (i.e., $\varepsilon_A = A\varepsilon_1$), the system remains underdefined for extraction of $\langle N_A(t)\rangle_t$ for any multi-species mixture. To be able to extract these values, one would have to introduce further of assumptions about the association process to link $G(x, y)$ over successive observations. Alternatively, for data with high signal-to-noise ratio, higher-order correlation analysis might be a viable option.[5,6] We considered these more advanced methods to be beyond the scope of this manuscript, especially considering that for our experimental system we expect rather complicated dynamics including significant effects from non-negligible particle size compared to the optical resolution. Instead, we simply fitted the traces with an asymmetric Gaussian to determine half-rise/half-decay times (Figure S1).

Supporting Figures

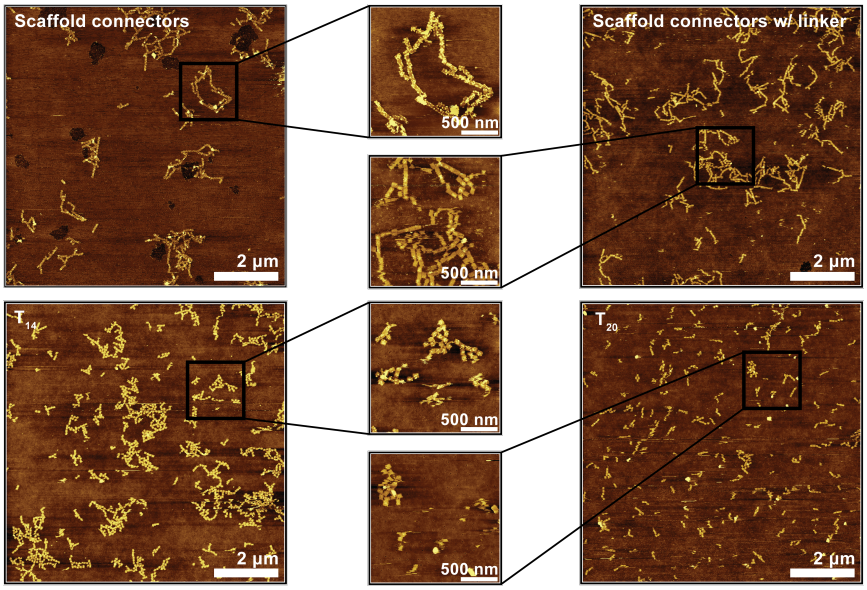

Figure S3: More AFM results. Shown are images comparable to those in main text Figure 3, but with different connector strands: Either scaffold connectors (20 h incubation, top) or short repeat connectors (2 h incubation, bottom). All images were acquired with 250 nM of the specified connector strand. Color-coded height scale in all panels in 6 nm.

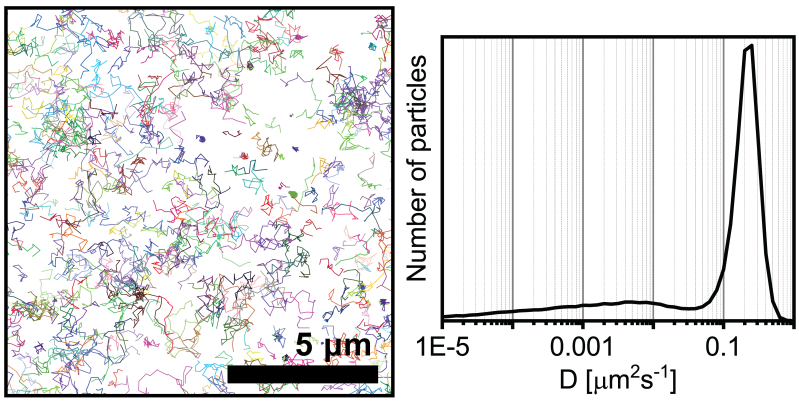

Figure S4: Example of single particle tracking results for monomeric DNA origami particles on DOPC SLBs. DNA origami particles are tethered to the membrane via 8 TEG-chol anchors. Track map (left) shows a random subset of tracks for better visibility. Colors are randomly assigned to individual tracks as a guide to the eye. The diffusion coefficient histogram to the right shows a minor peak at low mobility (trapped particles, a few of which are visible in the track map) and a pronounced peak of freely diffusing particles.

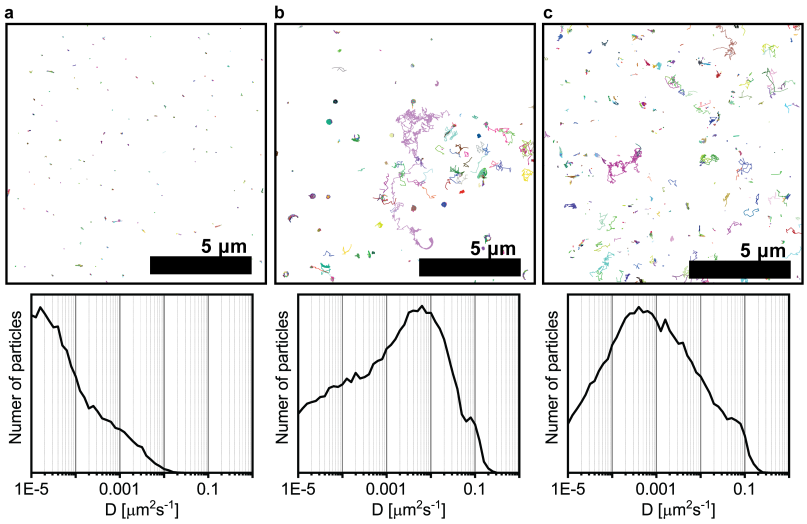

Figure S5: More single particle tracking results. Track maps are shown the same way as in Figure S4. **a:** Surface-immobilized (via streptavidin anchoring), tracking handle-labelled particles to assess the lower end of diffusion coefficients accessible via our method. **b:** Tracking handle-labelled DNA origami mixed and cross-linked (30 min, 50 nM each T_{14}, T_{20}, T_{40}, T_{60}, and T_{80}) with an excess of unlabelled particles (otherwise as in Figure S4). **c:** Same as panel b, but using scaffold connectors (with linker sequence, 20 h incubation before acquisition).

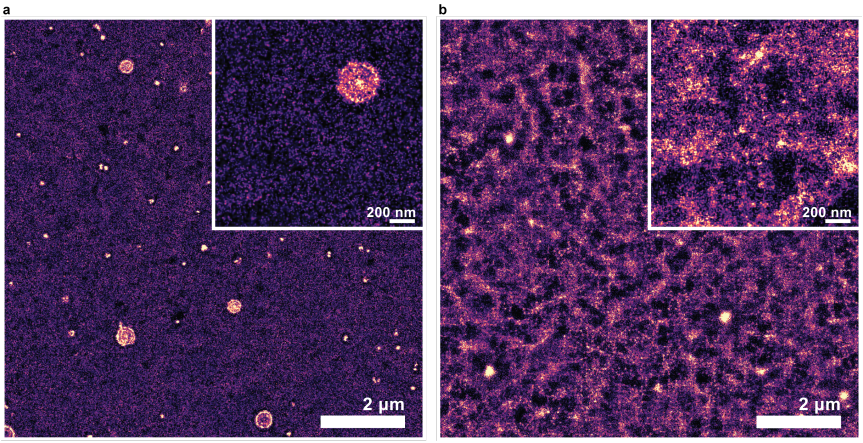

Figure S6: DNA-PAINT imaging of non-cross-linked DNA origami nanostructures. **a:** Similar conditions as in Figure 4, except without addition of connector strands. DNA-PAINT imaging shows a diffuse background from mobile particles, and a few immobilized particles at membrane defects (circular structures are larger holes in the supported lipid bilayer). **b:** Same as a, but with 3-fold higher density of DNA origami particles. Under such crowded conditions, particles are hindered in their motion and DNA-PAINT imaging reveals some structure, but with very low resolution.

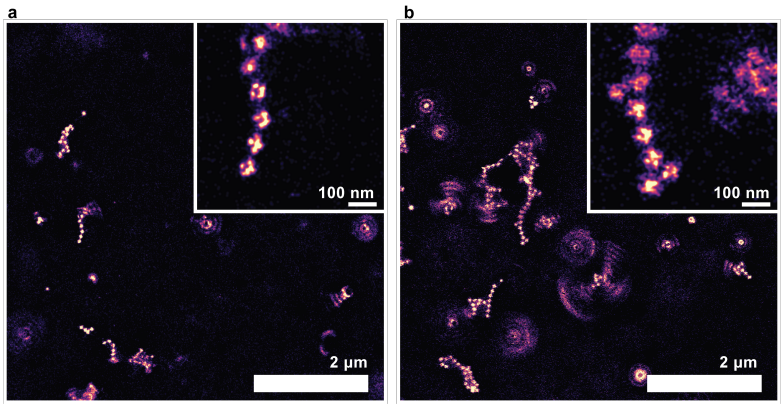

Figure S7: DNA-PAINT imaging of incompletely cross-linked DNA origami superstructures. Images have been acquired after 2 h cross-linking incubation with scaffold connectors without (**a**) or with (**b**) flexible linker sequence.

Supporting Tables

Table S1: Image analysis parameters.

Figure	Processing
1c overview	Localize MNG 450 box size 5; Render RCC undrift 450 frames, manual particle picking, pick similar, undrift from picked, export zoom 50 max density 1.7
1c average	Localize MNG 450 box size 5; Render RCC undrift 450 frames, manual particle picking, pick similar, undrift from picked, manual particle picking; Average3 Center of mass, oversampling 65, rotate, center of mass, rotate; Render export zoom 1000 max density 230
5,S1	tempVarianceAnalysis_v4.py with one frame lag, threshold_multiplication 0.5, bin_frames 3
4a overview	Localize MNG 500 box size 5; Render RCC undrift 450 frames, export zoom 7.5 max density 25
4a zoom	Localize MNG 500 box size 5; Render RCC undrift 450 frames, export zoom 100 max density 0.2
4b overview	Localize MNG 500 box size 5; Render RCC undrift 450 frames, export zoom 7.5 max density 30
4b zoom	Localize MNG 500 box size 5; Render RCC undrift 450 frames, export zoom 250 max density 0.15
4c T_{20} overview	Localize MNG 450 box size 5; Render RCC undrift 450 frames, export zoom 15 max density 8.33
4c T_{20} zoom	Localize MNG 450 box size 5; Render RCC undrift 450 frames, export zoom 250 max density 0.04

Continued on next page

Table S1

Figure	**Processing**
4c T_{40} overview	Localize MNG 450 box size 5; Render RCC undrift 450 frames, export zoom 15 max density 8
4c T_{40} zoom	Localize MNG 450 box size 5; Render RCC undrift 450 frames, export zoom 150 max density 0.12
4c T_{60} overview	Localize MNG 450 box size 5; Render RCC undrift 450 frames, export zoom 15 max density 8
4c T_{60} zoom	Localize MNG 450 box size 5; Render RCC undrift 450 frames, export zoom 150 max density 0.12
4c T_{80} overview	Localize MNG 450 box size 5; Render RCC undrift 450 frames, export zoom 15 max density 7.5
4c T_{80} zoom	Localize MNG 450 box size 5; Render RCC undrift 450 frames, export zoom 250 max density 0.035
S2	tempVarianceAnalysis_v4.py with one frame lag, threshold_multiplication 0.5, bin_frames 1 or 3
S4	Localize MNG 2500 box size 5; SPT.link_locs memory 2 search_range 3
S5a	Localize MNG 2500 box size 5; SPT.link_locs memory 2 search_range 1
S5b	Localize MNG 2500 box size 5; SPT.link_locs memory 2 search_range 2
S5c	Localize MNG 2500 box size 5; SPT.link_locs memory 2 search_range 2
S6a overview	Localize MNG 450 box size 5; Render RCC undrift 450 frames, export zoom 10 max density 5

Continued on next page

Table S1

Figure	**Processing**
S6a zoom	Localize MNG 450 box size 5; Render RCC undrift 450 frames, export zoom 60 max density 0.6
S6b overview	Localize MNG 450 box size 5; Render RCC undrift 450 frames, export zoom 10 max density 10
S6b zoom	Localize MNG 450 box size 5; Render RCC undrift 450 frames, export zoom 60 max density 0.25
S7a overview	Localize MNG 450 box size 5; Render RCC undrift 450 frames, export zoom 15 max density 7
S7a zoom	Localize MNG 450 box size 5; Render RCC undrift 450 frames, export zoom 150 max density 0.15
S7b overview	Localize MNG 450 box size 5; Render RCC undrift 450 frames, export zoom 15 max density 6
S7b zoom	Localize MNG 450 box size 5; Render RCC undrift 450 frames, export zoom 150 max density 0.08

Table S2: Unfunctionalized staple strands used in all experiments.

Name	Sequence
0[47]1[31]	AGAAAGGAACAACTAAAGGAATTCAAAAAAA
0[79]1[63]	ACAACTTTCAACAGTTTCAGCGGATGTATCGG
0[111]1[95]	TAAATGAATTTTCTGTATGGGATTAATTTCTT
0[143]1[127]	TCTAAAGTTTTGTCGTCTTTCCAGCCGACAA
0[175]0[144]	TCCACAGACAGCCCTCATAGTTAGCGTAACGA
0[207]1[191]	TCACCAGTACAAACTACAACGCCTAGTACCAG
0[239]1[223]	AGGAACCCATGTACCGTAACACTTGATATAA
0[271]1[255]	CCACCCTCATTTTCAGGGATAGCAACCGTACT
1[32]3[31]	AGGCTCCAGAGGCTTTGAGGACACGGGTAA
1[64]4[64]	TTTATCAGGACAGCATCGGAACGACACCAACC-TAAAACGAGGTCAATC
1[96]3[95]	AAACAGCTTTTTGCGGGATCGTCAACACTAAA
1[128]4[128]	TGACAACTCGCTGAGGCTTGCATTATAC-CAAGCGCGATGATAAA
1[160]2[144]	TTAGGATTGGCTGAGACTCCTCAATAACCGAT
1[192]4[192]	GCGGATAACCTATTATTCTGAAACAGACGATTG-GCCTTGAAGAGCCAC
1[224]3[223]	GTATAGCAAACAGTTAATGCCCAATCCTCA
1[256]4[256]	CAGGAGGTGGGGTCAGTGCCTTGAGTCTCT-GAATTTACCGGGAACCAG
2[47]0[48]	ACGGCTACAAAAGGAGCCTTTAATGTGAGAAT
2[79]0[80]	CAGCGAAACTTGCTTTCGAGGTGTTGCTAA
2[111]0[112]	AAGGCCGCTGATACCGATAGTTGCGACGTTAG
2[143]1[159]	ATATTCGGAACCATCGCCCACGCAGAGAAGGA

Continued on next page

Table S2

Name	Sequence
2[175]0[176]	TATTAAGAAGCGGGGTTTTGCTCGTAGCAT
2[207]0[208]	TTTCGGAAGTGCCGTCGAGAGGGTGAGTTTCG
2[239]0[240]	GCCCGTATCCGGAATAGGTGTATCAGCCCAAT
2[271]0[272]	GTTTTAACTTAGTACCGCCACCCAGAGCCA
3[32]5[31]	AATACGTTTGAAAGAGGACAGACTGACCTT
3[96]5[95]	ACACTCATCCATGTTACTTAGCCGAAAGCTGC
3[160]4[144]	TTGACAGGCCACCACCAGAGCCGCGATTTGTA
3[224]5[223]	TTAAAGCCAGAGCCGCCACCCTCGACAGAA
4[47]2[48]	GACCAACTAATGCCACTACGAAGGGGGTAGCA
4[79]2[80]	GCGCAGACAAGAGGCAAAAGAATCCCTCAG
4[111]2[112]	GACCTGCTCTTTGACCCCCAGCGAGGGAGTTA
4[143]3[159]	TCATCGCCAACAAAGTACAACGGACGCCAGCA
4[175]2[176]	CACCAGAAAGGTTGAGGCAGGTCATGAAAG
4[207]2[208]	CCACCCTCTATTCACAAACAAATACCTGCCTA
4[239]2[240]	GCCTCCCTCAGAATGGAAAGCGCAGTAACAGT
4[271]2[272]	AAATCACCTTCCAGTAAGCGTCAGTAATAA
5[32]7[31]	CATCAAGTAAAACGAACTAACGAGTTGAGA
5[96]7[95]	TCATTCAGATGCGATTTTAAGAACAGGCATAG
5[224]7[223]	TCAAGTTTCATTAAAGGTGAATATAAAAGA
6[47]4[48]	TACGTTAAAGTAATCTTGACAAGAACCGAACT
6[79]4[80]	TTATACCACCAAATCAACGTAACGAACGAG
6[111]4[112]	ATTACCTTTGAATAAGGCTTGCCCAAATCCGC
6[175]4[176]	CAGCAAAAGGAAACGTCACCAATGAGCCGC
6[207]4[208]	TCACCGACGCACCGTAATCAGTAGCAGAACCG

Continued on next page

Table S2

Name	Sequence
6[239]4[240]	GAAATTATTGCCTTTAGCGTCAGACCGGAACC
6[271]4[272]	ACCGATTGTCGGCATTTTCGGTCATAATCA
7[32]9[31]	TTTAGGACAAATGCTTTAAACAATCAGGTC
7[56]9[63]	ATGCAGATACATAACGGGAATCGT-CATAAATAAAGCAAAG
7[96]9[95]	TAAGAGCAAATGTTTAGACTGGATAGGAAGCC
7[224]9[223]	AACGCAAAGATAGCCGAACAAACCCTGAAC
7[248]9[255]	GTTTATTTTGTCACAATCTTACCGAAGCCCTT-TAATATCA
8[47]6[48]	ATCCCCCTATACCACATTCAACTAGAAAAATC
8[79]6[80]	AATACTGCCCAAAAGGAATTACGTGGCTCA
8[111]6[112]	AATAGTAAACACTATCATAACCCTCATTGTGA
8[207]6[208]	AAGGAAACATAAAGGTGGCAACATTATCACCG
8[239]6[240]	AAGTAAGCAGACACCACGGAATAATATTGACG
8[271]6[272]	AATAGCTATCAATAGAAAATTCAACATTCA
9[32]11[31]	TTTACCCCAACATGTTTTAAATTTCCATAT
9[64]11[63]	CGGATTGCAGAGCTTAATTGCTGAAACGAGTA
9[256]11[255]	GAGAGATAGAGCGTCTTTCCAGAGGTTTTGAA
10[47]8[48]	CTGTAGCTTGACTATTATAGTCAGTTCATTGA
10[79]8[80]	GATGGCTTATCAAAAAGATTAAGAGCGTCC
10[111]8[112]	TTGCTCCTTTCAAATATCGCGTTTGAGGGGGT
10[207]8[208]	ATCCCAATGAGAATTAACTGAACAGTTACCAG
10[239]8[240]	GCCAGTTAGAGGGTAATTGAGCGCTTTAAGAA
10[271]8[272]	ACGCTAACACCCACAAGAATTGAAAATAGC

Continued on next page

Table S2

Name	Sequence
11[32]13[31]	AACAGTTTTGTACCAAAAACATTTTATTTC
11[64]13[63]	GATTTAGTCAATAAAGCCTCAGAGAACCCTCA
11[128]13[127]	TTTGGGGATAGTAGTAGCATTAAAAGGCCG
11[160]12[144]	CCAATAGCTCATCGTAGGAATCATGGCATCAA
11[192]13[191]	TATCCGGTCTCATCGAGAACAAGCGACAAAAG
11[256]13[255]	GCCTTAAACCAATCAATAATCGGCACGCGCCT
12[47]10[48]	TAAATCGGGATTCCCAATTCTGCGATATAATG
12[79]10[80]	AAATTAAGTTGACCATTAGATACTTTTGCG
12[143]11[159]	TTCTACTACGCGAGCTGAAAAGGTTACCGCGC
12[239]10[240]	CTTATCATTCCCGACTTGCGGGAGCCTAATTT
12[271]10[272]	TGTAGAAATCAAGATTAGTTGCTCTTACCA
13[32]15[31]	AACGCAAAATCGATGAACGGTACCGGTTGA
13[64]15[63]	TATATTTTGTCATTGCCTGAGAGTGGAAGATT
13[128]15[127]	GAGACAGCTAGCTGATAAATTAATTTTTGT
13[160]14[144]	GTAATAAGTTAGGCAGAGGCATTTATGATATT
13[192]15[191]	GTAAAGTAATCGCCATATTTAACAAAACTTTT
13[256]15[255]	GTTTATCAATATGCGTTATACAAACCGACCGT
14[47]12[48]	AACAAGAGGGATAAAAATTTTTAGCATAAAGC
14[143]13[159]	CAACCGTTTCAAATCACCATCAATTCGAGCCA
14[175]12[176]	CATGTAATAGAATATAAAGTACCAAGCCGT
14[271]12[272]	TTAGTATCACAATAGATAAGTCCACGAGCA
15[32]17[31]	TAATCAGCGGATTGACCGTAATCGTAACCG
15[64]18[64]	GTATAAGCCAACCCGTCGGATTCTGAC-GACAGTATCGGCCGCAAGGCG

Continued on next page

Table S2

Name	Sequence
15[96]17[95]	ATATTTTGGCTTTCATCAACATTATCCAGCCA
15[128]18[128]	TAAATCAAAATAATTCGCGTCTCG-GAAACCAGGCAAAGGGAAGG
15[160]16[144]	ATCGCAAGTATGTAAATGCTGATGATAGGAAC
15[192]18[192]	TCAAATATAACCTCCGGCTTAGGTAA-CAATTTCATTTGAAGGCGAATT
15[224]17[223]	CCTAAATCAAAATCATAGGTCTAAACAGTA
15[256]18[256]	GTGATAAAAAGACGCTGAGAAGAGATAAC-CTTGCTTCTGTTCGGGAGA
16[47]14[48]	ACAAACGGAAAAGCCCCAAAAACACTGGAGCA
16[143]15[159]	GCCATCAAGCTCATTTTTTAACCACAAATCCA
16[175]14[176]	TATAACTAACAAAGAACGCGAGAACGCCAA
16[271]14[272]	CTTAGATTTAAGGCGTTAAATAAAGCCTGT
17[32]19[31]	TGCATCTTTCCCAGTCACGACGGCCTGCAG
17[96]19[95]	GCTTTCCGATTACGCCAGCTGGCGGCTGTTTC
17[160]18[144]	AGAAAACAAAGAAGATGATGAAACAGGCTGCG
17[224]19[223]	CATAAATCTTTGAATACCAAGTGTTAGAAC
18[47]16[48]	CCAGGGTTGCCAGTTTGAGGGGACCCGTGGGA
18[79]16[80]	GATGTGCTTCAGGAAGATCGCACAATGTGA
18[111]16[112]	TCTTCGCTGCACCGCTTCTGGTGCGGCCTTCC
18[143]17[159]	CAACTGTTGCGCCATTCGCCATTCAAACATCA
18[175]16[176]	CTGAGCAAAAATTAATTACATTTTGGGTTA
18[207]16[208]	CGCGCAGATTACCTTTTTTAATGGGAGAGACT
18[239]16[240]	CCTGATTGCAATATATGTGAGTGATCAATAGT

Continued on next page

Table S2

Name	Sequence
18[271]16[272]	CTTTTACAAAATCGTCGCTATTAGCGATAG
19[32]21[31]	GTCGACTTCGGCCAACGCGCGGGGTTTTTC
19[96]21[95]	CTGTGTGATTGCGTTGCGCTCACTAGAGTTGC
19[224]21[223]	CTACCATAGTTTGAGTAACATTTAAAATAT
20[47]18[48]	TTAATGAACTAGAGGATCCCCGGGGGGTAACG
20[79]18[80]	TTCCAGTCGTAATCATGGTCATAAAAGGGG
20[111]18[112]	CACATTAAAATTGTTATCCGCTCATGCGGGCC
20[175]18[176]	ATTATCATTCAATATAATCCTGACAATTAC
20[207]18[208]	GCGGAACATCTGAATAATGGAAGGTACAAAAT
20[239]18[240]	ATTTTAAAATCAAAATTATTTGCACGGATTCG
20[271]18[272]	CTCGTATTAGAAATTGCGTAGATACAGTAC
21[32]23[31]	TTTTCACTCAAAGGGCGAAAAACCATCACC
21[56]23[63]	AGCTGATTGCCCTTCAGAGTCCACTAT-TAAAGGGTGCCGT
21[96]23[95]	AGCAAGCGTAGGGTTGAGTGTTGTAGGGAGCC
21[120]23[127]	CCCAGCAGGCGAAAAATCCCTTATAAAT-CAAGCCGGCG
21[184]23[191]	TCAACAGTTGAAAGGAGCAAATGAAAAATCTA-GAGATAGA
21[224]23[223]	CTTTAGGGCCTGCAACAGTGCCAATACGTG
21[248]23[255]	AGATTAGAGCCGTCAAAAAACAGAGGTGAGGC-CTATTAGT
22[47]20[48]	CTCCAACGCAGTGAGACGGGCAACCAGCTGCA
22[79]20[80]	TGGAACAACCGCCTGGCCCTGAGGCCCGCT

Continued on next page

Table S2

Name	Sequence
22[111]20[112]	GCCCGAGAGTCCACGCTGGTTTGCAGCTAACT
22[207]20[208]	AGCCAGCAATTGAGGAAGGTTATCATCATTTT
22[239]20[240]	TTAACACCAGCACTAACAACTAATCGTTATTA
22[271]20[272]	CAGAAGATTAGATAATACATTTGTCGACAA
23[32]22[48]	CAAATCAAGTTTTTTGGGGTCGAAACGTGGA
23[64]22[80]	AAAGCACTAAATCGGAACCCTAATCCAGTT
23[96]22[112]	CCCGATTTAGAGCTTGACGGGGAAAAAGAATA
23[192]22[208]	ACCCTTCTGACCTGAAAGCGTAAGACGCTGAG
23[224]22[240]	GCACAGACAATATTTTTGAATGGGGTCAGTA
23[256]22[272]	CTTTAATGCGCGAACTGATAGCCCCACCAG

Table S3: Docking sites for DNA-PAINT.

Name	Sequence
5[160]6[144] PAINT	GCAAGGCCTCACCAGTAGCACCATGGGCTTGA TT TCCTCCTCCTCCTCCTCCT
6[143]5[159] PAINT	GATGGTTTGAACGAGTAGTAAATTTACCATTA TT TCCTCCTCCTCCTCCTCCT
7[120]9[127] PAINT	CGTTTACCAGACGACAAAGAAGTTTTGC-CATAATTCGA TT TCCTCCTCCTCCTCCTCCT
7[160]8[144] PAINT	TTATTACGAAGAACTGGCATGATTGCGAGAGG TT TCCTCCTCCTCCTCCTCCT
7[184]9[191] PAINT	CGTAGAAAATACATACCGAGGAAACGCAATAA-GAAGCGCA TT TCCTCCTCCTCCTCCTCCT
8[143]7[159] PAINT	CTTTTGCAGATAAAAACCAAAATAAAGACTCC TT TCCTCCTCCTCCTCCTCCT
8[175]6[176] PAINT	ATACCCAACAGTATGTTAGCAAATTAGAGC TT TCCTCCTCCTCCTCCTCCT
9[96]11[95] PAINT	CGAAAGACTTTGATAAGAGGTCATATTTCGCA TT TCCTCCTCCTCCTCCTCCT
9[128]11[127] PAINT	GCTTCAATCAGGATTAGAGAGTTATTTTCA TT TCCTCCTCCTCCTCCTCCT
9[160]10[144] PAINT	AGAGAGAAAAAAATGAAAATAGCAAGCAAACT TT TCCTCCTCCTCCTCCTCCT
9[192]11[191] PAINT	TTAGACGGCCAAATAAGAAACGATAGAAGGCT TT TCCTCCTCCTCCTCCTCCT
9[224]11[223] PAINT	AAAGTCACAAAATAAACAGCCAGCGTTTTA TT TCCTCCTCCTCCTCCTCCT

Continued on next page

Table S3

Name	Sequence
10[143]9[159] PAINT	CCAACAGGAGCGAACCAGACCGGAGCCTTTAC TT TCCTCCTCCTCCTCCTCCT
10[175]8[176] PAINT	TTAACGTCTAACATAAAAACAGGTAACGGA TT TCCTCCTCCTCCTCCTCCT
11[96]13[95] PAINT	AATGGTCAACAGGCAAGGCAAAGAGTAATGTG TT TCCTCCTCCTCCTCCTCCT
11[224]13[223] PAINT	GCGAACCTCCAAGAACGGGTATGACAATAA TT TCCTCCTCCTCCTCCTCCT
12[111]10[112] PAINT	TAAATCATATAACCTGTTTAGCTAACCTTTAA TT TCCTCCTCCTCCTCCTCCT
12[207]10[208] PAINT	GTACCGCAATTCTAAGAACGCGAGTATTATTT TT TCCTCCTCCTCCTCCTCCT
13[96]15[95] PAINT	TAGGTAAACTATTTTTGAGAGATCAAACGTTA TT TCCTCCTCCTCCTCCTCCT
13[224]15[223] PAINT	ACAACATGCCAACGCTCAACAGTCTTCTGA TT TCCTCCTCCTCCTCCTCCT
14[79]12[80] PAINT	GCTATCAGAAATGCAATGCCTGAATTAGCA TT TCCTCCTCCTCCTCCTCCT
14[111]12[112 PAINT]	GAGGGTAGGATTCAAAAGGGTGAGACATCCAA TT TCCTCCTCCTCCTCCTCCT
14[207]12[208 PAINT]	AATTGAGAATTCTGTCCAGACGACTAAACCAA TT TCCTCCTCCTCCTCCTCCT
14[239]12[240] PAINT	AGTATAAAGTTCAGCTAATGCAGATGTCTTTC TT TCCTCCTCCTCCTCCTCCT

Continued on next page

Table S3

Name	Sequence
16[79]14[80] PAINT	GCGAGTAAAAATATTTAAATTGTTACAAAG TT TCCTCCTCCTCCTCCTCCT
16[111]14[112] PAINT	TGTAGCCATTAAAATTCGCATTAAATGCCGGA TT TCCTCCTCCTCCTCCTCCT
16[207]14[208] PAINT	ACCTTTTTATTTTAGTTAATTTCATAGGGCTT TT TCCTCCTCCTCCTCCTCCT
16[239]14[240] PAINT	GAATTTATTTAATGGTTTGAAATATTCTTACC TT TCCTCCTCCTCCTCCTCCT
19[160]20[144] PAINT	GCAATTCACATATTCCTGATTATCAAAGTGTA TT TCCTCCTCCTCCTCCTCCT
20[143]19[159] PAINT	AAGCCTGGTACGAGCCGGAAGCATAGATGATG TT TCCTCCTCCTCCTCCTCCT
21[160]22[144] PAINT	TCAATATCGAACCTCAAATATCAATTCCGAAA TT TCCTCCTCCTCCTCCTCCT
22[143]21[159] PAINT	TCGGCAAATCCTGTTTGATGGTGGACCCTCAA TT TCCTCCTCCTCCTCCTCCT
22[175]20[176] PAINT	ACCTTGCTTGGTCAGTTGGCAAAGAGCGGA TT TCCTCCTCCTCCTCCTCCT
23[128]23[159] PAINT	AACGTGGCGAGAAAGGAAGGGAAACCAGTAA TT TCCTCCTCCTCCTCCTCCT
23[160]22[176] PAINT	TAAAAGGGACATTCTGGCCAACAAAGCATC TT TCCTCCTCCTCCTCCTCCT
12[175]10[176] PAINT	TTTTATTTAAGCAAATCAGATATTTTTTGT TT TCCTCCTCCTCCTCCTCCT

Table S4: Unfunctionalized staples for SPT (replacing unused DNA-PAINT docking sites).

Name	Sequence
5[160]6[144]	GCAAGGCCTCACCAGTAGCACCATGGGCTTGA
6[143]5[159]	GATGGTTTGAACGAGTAGTAAATTTACCATTA
7[120]9[127]	CGTTTACCAGACGACAAAGAAGTTTTGC-CATAATTCGA
7[160]8[144]	TTATTACGAAGAACTGGCATGATTGCGAGAGG
7[184]9[191]	CGTAGAAAATACATACCGAGGAAACGCAATAA-GAAGCGCA
8[143]7[159]	CTTTTGCAGATAAAAACCAAAATAAAGACTCC
8[175]6[176]	ATACCCAACAGTATGTTAGCAAATTAGAGC
9[96]11[95]	CGAAAGACTTTGATAAGAGGTCATATTTCGCA
9[128]11[127]	GCTTCAATCAGGATTAGAGAGTTATTTTCA
9[160]10[144]	AGAGAGAAAAAAATGAAAATAGCAAGCAAACT
9[192]11[191]	TTAGACGGCCAAATAAGAAACGATAGAAGGCT
9[224]11[223]	AAAGTCACAAAATAAACAGCCAGCGTTTTA
10[143]9[159]	CCAACAGGAGCGAACCAGACCGGAGCCTTTAC
10[175]8[176]	TTAACGTCTAACATAAAAACAGGTAACGGA
11[96]13[95]	AATGGTCAACAGGCAAGGCAAAGAGTAATGTG
11[224]13[223]	GCGAACCTCCAAGAACGGGTATGACAATAA
12[111]10[112]	TAAATCATATAACCTGTTTAGCTAACCTTTAA
12[207]10[208]	GTACCGCAATTCTAAGAACGCGAGTATTATTT
13[96]15[95]	TAGGTAAACTATTTTTGAGAGATCAAACGTTA
13[224]15[223]	ACAACATGCCAACGCTCAACAGTCTTCTGA
14[79]12[80]	GCTATCAGAAATGCAATGCCTGAATTAGCA

Continued on next page

Table S4

Name	Sequence
14[111]12[112]	GAGGGTAGGATTCAAAAGGGTGAGACATCCAA
14[207]12[208]	AATTGAGAATTCTGTCCAGACGACTAAACCAA
14[239]12[240]	AGTATAAAGTTCAGCTAATGCAGATGTCTTTC
16[79]14[80]	GCGAGTAAAAATATTTAAATTGTTACAAAG
16[111]14[112]	TGTAGCCATTAAAATTCGCATTAAATGCCGGA
16[207]14[208]	ACCTTTTTATTTTAGTTAATTTCATAGGGCTT
16[239]14[240]	GAATTTATTTAATGGTTTGAAATATTCTTACC
19[160]20[144]	GCAATTCACATATTCCTGATTATCAAAGTGTA
20[143]19[159]	AAGCCTGGTACGAGCCGGAAGCATAGATGATG
21[160]22[144]	TCAATATCGAACCTCAAATATCAATTCCGAAA
22[143]21[159]	TCGGCAAATCCTGTTTGATGGTGGACCCTCAA
22[175]20[176]	ACCTTGCTTGGTCAGTTGGCAAAGAGCGGA
23[128]23[159]	AACGTGGCGAGAAAGGAAGGGAAACCAGTAA
23[160]22[176]	TAAAAGGGACATTCTGGCCAACAAAGCATC

Table S5: Biotinylated staples for immobilization on glass.

Name	Sequence
4[63]6[56] Bio	[Bio]ATAAGGGAACCGGATATTCATTACGTCA-GGACGTTGGGAA
4[127]6[120] Bio	[Bio]TTGTGTCGTGACGAGAAACACCAAATT-TCAACTTTAAT
4[191]6[184] Bio	[Bio]CACCCTCAGAAACCATCGATAGCATTGA-GCCATTTGGGAA
4[255]6[248] Bio	[Bio]AGCCACCACTGTAGCGCGTTTTCAAGGG-AGGGAAGGTAAA
18[63]20[56] Bio	[Bio]ATTAAGTTTACCGAGCTCGAATTCGGGA-AACCTGTCGTGC
18[127]20[120] Bio	[Bio]GCGATCGGCAATTCCACACAACAGGTGC-CTAATGAGTG
18[191]20[184] Bio	[Bio]ATTCATTTTTGTTTGGATTATACTAAGAA-ACCACCAGAAG
18[255]20[248] Bio	[Bio]AACAATAACGTAAAACAGAAATAAAAATC-CTTTGCCCGAA

Table S6: TEG-chol anchor binding staples for membrane tethering.

Name	Sequence
4[63]6[56] Chol	TATGAGAAGTTAGGAATGTTAATAAGGGAAC-CGGATATTCATTACGTCAGGACGTTGGGAA
4[127]6[120] Chol	TATGAGAAGTTAGGAATGTTATTGTGTCGT-GACGAGAAACACCAAATTTCAACTTTAAT
4[191]6[184] Chol	TATGAGAAGTTAGGAATGTTACACCCTCA-GAAACCATCGATAGCATTGAGCCATTTGGGAA
4[255]6[248] Chol	TATGAGAAGTTAGGAATGTTAAGCCACCACTG-TAGCGCGTTTTCAAGGGAGGGAAGGTAAA
18[63]20[56] Chol	TATGAGAAGTTAGGAATGTTAATTAAGTTTACC-GAGCTCGAATTCGGGAAACCTGTCGTGC
18[127]20[120] Chol	TATGAGAAGTTAGGAATGTTAGCGATCG-GCAATTCCACACAACAGGTGCCTAATGAGTG
18[191]20[184] Chol	TATGAGAAGTTAGGAATGT-TAATTCATTTTTGTTTGGATTATACTAA-GAAACCACCAGAAG
18[255]20[248] Chol	TATGAGAAGTTAGGAATGTTAAACAATAACG-TAAAACAGAAATAAAAATCCTTTGCCCGAA

Table S7: A_7 extension staples.

Name	Sequence
0[303]1[295]	AAAAAAACAGAACCGCCACCCTCTCAGAAC-CGCCACCCT
1[8]0[0]	TCACGTTGAAAATCTCGCGAATAATAATTTT-TAAAAAAA
6[303]7[295]	AAAAAAACAAAGACAAAAGGGCGTATGGTT-TACCAGCGC
7[8]6[0]	GGTAGAAAGATTCATCGAACAACATTATTA-CAAAAAAAA
16[303]17[295]	AAAAAAAAATCCTTGAAAACATAATTAATTTTC-CCTTAG
17[8]16[0]	GTGTAGATGGGCGCATGGGATAGGT-CACGTTGAAAAAAA
22[303]23[295]	AAAAAAAAAAAATACCGAACGAACTAAAA-CATCGCCATT
23[8]22[0]	TGGCCCACTACGTGAACCGTCTATCAGGGC-GAAAAAAAA

Table S8: Connector strands.

Name	Sequence
T_{14}	TTTTTTTTTTTTTT
T_{20}	TTTTTTTTTTTTTTTTTTTT
T_{40}	TTTTTTTTTTTTTTTTTTTTTTTTTTTTTTTTTTTT-
	TTTTTTT
T_{60}	TTTTTTTTTTTTTTTTTTTTTTTTTTTTTTTTTTTT-
	TTTTTTTTTTTTTTTTTTTTTTTTTTTT
T_{80}	TTTTTTTTTTTTTTTTTTTTTTTTTTTTTTTTTTTT-
	TTTTTTTTTTTTTTTTTTTTTTTTTTTTTTTTTTTT-
	TTTTTTTTTTTTTT
20nt_T_6	TTTTTTCCCCCCTTTTTT
40nt_T_6	TTTTTTCCCCCCCCCCCCCCCCCCCCCCCCCC-
	CTTTTTT
60nt_T_6	TTTTTTCCCCCCCCCCCCCCCCCCCCCCCCCCC-
	CCCCCCCCCCCCCCCCCCCCTTTTTT
80nt_T_6	TTTTTTCCCCCCCCCCCCCCCCCCCCCCCCCC-
	CCCCCCCCCCCCCCCCCCCCCCCCCCCCCC-
	CCCCCCCCCCCCTTTTTT
20nt_T_7	TTTTTTTCCCCCCTTTTTTT
40nt_T_7	TTTTTTTCCCCCCCCCCCCCCCCCCCCCCCCC-
	CTTTTTTT
60nt_T_7	TTTTTTTCCCCCCCCCCCCCCCCCCCCCCCCCC-
	CCCCCCCCCCCCCCCCCCCCTTTTTTT

Continued on next page

Table S8

Name	Sequence
80nt_T_7	TTTTTTTCCCCCCCCCCCCCCCCCCCCCC-CCCCCCCCCCCCCCCCCCCCCCCCCCCCCC-CCCCCCCCCCCCCTTTTTTT
20nt_T_8	TTTTTTTTCCCCCCTTTTTTTT
40nt_T_8	TTTTTTTTCCCCCCCCCCCCCCCCCCCCCCCCCC-CTTTTTTTT
60nt_T_8	TTTTTTTTCCCCCCCCCCCCCCCCCCCCCCCCCC-CCCCCCCCCCCCCCCCCCCCTTTTTTTT
80nt_T_8	TTTTTTTTCCCCCCCCCCCCCCCCCCCCCC-CCCCCCCCCCCCCCCCCCCCCCCCCCCCCC-CCCCCCCCCCCCCTTTTTTTT
20nt_T_9	TTTTTTTTTCCCCCTTTTTTTTT
40nt_T_9	TTTTTTTTTCCCCCCCCCCCCCCCCCCCCCCCCC-CCTTTTTTTTT
60nt_T_9	TTTTTTTTTCCCCCCCCCCCCCCCCCCCCCCCCC-CCCCCCCCCCCCCCCCCCCCTTTTTTTTT
80nt_T_9	TTTTTTTTTCCCCCCCCCCCCCCCCCCCCCC-CCCCCCCCCCCCCCCCCCCCCCCCCCCCCC-CCCCCCCCCCCCCTTTTTTTT
ScaffoldIZ1L	GC GAA TAA TAA TTT TT CCCCCC CAG AAC CGC CAC CCT C
ScaffoldIZ2L	GA ACA ACA TTA TTA CA AAAAAA CAA AGA CAA AAG GGC C

Continued on next page

Table S8

Name	Sequence
ScaffoldIZ3L	GG GAT AGG TCA CGT TG AAAAAAA AAT CCT TGA AAA CAT A
ScaffoldIZ4L	CC GTC TAT CAG GGC GA AAAAAAA AAA AAT ACC GAA CGA ACT A
ScaffoldIZ1	GC GAA TAA TAA TTT TT CAG AAC CGC CAC CCT C
ScaffoldIZ2	GA ACA ACA TTA TTA CA CAA AGA CAA AAG GGC C
ScaffoldIZ3	GG GAT AGG TCA CGT TG AAT CCT TGA AAA CAT A
ScaffoldIZ4	CC GTC TAT CAG GGC GA AAA AAT ACC GAA CGA ACT A

Table S9: Miscellaneous oligonucleotides.

Name/Purpose	**Sequence**
TEG-Chol anchor	TAACATTCCTAACTTCTCATA[CHOL]
Docking site extension for SPT (12[175]10[176] A20)	TTTTATTTAAGCAAATCAGATATTTTTTGT TT AAGAAAGAAAAGAAGAAAAG
Tracking handle ([TCT]38-cA20)	TCT TCT TCT TCT TCT TCT TCT TCT TCT TCT TCT TCT TCT TCT TCT TCT TCT TCT TCT TCT TCT TCT TCT TCT TCT TCT TCT TCT TCT TCT TCT TCT TCT TCT TCT TCT TCT TCT CTT TTC TTC TTT TCT TTC TT
R1$_{\text{6nt}}$-Cy3B imager strand	GGAGGA-Cy3B
R1$_{\text{18nt}}$-Cy3B imager strand	GGAGGAGGAGGAGGAGGA-Cy3B
R5_s2$_{\text{8nt}}$-Cy3B imager strand	AGAAGAAG-Cy3B

References

(1) Kolin, D. L.; Wiseman, P. W. Advances in Image Correlation Spectroscopy: Measuring Number Densities, Aggregation States, and Dynamics of Fluorescently labeled Macromolecules in Cells. *Cell Biochemistry and Biophysics* **2007**, *49*, 141–164.

(2) Elson, E. L. In *Methods in enzymology*; Tetin, S. Y., Ed.; Academic Press, 2013; Vol. 518; pp 11–41.

(3) Widengren, J.; Mets, l. In *Single molecule detection in solution*; Zander, C., Enderlein, J.,

Keller, R. A., Eds.; Wiley-VCH Verlag GmbH & Co. KGaA: Weinheim, FRG, 2002; pp 69–120.

(4) Petrov, E. P.; Schwille, P. In *Standardization and quality assurance in fluorescence measurements II: Bioanalytical and biomedical applications*; Resch-Genger, U., Ed.; Springer Berlin Heidelberg: Berlin, Heidelberg, 2008; pp 145–197.

(5) Palmer, A.; Thompson, N. Molecular aggregation characterized by high order autocorrelation in fluorescence correlation spectroscopy. *Biophysical Journal* **1987**, *52*, 257–270.

(6) Sergeev, M.; Costantino, S.; Wiseman, P. W. Measurement of monomer-oligomer distributions via fluorescence moment image analysis. *Biophysical Journal* **2006**, *91*, 3884–3896.

B
Appendix to Chapter 6

Biophysical Journal, Volume *124*

Supplemental information

Fluorescence correlation spectroscopy for particle sizing: A notorious challenge

Jan-Hagen Krohn, Adam Mamot, Nastasja Kaletta, Yusuf Qutbuddin, and Petra Schwille

Supplemental Methods for shown example data

Production and gel analysis of chain-terminated ssRNA samples:

Transcription mixtures were prepared by mixing the following components in RNase-free 1.5 ml tubes: transcription buffer (40 mM Tris-HCl pH 7.9, 6 mM $MgCl_2$, 10 mM DTT, 10 mM NaCl, 2 mM spermidine, Thermo), mixture of NTPs (2 mM each, Thermo), mixture of 3'-dATP and 3'-dGTP (100 µM each, JenaBioscence), DNA template (40 ng/µl, pMLB_mGLopt_MinDE plasmid) (85), Aminoallyl-UTP-ATTO-488 (0.2, 0.6, 2, 6, 20, or 60 µM, Jena Bioscience), Ribolock (1 U/µl, Thermo), T7 RNA polymerase HC (10 U/µl, Thermo) and RNase-free water (final volume of 50 µl). After 2.5 h of incubation at 37°C, DNAse I (0.5 µl, 1 U/µl, RNase-free, Thermo) was added, and the incubation was continued for 30 min. Afterwards, the RNA products were isolated with Monarch RNA clean-up kit 10 µg (NEB) and resolved with agarose gel electrophoresis (1% Agarose, TT buffer, 100 V) (86). The gel was stained with SybrGold and the bands were visualized with Amersham Gel Imager 600 (GE Healthcare).

Confocal FCS data acquisition:

Spot FCS was performed at a PicoQuant MicroTime 200 confocal microscope equipped with a high-resolution water immersion objective (UPlanApo 60x NA 1.2, Evident). Fluorescence was excited at 483 nm using a pulsed ps diode laser (PicoQuant) operated at 40 MHz repetition rate, and signal from ca. 500 to 540 nm was detected on a SPAD photon counting detector (Excelitas).

Fluorescence signal from a solution of Alexa Fluor 488 carboxylate (20 nM, Invitrogen) diluted in measurement buffer (150 mM KCl, 5 mM EDTA, 25 mM Tris-HCl, pH 7.5) was used to optimize pinhole position and correction collar setting, and calibrate the confocal observation volume, before measurements.

5 to 10 µl of purified ssRNA were diluted with 45 µl of the same measurement buffer as the calibration samples, heat-denatured for 5 min at 95 °C, cooled for 3 min on ice, and transferred into wells of ibidi µ-slide 18 Well Glass Bottom chambers. Measurements were started within 10 min after transfer of samples into chambers. Data was acquired for 30 min with ca. 1 µW laser power at 30 °C.

FCS data analysis:

FCS data were exported using custom Python code based on tttrlib (87) using automated Fluorescence Lifetime Correlation Spectroscopy-based background correction (27). The code is available under https://github.com/Janhagenkrohn/FCS_Fixer.

Single component diffusion fitting with Eq. 3 and anomalous diffusion fitting with Eq. 6, and plotting of all ACFs and fits, were performed in Origin Pro 9.8.5.204 (OriginLab).

Fitting with maximum entropy method (MEM) or stretched exponential profiles was performed using custom Python code available under https://github.com/Janhagenkrohn/FCS_Spectrum_fitting. The MEM fitting algorithm was based on references (70, 74, 88). In particular, previously published MEM analysis strategies for FCS (74, 75) were extended with the test criterion from ref. (88) to automatically adapt the Lagrange multiplier to the signal to noise ratio of the data. 120 logarithmically spaced diffusion times ranging from 1 µs to 1 s were considered in analysis. After fitting, amplitudes were recalculated to mass fractions based on Eq. 4 in Origin Pro 9.8.5.204 (OriginLab).

The stretched exponential model was based on Eqs. 3 and 4 with an additional bin width term. A histogram of 70 $\langle N_j \rangle$ values over diffusion times ranging from the an assumed monomer diffusion time (13.5 µs, based on a size ladder of ssRNA designs with defined length) to 1 s was fitted while forcing $\langle N_j \rangle j$ (unbinned profile of mass fraction over j) to follow a stretched-exponential profile. Data was interpreted based on a relation of diffusion time and stoichiometry analogous to Eq. 6 as follows assuming a random coil polymer behavior:

	$\frac{\tau_{d,j}}{\tau_{d,monomer}} = j^{\frac{1}{2}}$	Eq. S1

Downstream analysis and plotting was performed in Origin Pro 9.8.5.204 (OriginLab).

Simulations:

Simulations were performed using custom Python code available on https://github.com/Janhagenkrohn/FCS_Spectrum_fitting. Briefly, lognormal distributions of particle count over stoichiometry were defined. Species-wise fluorescence signal and autocorrelation function weights were calculated by explicitly iterating over all label counts $j_{label} \leq j$ for each oligomer $j \leq j_{max}$ species and considering the lognormal concentration profile, binomial labelling statistics for a defined labelling probability p, and logarithmically spaced bin widths. Species-wise diffusion times were approximated using Eq. 2 with $\tau_{d,monomer} = 210$ µs. From these numbers, ACFs for each j and j_{label} were calculated and added iteratively. Note that Eq. 4 was not explicitly used in simulations. Further analysis and plotting was performed in Origin Pro 9.8.5.204 (OriginLab).

Supplemental Figures

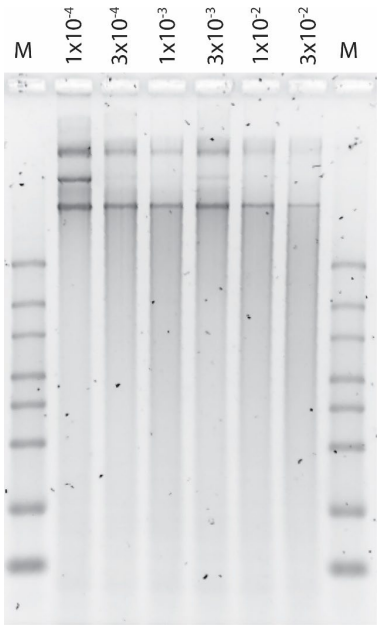

Figure S1: Agarose gel after SybrGold staining. Samples of the RNA products (120 ng), exhibiting different labelling ratio (from $1x10^{-4}$ to $3x10^{-2}$ of fluorescent UTP analog/NTPs) were diluted with loading buffer (48% formamide, 0.013% SDS, 0.25 mM EDTA, bromophenol blue), thermally denatured (5 min at 95°C, then 5 min at 4°C) and loaded onto the gel. M – riboruler high range RNA ladder (Thermo) was used as a size reference.

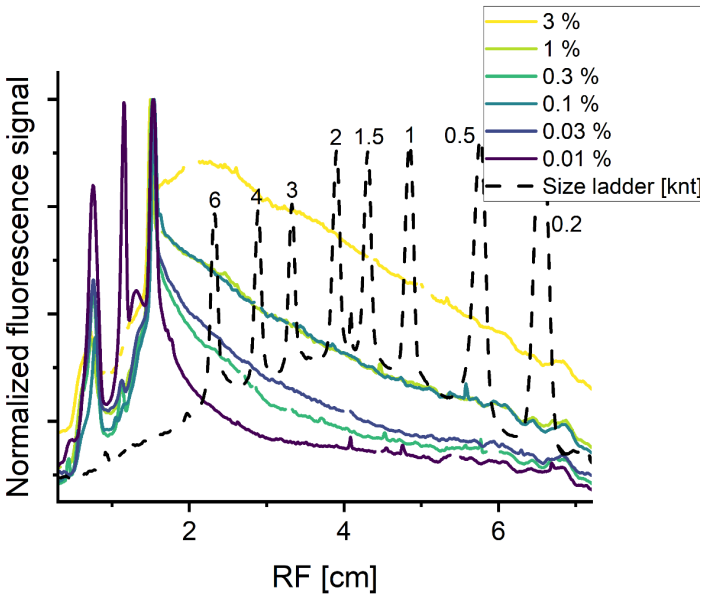

Figure S2: Size distribution of the ssRNA probes. Densitometric analysis of the agarose gel was performed with ImageJ to plot a lane profile for each ssRNA sample. For clarity, peaks originating from dust particles were removed manually from the profiles (compare Fig. S1).

List of Figures

Bibliography

[1] Qutbuddin, Y. *et al.* Design Features to Accelerate the Higher-Order Assembly of DNA Origami on Membranes. *The Journal of Physical Chemistry B* **125**, 13181–13191 (2021). URL https://doi.org/10.1021/acs.jpcb.1c07694. Publisher: American Chemical Society. [cited on pages vii and 49.]

[2] Krohn, J.-H., Babl, L., Isnel, L., Qutbuddin, Y. & Schwille, P. in *Measuring Partition Coefficients of In Vitro Biomolecular Condensates Using Fluorescence Correlation Spectroscopy* (ed.Dame, R. T.) *Bacterial Chromatin: Methods and Protocols* 455–475 (Springer US, New York, NY, 2024). URL https://doi.org/10.1007/978-1-0716-3930-6_21. [cited on pages vii and 65.]

[3] Krohn, J.-H., Mamot, A., Kaletta, N., Qutbuddin, Y. & Schwille, P. Fluorescence correlation spectroscopy for particle sizing: A notorious challenge. *Biophysical Journal* S0006349525001717 (2025). URL https://linkinghub.elsevier.com/retrieve/pii/S0006349525001717. [cited on pages vii and 89.]

[4] Merino-Salomón, A. *et al.* Crosslinking by ZapD drives the assembly of short FtsZ filaments into toroidal structures in solution (2025). URL https://elifesciences.org/reviewed-preprints/95557v2. [cited on pages vii, 101, 102, 103, and 106.]

[5] Balakrishnan, A. *et al.* Unraveling the hidden temporal range of fast β2-adrenergic receptor mobility by time-resolved fluorescence. *Communications Biology* **5**, 176 (2022). URL https://doi.org/10.1038/s42003-022-03106-4. [cited on pages vii and 37.]

[6] Kanaparthi, D. *et al.* The reproduction of gram-negative protoplasts and the influence of environmental conditions on this process. *iScience* **26**, 108149 (2023). URL https://linkinghub.elsevier.com/retrieve/pii/S2589004223022265. [cited on page vii.]

[7] Kanaparthi, D. *et al.* The reproduction process of Gram-positive protocells. *Scientific Reports* **14**, 7075 (2024). URL https://www.nature.com/articles/s41598-024-57369-4. [cited on page vii.]

[8] Betaneli, V., Mücksch, J. & Schwille, P. in *Fluorescence Correlation Spectroscopy to Examine Protein–Lipid Interactions in Membranes* (ed.Kleinschmidt, J. H.) *Lipid-Protein Interactions: Methods and Protocols*, Vol. 2003 415–447 (Springer New York, New York, NY, 2019). URL http://link.springer.com/10.1007/978-1-4939-9512-7_18. [cited on pages vii and 125.]

[9] Wall, W. in *Timeline of the Optical Telescope* (ed.Wall, W.) *A History of Optical Telescopes in Astronomy* 129–148 (Springer International Publishing, Cham, 2018). URL http://link.springer.com/10.1007/978-3-319-99088-0_10. Series Title: Historical & Cultural Astronomy. [cited on pages 5 and 7.]

[10] Hooke, R. *Micrographia, or, Some physiological descriptions of minute bodies made by magnifying glasses with observations and inquiries thereupon* (The Royal Society, London, 1665). [cited on page 5.]

[11] Virchow, R. in *Rudolf Virchow: Cellular-Pathologie* (ed.Eckart, W. U.) *Rudolf Virchow und Gustav Adolph Spiess: Cellular-Pathologie versus Humoral- und Solidarpathologie* 31–68 (Springer Berlin Heidelberg, Berlin, Heidelberg, 2016). URL http://link.springer.com/10.1007/978-3-642-41681-1_2. [cited on page 5.]

[12] Eckert, M. Max von Laue and the discovery of X-ray diffraction in 1912. *Annalen der Physik* **524** (2012). URL https://onlinelibrary.wiley.com/doi/10.1002/andp.201200724. [cited on page 5.]

[13] Holzer, B. Introduction to Particle Accelerators and their Limitations. *CERN Yellow Reports* (2016). URL https://e-publishing.cern.ch/index.php/CYR/article/view/212. Artwork Size: 29 Pages Publisher: CERN, Geneva. [cited on page 5.]

[14] Eschenmoser, A. The search for the chemistry of life's origin. *Tetrahedron* **63**, 12821–12844 (2007). URL https://linkinghub.elsevier.com/retrieve/pii/S0040402007017176. [cited on page 5.]

[15] Kriebisch, C. M. *et al.* A roadmap toward the synthesis of life. *Chem* 102399 (2025). URL https://linkinghub.elsevier.com/retrieve/pii/S2451929424006442. [cited on page 5.]

[16] Karsenti, E. Self-organization in cell biology: a brief history. *Nature Reviews Molecular Cell Biology* **9**, 255–262 (2008). URL https://www.nature.com/articles/nrm2357. [cited on page 6.]

[17] Frey, E., Halatek, J., Kretschmer, S. & Schwille, P. in *Protein Pattern Formation* (eds Bassereau, P. & Sens, P.) *Physics of Biological Membranes* 229–260 (Springer International Publishing, Cham, 2018). URL http://link.springer.com/10.1007/978-3-030-00630-3_10. [cited on pages 6 and 25.]

[18] Schrödinger, E. *What is Life?: With Mind and Matter and Autobiographical Sketches* (Cambridge University Press, Cambridge, 2012). [cited on page 6.]

[19] Berg, J. M., Tymoczko, J. L., Gatto jr., G. J. & Stryer, L. in *Molekulare Motoren* (eds Berg, J. M., Tymoczko, J. L., Gatto jr., G. J. & Stryer, L.) *Stryer Biochemie* 1201–1226 (Springer Berlin Heidelberg, Berlin, Heidelberg, 2018). URL https://doi.org/10.1007/978-3-662-54620-8_35. [cited on pages 6 and 30.]

[20] Danchin, A. & Sekowska, A. The logic of metabolism. *Perspectives in Science* **6**, 15–26 (2015). URL https://linkinghub.elsevier.com/retrieve/pii/S2213020915000282. [cited on page 6.]

[21] Ramm, B., Heermann, T. & Schwille, P. The E. coli MinCDE system in the regulation of protein patterns and gradients. *Cellular and Molecular Life Sciences* **76**, 4245–4273 (2019). URL http://link.springer.com/10.1007/s00018-019-03218-x. [cited on pages 6, 24, and 25.]

[22] Banani, S. F., Lee, H. O., Hyman, A. A. & Rosen, M. K. Biomolecular condensates: organizers of cellular biochemistry. *Nature Reviews Molecular Cell Biology* **18**, 285–298 (2017). URL http://www.nature.com/articles/nrm.2017.7. [cited on pages 6 and 26.]

[23] Südhof, T. Neurotransmitter Release: The Last Millisecond in the Life of a Synaptic Vesicle. *Neuron* **80**, 675–690 (2013). URL https://doi.org/10.1016/j.neuron.2013.10.022. Publisher: Elsevier. [cited on page 6.]

[24] Špelda, D. The role of the telescope and microscope in the constitution of the Idea of scientific progress. *The Seventeenth Century* **34**, 107–126 (2019). URL https://www.tandfonline.com/doi/full/10.1080/0268117X.2017.1356743. [cited on page 7.]

[25] Streitenberger, P. & Schneider, D. Otto von Guericke and the Founding of the Science of Air Pressure. *Vakuum in Forschung und Praxis* **14**, 360–369 (2002). URL https://onlinelibrary.wiley.com/doi/10.1002/vipr.200290008. [cited on page 7.]

[26] Stokes, G. G. On the Change of Refrangibility of Light. *Philosophical Transactions of the Royal Society of London* **142**, 463–562 (1852). Publisher: The Royal Society. [cited on page 10.]

[27] Coons, A. H., Creech, H. J., Jones, R. N. & Berliner, E. The Demonstration of Pneumococcal Antigen in Tissues by the Use of Fluorescent Antibody. *J Immunol* **45**, 159–170 (1942). URL https://journals.aai.org/jimmunol/article/45/3/159/63211/The-Demonstration-of-Pneumococcal-Antigen-in. [cited on page 10.]

[28] Gust, A. *et al.* A Starting Point for Fluorescence-Based Single-Molecule Measurements in Biomolecular Research. *Molecules* **19**, 15824–15865 (2014). URL http://www.mdpi.com/1420-3049/19/10/15824. [cited on page 10.]

[29] Tian, H., Fürstenberg, A. & Huber, T. Labeling and Single-Molecule Methods To Monitor G Protein-Coupled Receptor Dynamics. *Chem Rev* **117**, 186–245 (2017). [cited on page 10.]

[30] Wäldchen, S., Lehmann, J., Klein, T., van de Linde, S. & Sauer, M. Light-induced cell damage in live-cell super-resolution microscopy. *Scientific Reports* **5** (2015). URL http://www.nature.com/articles/srep15348. [cited on page 10.]

[31] Strickler, S. J. & Berg, R. A. Relationship between Absorption Intensity and Fluorescence Lifetime of Molecules. *The Journal of Chemical Physics* **37**, 814–822 (1962). URL http://aip.scitation.org/doi/10.1063/1.1733166. [cited on page 11.]

[32] Cesa, Y. *et al.* Manipulation of the local density of photonic states to elucidate fluorescent protein emission rates. *Physical Chemistry Chemical Physics* **11**, 2525 (2009). URL http://xlink.rsc.org/?DOI=b817902f. [cited on page 12.]

[33] Chizhik, A. I., Gregor, I., Ernst, B. & Enderlein, J. Nanocavity-Based Determination of Absolute Values of Photoluminescence Quantum Yields. *ChemPhysChem* **14**, 505–513 (2013). URL http://doi.wiley.com/10.1002/cphc.201200931. [cited on page 12.]

[34] Becker, W. *The bh TCSPC Handbook* 8th edition edn (Becker & Hickl GmbH, Berlin, 2019). [cited on page 12.]

[35] Verveer, P. J. & Hanley, Q. S. in *Chapter 2 Frequency domain FLIM theory, instrumentation, and data analysis* (ed.Gadella, T. W. J.) *Laboratory Techniques in Biochemistry and Molecular Biology*, Vol. 33 59–94 (Elsevier, 2009). URL https://www.sciencedirect.com/science/article/pii/S0075753508000028. [cited on page 12.]

[36] Heilemann, M. *et al.* Subdiffraction-Resolution Fluorescence Imaging with Conventional Fluorescent Probes. *Angewandte Chemie International Edition* **47**, 6172–6176 (2008). URL http://doi.wiley.com/10.1002/anie.200802376. [cited on pages 13, 34, and 47.]

[37] Volpato, A. *et al.* Extending fluorescence anisotropy to large complexes using reversibly switchable proteins. *Nature Biotechnology* **41**, 552–559 (2023). URL https://doi.org/10.1038/s41587-022-01489-7. [cited on page 13.]

[38] Abbe, E. Beiträge zur Theorie des Mikroskops und der mikroskopischen Wahrnehmung. *Archiv für Mikroskopische Anatomie* **9**, 413–468 (1873). URL http://link.springer.com/10.1007/BF02956173. [cited on page 13.]

[39] Hecht, E. *Optik* (De Gruyter, 2018). URL https://www.degruyter.com/view/title/525251. [cited on pages 15 and 122.]

[40] Wolf, E. Electromagnetic diffraction in optical systems - I. An integral representation of the image field. *Proceedings of the Royal Society of London. Series A. Mathematical and Physical Sciences* **253**, 349–357 (1959). URL http://www.royalsocietypublishing.org/doi/10.1098/rspa.1959.0199. [cited on pages 15 and 123.]

[41] Richards, B. & Wolf, E. Electromagnetic diffraction in optical systems - II. Structure of the image field in an aplanatic system. *Proceedings of the Royal Society of London. Series A. Mathematical and Physical Sciences* **253**, 358–379 (1959). URL http://www.royalsocietypublishing.org/doi/10.1098/rspa.1959.0200. [cited on pages 15 and 123.]

[42] Keller, H. E. in *Objective lenses for confocal microscopy* (ed.Pawley, J.) *Handbook of biological confocal microscopy* 77–86 (Springer, Boston, MA, USA, 1995). [cited on page 15.]

[43] Minsky, M. Microscopy apparatus (1961). URL https://www.freepatentsonline.com/3013467.html. US Patent 3013467. [cited on page 16.]

[44] White, J. G., Amos, W. B. & Fordham, M. An evaluation of confocal versus conventional imaging of biological structures by fluorescence light microscopy. *The Journal of Cell Biology* **105**, 41–48 (1987). URL https://rupress.org/jcb/article/105/1/41/28932/An-evaluation-of-confocal-versus-conventional. [cited on page 16.]

[45] Naora, H. Microspectrophotometry and Cytochemical Analysis of Nucleic Acids. *Science* **114**, 279–280 (1951). [cited on page 16.]

[46] Axelrod, D. Cell-substrate contacts illuminated by total internal reflection fluorescence. *The Journal of cell biology* **89**, 141–145 (1981). URL https://rupress.org/jcb/article/89/1/141/59168/Cell-substrate-contacts-illuminated-by-total. [cited on pages 17 and 18.]

[47] Axelrod, D. Evanescent Excitation and Emission in Fluorescence Microscopy. *Biophysical Journal* **104**, 1401–1409 (2013). URL https://linkinghub.elsevier.com/retrieve/pii/S0006349513002634. [cited on page 17.]

[48] Priyadarshi, A. *et al.* A transparent waveguide chip for versatile total internal reflection fluorescence-based microscopy and nanoscopy. *Communications Materials* **2**, 85 (2021). URL https://www.nature.com/articles/s43246-021-00192-5. [cited on page 18.]

[49] Schermelleh, L. *et al.* Super-resolution microscopy demystified. *Nature Cell Biology* **21**, 72–84 (2019). URL https://doi.org/10.1038/s41556-018-0251-8. [cited on page 18.]

[50] Gwosch, K. C. *et al.* MINFLUX nanoscopy delivers 3D multicolor nanometer resolution in cells. *Nature Methods* (2020). URL http://www.nature.com/articles/s41592-019-0688-0. [cited on page 18.]

[51] Reinhardt, S. C. M. *et al.* Ångström-resolution fluorescence microscopy. *Nature* **617**, 711–716 (2023). URL https://doi.org/10.1038/s41586-023-05925-9. [cited on page 18.]

[52] Brown, R. A brief account of microscopical observations made in the months of June, July and August 1827, on the particles contained in the pollen of plants; and on the general existence of active molecules in organic and inorganic bodies. *Philosophical Magazine* **4**, 161–173 (1828). [cited on page 18.]

[53] Von Smoluchowski, M. Zur kinetischen Theorie der Brownschen Molekularbewegung und der Suspensionen. *Annalen der Physik* **326**, 756–780 (1906). URL https://onlinelibrary.wiley.com/doi/10.1002/andp.19063261405. [cited on page 19.]

[54] Einstein, A. Über die von der molekularkinetischen Theorie der Wärme geforderte Bewegung von in ruhenden Flüssigkeiten suspendierten Teilchen. *Annalen der Physik* **322**, 549–560 (1905). [cited on page 19.]

[55] Broersma, S. Viscous Force Constant for a Closed Cylinder. *The Journal of Chemical Physics* **32**, 1632–1635 (1960). URL https://pubs.aip.org/jcp/article/32/6/1632/78635/Viscous-Force-Constant-for-a-Closed-Cylinder. [cited on pages 21 and 129.]

[56] Broersma, S. Viscous force and torque constants for a cylinder. *The Journal of Chemical Physics* **74**, 6989–6990 (1981). URL https://pubs.aip.org/jcp/article/74/12/6989/767471/Viscous-force-and-torque-constants-for-a-cylinder. [cited on pages 21 and 129.]

[57] Seils, J. & Pecora, R. Dynamics of a 2311 Base Pair Superhelical DNA in Dilute and Semidilute Solutions. *Macromolecules* **28**, 661–673 (1995). [cited on pages 21 and 129.]

[58] Saffman, P. G. & Delbrück, M. Brownian motion in biological membranes. *Proc Natl Acad Sci U S A* **72**, 3111–3 (1975). URL https://www.pnas.org/doi/10.1073/pnas.72.8.3111. [cited on page 21.]

[59] Hughes, B. D., Pailthorpe, B. A. & White, L. R. The translational and rotational drag on a cylinder moving in a membrane. *Journal of Fluid Mechanics* **110** (1981). [cited on page 21.]

[60] Petrov, E. P. & Schwille, P. Translational diffusion in lipid membranes beyond the Saffman-Delbrück approximation. *Biophys J* **94**, L41–3 (2008). [cited on page 21.]

[61] Veerapathiran, S. & Wohland, T. The imaging FCS diffusion law in the presence of multiple diffusive modes. *Methods* **140-141**, 140–150 (2018). URL https://linkinghub.elsevier.com/retrieve/pii/S1046202317302293. [cited on page 21.]

[62] Saxton, M. J. A Biological Interpretation of Transient Anomalous Subdiffusion. I. Qualitative Model. *Biophysical Journal* **92**, 1178–1191 (2007). URL https://linkinghub.elsevier.com/retrieve/pii/S0006349507709293. [cited on page 21.]

[63] Howse, J. R. *et al.* Self-Motile Colloidal Particles: From Directed Propulsion to Random Walk. *Physical Review Letters* **99**, 048102 (2007). URL https://link.aps.org/doi/10.1103/PhysRevLett.99.048102. [cited on page 22.]

[64] Günther, J.-P., Börsch, M. & Fischer, P. Diffusion Measurements of Swimming Enzymes with Fluorescence Correlation Spectroscopy. *Accounts of Chemical Research* **51**, 1911–1920 (2018). URL https://doi.org/10.1021/acs.accounts.8b00276. Publisher: American Chemical Society. [cited on page 22.]

[65] Ackers, G. K. & Holt, J. M. Asymmetric Cooperativity in a Symmetric Tetramer: Human Hemoglobin. *Journal of Biological Chemistry* **281**, 11441–11443 (2006). URL https://linkinghub.elsevier.com/retrieve/pii/S0021925819466428. [cited on page 23.]

[66] Oparin, A. I. in *The Origin of Life* (ed.Bernal, J.) *The Origin of Life* p. 199–234 (Weidenfeld & Nicolson, London, 1967). [cited on page 25.]

[67] Wilson, E. B. The Structure of Protoplasm. *Science* **10**, 33–45 (1899). URL https://www.science.org/doi/10.1126/science.10.237.33. [cited on page 25.]

[68] Hyman, A. A. & Simons, K. Beyond Oil and Water-Phase Transitions in Cells. *Science* **337**, 1047–1049 (2012). URL https://www.sciencemag.org/lookup/doi/10.1126/science.1223728. [cited on page 25.]

[69] Brangwynne, C. P. *et al.* Germline P Granules Are Liquid Droplets That Localize by Controlled Dissolution/Condensation. *Science* **324**, 1729–1732 (2009). URL https://www.sciencemag.org/lookup/doi/10.1126/science.1172046. [cited on pages 25 and 26.]

[70] McSwiggen, D. T., Mir, M., Darzacq, X. & Tjian, R. Evaluating phase separation in live cells: diagnosis, caveats, and functional consequences. *Genes & Development* **33**, 1619–1634 (2019). URL http://genesdev.cshlp.org/lookup/doi/10.1101/gad.331520.119. [cited on page 26.]

[71] Hyman, A. A., Weber, C. A. & Jülicher, F. Liquid-Liquid Phase Separation in Biology. *Annual Review of Cell and Developmental Biology* **30**, 39–58 (2014). URL http://www.annualreviews.org/doi/10.1146/annurev-cellbio-100913-013325. [cited on page 26.]

[72] Shin, Y. & Brangwynne, C. P. Liquid phase condensation in cell physiology and disease. *Science* **357**, eaaf4382 (2017). URL https://www.sciencemag.org/lookup/doi/10.1126/science.aaf4382. [cited on page 26.]

[73] Alberti, S., Gladfelter, A. & Mittag, T. Considerations and Challenges in Studying Liquid-Liquid Phase Separation and Biomolecular Condensates. *Cell* **176**, 419–434 (2019). URL https://linkinghub.elsevier.com/retrieve/pii/S0092867418316490. [cited on page 27.]

[74] Zhu, S. *et al.* Demixing is a default process for biological condensates formed via phase separation. *Science* **384**, 920–928 (2024). URL https://www.science.org/doi/10.1126/science.adj7066. [cited on page 26.]

[75] Setru, S. U. *et al.* A hydrodynamic instability drives protein droplet formation on microtubules to nucleate branches. *Nature Physics* **17**, 493–498 (2021). URL https://doi.org/10.1038/s41567-020-01141-8. [cited on page 26.]

[76] Klosin, A. *et al.* Phase separation provides a mechanism to reduce noise in cells. *Science* **367**, 464–468 (2020). URL https://www.sciencemag.org/lookup/doi/10.1126/science.aav6691. [cited on page 26.]

[77] Geiger, F. *et al.* Liquid–liquid phase separation underpins the formation of replication factories in rotaviruses. *The EMBO Journal* **40**, e107711 (2021). URL https://doi.org/10.15252/embj.2021107711. Publisher: John Wiley & Sons, Ltd. [cited on pages 26 and 27.]

[78] Ray, S. *et al.* α-Synuclein aggregation nucleates through liquid–liquid phase separation. *Nature Chemistry* **12**, 705–716 (2020). URL http://www.nature.com/articles/s41557-020-0465-9. [cited on page 26.]

[79] Babl, L. *et al.* CTP-controlled liquid–liquid phase separation of ParB. *Journal of Molecular Biology* **434**, 167401 (2022). URL https://www.sciencedirect.com/science/article/pii/S0022283621006380. [cited on page 26.]

[80] Babl, L., Merino-Salomón, A., Kanwa, N. & Schwille, P. Membrane mediated phase separation of the bacterial nucleoid occlusion protein Noc. *Scientific Reports* **12**, 17949 (2022). URL https://www.nature.com/articles/s41598-022-22680-5. [cited on page 26.]

[81] Merino-Salomón, A., Babl, L. & Schwille, P. Self-organized protein patterns: The MinCDE and ParABS systems. *Current Opinion in Cell Biology* **72**, 106–115 (2021). URL https://linkinghub.elsevier.com/retrieve/pii/S0955067421000788. [cited on page 26.]

[82] Gözen, I. *et al.* Protocells: Milestones and Recent Advances. *Small* **n/a**, 2106624 (2022). URL https://doi.org/10.1002/smll.202106624. Publisher: John Wiley & Sons, Ltd. [cited on pages 26 and 28.]

[83] Bartolucci, G. *et al.* Sequence self-selection by cyclic phase separation. *Proceedings of the National Academy of Sciences* **120**, e2218876120 (2023). URL https://pnas.org/doi/10.1073/pnas.2218876120. [cited on page 26.]

[84] Peter, B., Levrier, A. & Schwille, P. Spatiotemporal Propagation of a Minimal Catalytic RNA Network in GUV Protocells by Temperature Cycling and Phase Separation. *Angewandte Chemie International Edition* **62**, e202218507 (2023). URL https://onlinelibrary.wiley.com/doi/10.1002/anie.202218507. [cited on page 26.]

[85] Ianeselli, A. *et al.* Non-equilibrium conditions inside rock pores drive fission, maintenance and selection of coacervate protocells. *Nature Chemistry* **14**, 32–39 (2022). URL https://doi.org/10.1038/s41557-021-00830-y. [cited on page 26.]

[86] Martin, E. W. *et al.* Valence and patterning of aromatic residues determine the phase behavior of prion-like domains. *Science* **367**, 694–699 (2020). URL https://www.sciencemag.org/lookup/doi/10.1126/science.aaw8653. [cited on page 26.]

[87] Jawerth, L. *et al.* Protein condensates as aging Maxwell fluids. *Science* **370**, 1317–1323 (2020). URL https://www.sciencemag.org/lookup/doi/10.1126/science.aaw4951. [cited on page 27.]

[88] Adkins, R. *et al.* Dynamics of active liquid interfaces. *Science* **377**, 768–772 (2022). URL https://www.science.org/doi/10.1126/science.abo5423. [cited on page 27.]

[89] Li, J. *et al.* Programmable spatial organization of liquid-phase condensations. *Chem* **8**, 784–800 (2022). URL https://linkinghub.elsevier.com/retrieve/pii/S2451929421005829. [cited on page 27.]

[90] Banerjee, P. R., Milin, A. N., Moosa, M. M., Onuchic, P. L. & Deniz, A. A. Reentrant Phase Transition Drives Dynamic Substructure Formation in Ribonucleoprotein Droplets. *Angewandte Chemie International Edition* **56**, 11354–11359 (2017). URL http://doi.wiley.com/10.1002/anie.201703191. [cited on pages 27 and 144.]

[91] Li, W. *et al.* Catalytic Assembly of Peptides Mediated by Complex Coacervates. *ACS Nano* **19**, 2306–2314 (2025). URL https://pubs.acs.org/doi/10.1021/acsnano.4c12320. [cited on page 27.]

[92] Huggins, M. L. Solutions of Long Chain Compounds. *The Journal of Chemical Physics* **9**, 440–440 (1941). URL https://pubs.aip.org/jcp/article/9/5/440/218119/Solutions-of-Long-Chain-Compounds. [cited on page 28.]

[93] Flory, P. J. Thermodynamics of High Polymer Solutions. *The Journal of Chemical Physics* **10**, 51–61 (1942). URL https://pubs.aip.org/jcp/article/10/1/51/177891/Thermodynamics-of-High-Polymer-Solutions. [cited on page 28.]

[94] Mao, S., Kuldinow, D., Haataja, M. P. & Košmrlj, A. Phase behavior and morphology of multicomponent liquid mixtures. *Soft Matter* **15**, 1297–1311 (2019). URL http://dx.doi.org/10.1039/C8SM02045K. Publisher: The Royal Society of Chemistry. [cited on page 28.]

[95] Pullarkat, P., Fernandez, P. & Ott, A. Rheological properties of the Eukaryotic cell cytoskeleton. *Physics Reports* **449**, 29–53 (2007). URL https://linkinghub.elsevier.com/retrieve/pii/S0370157307001305. [cited on page 30.]

[96] Neuhaus, J.-M., Wanger, M., Keiser, T. & Wegner, A. Treadmilling of actin. *Journal of Muscle Research & Cell Motility* **4**, 507–527 (1983). URL https://doi.org/10.1007/BF00712112. [cited on page 30.]

[97] Gayathri, P. & Harne, S. in *Structure and Dynamics of Actin-Like Cytomotive Filaments in Plasmid Segregation* (eds Löwe, J. & Amos, L. A.) *Prokaryotic Cytoskeletons: Filamentous Protein Polymers Active in the Cytoplasm of Bacterial and Archaeal Cells* 299–321 (Springer International Publishing, Cham, 2017). URL https://doi.org/10.1007/978-3-319-53047-5_10. [cited on page 30.]

[98] Battaje, R. R. & Panda, D. Lessons from bacterial homolog of tubulin, FtsZ for microtubule dynamics. *Endocrine-Related Cancer* **24**, T1–T21 (2017). URL https://erc.bioscientifica.com/view/journals/erc/24/9/T1.xml. [cited on page 30.]

[99] Huang, K.-H., Durand-Heredia, J. & Janakiraman, A. FtsZ Ring Stability: of Bundles, Tubules, Crosslinks, and Curves. *Journal of Bacteriology* **195**, 1859–1868 (2013). URL https://journals.asm.org/doi/10.1128/JB.02157-12. [cited on pages 30, 87, and 102.]

[100] Seeman, N. C. *Structural DNA Nanotechnology* 1 edn (Cambridge University Press, 2015). URL https://www.cambridge.org/core/product/identifier/9781139015516/type/book. [cited on page 31.]

[101] Seeman, N. C. & Sleiman, H. F. DNA nanotechnology. *Nature Reviews Materials* **3**, 17068 (2017). URL https://www.nature.com/articles/natrevmats201768. [cited on page 31.]

[102] He, S., Ge, Z., Zuo, X., Fan, C. & Mao, X. Dynamic regulation of DNA nanostructures by noncanonical nucleic acids. *NPG Asia Materials* **13**, 42 (2021). URL https://www.nature.com/articles/s41427-021-00309-9. [cited on page 31.]

[103] Wu, N. & Willner, I. pH-Stimulated Reconfiguration and Structural Isomerization of Origami Dimer and Trimer Systems. *Nano Letters* **16**, 6650–6655 (2016). URL https://pubs.acs.org/doi/10.1021/acs.nanolett.6b03418. [cited on page 31.]

[104] Kortemme, T. De novo protein design—From new structures to programmable functions. *Cell* **187**, 526–544 (2024). URL https://doi.org/10.1016/j.cell.2023.12.028. Publisher: Elsevier. [cited on page 31.]

[105] Hu, Q., Li, H., Wang, L., Gu, H. & Fan, C. DNA Nanotechnology-Enabled Drug Delivery Systems. *Chemical Reviews* **119**, 6459–6506 (2019). URL https://pubs.acs.org/doi/10.1021/acs.chemrev.7b00663. [cited on page 31.]

[106] Trofymchuk, K. *et al.* Addressable nanoantennas with cleared hotspots for single-molecule detection on a portable smartphone microscope. *Nature Communications* **12**, 950 (2021). URL https://www.nature.com/articles/s41467-021-21238-9. [cited on page 31.]

[107] Wang, S. *et al.* DNA Origami-Enabled Biosensors. *Sensors* **20**, 6899 (2020). URL https://www.mdpi.com/1424-8220/20/23/6899. [cited on page 31.]

[108] Yang, Y. *et al.* Self-assembly of size-controlled liposomes on DNA nanotemplates. *Nature Chemistry* **8**, 476–483 (2016). URL https://doi.org/10.1038/nchem.2472. [cited on page 31.]

[109] Wassermann, L. M., Scheckenbach, M., Baptist, A. V., Glembockyte, V. & Heuer-Jungemann, A. Full Site-Specific Addressability in DNA Origami-Templated Silica Nanostructures. *Advanced Materials* **35**, 2212024 (2023). URL https://onlinelibrary.wiley.com/doi/10.1002/adma.202212024. [cited on page 31.]

[110] Wilson, H. & Wang, Q. ABEL-FRET: tether-free single-molecule FRET with hydrodynamic profiling. *Nature Methods* **18**, 816–820 (2021). URL https://www.nature.com/articles/s41592-021-01173-9. [cited on page 31.]

[111] Voigt, N. V. *et al.* Single-molecule chemical reactions on DNA origami. *Nature Nanotechnology* **5**, 200–203 (2010). URL https://doi.org/10.1038/nnano.2010.5. [cited on page 31.]

[112] Kuzyk, A. *et al.* DNA-based self-assembly of chiral plasmonic nanostructures with tailored optical response. *Nature* **483**, 311–314 (2012). URL https://doi.org/10.1038/nature10889. [cited on page 31.]

[113] Berger, R. M. L. *et al.* Nanoscale FasL Organization on DNA Origami to Decipher Apoptosis Signal Activation in Cells. *Small* **17**, 2101678 (2021). URL https://onlinelibrary.wiley.com/doi/10.1002/smll.202101678. [cited on page 31.]

[114] Khoshouei, A. *et al.* Designing Rigid DNA Origami Templates for Molecular Visualization Using Cryo-EM. *Nano Letters* acs.nanolett.4c00915 (2024). URL https://pubs.acs.org/doi/10.1021/acs.nanolett.4c00915. [cited on page 31.]

[115] Rothemund, P. W. K. Folding DNA to create nanoscale shapes and patterns. *Nature* **440**, 297–302 (2006). URL http://www.nature.com/articles/nature04586. [cited on page 32.]

[116] Dey, S. *et al.* DNA origami. *Nature Reviews Methods Primers* **1**, 13 (2021). URL http://www.nature.com/articles/s43586-020-00009-8. [cited on page 32.]

[117] Moerner, W. E. & Kador, L. Optical detection and spectroscopy of single molecules in a solid. *Physical Review Letters* **62**, 2535–2538 (1989). URL https://link.aps.org/doi/10.1103/PhysRevLett.62.2535. [cited on page 33.]

[118] Orrit, M. & Bernard, J. Single pentacene molecules detected by fluorescence excitation in a p-terphenyl crystal. *Physical Review Letters* **65**, 2716–2719 (1990). URL https://link.aps.org/doi/10.1103/PhysRevLett.65.2716. [cited on page 33.]

[119] Nguyen, D. C., Keller, R. A., Jett, J. H. & Martin, J. C. Detection of single molecules of phycoerythrin in hydrodynamically focused flows by laser-induced fluorescence. *Analytical Chemistry* **59**, 2158–2161 (1987). URL https://pubs.acs.org/doi/abs/10.1021/ac00144a032. [cited on page 33.]

[120] Brooks Shera, E., Seitzinger, N. K., Davis, L. M., Keller, R. A. & Soper, S. A. Detection of single fluorescent molecules. *Chemical Physics Letters* **174**, 553–557 (1990). URL https://linkinghub.elsevier.com/retrieve/pii/000926149085485U. [cited on page 33.]

[121] Betzig, E. & Chichester, R. J. Single Molecules Observed by Near-Field Scanning Optical Microscopy. *Science* **262**, 1422–1425 (1993). URL https://www.science.org/doi/10.1126/science.262.5138.1422. [cited on page 33.]

[122] Calebiro, D. *et al.* Single-molecule analysis of fluorescently labeled G-protein-coupled receptors reveals complexes with distinct dynamics and organization. *Proc Natl Acad Sci U S A* **110**, 743–8 (2013). URL https://pubmed.ncbi.nlm.nih.gov/23267088/. [cited on pages 34 and 35.]

[123] Zhang, W. *et al.* Single-molecule imaging reveals transforming growth factor-β-induced type II receptor dimerization. *Proceedings of the National Academy of*

Sciences **106**, 15679–15683 (2009). URL https://pnas.org/doi/full/10.1073/pnas.0908279106. [cited on page 34.]

[124] Fricke, F., Beaudouin, J., Eils, R. & Heilemann, M. One, two or three? Probing the stoichiometry of membrane proteins by single-molecule localization microscopy. *Scientific Reports* **5**, 14072 (2015). URL https://www.nature.com/articles/srep14072. [cited on page 34.]

[125] Jungmann, R. *et al.* Quantitative super-resolution imaging with qPAINT. *Nature Methods* **13**, 439–442 (2016). URL http://www.nature.com/articles/nmeth.3804. [cited on page 34.]

[126] Sisamakis, E., Valeri, A., Kalinin, S., Rothwell, P. J. & Seidel, C. A. in *Chapter 18 - Accurate Single-Molecule FRET Studies Using Multiparameter Fluorescence Detection* (ed.Walter, N. G.) *Methods in Enzymology*, Vol. 475 455–514 (Academic Press, 2010). URL https://www.sciencedirect.com/science/article/pii/S0076687910750187. [cited on page 34.]

[127] Ha, T. *et al.* Fluorescence resonance energy transfer at the single-molecule level. *Nature Reviews Methods Primers* **4**, 21 (2024). URL https://doi.org/10.1038/s43586-024-00298-3. [cited on page 34.]

[128] Nettels, D. *et al.* Single-molecule FRET for probing nanoscale biomolecular dynamics. *Nature Reviews Physics* **6**, 587–605 (2024). URL https://doi.org/10.1038/s42254-024-00748-7. [cited on page 34.]

[129] Sharonov, A. & Hochstrasser, R. M. Wide-field subdiffraction imaging by accumulated binding of diffusing probes. *Proceedings of the National Academy of Sciences* **103**, 18911–18916 (2006). URL http://www.pnas.org/cgi/doi/10.1073/pnas.0609643104. [cited on page 34.]

[130] Betzig, E. *et al.* Imaging Intracellular Fluorescent Proteins at Nanometer Resolution. *Science* **313**, 1642–1645 (2006). URL http://www.sciencemag.org/cgi/doi/10.1126/science.1127344. [cited on pages 34 and 47.]

[131] Rust, M. J., Bates, M. & Zhuang, X. Sub-diffraction-limit imaging by stochastic optical reconstruction microscopy (STORM). *Nature Methods* **3**, 793–796 (2006). URL http://www.nature.com/doifinder/10.1038/nmeth929. [cited on pages 34 and 47.]

[132] Xiang, L., Chen, K. & Xu, K. Single Molecules Are Your Quanta: A Bottom-Up Approach toward Multidimensional Super-resolution Microscopy. *ACS Nano* **15**, 12483–12496 (2021). URL https://doi.org/10.1021/acsnano.1c04708. Publisher: American Chemical Society. [cited on page 34.]

[133] Manzo, C. & Garcia-Parajo, M. F. A review of progress in single particle tracking: from methods to biophysical insights. *Reports on Progress in Physics* **78**, 124601 (2015). URL https://iopscience.iop.org/article/10.1088/0034-4885/78/12/124601. [cited on pages 34 and 35.]

[134] Elf, J. & Barkefors, I. Single-Molecule Kinetics in Living Cells. *Annual Review of Biochemistry* **88**, 635–659 (2019). URL https://www.annualreviews.org/doi/10.1146/annurev-biochem-013118-110801. [cited on page 34.]

[135] Deschout, H. *et al.* Precisely and accurately localizing single emitters in fluorescence microscopy. *Nature Methods* **11**, 253–266 (2014). URL http://www.nature.com/articles/nmeth.2843. [cited on page 34.]

[136] Enderlein, J. Tracking of fluorescent molecules diffusing within membranes. *Applied Physics B* **71**, 773–777 (2000). URL http://link.springer.com/10.1007/s003400000409. [cited on page 34.]

[137] Balzarotti, F. *et al.* Nanometer resolution imaging and tracking of fluorescent molecules with minimal photon fluxes. *Science* **355**, 606–612 (2017). URL http://www.sciencemag.org/lookup/doi/10.1126/science.aak9913. [cited on page 34.]

[138] Jungmann, R. *et al.* Single-Molecule Kinetics and Super-Resolution Microscopy by Fluorescence Imaging of Transient Binding on DNA Origami. *Nano Letters* **10**, 4756–4761 (2010). URL https://pubs.acs.org/doi/10.1021/nl103427w. [cited on pages 34 and 47.]

[139] Geerts, H. *et al.* Nanovid tracking: a new automatic method for the study of mobility in living cells based on colloidal gold and video microscopy. *Biophysical Journal* **52**, 775–782 (1987). URL https://linkinghub.elsevier.com/retrieve/pii/S000634958783271X. [cited on page 35.]

[140] De Brabander, M., Nuydens, R., Geerts, H. & Hopkins, C. R. Dynamic behavior of the transferrin receptor followed in living epidermoid carcinoma (A431) cells with nanovid microscopy. *Cell Motility* **9**, 30–47 (1988). URL https://onlinelibrary.wiley.com/doi/10.1002/cm.970090105. [cited on page 35.]

[141] Schmidt, T., Schütz, G. J., Baumgartner, W., Gruber, H. J. & Schindler, H. Imaging of single molecule diffusion. *Proceedings of the National Academy of Sciences* **93**, 2926–2929 (1996). URL https://doi.org/10.1073/pnas.93.7.2926. Publisher: Proceedings of the National Academy of Sciences. [cited on page 35.]

[142] Axelrod, D., Koppel, D., Schlessinger, J., Elson, E. & Webb, W. Mobility measurement by analysis of fluorescence photobleaching recovery kinetics. *Biophysical Journal* **16**, 1055–1069 (1976). URL https://linkinghub.elsevier.com/retrieve/pii/S0006349576857554. [cited on page 35.]

[143] Lorén, N. *et al.* Fluorescence recovery after photobleaching in material and life sciences: putting theory into practice. *Quarterly Reviews of Biophysics* **48**, 323–387 (2015). URL https://www.cambridge.org/core/product/identifier/S0033583515000013/type/journal_article. [cited on page 35.]

[144] Taylor, N. O., Wei, M.-T., Stone, H. A. & Brangwynne, C. P. Quantifying Dynamics in Phase-Separated Condensates Using Fluorescence Recovery after Photobleaching. *Biophysical Journal* **117**, 1285–1300 (2019). URL https://

www.sciencedirect.com/science/article/pii/S0006349519307477. [cited on page 35.]

[145] Magde, D., Elson, E. & Webb, W. W. Thermodynamic Fluctuations in a Reacting System—Measurement by Fluorescence Correlation Spectroscopy. *Physical Review Letters* **29**, 705–708 (1972). [cited on pages 35 and 36.]

[146] Elson, E. L. in *Brief Introduction to Fluorescence Correlation Spectroscopy* (ed.Tetin, S. Y.) *Methods in Enzymology*, Vol. 518 11–41 (Elsevier, 2013). URL https://linkinghub.elsevier.com/retrieve/pii/B9780123884220000029. [cited on page 35.]

[147] Wohland, T., Maiti, S. & Macháň, R. *An Introduction to Fluorescence Correlation Spectroscopy* (IOP Publishing, 2020). URL https://dx.doi.org/10.1088/978-0-7503-2080-1. [cited on pages 35, 37, and 62.]

[148] Magde, D., Elson, E. L. & Webb, W. W. Fluorescence correlation spectroscopy. II. An experimental realization. *Biopolymers* **13**, 29–61 (1974). URL https://onlinelibrary.wiley.com/doi/10.1002/bip.1974.360130103. [cited on page 36.]

[149] Petrov, E. P. & Schwille, P. in *State of the Art and Novel Trends in Fluorescence Correlation Spectroscopy* (ed.Resch-Genger, U.) *Standardization and Quality Assurance in Fluorescence Measurements II*, Vol. 6 145–197 (Springer Berlin Heidelberg, Berlin, Heidelberg, 2008). URL http://link.springer.com/10.1007/4243_2008_032. ISSN: 1617-1306, 1865-1313 Series Title: Springer Series on Fluorescence. [cited on pages 36 and 62.]

[150] Wachsmuth, M., Waldeck, W. & Langowski, J. Anomalous diffusion of fluorescent probes inside living cell nuclei investigated by spatially-resolved fluorescence correlation spectroscopy. *Journal of Molecular Biology* **298**, 677–689 (2000). URL https://linkinghub.elsevier.com/retrieve/pii/S0022283600936921. [cited on page 37.]

[151] Sarkar, A. *et al.* Binding Constant Determined from the Angstrom-Scale Change in Hydrodynamic Radius of Transferrin upon Binding with Europium Using Dual-Focus Fluorescence Correlation Spectroscopy. *The Journal of Physical Chemistry Letters* **11**, 1148–1153 (2020). URL https://pubs.acs.org/doi/10.1021/acs.jpclett.9b03722. [cited on pages 37 and 41.]

[152] Bock, A. *et al.* Optical Mapping of cAMP Signaling at the Nanometer Scale. *Cell* **182**, 1519–1530.e17 (2020). URL https://linkinghub.elsevier.com/retrieve/pii/S0092867420309430. [cited on page 37.]

[153] Le, T. T. *et al.* Real-time RNA profiling within a single bacterium. *Proceedings of the National Academy of Sciences* **102**, 9160–9164 (2005). URL https://pnas.org/doi/full/10.1073/pnas.0503311102. [cited on page 37.]

[154] Herrick-Davis, K., Grinde, E., Cowan, A. & Mazurkiewicz, J. E. Fluorescence Correlation Spectroscopy Analysis of Serotonin, Adrenergic, Muscarinic, and Dopamine Receptor Dimerization: The Oligomer Number Puzzle. *Molecular*

Pharmacology **84**, 630–642 (2013). URL http://molpharm.aspetjournals.org/cgi/doi/10.1124/mol.113.087072. [cited on page 37.]

[155] Steiert, F. *et al.* Insights into receptor structure and dynamics at the surface of living cells. *Nature Communications* **14**, 1596 (2023). URL https://www.nature.com/articles/s41467-023-37284-4. [cited on page 37.]

[156] Mazouchi, A., Bahram, A. & Gradinaru, C. C. Sub-Diffusion Decays in Fluorescence Correlation Spectroscopy: Dye Photophysics or Protein Dynamics? *The Journal of Physical Chemistry B* **117**, 11100–11111 (2013). URL https://doi.org/10.1021/jp4010746. Publisher: American Chemical Society. [cited on page 37.]

[157] Haupts, U., Maiti, S., Schwille, P. & Webb, W. W. Dynamics of fluorescence fluctuations in green fluorescent protein observed by fluorescence correlation spectroscopy. *Proceedings of the National Academy of Sciences* **95**, 13573–13578 (1998). [cited on page 37.]

[158] Czogalla, A., Kauert, D. J., Seidel, R., Schwille, P. & Petrov, E. P. DNA Origami Nanoneedles on Freestanding Lipid Membranes as a Tool To Observe Isotropic–Nematic Transition in Two Dimensions. *Nano Letters* **15**, 649–655 (2015). URL https://doi.org/10.1021/nl504158h. Publisher: American Chemical Society. [cited on page 37.]

[159] Krichevsky, O. & Bonnet, G. Fluorescence correlation spectroscopy: the technique and its applications. *Reports on Progress in Physics* **65**, 251–297 (2002). URL https://iopscience.iop.org/article/10.1088/0034-4885/65/2/203. [cited on page 37.]

[160] Widengren, J. & Mets, . in *Conceptual Basis of Fluorescence Correlation Spectroscopy and Related Techniques as Tools in Bioscience* (eds Zander, C., Enderlein, J. & Keller, R. A.) *Single Molecule Detection in Solution* 69–120 (Wiley-VCH Verlag GmbH & Co. KGaA, Weinheim, FRG, 2002). URL http://doi.wiley.com/10.1002/3527600809.ch3. [cited on pages 37 and 62.]

[161] Schwille, P., Meyer-Almes, F. & Rigler, R. Dual-color fluorescence cross-correlation spectroscopy for multicomponent diffusional analysis in solution. *Biophysical Journal* **72**, 1878–1886 (1997). URL https://linkinghub.elsevier.com/retrieve/pii/S0006349597788337. [cited on page 40.]

[162] Ries, J., Petrášek, Z., García-Sáez, A. J. & Schwille, P. A comprehensive framework for fluorescence cross-correlation spectroscopy. *New Journal of Physics* **12** (2010). [cited on pages 40 and 111.]

[163] Felekyan, S., Kalinin, S., Sanabria, H., Valeri, A. & Seidel, C. A. M. Filtered FCS: Species Auto- and Cross-Correlation Functions Highlight Binding and Dynamics in Biomolecules. *ChemPhysChem* **13**, 1036–1053 (2012). URL http://doi.wiley.com/10.1002/cphc.201100897. [cited on pages 40 and 124.]

[164] Štefl, M., Herbst, K., Rübsam, M., Benda, A. & Knop, M. Single-Color Fluorescence Lifetime Cross-Correlation Spectroscopy In Vivo. *Biophysical Journal* **119**,

1359–1370 (2020). URL https://linkinghub.elsevier.com/retrieve/pii/S0006349520306469. [cited on page 40.]

[165] Wenger, J. & Rigneault, H. Photonic Methods to Enhance Fluorescence Correlation Spectroscopy and Single Molecule Fluorescence Detection. *International Journal of Molecular Sciences* **11**, 206–221 (2010). URL http://www.mdpi.com/1422-0067/11/1/206. [cited on page 40.]

[166] Thompson, N., Burghardt, T. & Axelrod, D. Measuring surface dynamics of biomolecules by total internal reflection fluorescence with photobleaching recovery or correlation spectroscopy. *Biophysical Journal* **33**, 435–454 (1981). URL https://linkinghub.elsevier.com/retrieve/pii/S0006349581849053. [cited on page 40.]

[167] Ruckstuhl, T. & Seeger, S. Attoliter detection volumes by confocal total-internal-reflection fluorescence microscopy. *Optics Letters* **29**, 569 (2004). URL https://www.osapublishing.org/abstract.cfm?URI=ol-29-6-569. [cited on page 40.]

[168] Hassler, K. *et al.* Total internal reflection fluorescence correlation spectroscopy (TIR-FCS) with low background and high count-rate per molecule. *Optics Express* **13**, 7415 (2005). URL https://www.osapublishing.org/oe/abstract.cfm?uri=oe-13-19-7415. [cited on page 40.]

[169] Ohsugi, Y., Saito, K., Tamura, M. & Kinjo, M. Lateral Mobility of Membrane-Binding Proteins in Living Cells Measured by Total Internal Reflection Fluorescence Correlation Spectroscopy. *Biophysical Journal* **91**, 3456–3464 (2006). URL https://linkinghub.elsevier.com/retrieve/pii/S0006349506720574. [cited on page 40.]

[170] Kannan, B. *et al.* Spatially Resolved Total Internal Reflection Fluorescence Correlation Microscopy Using an Electron Multiplying Charge-Coupled Device Camera. *Analytical Chemistry* **79**, 4463–4470 (2007). URL https://pubs.acs.org/doi/10.1021/ac0624546. [cited on pages 40 and 41.]

[171] Mücksch, J. *et al.* Quantifying Reversible Surface Binding via Surface-Integrated Fluorescence Correlation Spectroscopy. *Nano Letters* **18**, 3185–3192 (2018). URL https://pubs.acs.org/doi/10.1021/acs.nanolett.8b00875. [cited on page 40.]

[172] Ries, J., Ruckstuhl, T., Verdes, D. & Schwille, P. Supercritical Angle Fluorescence Correlation Spectroscopy. *Biophysical Journal* **94**, 221–229 (2008). URL https://linkinghub.elsevier.com/retrieve/pii/S0006349508707811. [cited on page 40.]

[173] Eggeling, C. *et al.* Direct observation of the nanoscale dynamics of membrane lipids in a living cell. *Nature* **457**, 1159 (2008). URL https://doi.org/10.1038/nature07596. [cited on page 41.]

[174] Honigmann, A. *et al.* Scanning STED-FCS reveals spatiotemporal heterogeneity of lipid interaction in the plasma membrane of living cells. *Nature Communications* **5**, 5412 (2014). URL https://doi.org/10.1038/ncomms6412. [cited on pages 41 and 144.]

[175] Hell, S. W. & Wichmann, J. Breaking the diffraction resolution limit by stimulated emission: stimulated-emission-depletion fluorescence microscopy. *Optics Letters* **19**, 780 (1994). URL https://www.osapublishing.org/abstract.cfm?URI=ol-19-11-780. [cited on page 41.]

[176] Klar, T. A. & Hell, S. W. Subdiffraction resolution in far-field fluorescence microscopy. *Optics Letters* **24**, 954 (1999). URL https://www.osapublishing.org/abstract.cfm?URI=ol-24-14-954. [cited on page 41.]

[177] Kitson, S. C., Jonsson, P., Rarity, J. G. & Tapster, P. R. Intensity fluctuation spectroscopy of small numbers of dye molecules in a microcavity. *Physical Review A* **58**, 620–627 (1998). URL https://link.aps.org/doi/10.1103/PhysRevA.58.620. [cited on page 41.]

[178] Borejdo, J., Calander, N., Gryczynski, Z. & Gryczynski, I. Fluorescence correlation spectroscopy in surface plasmon coupled emission microscope. *Optics Express* **14**, 7878 (2006). URL https://www.osapublishing.org/oe/abstract.cfm?uri=oe-14-17-7878. [cited on page 41.]

[179] Regmi, R. *et al.* Planar Optical Nanoantennas Resolve Cholesterol-Dependent Nanoscale Heterogeneities in the Plasma Membrane of Living Cells. *Nano Letters* **17**, 6295–6302 (2017). URL http://pubs.acs.org/doi/10.1021/acs.nanolett.7b02973. [cited on page 41.]

[180] Brinkmeier, M., Dörre, K., Stephan, J. & Eigen, M. Two-Beam Cross-Correlation: A Method To Characterize Transport Phenomena in Micrometer-Sized Structures. *Analytical Chemistry* **71**, 609–616 (1999). URL https://pubs.acs.org/doi/10.1021/ac980820i. [cited on pages 41 and 122.]

[181] Dertinger, T. *et al.* Two-Focus Fluorescence Correlation Spectroscopy: A New Tool for Accurate and Absolute Diffusion Measurements. *ChemPhysChem* **8**, 433–443 (2007). URL http://doi.wiley.com/10.1002/cphc.200600638. [cited on pages 41 and 122.]

[182] Digman, M. A. & Gratton, E. Imaging Barriers to Diffusion by Pair Correlation Functions. *Biophysical Journal* **97**, 665–673 (2009). URL https://linkinghub.elsevier.com/retrieve/pii/S0006349509009564. [cited on pages 41 and 122.]

[183] Digman, M. A. & Gratton, E. Lessons in Fluctuation Correlation Spectroscopy. *Annual Review of Physical Chemistry* **62**, 645–668 (2011). URL https://www.annualreviews.org/doi/10.1146/annurev-physchem-032210-103424. [cited on page 41.]

[184] Wohland, T., Shi, X., Sankaran, J. & Stelzer, E. H. Single Plane Illumination Fluorescence Correlation Spectroscopy (SPIM-FCS) probes inhomogeneous three-dimensional environments. *Optics Express* **18**, 10627 (2010). URL https://

www.osapublishing.org/oe/abstract.cfm?uri=oe-18-10-10627. [cited on page 41.]

[185] Bag, N. & Wohland, T. Imaging Fluorescence Fluctuation Spectroscopy: New Tools for Quantitative Bioimaging. *Annual Review of Physical Chemistry* **65**, 225–248 (2014). URL http://www.annualreviews.org/doi/10.1146/annurev-physchem-040513-103641. [cited on page 41.]

[186] Petersen, N. Scanning fluorescence correlation spectroscopy. I. Theory and simulation of aggregation measurements. *Biophysical Journal* **49**, 809–815 (1986). URL https://www.sciencedirect.com/science/article/pii/S0006349586837092. [cited on page 41.]

[187] Digman, M. A. *et al.* Measuring Fast Dynamics in Solutions and Cells with a Laser Scanning Microscope. *Biophysical Journal* **89**, 1317–1327 (2005). URL https://doi.org/10.1529/biophysj.105.062836. Publisher: Elsevier. [cited on page 41.]

[188] Petrášek, Z. & Schwille, P. Precise Measurement of Diffusion Coefficients using Scanning Fluorescence Correlation Spectroscopy. *Biophysical Journal* **94**, 1437–1448 (2008). URL https://linkinghub.elsevier.com/retrieve/pii/S000634950870660X. [cited on page 41.]

[189] Ries, J., Chiantia, S. & Schwille, P. Accurate Determination of Membrane Dynamics with Line-Scan FCS. *Biophysical Journal* **96**, 1999–2008 (2009). URL https://linkinghub.elsevier.com/retrieve/pii/S0006349509002112. [cited on pages 41 and 118.]

[190] Palmer, A. & Thompson, N. Molecular aggregation characterized by high order autocorrelation in fluorescence correlation spectroscopy. *Biophysical Journal* **52**, 257–270 (1987). URL https://linkinghub.elsevier.com/retrieve/pii/S0006349587832137. [cited on page 41.]

[191] Qian, H. & Elson, E. On the analysis of high order moments of fluorescence fluctuations. *Biophysical Journal* **57**, 375–380 (1990). URL https://linkinghub.elsevier.com/retrieve/pii/S000634959082539X. [cited on page 41.]

[192] Chen, Y., Müller, J. D., So, P. T. & Gratton, E. The Photon Counting Histogram in Fluorescence Fluctuation Spectroscopy. *Biophysical Journal* **77**, 553–567 (1999). URL https://linkinghub.elsevier.com/retrieve/pii/S0006349599769122. [cited on pages 41 and 116.]

[193] Qian, H. & Elson, E. L. Distribution of molecular aggregation by analysis of fluctuation moments. *Proceedings of the National Academy of Sciences* **87**, 5479–5483 (1990). URL http://www.pnas.org/cgi/doi/10.1073/pnas.87.14.5479. [cited on page 41.]

[194] Perroud, T. D., Huang, B. & Zare, R. N. Effect of Bin Time on the Photon Counting Histogram for One-Photon Excitation. *ChemPhysChem* **6**, 905–912 (2005). URL https://chemistry-europe.onlinelibrary.wiley.com/doi/10.1002/cphc.200400547. [cited on pages 41, 131, and 134.]

[195] Skakun, V. V., Engel, R., Digris, A. V., Borst, J. W. & Visser, A. J. W. G. Global analysis of autocorrelation functions and photon counting distributions. *Frontiers in Bioscience* **E3**, 489–505 (2011). URL https://imrpress.com/journal/FBE/3/2/10.2741/E264. [cited on pages 41, 131, 134, and 135.]

[196] Grome, M. W., Zhang, Z., Pincet, F. & Lin, C. Vesicle Tubulation with Self-Assembling DNA Nanosprings. *Angewandte Chemie International Edition* **57**, 5330–5334 (2018). URL https://doi.org/10.1002/anie.201800141. Publisher: John Wiley & Sons, Ltd. [cited on page 47.]

[197] Berg, W. R. *et al.* Light-Activated Assembly of DNA Origami into Dissipative Fibrils. *Angewandte Chemie International Edition* **62**, e202314458 (2023). URL https://onlinelibrary.wiley.com/doi/10.1002/anie.202314458. [cited on page 47.]

[198] Gavrilović, S., Brüggenthies, G. A., Weck, J. M., Heuer-Jungemann, A. & Schwille, P. Protein-Assisted Large-Scale Assembly and Differential Patterning of DNA Origami Lattices. *Small* 2309680 (2024). URL https://onlinelibrary.wiley.com/doi/10.1002/smll.202309680. [cited on pages 47, 48, and 143.]

[199] Tikhomirov, G., Petersen, P. & Qian, L. Fractal assembly of micrometre-scale DNA origami arrays with arbitrary patterns. *Nature* **552**, 67–71 (2017). URL https://doi.org/10.1038/nature24655. [cited on page 47.]

[200] Jungmann, R. *et al.* DNA origami-based nanoribbons: assembly, length distribution, and twist. *Nanotechnology* **22**, 275301 (2011). URL https://iopscience.iop.org/article/10.1088/0957-4484/22/27/275301. [cited on page 47.]

[201] Schnitzbauer, J., Strauss, M. T., Schlichthaerle, T., Schueder, F. & Jungmann, R. Super-resolution microscopy with DNA-PAINT. *Nature Protocols* **12**, 1198–1228 (2017). URL http://www.nature.com/articles/nprot.2017.024. [cited on page 47.]

[202] Schueder, F. *et al.* An order of magnitude faster DNA-PAINT imaging by optimized sequence design and buffer conditions. *Nature Methods* **16**, 1101–1104 (2019). URL http://www.nature.com/articles/s41592-019-0584-7. [cited on page 47.]

[203] Strauss, S. & Jungmann, R. Up to 100-fold speed-up and multiplexing in optimized DNA-PAINT. *Nature Methods* (2020). URL https://doi.org/10.1038/s41592-020-0869-x. [cited on page 47.]

[204] Kanwa, N., Gavrilovic, S., Brüggenthies, G. A., Qutbuddin, Y. & Schwille, P. Inducing Lipid Domains in Membranes by Self-Assembly of DNA Origami. *Advanced Materials Interfaces* **10**, 2202500 (2023). URL https://doi.org/10.1002/admi.202202500. Publisher: John Wiley & Sons, Ltd. [cited on pages 48 and 143.]

[205] Ramm, B., Khmelinskaia, A., Franquelim, H. G. & Schwille, P. in *Patterning DNA Origami on Membranes Through Protein Self-Organization* (eds Jonoska, N. & Winfree, E.) *Visions of DNA Nanotechnology at 40 for the Next 40* 411–431

(Springer Nature Singapore, Singapore, 2023). URL https://link.springer.com/10.1007/978-981-19-9891-1_22. Series Title: Natural Computing Series. [cited on page 49.]

[206] Zhulou, W. *et al.* Principles of fluorescence correlation spectroscopy applied to studies of biomolecular liquid–liquid phase separation. *Biophysics Reports* **7**, 1 (2022). URL http://www.biophysics-reports.org/en/article/id/f9a45a03-586c-4d18-8e8d-fb06fe655056. [cited on page 62.]

[207] Bracha, D. *et al.* Mapping Local and Global Liquid Phase Behavior in Living Cells Using Photo-Oligomerizable Seeds. *Cell* **175**, 1467–1480.e13 (2018). URL https://www.sciencedirect.com/science/article/pii/S0092867418314041. [cited on page 62.]

[208] Shakya, A. & King, J. T. DNA Local-Flexibility-Dependent Assembly of Phase-Separated Liquid Droplets. *Biophysical Journal* **115**, 1840–1847 (2018). URL https://linkinghub.elsevier.com/retrieve/pii/S0006349518311032. [cited on page 62.]

[209] Shakya, A., Park, S., Rana, N. & King, J. T. Liquid-Liquid Phase Separation of Histone Proteins in Cells: Role in Chromatin Organization. *Biophysical Journal* **118**, 753–764 (2020). URL https://www.sciencedirect.com/science/article/pii/S0006349519344078. [cited on page 62.]

[210] Chong, S. *et al.* Imaging dynamic and selective low-complexity domain interactions that control gene transcription. *Science* **361**, eaar2555 (2018). URL https://www.sciencemag.org/lookup/doi/10.1126/science.aar2555. [cited on page 62.]

[211] Alshareedah, I., Thurston, G. M. & Banerjee, P. R. Quantifying viscosity and surface tension of multicomponent protein-nucleic acid condensates. *Biophysical Journal* **120**, 1161–1169 (2021). URL https://linkinghub.elsevier.com/retrieve/pii/S0006349521000357. [cited on page 62.]

[212] Zhou, H.-X., Spille, J.-H. & Banerjee, P. R. (eds) *Phase-Separated Biomolecular Condensates: Methods and Protocols* Vol. 2563 of *Methods in Molecular Biology* (Springer US, New York, NY, 2023). URL https://link.springer.com/10.1007/978-1-0716-2663-4. [cited on pages 62 and 63.]

[213] Shakya, A. & King, J. T. Non-Fickian Molecular Transport in Protein–DNA Droplets. *ACS Macro Letters* **7**, 1220–1225 (2018). URL https://doi.org/10.1021/acsmacrolett.8b00565. Publisher: American Chemical Society. [cited on page 62.]

[214] Guillén-Boixet, J. *et al.* RNA-Induced Conformational Switching and Clustering of G3BP Drive Stress Granule Assembly by Condensation. *Cell* **181**, 346–361.e17 (2020). URL https://linkinghub.elsevier.com/retrieve/pii/S0092867420303421. [cited on pages 62 and 144.]

[215] Wei, M.-T. *et al.* Phase behaviour of disordered proteins underlying low density and high permeability of liquid organelles. *Nature Chemistry* **9**, 1118–1125 (2017). URL http://www.nature.com/articles/nchem.2803. [cited on page 62.]

[216] Donnert, G. *et al.* Macromolecular-scale resolution in biological fluorescence microscopy. *Proceedings of the National Academy of Sciences* **103**, 11440–11445 (2006). URL https://doi.org/10.1073/pnas.0604965103. Publisher: Proceedings of the National Academy of Sciences. [cited on page 62.]

[217] Widengren, J. & Rigler, R. Mechanisms of photobleaching investigated by fluorescence correlation spectroscopy. *Bioimaging* **4**, 149–157 (1996). URL https://doi.org/10.1002/1361-6374(199609)4:3<149::AID-BIO5>3.0.CO;2-D. Publisher: John Wiley & Sons, Ltd. [cited on page 62.]

[218] Petrášek, Z., Ries, J. & Schwille, P. in *Chapter 15 - Scanning FCS for the Characterization of Protein Dynamics in Live Cells* (ed.Walter, N. G.) *Methods in Enzymology*, Vol. 472 317–343 (Academic Press, 2010). URL https://www.sciencedirect.com/science/article/pii/S007668791072005X. [cited on pages 62 and 122.]

[219] Schlüßler, R. *et al.* Correlative all-optical quantification of mass density and mechanics of subcellular compartments with fluorescence specificity. *eLife* **11**, e68490 (2022). URL https://doi.org/10.7554/eLife.68490. Publisher: eLife Sciences Publications, Ltd. [cited on page 62.]

[220] Heintzmann, R. & Huser, T. Super-Resolution Structured Illumination Microscopy. *Chemical Reviews* **117**, 13890–13908 (2017). URL http://pubs.acs.org/doi/10.1021/acs.chemrev.7b00218. [cited on page 62.]

[221] Enderlein, J., Gregor, I., Patra, D., Dertinger, T. & Kaupp, U. B. Performance of Fluorescence Correlation Spectroscopy for Measuring Diffusion and Concentration. *ChemPhysChem* **6**, 2324–2336 (2005). URL http://doi.wiley.com/10.1002/cphc.200500414. [cited on page 62.]

[222] Lehmann, S., Seiffert, S. & Richtering, W. Refractive Index Mismatch Can Misindicate Anomalous Diffusion in Single-Focus Fluorescence Correlation Spectroscopy. *Macromolecular Chemistry and Physics* **216**, 156–163 (2015). URL http://doi.wiley.com/10.1002/macp.201400349. [cited on page 62.]

[223] Dix, J. A. & Verkman, A. Crowding Effects on Diffusion in Solutions and Cells. *Annual Review of Biophysics* **37**, 247–263 (2008). URL https://www.annualreviews.org/doi/10.1146/annurev.biophys.37.032807.125824. [cited on page 62.]

[224] Fisher, R. S. & Elbaum-Garfinkle, S. Tunable multiphase dynamics of arginine and lysine liquid condensates. *Nature Communications* **11**, 4628 (2020). URL https://doi.org/10.1038/s41467-020-18224-y. [cited on page 62.]

[225] Gidi, Y., Bayram, S., Ablenas, C. J., Blum, A. S. & Cosa, G. Efficient One-Step PEG-Silane Passivation of Glass Surfaces for Single-Molecule Fluorescence Studies. *ACS Applied Materials & Interfaces* **10**, 39505–39511 (2018). URL https://pubs.acs.org/doi/10.1021/acsami.8b15796. [cited on page 62.]

[226] Yao, R.-W. & Rosen, M. K. Advanced surface passivation for high-sensitivity studies of biomolecular condensates. *Proceedings of the National Academy of Sciences* **121**, e2403013121 (2024). URL https://pnas.org/doi/10.1073/pnas.2403013121. [cited on page 62.]

[227] Sherman, E. *et al.* Using Fluorescence Correlation Spectroscopy to Study Conformational Changes in Denatured Proteins. *Biophysical Journal* **94**, 4819–4827 (2008). URL https://www.sciencedirect.com/science/article/pii/S0006349508703497. [cited on page 63.]

[228] Pal, N., Verma, S. D., Singh, M. K. & Sen, S. Fluorescence Correlation Spectroscopy: An Efficient Tool for Measuring Size, Size-Distribution and Polydispersity of Microemulsion Droplets in Solution. *Analytical Chemistry* **83**, 7736–7744 (2011). URL https://doi.org/10.1021/ac2012637. Publisher: American Chemical Society. [cited on page 63.]

[229] Chattopadhyay, K., Saffarian, S., Elson, E. L. & Frieden, C. Measuring Unfolding of Proteins in the Presence of Denaturant Using Fluorescence Correlation Spectroscopy. *Biophysical Journal* **88**, 1413–1422 (2005). URL https://linkinghub.elsevier.com/retrieve/pii/S0006349505732070. [cited on page 63.]

[230] Banachowicz, E., Patkowski, A., Meier, G., Klamecka, K. & Gapiński, J. Successful FCS Experiment in Nonstandard Conditions. *Langmuir* **30**, 8945–8955 (2014). URL https://doi.org/10.1021/la5015708. Publisher: American Chemical Society. [cited on page 63.]

[231] Mahl, D., Diendorf, J., Meyer-Zaika, W. & Epple, M. Possibilities and limitations of different analytical methods for the size determination of a bimodal dispersion of metallic nanoparticles. *Colloids and Surfaces A: Physicochemical and Engineering Aspects* **377**, 386–392 (2011). URL https://linkinghub.elsevier.com/retrieve/pii/S0927775711000586. [cited on page 88.]

[232] Minelli, C. *et al.* Measuring the size and density of nanoparticles by centrifugal sedimentation and flotation. *Analytical Methods* **10**, 1725–1732 (2018). URL https://xlink.rsc.org/?DOI=C8AY00237A. [cited on page 88.]

[233] Caputo, F. *et al.* Measuring particle size distribution and mass concentration of nanoplastics and microplastics: addressing some analytical challenges in the sub-micron size range. *Journal of Colloid and Interface Science* **588**, 401–417 (2021). URL https://linkinghub.elsevier.com/retrieve/pii/S0021979720317094. [cited on page 88.]

[234] Hassan, P. A., Rana, S. & Verma, G. Making Sense of Brownian Motion: Colloid Characterization by Dynamic Light Scattering. *Langmuir* **31**, 3–12 (2015). URL https://doi.org/10.1021/la501789z. Publisher: American Chemical Society. [cited on pages 88 and 141.]

[235] Fischer, K. & Schmidt, M. Pitfalls and novel applications of particle sizing by dynamic light scattering. *Biomaterials* **98**, 79–91 (2016). URL https:

//linkinghub.elsevier.com/retrieve/pii/S0142961216301648. [cited on page 88.]

[236] Stetefeld, J., McKenna, S. A. & Patel, T. R. Dynamic light scattering: a practical guide and applications in biomedical sciences. *Biophysical Reviews* **8**, 409–427 (2016). URL http://link.springer.com/10.1007/s12551-016-0218-6. [cited on page 88.]

[237] Wohland, T., Rigler, R. & Vogel, H. The Standard Deviation in Fluorescence Correlation Spectroscopy. *Biophysical Journal* **80**, 2987–2999 (2001). URL https://linkinghub.elsevier.com/retrieve/pii/S0006349501762649. [cited on page 110.]

[238] Peulen, T.-O. *et al.* tttrlib: modular software for integrating fluorescence spectroscopy, imaging, and molecular modeling. *Bioinformatics* **41**, btaf025 (2025). URL https://academic.oup.com/bioinformatics/article/doi/10.1093/bioinformatics/btaf025/7965894. [cited on page 110.]

[239] Brock, R., Hink, M. A. & Jovin, T. M. Fluorescence Correlation Microscopy of Cells in the Presence of Autofluorescence. *Biophysical Journal* **75**, 2547–2557 (1998). URL https://linkinghub.elsevier.com/retrieve/pii/S0006349598776994. [cited on page 111.]

[240] Gong, S., Labanca, I., Rech, I. & Ghioni, M. *A simple and flexible FPGA based autocorrelator for afterpulse characterization of single-photon detectors*, 1–6 (IEEE, Castelldefels-Barcelona, Spain, 2014). URL http://ieeexplore.ieee.org/document/6808797/. [cited on pages 111 and 112.]

[241] Koppel, D. E. Statistical accuracy in fluorescence correlation spectroscopy. *Physical Review A* **10**, 1938–1945 (1974). URL https://link.aps.org/doi/10.1103/PhysRevA.10.1938. [cited on page 111.]

[242] Müller, B. K., Zaychikov, E., Bräuchle, C. & Lamb, D. C. Pulsed Interleaved Excitation. *Biophysical Journal* **89**, 3508–3522 (2005). URL https://linkinghub.elsevier.com/retrieve/pii/S000634950572991X. [cited on page 112.]

[243] Zhao, M. *et al.* Afterpulsing and its correction in fluorescence correlation spectroscopy experiments. *Applied Optics* **42**, 4031 (2003). URL https://www.osapublishing.org/abstract.cfm?URI=ao-42-19-4031. [cited on page 112.]

[244] Böhmer, M., Wahl, M., Rahn, H.-J., Erdmann, R. & Enderlein, J. Time-resolved fluorescence correlation spectroscopy. *Chemical Physics Letters* **353**, 439–445 (2002). URL http://linkinghub.elsevier.com/retrieve/pii/S0009261402000441. [cited on page 113.]

[245] Enderlein, J. & Gregor, I. Using fluorescence lifetime for discriminating detector afterpulsing in fluorescence-correlation spectroscopy. *Review of Scientific Instruments* **76**, 033102 (2005). URL http://aip.scitation.org/doi/10.1063/1.1863399. [cited on page 113.]

[246] Rüttinger, S., Kapusta, P., Patting, M., Wahl, M. & Macdonald, R. On the Resolution Capabilities and Limits of Fluorescence Lifetime Correlation Spectroscopy (FLCS) Measurements. *Journal of Fluorescence* **20**, 105–114 (2010). URL http://link.springer.com/10.1007/s10895-009-0528-1. [cited on page 113.]

[247] Enderlein, J. & Erdmann, R. Fast fitting of multi-exponential decay curves. *Optics Communications* **134**, 371–378 (1997). URL https://linkinghub.elsevier.com/retrieve/pii/S0030401896003847. [cited on page 114.]

[248] Margineanu, A. *et al.* Complexation of Lipofectamine and Cholesterol-Modified DNA Sequences Studied by Single-Molecule Fluorescence Techniques. *Biomacromolecules* **8**, 3382–3392 (2007). URL https://pubs.acs.org/doi/10.1021/bm700486q. [cited on page 115.]

[249] Ries, J. *et al.* Automated suppression of sample-related artifacts in Fluorescence Correlation Spectroscopy. *Optics Express* **18**, 11073 (2010). URL https://www.osapublishing.org/oe/abstract.cfm?uri=oe-18-11-11073. [cited on pages 115 and 120.]

[250] Seltmann, A., Carravilla, P., Reglinski, K., Eggeling, C. & Waithe, D. Neural network informed photon filtering reduces fluorescence correlation spectroscopy artifacts. *Biophysical Journal* **123**, 745–755 (2024). URL https://linkinghub.elsevier.com/retrieve/pii/S0006349524001322. [cited on page 115.]

[251] Fradin, C., Abu-Arish, A., Granek, R. & Elbaum, M. Fluorescence Correlation Spectroscopy Close to a Fluctuating Membrane. *Biophysical Journal* **84**, 2005–2020 (2003). URL https://linkinghub.elsevier.com/retrieve/pii/S0006349503750097. [cited on pages 119 and 122.]

[252] Benda, A. *et al.* How To Determine Diffusion Coefficients in Planar Phospholipid Systems by Confocal Fluorescence Correlation Spectroscopy. *Langmuir* **19**, 4120–4126 (2003). URL https://pubs.acs.org/doi/10.1021/la0270136. [cited on pages 120 and 122.]

[253] Kohler, J., Hur, K.-H. & Mueller, J. D. Autocorrelation function of finite-length data in fluorescence correlation spectroscopy. *Biophysical Journal* **122**, 241–253 (2023). URL https://linkinghub.elsevier.com/retrieve/pii/S0006349522008657. [cited on page 121.]

[254] Milon, S., Hovius, R., Vogel, H. & Wohland, T. Factors influencing fluorescence correlation spectroscopy measurements on membranes: simulations and experiments. *Chemical Physics* **288**, 171–186 (2003). URL https://linkinghub.elsevier.com/retrieve/pii/S0301010403000181. [cited on page 122.]

[255] Elsayad, K. *et al.* Spectrally coded optical nanosectioning (SpecON) with biocompatible metal-dielectric-coated substrates. *Proceedings of the National Academy of Sciences* **110**, 20069–20074 (2013). URL http://www.pnas.org/cgi/doi/10.1073/pnas.1307222110. [cited on page 123.]

[256] Krohn, J.-H. *Mirror-Enhanced Time-Resolved Fluorescence Spectroscopy to Probe Membrane Dynamics*. Master's thesis, Julius-Maximilians-Universität Würzburg, Würzburg (2019). [cited on page 123.]

[257] Sorscher, S. M. & Klein, M. P. Profile of a focussed collimated laser beam near the focal minimum characterized by fluorescence correlation spectroscopy. *Review of Scientific Instruments* **51**, 98–102 (1980). URL http://aip.scitation.org/doi/10.1063/1.1136028. [cited on page 122.]

[258] Štefl, M., Macháň, R. & Hof, M. in *Z-Scan Fluorescence Correlation Spectroscopy: A Powerful Tool for Determination of Lateral Diffusion in Biological Systems* (ed.Geddes, C. D.) *Reviews in Fluorescence 2009*, Vol. 2009 321–344 (Springer New York, New York, NY, 2011). URL http://link.springer.com/10.1007/978-1-4419-9672-5_12. Series Title: Reviews in Fluorescence. [cited on page 122.]

[259] Weinberger, A. *et al.* Gel-Assisted Formation of Giant Unilamellar Vesicles. *Biophysical Journal* **105**, 154–164 (2013). URL https://linkinghub.elsevier.com/retrieve/pii/S0006349513005808. [cited on page 124.]

[260] Felekyan, S. *et al.* Full correlation from picoseconds to seconds by time-resolved and time-correlated single photon detection. *Review of Scientific Instruments* **76**, 083104 (2005). URL https://doi.org/10.1063/1.1946088. Publisher: American Institute of Physics. [cited on page 124.]

[261] Kim, S. A., Heinze, K. G. & Schwille, P. Fluorescence correlation spectroscopy in living cells. *Nature Methods* **4**, 963–973 (2007). URL http://www.nature.com/articles/nmeth1104. [cited on page 125.]

[262] Newville, M. *et al.* lmfit/lmfit-py: 1.3.2 (2024). URL https://zenodo.org/doi/10.5281/zenodo.598352. [cited on page 128.]

[263] Huang, B., Perroud, T. D. & Zare, R. N. Photon Counting Histogram: One-Photon Excitation. *ChemPhysChem* **5**, 1523–1531 (2004). URL https://chemistry-europe.onlinelibrary.wiley.com/doi/10.1002/cphc.200400176. [cited on pages 131, 132, and 133.]

[264] Singer, S. & Nelder, J. Nelder-Mead algorithm. *Scholarpedia* **4**, 2928 (2009). URL http://www.scholarpedia.org/article/Nelder-Mead_algorithm. [cited on page 134.]

[265] Skakun, V. V., Digris, A. V. & Apanasovich, V. V. in *Global Analysis of Autocorrelation Functions and Photon Counting Distributions in Fluorescence Fluctuation Spectroscopy* (eds Engelborghs, Y. & Visser, A. J.) *Fluorescence Spectroscopy and Microscopy: Methods and Protocols* 719–741 (Humana Press, Totowa, NJ, 2014). URL https://doi.org/10.1007/978-1-62703-649-8_33. [cited on page 135.]

[266] Skilling, J. & Bryan, R. K. Maximum entropy image reconstruction: general algorithm. *Monthly Notices of the Royal Astronomical Society* **211**, 111–124 (1984). URL https://academic.oup.com/mnras/article-lookup/doi/10.1093/mnras/211.1.111. [cited on page 137.]

[267] Sengupta, P., Garai, K., Balaji, J., Periasamy, N. & Maiti, S. Measuring Size Distribution in Highly Heterogeneous Systems with Fluorescence Correlation

Spectroscopy. *Biophysical Journal* **84**, 1977–1984 (2003). URL https://www.sciencedirect.com/science/article/pii/S0006349503750061. [cited on page 137.]

[268] Xue, L., Jin, S., Nagasaka, S., Higgins, D. A. & Ito, T. Investigation of Molecular Diffusion at Block Copolymer Thin Films Using Maximum Entropy Method-Based Fluorescence Correlation Spectroscopy and Single Molecule Tracking. *Journal of Fluorescence* **32**, 1779–1787 (2022). URL https://doi.org/10.1007/s10895-022-02975-6. [cited on page 137.]

[269] Provencher, S. W. A constrained regularization method for inverting data represented by linear algebraic or integral equations. *Computer Physics Communications* **27**, 213–227 (1982). URL https://ui.adsabs.harvard.edu/abs/1982CoPhC..27..213P. [cited on page 137.]

[270] Starchev, K., Buffle, J. & Pérez, E. Applications of Fluorescence Correlation Spectroscopy: Polydispersity Measurements. *Journal of Colloid and Interface Science* **213**, 479–487 (1999). URL https://www.sciencedirect.com/science/article/pii/S0021979799961283. [cited on page 137.]

[271] Pánek, J., Loukotová, L., Hrubý, M. & Štěpánek, P. Distribution of Diffusion Times Determined by Fluorescence (Lifetime) Correlation Spectroscopy. *Macromolecules* **51**, 2796–2804 (2018). URL https://doi.org/10.1021/acs.macromol.7b02158. Publisher: American Chemical Society. [cited on page 137.]

[272] Tsekouras, K., Siegel, A., Day, R. & Pressé, S. Inferring Diffusion Dynamics from FCS in Heterogeneous Nuclear Environments. *Biophysical Journal* **109**, 7–17 (2015). URL https://linkinghub.elsevier.com/retrieve/pii/S0006349515005470. [cited on page 137.]

[273] Steinbach, P. *et al.* Determination of rate distributions from kinetic experiments. *Biophysical Journal* **61**, 235–245 (1992). URL https://linkinghub.elsevier.com/retrieve/pii/S0006349592818301. [cited on page 138.]

[274] Chen, H. *et al.* Ionic strength-dependent persistence lengths of single-stranded RNA and DNA. *Proceedings of the National Academy of Sciences* **109**, 799–804 (2012). URL https://pnas.org/doi/full/10.1073/pnas.1119057109. [cited on page 139.]

[275] Tavakoli, M. *et al.* Pitching Single-Focus Confocal Data Analysis One Photon at a Time with Bayesian Nonparametrics. *Physical Review X* **10** (2020). URL https://link.aps.org/doi/10.1103/PhysRevX.10.011021. [cited on page 142.]

[276] Tang, W. H. *et al.* Deep learning reduces data requirements and allows real-time measurements in imaging FCS. *Biophysical Journal* **123**, 655–666 (2024). URL https://linkinghub.elsevier.com/retrieve/pii/S000634952304119X. [cited on page 142.]

[277] Hübner, K. *et al.* Determining the In-Plane Orientation and Binding Mode of Single Fluorescent Dyes in DNA Origami Structures. *ACS Nano* **15**, 5109–5117

(2021). URL https://doi.org/10.1021/acsnano.0c10259. Publisher: American Chemical Society. [cited on page 143.]

[278] Zwicker, D., Seyboldt, R., Weber, C. A., Hyman, A. A. & Jülicher, F. Growth and division of active droplets provides a model for protocells. *Nature Physics* **13**, 408–413 (2017). URL http://www.nature.com/articles/nphys3984. [cited on page 144.]

[279] Donau, C. & Boekhoven, J. The chemistry of chemically fueled droplets. *Trends in Chemistry* **5**, 45–60 (2023). URL https://linkinghub.elsevier.com/retrieve/pii/S2589597422002751. [cited on page 144.]

[280] Feric, M. *et al.* Coexisting Liquid Phases Underlie Nucleolar Subcompartments. *Cell* **165**, 1686–1697 (2016). URL https://linkinghub.elsevier.com/retrieve/pii/S0092867416304925. [cited on page 144.]

Acknowledgements

Modern science is done by teams, not by individuals. While this statement is commonplace, I have seen research groups where this is not understood. I am fortunate and grateful that the Schwille lab where I did the work that forms the basis of this thesis is *not* such a place. I thank all members of the lab for their support, their ideas, and their patience in discussing and solving problems. I thank Petra especially for providing an environment where almost anything can be done, in terms of both scientific freedom and infrastructure. I also thank Yusuf for valuable albeit not always visible contributions to just about everything I worked on. And I thank Frank as well as the technicians for all the work they put into keeping the lab environment running smoothly. A special thanks also goes to my former MSc students Gereon, Lise, and Niko, as well as all the others who consulted me for advice or training: Your questions and doubts always were the best indicators for me to find gaps in my own knowledge.

Outside the Schwille lab, I would like to thank the communities of CeNS, IMPRS-ML, and ORIGINS: Although for different reasons I never was in touch with them as much as I would have liked, they were important for giving me orientation in my work, and for integrating me into the Munich scientific community. Similarly, I am grateful to Don Lamb and Ralf Jungmann for being genuinely useful TAC members. The MPIB Imaging Facility, the Munich microscopy community, and the various microscopy companies (especially ZEISS and Nikon) deserve special mention for countless insightful discussions and an amazing willingness to meet (often on short notice) at a microscope and try out this or that idea.

Finally, I would like to apologize to all those people with whom I started experiments that, most often due to poor time management more than anything else, never become a publication.